Coherent Control of a Single ^{13}C Nuclear Spin Strongly Coupled to a Tin-Vacancy Center in Diamond

Jeremias Resch

Karlsruhe 2026

Coherent Control of a Single ^{13}C Nuclear Spin Strongly Coupled to a Tin-Vacancy Center in Diamond

Zur Erlangung des akademischen Grades eines

DOKTORS DER NATURWISSENSCHAFTEN (Dr. rer. nat.)

von der KIT-Fakultät für Physik des
Karlsruher Instituts für Technologie (KIT) angenommene

DISSERTATION

von

Jeremias Resch, M.Sc.

aus Pforzheim

Tag der mündlichen Prüfung: 03.07.2026
Referent: Prof. Dr. David Hunger
Korreferent: Prof. Dr. Wolfgang Wernsdorfer

Zusammenfassung

Gruppe-IV-Farbzentren in Diamant eignen sich als Quantennetzwerkknoten, da sie optisch adressierbare elektronische Zustände mit Spinfreiheitsgraden in einem Festkörper kombinieren. Aufgrund ihrer Inversionssymmetrie können sie schmale und stabile optische Übergänge aufweisen. Für Anwendungen in Quantennetzwerken ist eine optische Schnittstelle allein jedoch nicht ausreichend. Vielmehr muss die Plattform auch kohärente Spinkontrolle, langlebige Quantenspeicher und Betrieb unter kryogenen Bedingungen ermöglichen.

Diese Arbeit untersucht das Zinn-Fehlstellen-Zentrum (SnV-Zentrum) in Diamant als Spin-Qubit-Plattform, mit einem Fokus auf die kohärente Kontrolle des SnV-Elektronenspins und eines ^{13}C-Kernspins in der unmittelbaren Umgebung. Supraleitende koplanare Wellenleiter werden verwendet, um Mikrowellen- und Radiofrequenzfelder bereitzustellen und gleichzeitig die in das kryogene System eingebrachte Wärme zu reduzieren.

Aufbauend auf dieser Elektronenspin-Kontrolle wird ein einzelner stark gekoppelter ^{13}C-Kernspin anhand seiner großen, optisch detektierten magnetischen Hyperfeinaufspaltung von etwa 45 MHz identifiziert. Durch die Kombination aus optischem und mikrowellenunterstütztem Pumpen wird eine präzise Initialisierung des Elektronen- und Kernspins erreicht. Kohärente Radiofrequenzkontrolle des Kernspins wird demonstriert, und eine Einzel-Qubit-Gatterfidelität von mehr als 99,9% gemessen. Durch dynamische Entkopplung wird die Kohärenzzeit des Kernspins auf 1,35 s verlängert.

Abschließend wird die Robustheit des Kernspins unter optischer Anregung untersucht. Die gemessene Differenz zwischen den Hyperfeinaufspaltungen im Grund- und im angeregten Zustand ist vergleichsweise klein. Dies deutet darauf hin, dass der Beitrag zur nuklearen Dephasierung durch differentielle Phasenakkumulation während der optischen Anregung schwach ist, auch wenn optisch induzierte Depolarisation weiterhin limitierend sein kann. Gleichzeitig zeigt die geringe Photonensammeleffizienz des Systems, dass Einbettung in photonische Strukturen für zukünftige Experimente mit effizienten optischen Schnittstellen erforderlich sein wird. Insgesamt demonstrieren diese Ergebnisse kohärente Kontrolle eines SnV-Elektronenspins und eines stark gekoppelten ^{13}C-Kernspins und liefern eine Grundlage, um SnV-basierte Systeme im Kontext zukünftiger Quantennetzwerkknoten zu untersuchen.

Abstract

Group-IV color centers in diamond are promising platforms for quantum-network nodes because they combine optically addressable electronic states with spin degrees of freedom in a solid-state host. Their inversion symmetry can lead to narrow and stable optical transitions, which are essential for spin-photon interfaces. For quantum-network applications, however, an optical interface alone is not sufficient. The system must also allow coherent spin control, provide access to long-lived quantum memories, and remain compatible with cryogenic operation.

In this thesis, we investigate the tin-vacancy (SnV) center in diamond as a spin-qubit platform, focusing on coherent control of the SnV electron spin and of a proximal ^{13}C nuclear spin. We use superconducting coplanar waveguides to deliver microwave and radio-frequency fields while reducing the heat introduced into the cryogenic system.

Building on this electron-spin control, we identify a single strongly coupled ^{13}C nuclear spin through a hyperfine splitting of approximately 45 MHz, resolved by optically detected magnetic resonance. By combining optical and microwave-assisted pumping, we achieve high-fidelity initialization of the electron and nuclear spins. We demonstrate coherent radio-frequency control of the nuclear spin, and randomized benchmarking yields single-qubit gate fidelities exceeding 99.9%. Dynamical decoupling extends the nuclear-spin coherence time to 1.35 s.

Finally, we investigate the robustness of the nuclear spin under optical excitation. The measured difference between the ground- and excited-state hyperfine splittings is small. This suggests that the dephasing contribution from differential nuclear phase accumulation during optical excitation is weak, although optical-excitation-induced depolarization may still limit the achievable fidelity. At the same time, the low photon collection efficiency of the bulk system highlights the need for photonic enhancement in future experiments, such as single-shot readout and cavity-enhanced light-matter interaction, which are important for achieving high entanglement rates in scalable quantum-network architectures. Taken together, our results demonstrate coherent control of an SnV electron spin and of a strongly coupled ^{13}C nuclear spin, and provide a basis for developing SnV-based systems in the context of future quantum-network nodes.

Contents

1. Introduction

Quantum networks [1] aim to connect remote quantum systems via optical photons, enabling new applications such as secure communication [2, 3], quantum computing [4, 5], and quantum-enhanced metrology [6]. A central requirement for building such a quantum network is a physical system that combines a long-lived stationary qubit with an efficient optical interface. The stationary qubit stores quantum information, while photons transfer it between remote nodes.

The main difficulty is that quantum information must be transmitted over long distances through lossy optical channels. Therefore, direct transmission is limited by photon loss. Even a small but finite absorption probability for a photon propagating through an optical fiber leads to an exponential loss of information with increasing distance, which limits the rate at which quantum information can be distributed [7–9]. Unlike classical signals, quantum information, more specifically an arbitrary quantum superposition state, cannot be amplified [10] to increase the maximum communication distance.

A quantum repeater [7] circumvents this limitation by segmenting a long communication channel into shorter links. Such devices allow entanglement to be established independently within each sub-link [8, 11, 12]. In subsequent entanglement-swapping steps, for example by performing Bell-state measurements, the entanglement can be extended across neighboring sub-links and thereby shared between the most distant nodes [12, 13]. This shared entanglement can then be used as a resource for quantum communication protocols, such as quantum teleportation [14, 15]. Detailed overviews of these concepts can be found, for example, in Refs. [11, 16].

The implementation of such a quantum repeater requires the ability to perform local operations on stationary qubits, the generation of entanglement between distant stationary qubits, and quantum memories capable of storing entangled states for sufficiently long times [8]. A quantum memory is needed because the success of entanglement-generation protocols is probabilistic [8, 9]. It allows successful segments to be preserved while only failed attempts have to be repeated. This is critical for achieving a scaling of the communication efficiency with channel length that is better than the direct exponential decay [8, 9]. Thus, the memory has to be long-lived so that quantum information can be stored for sufficiently long times even in protocols with low success probabilities. This leads to an important trade-off. To obtain long memory times, the memory qubit should be well decoupled from its local environment, since unwanted interactions lead to decoherence. However, the qubit cannot be completely isolated, because it still has to be initialized, read out, and controlled with high fidelity. A useful quantum memory therefore has to be isolated from noise, but accessible to control.

Spin defects in solids are promising candidates for such quantum-network nodes because they provide stationary spin qubits that can exhibit long coherence times, while their optical transitions allow the spin state to be optically addressed. To transfer information encoded in a photonic qubit to such a stationary memory, an efficient spin-photon interface is required. In addition to these requirements, the operating frequency of the spin-photon interface should either lie in the telecom band [17–19] or be convertible to it [12, 20–25] to enable operation over long distances.

Remote entanglement has been demonstrated in several material platforms [26], including quantum dots [17, 18], trapped ions [27], neutral atoms [22, 28], and color centers in diamond, in particular the nitrogen-vacancy center [29, 30] and the silicon-vacancy center [31].

Diamond color centers as solid-state quantum nodes. Color centers in diamond provide optically addressable electronic states within the wide bandgap of the host material. In the following, we discuss the main advantages and limitations of diamond color centers, following the overview in Ref. [26].

One key advantage of diamond is its clean solid-state environment. Owing to the low natural abundance of nuclear spins and charge carriers, as well as the possibility of growing isotopically purified material [32], diamond color centers can exhibit long electron-spin coherence times [33, 34]. These electronic systems can be further extended by coupling the electron spin to additional memory qubits, such as naturally occurring nuclear spins in the vicinity [35] or the host nuclear spin of the color center [36]. This makes color centers in diamond a promising material platform. Among the most mature color centers is the nitrogen-vacancy center, or NV center, which is so far the only solid-state spin-qubit platform for which entanglement between three individually addressable quantum-network nodes has been demonstrated [37].

In this experiment, entanglement is generated through the spontaneous emission of photons. First, spin-photon entanglement is created by preparing each qubit, i.e. the electron spin of the NV center, in a superposition state and subsequently applying a resonant optical pulse that probes one of the qubit eigenstates. This creates entanglement between the spin state and the presence or absence of a photon. The emitted photonic modes are then interfered on a beam splitter to erase which-path information. The detection of a single photon after the beam splitter heralds the desired spin-spin entangled state. [15, 26, 37]

However, the achievable entanglement rates are limited by the low emission probability of coherent and indistinguishable photons [15, 38, 39]. For the NV center, this is mainly caused by the low branching ratio into the zero-phonon line compared to the phonon sideband, i.e. the low Debye-Waller factor [40]. Therefore, even with high total collection efficiencies of up to 10% using photonic structures such as solid-immersion lenses [37, 41], the achievable entanglement rates between individual nodes remain limited to $\sim 10\,\mathrm{Hz}$ [37].

Incorporating color centers into optical resonators like photonic crystal nanocavities can increase the coupling between the emitter and the optical mode. This also enables alternative spin-photon entanglement schemes, such as reflection-based protocols [31, 42]. However, due to the static dipole moment of the NV center [43, 44], its optical transitions are very sensitive to charge fluctuations [45, 46]. As a result, incorporating NV centers into nanophotonic structures with nearby noisy surfaces remains challenging [47, 48], although recent work has shown promising progress in the integration of NV centers [44]. One other possible solution is the use of minimally processed diamond membranes of micron thickness [49] integrated into fiber-based Fabry-Pérot microcavities [50–53]. Nevertheless, within such micron-thin membranes the emitters can still be subject to severe spectral diffusion of the optical transition [39, 46, 54].

Group-IV color centers and the advantages of the SnV center. Group-IV color centers in diamond, such as the silicon-vacancy (SiV), germanium-vacancy (GeV), tin-vacancy (SnV), and lead-vacancy (PbV) centers, offer improved optical properties due to their inversion symmetry [26]. This symmetry leads to a higher branching ratio into the zero-phonon line [26, 55] and yields improved spectral stability even in the presence of nearby surfaces. This makes it possible to structure nanophotonic devices around group-IV color centers while maintaining the coherence of the emitted photons [56, 57].

A major drawback of group-IV centers is their sensitivity to phonon-induced dephasing [58]. This sensitivity originates from their electronic level structure: the ground state consists of two orbital branches that are additionally spin-degenerate in the absence of an external magnetic field. By contrast, the NV center does not contain a second low-lying orbital state in its ground-state spin manifold [59]. For the SiV center, the relatively small ground-state splitting therefore requires operation in the 100 mK regime to achieve long spin coherence times [60].

Nevertheless, the SiV center has become the most advanced group-IV platform for nanophotonic quantum-network experiments. Early work demonstrated the integration of SiV centers into diamond photonic crystal nanocavities, realizing a cavity-enhanced optical interface [61]. Subsequent experiments established the SiV electron spin as a quantum memory with single-shot readout at millikelvin temperatures [60] and developed integrated nanophotonic quantum registers based on an SiV electron spin coupled to nearby nuclear spins [62, 63]. These ingredients enabled memory-enhanced quantum communication using asynchronous Bell-state measurements [64], efficient generation of shaped single photons from an integrated nanophotonic system [57], and robust multi-qubit network nodes in which the SiV electron spin acts as an optical communication qubit while a strongly coupled nuclear spin serves as a long-lived memory [65]. More recently, SiV-based nanophotonic nodes have been interfaced with telecom photons using quantum frequency conversion [23], enabling remote entanglement of nanophotonic quantum memory nodes through deployed telecom fiber links [31]. These experiments define the present state of the art for group-IV quantum-network nodes, but they also highlight the demanding requirements of the SiV platform, in particular millikelvin operation, strain engineering, efficient microwave control with minimal heating, and robust nuclear-spin memories.

These results provide important design guidelines for group-IV quantum-network nodes. In memory-enhanced quantum communication, the electron spin provides the optical interface. However, using the same electron spin also as the memory makes the stored state sensitive to every photon interacting with the cavity [64]. Transferring the state to a nuclear spin can mitigate this problem, because the stored quantum information is then less sensitive to subsequent optical attempts. Nuclear spin memories can nevertheless dephase during optical readout because the hyperfine interaction differs between ground and excited states, as demonstrated in SiV-based multi-qubit nodes [65]. Weakly coupled ^{13}C spins can be robust under optical excitation, but their control generally requires more involved pulse protocols [63, 66, 67]. A strongly coupled proximal ^{13}C spin therefore offers an intermediate regime between direct controllability and optical robustness.

A second important requirement is efficient spin control with minimal heating. Previous SiV work identified microwave-induced heating as a limitation and motivated superconducting microwave delivery structures for low-temperature electron- and nuclear-spin control [60, 62, 63]. This requirement becomes particularly important in experiments where many microwave or radio-frequency pulses are needed for coherent control like dynamical decoupling.

The heavier group-IV centers provide a complementary route toward improved quantum-network nodes. Since the ground-state splitting increases for the heavier group-IV elements [68], phonon-induced dephasing is exponentially suppressed at the same operating temperature [69]. This allows heavier group-IV color centers to operate at elevated temperatures while maintaining the coherence properties. Among them, the SnV center is particularly promising because its large spin-orbit splitting can relax the temperature requirements compared with the SiV center. In addition, operating in a comparatively low-strain regime can preserve the strong anisotropy of the effective g-tensor in both the electronic ground and excited states. As a result, sizable splittings of spin-conserving optical transitions can be achieved already at moderate magnetic fields, corresponding to relatively low qubit frequencies.

However, this advantage comes with an additional challenge. Direct microwave driving of the spin transition is forbidden to first order because transitions between the two spin states also require a change in the orbital magnetic quantum number [26, 55]. The resulting microwave coupling depends on the ratio of strain to spin-orbit coupling and therefore becomes weaker for the heavier group-IV color centers. As a result, efficient microwave control becomes increasingly challenging. This is particularly relevant because microwave-induced heating can compromise operation at low temperatures.

A central requirement is therefore a detailed understanding of the spin and optical properties of the SnV center. These properties are governed by the interplay of spin-orbit coupling, strain, and the Zeeman interaction, leading to angle-dependent transition frequencies, strain-modified Rabi frequencies, and magnetic-field-dependent optical cyclicity. Based on this understanding, the coherent dynamics of the spin system can be described using the theoretical tools of driven two-level systems, phonon-induced relaxation models, spin-bath-induced dephasing, dynamical decoupling, and randomized benchmarking. This

framework forms the basis for the experimental and theoretical work presented in this thesis.

Scope of this thesis. This thesis studies coherent control and decoherence in a coupled electron-nuclear spin system formed by a single SnV center and a proximal ^{13}C nuclear spin. The experimental platform consists of single SnV centers in diamond coupled to superconducting microwave delivery structures. Optical excitation and photoluminescence detection provide initialization and readout, while microwave and radio-frequency fields drive the electron and nuclear spin transitions.

The central goal is to understand how spin-orbit coupling, strain, magnetic fields, hyperfine interaction, and optical excitation determine the control, coherence, and optical robustness of this system. First, a low-strain SnV center is characterized as an electron-spin qubit. Building on this, a strongly coupled ^{13}C nuclear spin is investigated as a potential quantum memory. Owing to its much smaller magnetic moment, the nuclear spin is less sensitive to magnetic noise and can exhibit substantially longer coherence times than the electron spin. At the same time, the hyperfine interaction enables electron-spin-assisted initialization, optical detection, and direct radio-frequency control of the nuclear spin.

This thesis is structured as follows. Chapter 2 introduces the physical properties of the negatively charged tin-vacancy center in diamond, including its electronic level structure, effective Hamiltonian, strain and magnetic-field dependence, and magneto-optical response. It also introduces the experimental platform and measurement techniques used throughout this work. Chapter 3 summarizes the theoretical framework for coherent spin control and decoherence, covering driven two-level dynamics, phonon-induced relaxation, spin-bath-induced dephasing, dynamical decoupling, and randomized benchmarking. Chapter 4 presents coherent control of the electron spin of a low-strain SnV center. Chapter 5 focuses on the coupled ^{13}C nuclear spin, including hyperfine interaction, initialization, radio-frequency control, gate benchmarking, dynamical decoupling, and coherence under optical excitation. Finally, Chapter 6 summarizes the main results and discusses future directions.

Relation to published work. Several results discussed in this thesis were obtained in close collaboration with Ioannis Karapatzakis and other co-workers and have been published in peer-reviewed journals [70, 71]. The experimental platform was developed jointly. In particular, the superconducting microwave waveguides were designed and fabricated by Ioannis Karapatzakis, while the optical measurements, spin-control experiments, and analysis presented in this thesis were carried out as part of this close collaborative project. This platform forms the experimental basis for the work presented here. The main contributions of this thesis are the coherent control of the electron spin of a low-strain SnV center and of a proximal ^{13}C nuclear spin, together with the analysis of spin control, coherence, and optical robustness in the coupled electron-nuclear system. Results that are discussed in the thesis of Ioannis Karapatzakis [72] are included where they provide necessary context.

2. Electronic structure and spectroscopy of the tin-vacancy center in diamond

Group-IV color centers in diamond combine favorable optical properties with single spin addressability. Their inversion symmetry leads to dominant emission into the coherent zero-phonon line and strongly reduces their sensitivity to electric-field noise due to the absence of a permanent electric dipole moment. At the same time, the presence of two orbital ground states introduces phonon-induced spin decoherence. Among the group-IV defects, the tin-vacancy (SnV) center has a comparably large orbital ground-state splitting of approximately 820 GHz, which makes it a particularly promising.

In this chapter, we develop an intuitive and quantitative description of the SnV center used in this thesis. We begin by establishing its level structure under the combined action of spin-orbit coupling, strain, and external magnetic fields. The resulting effective Hamiltonian defines the qubit splittings that form the basis for all subsequent discussions.

We then extend this static picture to include coherent microwave driving of the lowest spin sublevels. This leads to an effective Rabi frequency that depends on both strain and the relative orientation of the dc and ac magnetic fields with respect to the SnV quantization axis. After introducing the experimental setup and measurement techniques, we turn to the optical properties of the SnV center by considering resonant excitation between ground and excited states. The resulting spectra provide direct experimental access to e.g. strain and spectral stability. Finally, we introduce a rate-equation model for the so-called optical cyclicity, quantifying the average number of photons that can be scattered before an electron spin flip occurs. This framework connects the static energy level structure to the experimentally relevant process of spin initialization and optical readout.

2.1. Electronic level structure and effective Hamiltonian

The SnV center in diamond possesses a well-defined crystallographic symmetry. Its principal symmetry axis is aligned along the $\langle 111 \rangle$ direction of the diamond lattice. This axis is simultaneously a threefold rotation axis, which classifies the SnV center as a trigonal defect. The full symmetry of the defect is described by the D_{3d} point group. The creation of a vacancy in the diamond lattice results in sp^3-hybridized dangling bonds. In the case of the SnV center the electronic structure is dominated primarily by the six dangling bonds originating from the six nearest-neighbor carbon atoms surrounding the two vacancies. These six orbitals are energetically the most relevant and form the basis for constructing

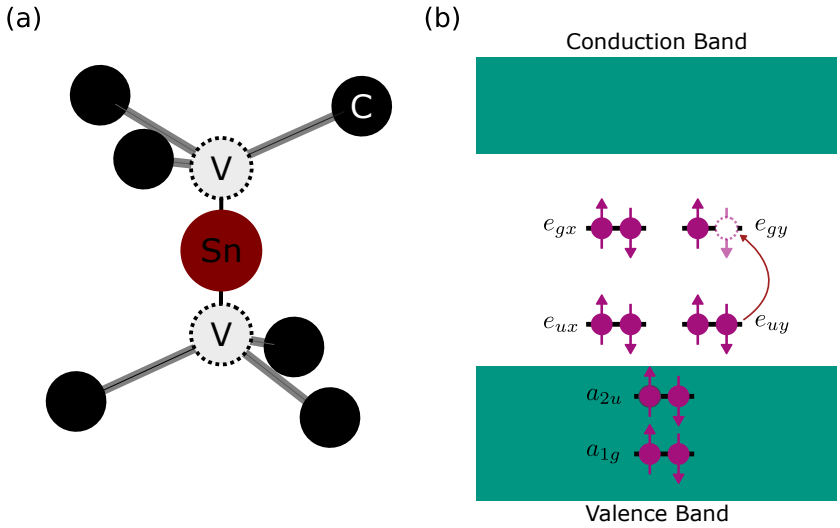

Figure 2.1.: The tin-vacancy (SnV) center in diamond. (a) Geometrical structure of the tin-vacancy center. A tin (Sn) atom occupies an interstitial position in the diamond lattice between two neighboring vacancies. The dangling bonds of the six adjacent next-neighbor carbon atoms form the molecular structure of the SnV center. (b) Electronic structure of the SnV center. The orbitals arise from symmetry-adapted linear combinations of the dangling-bond orbitals. A single hole in the e_g states forms the ground state. Upon excitation of an electron from the e_u states, a hole is created in the e_u manifold, forming the excited state. Energy shifts associated with the electronic excitation are not shown. As both configurations correspond to single-hole states, the SnV center forms an effective spin-1/2 system.

the electronic states of the defect. To account for the symmetry of the SnV center, linear combinations of these six dangling-bond orbitals are constructed such that they transform according to the symmetry operations of the D_{3d} point group. This procedure is carried out e.g. in Ref. [73] by projecting this dangling bonds onto the irreducible representations of the point group. In general, a representation of a point group is defined as a set of matrices that reproduce the multiplication rules of the group elements. If such a representation can be written in block-diagonal form and cannot be decomposed further into smaller sub-matrices, it is referred to as an irreducible representation. The number of irreducible representations of a group is equal to the number of its classes. The D_{3d} point group contains the following symmetry operations: the trivial identity operation, inversion, threefold rotations about the $\langle 111 \rangle$ axis, twofold rotations about axes along $\langle 1\bar{1}0 \rangle$, $\langle 01\bar{1} \rangle$ and $\langle 10\bar{1} \rangle$, mirror reflections, and improper rotations. These operations are grouped into six classes, and consequently the D_{3d} point group possesses six irreducible representations. By explicitly analyzing how the six dangling-bond orbitals transform under these symmetry operations, as performed in Ref. [73], one obtains the irreducible representation associated with the dangling bonds

$$\Gamma^{\sigma} = A_{1g} + E_g + A_{2u} + E_u \,, \tag{2.1}$$

where the superscript σ denotes the dangling-bond basis. The representations labeled by A are non-degenerate, whereas those labeled by E are twofold degenerate. The subscripts g (gerade) and u (ungerade) indicate even and odd parity under inversion, respectively. Comparing to spherical harmonics shows that the A_{1g} symmetry is related to the fully symmetric s-orbital, E_u to the p_x and p_y orbitals, A_{2u} to p_z and E_g to d-like orbitals with

non-zero magnetic quantum numbers. The symmetry-adapted eigenstates of the defect are obtained by forming specific linear combinations of the six dangling-bond orbitals that transform according to these irreducible representations. These linear combinations are known as symmetry-adapted linear combinations (SALCs) [73, 74]. The use of SALCs provides a basis for describing the electronic structure of the SnV center, as it explicitly incorporates the symmetry constraints. From density functional theory (DFT) calculations one knows the doubly degenerate e_g orbitals reside in the band gap of the diamond [75]. The e_u orbital lies close to the valence band with the energy gap to the valence band depending on the electron configuration [76]. The a_{1g} and a_{2u} orbital lie within in the valence band and thus don't contribute to the orbitals within the bandgap. Here lowercase letters are used, to distinguish the resulting orbitals from the corresponding irreducible representations of the point group. The negatively charged SnV center has eleven electrons occupying the ground-state configuration $a_{1g}^2 a_{2u}^2 e_u^4 e_g^3$ [75]: six originate from the dangling carbon bonds, four from the tin atom, and one from a nearby donor. As the e_g orbitals are degenerate, we can write the ground state as a hole in the one of the e_{gx} or e_{gy} states [73], which makes it effectively a single hole system and thus a spin 1/2 system [55]. This leads to the ground state

$$^2E_g = \{|e_{gy}\uparrow\rangle, |e_{gy}\downarrow\rangle, |e_{gx}\uparrow\rangle, |e_{gx}\downarrow\rangle\}, \tag{2.2}$$

where we explicitly wrote down the different possible spin orientations of the hole spin. The resulting ground-state configuration is shown in Fig. 2.1(b).

The excited state is created by exciting one electron from the e_u orbitals to the e_g orbitals, resulting in the configuration $a_{1g}^2 a_{2u}^2 e_u^3 e_g^4$. This is a dipole-allowed transition as the dipole operator $\hat{p}$ has the symmetry $A_{2u} + E_u$ in the D_{3d} symmetry, where A_{2u} represents the value $m_l = 0$ and E_u the values $m_l = \pm 1$ in the angular momentum picture. It can be shown that the matrix elements will not vanish due to symmetry reasons, if the matrix element has a contribution transforming under the fully symmetric representation A_{1g} or equivalently if the symmetry of the final state occurs in the product of the representations of the initial state with the dipole operator. So starting in e_u gives the transformed state $\hat{p}|e_u\rangle$ transforming as $(A_{2u} + E_u) \otimes E_u \propto A_{1g} + A_{2g} + E_g$, which contains E_g, meaning the transition to e_g orbitals is dipole allowed. This is on par with the discussion above, contributing E_u to p-like and E_g to d-like angular momentum and having a difference of $\Delta l = \pm 1$. Exciting one electron to the e_g orbitals fills them completely but leaves a single hole in the e_u orbitals. Thus the excited state can be written as

$$^2E_u = \{|e_{uy}\uparrow\rangle, |e_{uy}\downarrow\rangle, |e_{ux}\uparrow\rangle, |e_{ux}\downarrow\rangle\}. \tag{2.3}$$

Starting with these degenerate states for ground and excited state, one can look at perturbations on the defect. Especially for the SnV center spin-orbit coupling, Jahn-Teller effect, strain and external magnetic fields are relevant to describe the observed spectra.

All calculations of these perturbations presented in the following section are carried out for the electronic ground state of the SnV center. However, the same calculation applies directly to the excited state. Whenever it is necessary to explicitly distinguish between ground and excited states, the corresponding quantities are labeled by the superscripts g and e for ground and excited state, respectively.

2.1.1. Spin-orbit coupling

The spin-orbit interaction arises due to the relativistic coupling of the orbital motion of the electron inside the electric field potential of the Sn nucleus. The resulting orbital angular momentum and thus the resulting magnetic dipole moment couples to the intrinsic spin of the electron. The interaction energy of these two magnetic moments is given by

$$\hat{H}_{\mathrm{SO}} = -\lambda \boldsymbol{L} \cdot \boldsymbol{S}\,, \tag{2.4}$$

where $\boldsymbol{L} = (\hat{L}_x, \hat{L}_y, \hat{L}_z)$ is the orbital angular momentum operator and $\boldsymbol{S} = \frac{\hbar}{2}(\hat{\sigma}_x, \hat{\sigma}_y, \hat{\sigma}_z)$ the electron spin operator. The quantity λ represents the spin-orbit coupling strength [55, 73]. For the ground state one obtains a spin-orbit coupling strength of $\lambda^g = 820\,\mathrm{GHz}$ [70, 77]. This is larger than the coupling strength of the SiV center of 48 GHz [60] and larger than for the GeV center of 152 GHz [78].

For the excited state one observers a higher spin-orbit coupling constant of $\lambda^e = 3000\,\mathrm{GHz}$ [55, 79]. This can be attributed to the admixture of p-like Sn valence orbitals. This contribution has not been considered so far and is negligible for the E_g ground state, but becomes finite for the E_u excited state [73, 75]. As a result, the excited-state electron wavefunction has increased spatial overlap within the proximity the Sn nucleus. Since spin-orbit coupling depends on the gradient of the potential, this closer proximity to the Sn atom provides a qualitative explanation for the larger spin-orbit coupling in the excited state [74].

Carrying out the calculation of the orbital angular momentum operator $\boldsymbol{L}$ in the $D_{3\mathrm{d}}$ symmetry, one finds that only the $\hat{L}_z$ component remains as an effective operator with eigenvalues ± 1, as the z component is the only component coupling to the relevant e_g or e_u orbitals [73, 74]. The a_{2u} orbital, which is associated with the $m_l = 0$ magnetic quantum number, is much lower in energy and lies within the valence band [73]. This leaves the spin orbit coupling as

$$\hat{H}_{\mathrm{SO}}^{xy} = -\lambda \boldsymbol{L} \cdot \boldsymbol{S} = -\lambda \hat{L}_z \otimes \hat{S}_z = i\frac{\lambda}{2}\begin{pmatrix} 0 & -1 \\ 1 & 0 \end{pmatrix} \otimes \hat{\sigma}_z\,, \tag{2.5}$$

where the superscript xy denotes the explicit representation in the basis of the introduced e_{gxy} or e_{uxy} orbitals

$$\mathcal{B}^{xy} = \{|e_{gy}\uparrow\rangle, |e_{gy}\downarrow\rangle, |e_{gx}\uparrow\rangle, |e_{gx}\downarrow\rangle\}\,. \tag{2.6}$$

Solving the corresponding eigenvalue problem diagonalizes the spin-orbit Hamiltonian $\hat{H}_{\mathrm{SO}}^{xy}$. The normalized transposed matrix of eigenvectors is

$$\hat{T} = \frac{1}{\sqrt{2}}\begin{pmatrix} 0 & i & 0 & -i \\ -i & 0 & i & 0 \\ 0 & 1 & 0 & 1 \\ 1 & 0 & 1 & 0 \end{pmatrix}. \tag{2.7}$$

The change from the xy to spin-orbit basis can be done by the unitary transformation

$$\hat{H}_{\mathrm{SO}}^{so} = \hat{T}^{-1} \cdot \hat{H}_{\mathrm{SO}}^{xy} \cdot \hat{T}\,, \tag{2.8}$$

where $\hat{H}^{so}_{\mathrm{SO}}$ is the resulting diagonal matrix and the superscript *so* denoting the change into the new eigenbasis. Using this definition of the matrix $\hat{T}$ already captures the assignment of the aligned spin and orbital angular momentum as the lower energy branch belonging to the eigenvalue $-\lambda/2$ [55, 72]. Thus, we write the new eigenbasis, sorted in ascending order of energy, as

$$\mathcal{B}^{\mathrm{so}} = \{|e_- \downarrow\rangle, |e_+ \uparrow\rangle, |e_+ \downarrow\rangle, |e_- \uparrow\rangle\}, \tag{2.9}$$

where $|e_\pm\rangle$ are complex superpositions of the $|e_{gx}\rangle$ and $|e_{gy}\rangle$ eigenstates. This basis forms two spin-degenerate doublets, consisting of states with aligned and anti-aligned spin and orbital contributions.

Note that this electron-spin ordering differs from the convention used in our earlier work [70], where the ordering is given by

$$\{|e_+ \uparrow\rangle, |e_- \downarrow\rangle, |e_- \uparrow\rangle, |e_+ \downarrow\rangle\}. \tag{2.10}$$

There, the ordering was chosen to follow the structure of the Zeeman effect. In the following section, however, we present a theory closely related to that of Pieplow *et al.* [80]; we therefore adopt their convention for the ordering of the spin-orbit eigenstates. This choice does not change any physical observables, but care must be taken when comparing interaction Hamiltonians in different bases.

To obtain a more intuitive picture, one usually introduces an effective total angular momentum quantum number $m_j = \{\pm\frac{1}{2}, \pm\frac{3}{2}\}$. In this picture, the resulting $e_\pm$ orbitals are treated as effective $m_l = \pm 1$ states. This assignment follows from the structure of the spin-orbit eigenstates, which resemble the angular-momentum structure of p orbitals [73, 74]. Consequently, $m_j = \pm\frac{3}{2}$ corresponds to aligned orbital and spin angular momenta, whereas $m_j = \pm\frac{1}{2}$ corresponds to anti-aligned orientations. This is why the lower orbital branch of the ground state is commonly denoted as $E_g^{\frac{3}{2}}$, while the higher orbital branch is denoted as $E_g^{\frac{1}{2}}$ [55, 70, 72].

2.1.2. Effect of strain

Degenerate orbital states that couple to vibrational modes are subject to Jahn-Teller instabilities [81]. In the dynamical Jahn-Teller (DJT) regime vibronic mixing between the orbital doublet and the phonon-modes preserve the average symmetry rather than producing a static distortion. This vibronic coupling results in an effective quenching of the orbital angular momentum, which is the known as the Ham-reduction [55, 81]. The underlying reason is that the eigenstates are no longer purely electronic, but vibronic, i.e. coupled electronic-vibrational states [81]. As a consequence, both the spin-orbit coupling and the response to external magnetic fields are reduced compared to their bare electronic values [55], an effect we return to in Sec. 2.1.3.

For a linear DJT interaction, the coupling can be written as

$$\hat{H}^{xy}_{\mathrm{jt}} = \left(\Upsilon_x \hat{\sigma}_z + \Upsilon_y \hat{\sigma}_x\right) \otimes \hat{1}_2, \tag{2.11}$$

where Υ_x and Υ_y denote the DJT coupling strengths [73].

Due to external stress applied to the diamond lattice [69, 70], or internal strain arising from lattice imperfections, the SnV center is also subject to strain. This strain acts similar to the DJT on the orbitals and can be introduced under considerations of the defect symmetry [73] as

$$\hat{H}^{xy}_{\text{strain}} = (\epsilon_{A_1}\hat{1}_2 - \epsilon_{E_x}\hat{\sigma}_z + \epsilon_{E_y}\hat{\sigma}_x) \otimes \hat{1}_2\,. \tag{2.12}$$

The strain amplitudes ϵ can be rewritten using the strain tensor in the SnV center coordinate frame [69, 82, 83] as

$$\epsilon_{A_1} = t_\perp(\epsilon_{xx} + \epsilon_{yy}) + t_\parallel\epsilon_{zz}\,, \tag{2.13}$$
$$\epsilon_{E_x} = d(\epsilon_{xx} - \epsilon_{yy}) + f\epsilon_{zx}\,, \tag{2.14}$$
$$\epsilon_{E_y} = -2d\epsilon_{xy} + f\epsilon_{yz}\,. \tag{2.15}$$

From Eq. 2.12 one can directly see that the ϵ_{A_1} component just results in a global shift of all orbitals and is thus often omitted. The strain-susceptibilities d and f can be calculated using DFT and are given e.g. in Ref. [82].

From now on, we will follow closely the derivation of the perturbations of the ground-state Hamiltonian done by Pieplow *et al.* [80].

We assume uniaxial stress, which reduces the strain Hamiltonian to

$$\hat{H}^{xy}_{\text{strain, uniaxial}} = -\left(d(\epsilon_{xx} - \epsilon_{yy})\hat{\sigma}_z + 2de_{xy}\hat{\sigma}_x\right) \otimes \hat{1}_2\,. \tag{2.16}$$

Repeating the same procedure as performed above for the spin-orbit coupling and diagonalizing now the sum of spin-orbit $\hat{H}^{xy}_{\text{SO}}$, DJT $\hat{H}^{xy}_{\text{jt}}$ and strain $H^{xy}_{\text{strain, uniaxial}}$ contributions, results in the new eigenbasis

$$\mathcal{B}^{jt} = \{|\tilde{e}_-\downarrow\rangle, |\tilde{e}_+\uparrow\rangle, |\tilde{e}_+\downarrow\rangle, |\tilde{e}_-\uparrow\rangle\}\,, \tag{2.17}$$

with the corresponding eigenvalues

$$\nu = \frac{1}{2}\sqrt{\lambda^2 + 4\alpha^2}\,. \tag{2.18}$$

To simplify the result, we defined the variables $\alpha = \sqrt{v_x^2 + v_y^2}$, $v_x = -d(\epsilon_{xx} - \epsilon_{yy}) + \Upsilon_x$, and $v_y = -2d\epsilon_{xy} + \Upsilon_y$. We follow the sign convention for the strain amplitudes used in Refs. [69, 82]. In contrast to Ref. [80], factors of $\frac{1}{2}$ are not absorbed into the coupling constants.

The unitary transformation from $\mathcal{B}^{xy}$ to $\mathcal{B}^{jt}$ is given by

$$\hat{P} = \frac{1}{\sqrt{1 + \frac{4(\nu - v_x)^2}{\lambda^2 + 4v_y^2}}} \begin{pmatrix} 0 & \frac{2v_x - 2\nu}{2v_y + i\lambda} & 0 & \frac{2v_x + 2\nu}{2v_y + i\lambda} \\ \frac{2v_x - 2\nu}{2v_y - i\lambda} & 0 & \frac{2v_x + 2\nu}{2v_y - i\lambda} & 0 \\ 0 & 1 & 0 & 1 \\ 1 & 0 & 1 & 0 \end{pmatrix}. \tag{2.19}$$

Considering the first eigenstate of the new eigenbasis $\mathcal{B}^{jt}$, we obtain

$$|\tilde{e}_- \downarrow\rangle = \frac{1}{\sqrt{1 + \frac{4(\nu - v_x)^2}{\lambda^2 + 4v_y^2}}} \left(\frac{2v_x - \nu}{2v_y - i\lambda} |e_{gy} \downarrow\rangle + |e_{gx} \downarrow\rangle \right) . \tag{2.20}$$

In the absence of strain and DJT interactions, this state reduces to the pure the spin-orbit eigenstate $|\tilde{e}_- \downarrow\rangle \rightarrow |e_- \downarrow\rangle$. In contrast, in the limit of dominant ϵ_{E_x} strain, the eigenstate approaches the pure orbital state $|\tilde{e}_- \downarrow\rangle \rightarrow |e_{gx} \downarrow\rangle$. This behavior reflects the competition between strain and spin-orbit coupling in determining the orbital character of the eigenstates. While spin-orbit coupling favors complex orbital combinations, strong strain aligns the orbital wavefunction along the symmetry axes of the defect [69].

2.1.3. Zeeman response to a static magnetic field

The response of the system to an external dc magnetic field is described by the Zeeman effect, which consists out of an orbital and spin contribution.

Orbital Zeeman effect. The orbital contribution to the Zeeman effect can be written as

$$\hat{H}_{\mathrm{ZL}} = \gamma_l B_z \hat{f}_{\{\pm\frac{3}{2},\pm\frac{1}{2}\}} \hat{L}_z \otimes \hat{1}_2 . \tag{2.21}$$

The factor γ_l denotes the gyromagnetic ratio given by $\gamma_l = \mu_{\mathrm{B}}/\hbar = 14\,\mathrm{GHz\,T^{-1}}$. The matrix $\hat{f}_{\{\pm\frac{3}{2},\pm\frac{1}{2}\}}$ incorporates the quenching of the orbital angular momentum due to the DJT, with the subscripts indicating the dependency on the magnetic quantum number. The corresponding quenching factor can be expressed as a product out of two contributions $f_{m_j} = p_{m_j} g_{m_j}$, where p_{m_j} is the Ham-reduction factor due to the DJT effect and g_{m_j} the so-called Steven's factor [55]. The Steven's factor reflects the absence of a full rotational symmetry of the orbital wavefunctions, which instead transform with the symmetry of the point group of the defect, making the $\hat{L}_z$ an effective operator only. Further, the e_g orbitals, which are considered to be $m_l = +1$ orbitals, gain an admixture of $m_l = -2$ components, leading to a further reduction of the orbital angular momentum [55]. For the e_u orbitals, the p-like orbitals of the Sn contribute more, leading to less reduction. Experimentally, only the product of both, i.e. f_{m_j}, can accessed.

Assigning separate quenching factors to the effective total angular momentum j of the lower and upper orbital branches allows for a more precise characterization of orbital quenching than the commonly used mean quenching factor f and asymmetry parameter δ [55, 82, 84]. Nevertheless, we later adopt the mean quenching factor and asymmetry parameter to keep the theory compact. This simplification is justified by our earlier work [70], where the individual quenching factors were determined with high precision by comparing SnV centers subject to different strain magnitudes. This distinction is important, as for an unstrained emitter and a magnetic field aligned with the defect quantization axis the Zeeman splitting of the lower orbital branch depends solely on the $m_j = \pm\frac{3}{2}$ quenching

factor [70]. In contrast, for strained emitters the splitting of the lower branch also acquires a dependence on the $m_j = \pm\frac{1}{2}$ contribution, which can be determined from these strained emitters.

Writing the orbital Zeeman effect in the spin-orbit basis is straight-forward, when keeping the ordering of the eigenstates in mind, and results in the Hamiltonian

$$\hat{H}^{so}_{\mathrm{ZL}} = \gamma_l B_z \begin{pmatrix} -f_{\frac{3}{2}} & 0 & 0 & 0 \\ 0 & f_{\frac{3}{2}} & 0 & 0 \\ 0 & 0 & f_{\frac{1}{2}} & 0 \\ 0 & 0 & 0 & -f_{\frac{1}{2}} \end{pmatrix}, \tag{2.22}$$

where we dropped the ±1 in the subscript for better readability. A transformation into the xy-basis can be performed by using the transformation matrix $\hat{T}$ introduced above, resulting in

$$\hat{H}^{xy}_{\mathrm{ZL}} = \frac{\gamma_l B_z}{2} \begin{pmatrix} f_{\frac{3}{2}} - f_{\frac{1}{2}} & 0 & i\left(f_{\frac{3}{2}} + f_{\frac{1}{2}}\right) & 0 \\ 0 & f_{\frac{1}{2}} - f_{\frac{3}{2}} & 0 & i\left(f_{\frac{3}{2}} + f_{\frac{1}{2}}\right) \\ -i\left(f_{\frac{3}{2}} + f_{\frac{1}{2}}\right) & 0 & f_{\frac{3}{2}} - f_{\frac{1}{2}} & 0 \\ 0 & -i\left(f_{\frac{3}{2}} + f_{\frac{1}{2}}\right) & 0 & f_{\frac{3}{2}} - f_{\frac{1}{2}} \end{pmatrix}. \tag{2.23}$$

One can directly see, that the orbital Zeeman effect does not mix the electron spin states, but the e_x and e_y orbitals into each other.

Electron-spin Zeeman effect. The electron-spin contribution to the Zeeman effect in the xy basis is given by

$$\hat{H}^{xy}_{\mathrm{ZS}} = \gamma_s \hat{1}_2 \otimes \hat{\boldsymbol{S}} \cdot \boldsymbol{B} = \frac{\gamma_s}{2} \begin{pmatrix} B_z & B_\perp & 0 & 0 \\ B_\perp^* & -B_z & 0 & 0 \\ 0 & 0 & B_z & B_\perp \\ 0 & 0 & B_\perp^* & -B_z \end{pmatrix}, \tag{2.24}$$

where γ_s is the gyromagnetic ratio for a free electron of $\gamma_s = g\mu_\mathrm{B}/\hbar = 28\,\mathrm{GHz\,T^{-1}}$ and $B_\perp = B_x - iB_y$. Following Ref. [80], we express the full Zeeman Hamiltonian in the combined spin-orbit, DJT and strain eigenbasis $\mathcal{B}^{jt}$ introduced in Eq. 2.17. The Hamiltonian in this basis is obtained by a unitary basis transformations according to

$$\hat{H}^{jt}_{\mathrm{Z}} = \hat{H}^{jt}_{\mathrm{ZL}} + \hat{H}^{jt}_{\mathrm{ZS}} = \hat{P}^{-1} \cdot \left(\hat{H}^{xy}_{\mathrm{ZL}} + \hat{H}^{xy}_{\mathrm{ZS}}\right) \cdot \hat{P}\,, \tag{2.25}$$

where $\hat{P}$ represents the transformation into the combined basis given in Eq. 2.19.

Performing this transformation explicitly, the Zeeman Hamiltonian can be written in the block form

$$\hat{H}^{jt}_{\mathrm{Z}} = \begin{pmatrix} \hat{\omega} & \hat{\Omega}/2 \\ \hat{\Omega}^\dagger/2 & \hat{\Delta} \end{pmatrix}. \tag{2.26}$$

This represents the Zeeman Hamiltonian in an intuitive way. The lower orbital branch of $\mathcal{B}^{jt}$, i.e. the states $\{|\tilde{e}_- \downarrow\rangle, |\tilde{e}_+ \uparrow\rangle\}$, are represented by the sub-matrix $\hat{\omega}$ and the higher orbital branch by the sub matrix $\hat{\Delta}$. The off-diagonals $\hat{\Omega}$ represent the coupling between these two orbital branches.

The sub-matrices can be explicitly calculated. For the lower orbital branch, one obtains

$$\hat{\omega}^{jt} = \gamma_s \left(\Phi(B_x, B_y)\sigma_x + \Phi(-B_y, B_x)\sigma_y + \Theta(B_z)\sigma_z\right) . \tag{2.27}$$

This expression has the form of an effective Zeeman Hamiltonian for a spin-1/2 system, with the Pauli matrices acting in the subspace of the lower orbital branch. The function $\Phi(B_x, B_y)$ describes the coupling to transverse magnetic field components and arise from the interplay of spin-orbit coupling, DJT interaction and strain, as discussed above. In contrast, the term $\Theta(B_z)$ captures the coupling to a magnetic field component aligned with the defect symmetry axis. This coupling to the parallel field component is given by

$$\Theta(B_z) = -B_z \left(\frac{\gamma_l}{\gamma_s}\left(f\cos(x) + \delta\right) + \frac{1}{2}\right) , \tag{2.28}$$

while the transverse coupling is given by

$$\Phi(B_x, B_y) = \frac{1}{2(\lambda^2 + 4v_y^2)}\left(4B_x v_y^2 + 2B_y v_y \lambda + 2v_x \cos(x)(-2v_y B_y + \lambda B_x)\right) . \tag{2.29}$$

Here, the average orbital quenching factor and asymmetry are defined as

$$f = \frac{1}{2}\left(f_{\frac{1}{2}} + f_{\frac{3}{2}}\right), \quad \delta = \frac{1}{2}\left(f_{\frac{3}{2}} - f_{\frac{1}{2}}\right) , \tag{2.30}$$

and the strain-spin-orbit-mixing angle is given by

$$x = \arctan(2\alpha/\lambda) . \tag{2.31}$$

To simplify the response to external magnetic fields, we use the adiabatic elimination approach introduced in Refs. [80, 85], which allows us to reduce the dynamics to the relevant qubit subspace formed by the lower orbital branch. To achieve this, we decompose the full state vector into a relevant component

$$\boldsymbol{\psi}(t) = (|\tilde{e}_- \downarrow\rangle(t), |\tilde{e}_+ \uparrow\rangle(t)) \tag{2.32}$$

and an irrelevant part $\boldsymbol{\epsilon}(t)$ associated with the upper orbital branch. This decomposition leads to the coupled Schrödinger equations

$$i\frac{\partial}{\partial t}\boldsymbol{\psi}(t) = \hat{\omega}\boldsymbol{\psi}(t) + \frac{\hat{\Omega}}{2}\boldsymbol{\epsilon}(t) , \tag{2.33}$$

$$i\frac{\partial}{\partial t}\boldsymbol{\epsilon}(t) = \hat{\Delta}\boldsymbol{\epsilon}(t) + \frac{\hat{\Omega}^\dagger}{2}\boldsymbol{\psi}(t) . \tag{2.34}$$

$$\tag{2.35}$$

If the conditions

$$|\hat{\omega}| \ll |\hat{\Delta}|, \quad |\hat{\Omega}| \ll |\hat{\Delta}| \tag{2.36}$$

are satisfied, i.e. the coupling between relevant and irrelevant subspace is small compared to the energy detuning of the irrelevant subspace, the second equation can be set to zero. This approximation is called the adiabatic elimination [85]. Solving for $\boldsymbol{\epsilon}(t)$ and substituting the result into the first equation for $\boldsymbol{\psi}(t)$ yields the effective Hamiltonian

$$\hat{H}^{\text{eff}} = \hat{\omega} - \frac{1}{4}\hat{\Omega}\hat{\Delta}^{-1}\hat{\Omega}^{\dagger}\,. \tag{2.37}$$

The second term introduces corrections on the order of $|\Omega|^2/|\Delta|$ to the diagonal and off-diagonal terms of the effective Hamiltonian $\hat{H}^{\text{eff}}$ [85]. For a large spin-orbit coupling, corresponding to a large $|\hat{\Delta}|$, these corrections can be neglected [80]. Thus, we set the effective Hamiltonian to

$$\hat{H}_{\text{Z}}^{jt,\text{eff}} = \hat{\omega} = \gamma_s \left(\Phi(B_x, B_y)\sigma_x + \Phi(-B_y, B_x)\sigma_y + \Theta\sigma_z\right)\,. \tag{2.38}$$

Diagonalizing this Hamiltonian yields $\hat{H}_{\text{Z}} = -\frac{\Delta_q}{2}\sigma_z$ with the spin splitting, or also called qubit splitting,

$$\Delta_q = 2\gamma_s\sqrt{\Theta^2 + \Phi(B_x, B_y)^2 + \Phi(-B_y, B_x)^2} = \gamma_s\sqrt{4\Theta^2 + B_{\perp}^2\sin(x)^2}\,. \tag{2.39}$$

We note that, assuming a common quenching factor as in Ref. [80], i.e. setting $\delta = 0$, the diagonal terms in Eq. 2.38 reproduce the results reported in the reference. Further, Ref. [80] uses an electron-spin gyromagnetic ratio that is smaller by a factor of two than the convention used here; throughout this thesis, we use the standard convention $\gamma_s = g\mu_{\text{B}}/\hbar$.

This simple expression for the qubit splitting allows to look at the interplay of strain and off-axis fields on the system. The sine term in the qubit splitting reflects the strain-induced off-axis magnetic field susceptibility of the system. As illustrated in Figure 2.2(b), for infinite strain the sine term approaches unity giving an equal response of the SnV center to every B-field orientation. This can be understood as the strain removing fully the quantization axis given by the spin-orbit coupling as discussed in the previous section. On the other hand in the case of zero strain only the cosine term in the parallel coupling $\Theta(B_z)$ remains, making the system fully sensitive to the spin-orbit quantization and removes the influence of off-axis B-field components in the qubit splitting.

This can also be thought of an anisotropic g tensor of the SnV center. The g tensor is axially symmetric and coaxial to the SnV center's quantization axis and thus has two independent components $g_{\perp}$ and $g_{\parallel}$ [86, 87]. The experimentally observed value of g thus depends on the polar angle between applied magnetic field and the principle axis θ_{dc} and can be written as [86]

$$g(\theta_{\text{dc}}) = \sqrt{g_{\parallel}^2\cos^2(\theta_{\text{dc}}) + g_{\perp}^2\sin^2(\theta_{\text{dc}})}\,. \tag{2.40}$$

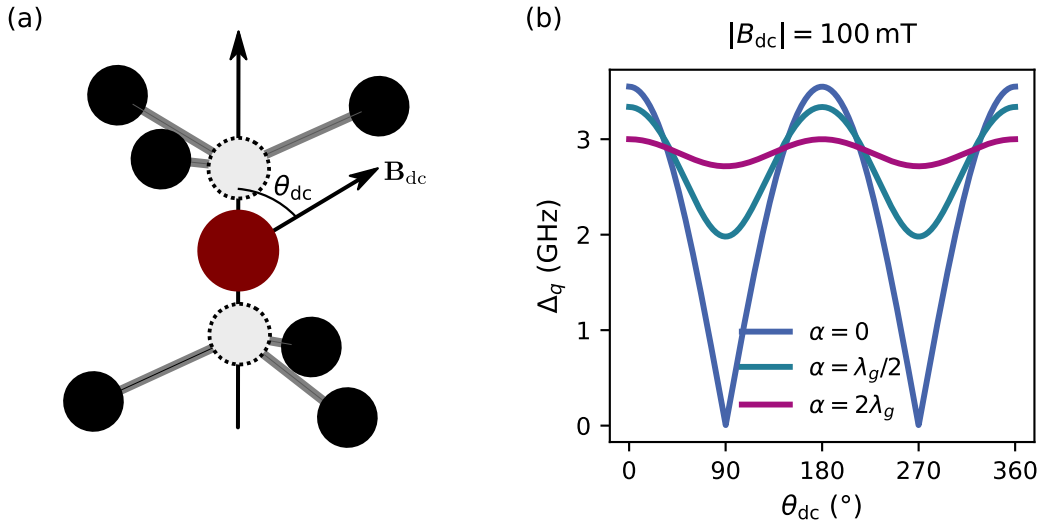

Figure 2.2.: The tin-vacancy center under off-axis magnetic fields. (a) Schematic depicting the SnV center and an external dc magnetic field with respect to the quantization axis. (b) The calculated qubit splitting as a function of the polar angle towards the SnV quantization axis depicted for different strain amplitudes. No splitting is observed for zero strain under an external field applied perpendicular to the quantization axis. For increasing strain the splitting approaches that for an free electron for arbitrary field orientations.

The components $g_\parallel$ and $g_\perp$ can be computed by comparing the Zeeman splitting to a free electron. This yields

$$g_\parallel = g\,(f\cos(x) + \delta + 1)\,, \tag{2.41}$$

and

$$g_\perp = g\sin(x)\,, \tag{2.42}$$

where $g \approx 2$ is the g-factor of a free electron. For example, for a strain of $\alpha_g = 41\,\mathrm{GHz}$, which matches the experimental value for the SnV center used within this thesis, evaluating Eq. 2.28 yields $g_\parallel/g \approx 1.27$ and $g_\perp/g \approx 0.1$, making the tensor highly anisotropic. For $\alpha_g \gg \lambda_{so}$, both ratios approach unity, as shown in Fig. 2.4.

The difference in g between the ground and excited states separates the spin-conserving optical transitions. In systems with a larger strain-to-spin-orbit-coupling ratio, such as the SiV center, strain can exceed the spin-orbit coupling. In this regime, much larger dc magnetic fields are required to resolve the spin-conserving optical transitions [65].

To compare the qubit splitting with formulas derived in our earlier work [70] and to provide intuition for experimental settings, we consider selected strain magnitudes and external magnetic-field orientations. As a first case, assuming a magnetic field purely along the quantization axis of the SnV center and no strain or DJT effect, we retrieve the qubit splitting as

$$\Delta_q(B = B_z, \alpha = 0) = \left(\gamma_s + 2\gamma_I f_{\frac{3}{2}}\right) B_z\,. \tag{2.43}$$

For a purely perpendicular field $B = B_\perp$ and finite strain, we get the simple relation

$$\Delta_q(B = B_\perp) = \gamma_s |B_\perp| \sin(x)\,, \tag{2.44}$$

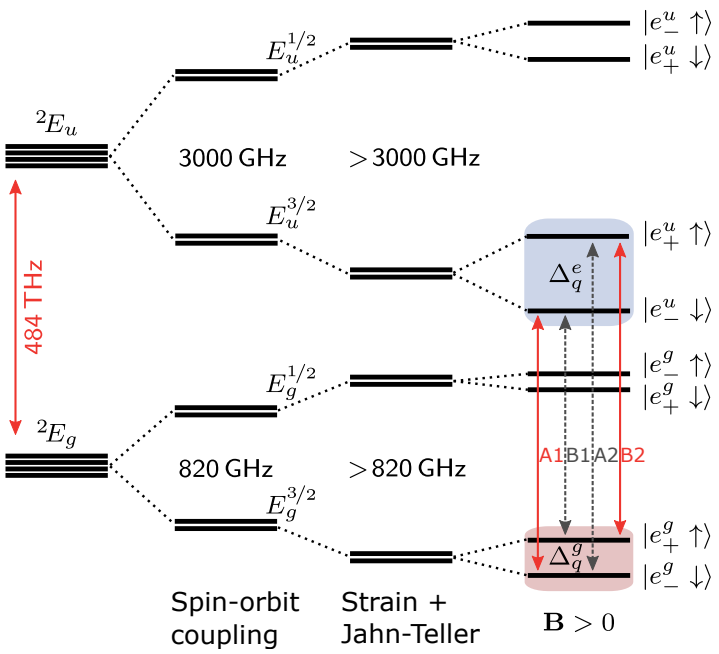

Figure 2.3.: Level scheme of the SnV center including spin-orbit coupling, DJT interaction, strain, and an external dc magnetic field $\boldsymbol{B}$. Spin-orbit coupling lifts the fourfold orbital degeneracy and results in two spin-degenerate doublets. Strain and the DJT interaction further shift and mix these levels. The application of an external dc magnetic field removes the remaining spin degeneracy via the Zeeman interaction. The light red and light blue boxes indicate the energy levels that are relevant for the experiments and theoretical analysis presented throughout this thesis. Additionally, the spin-conserving optical transitions A1 and B2, as well as the spin-flipping transitions, are depicted. On the right-hand side, the corresponding orbital and spin eigenstates are shown in the spin-orbit-basis.

which allows for the determination of the strain magnitude using perpendicular magnetic fields.

Experimentally, the qubit frequency is not directly accessible without knowing the positions of the optical transitions under an applied magnetic field. It is therefore more useful to consider the frequency difference between the spin-conserving transitions A1 and B2, indicated in Fig. 2.3. This difference can be expressed as the difference between the ground-state qubit splitting and the splitting of the lowest excited-state spin doublet:

$$\mathrm{A1} - \mathrm{B2} = \Delta^g_q - \Delta^e_q \,. \tag{2.45}$$

For example for purely perpendicular magnetic fields, this results in

$$\mathrm{A1} - \mathrm{B2} = \gamma_s |B_\perp| \left\{ \sin\left[\arctan\left(\frac{2\alpha^g}{\lambda^g}\right)\right] - \sin\left[\arctan\left(\frac{2\alpha^e}{\lambda^e}\right)\right] \right\} . \tag{2.46}$$

As λ^g and λ^e are known, only the strain magnitudes in ground and excited state are left as parameters. Using the coarse relation that $\alpha^e \approx 1.7\alpha^g$ [70], one can use this magnetic field setting for a fast estimation of the strain magnitude without the need of a full angle dependent fit of the Hamiltonian.

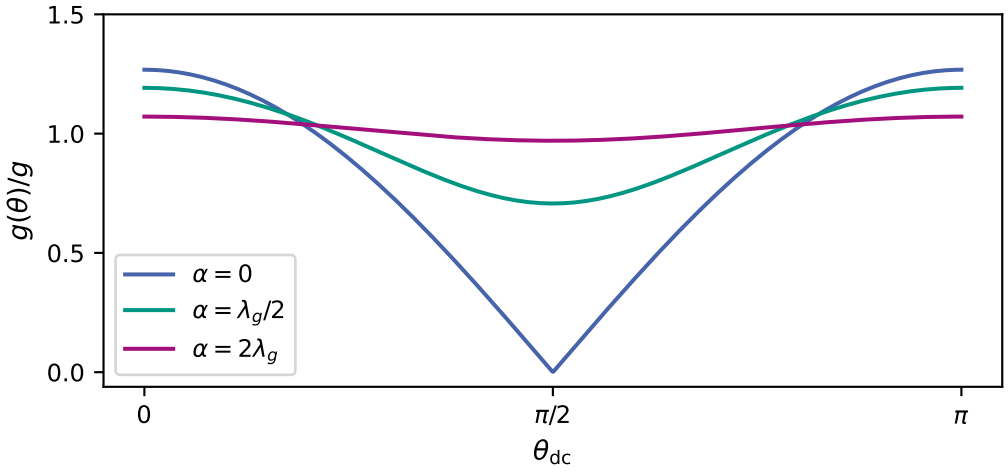

Figure 2.4.: Anisotropic g tensor of the SnV center. The tensor is axially symmetric coaxial to the SnV centers quantization axis and thus depends only on the angle θ_{dc}. For low strain a high asymmetry is observed, for high strain the g value approaches that of the free electron of $g = 2$ for any magnetic field angle.

2.2. Strain- and magnetic-field-dependent spin driving

The two lowest-energy states forming the qubit have opposite spin projections and belong to different orbital states. This poses a challenge, because magnetic dipole transitions generally cannot change the orbital character of a spin-orbit eigenstate [69] and can change the angular momentum only by one unit [86, 88]. This can be seen directly by inspecting the Zeeman Hamiltonian in the spin-orbit basis. When strain is introduced, however, the spin-orbit-coupled orbitals mix with those of the higher orbital branch. This leads to a finite overlap in orbital character between the two lower qubit states and enables magnetic dipole transitions between spin sublevels that would otherwise belong to different orbital manifolds.

This overlap can be evaluated explicitly. From the derivation of the eigenbasis under strain (see Eq. 2.20) we know that in the limit of large strain along certain directions, the orbitals approach the pure e_{gx} and e_{gy} states. To investigate this effect, we consider the Hamiltonian $\hat{H} = \hat{H}_{\mathrm{SO}} + \hat{H}_{\mathrm{jt}} + \hat{H}_{\mathrm{strain}} + \hat{H}_{\mathrm{dc}}$ in the absence of an externally applied magnetic

field. Following Ref. [70], we set the strain parameters to $v_x = \alpha$ and $v_y = 0$. We obtain the following eigenstates

$$|\tilde{e}_- \downarrow\rangle = \frac{\sqrt{2}}{\sqrt{R_-^2 + 2}} \left(|e_- \downarrow\rangle + R_- |e_+ \downarrow\rangle\right) , \tag{2.47}$$

$$|\tilde{e}_+ \uparrow\rangle = \frac{\sqrt{2}}{\sqrt{R_-^2 + 2}} \left(|e_+ \uparrow\rangle + R_- |e_- \uparrow\rangle\right) , \tag{2.48}$$

$$|\tilde{e}_+ \downarrow\rangle = \frac{\sqrt{2}}{\sqrt{R_+^2 + 2}} \left(R_+ |e_+ \downarrow\rangle + |e_- \downarrow\rangle\right) , \tag{2.49}$$

$$|\tilde{e}_- \uparrow\rangle = \frac{\sqrt{2}}{\sqrt{R_+^2 + 2}} \left(R_+ |e_- \uparrow\rangle + |e_+ \uparrow\rangle\right) , \tag{2.50}$$

in agreement with Ref. [89]. In the following, we adopt the notation of Ref. [89] and define $R_\pm = (1 \pm \sqrt{r^2 + 1})/r$, where $r = \tan(x) = 2\alpha/\lambda$ denotes the ratio between strain and spin-orbit coupling, as defined in Eq. 2.31. We explicitly include the proper normalization of the eigenstates to ensure the correct limiting behavior for vanishing and infinitely large strain. Expanding to first order in α, we obtain the eigenstates of the lower orbital doublet as

$$|\tilde{e}_- \downarrow\rangle \approx |e_- \downarrow\rangle - \frac{\alpha}{\lambda} |e_+ \downarrow\rangle , \tag{2.51}$$

$$|\tilde{e}_+ \uparrow\rangle \approx |e_+ \uparrow\rangle - \frac{\alpha}{\lambda} |e_- \uparrow\rangle . \tag{2.52}$$

This implies that, as shown here in the absence of an applied off-axis dc magnetic field, strain mixes only the two orbitals with equal spin projections. This strain-induced mixing provides an intuitive explanation for why strain enables faster Rabi driving. This can be shown by calculating the transition matrix element normalized to the free-electron Rabi frequency [90]

$$\Omega_{\text{free}} = \gamma_s B_\perp^{\text{ac}} = 28\,\text{MHz}\,\text{mT}^{-1} B_\perp^{\text{ac}} . \tag{2.53}$$

using the states introduced above. We find

$$\frac{\langle \tilde{e}_- \downarrow | \hat{H}_{\text{ac}} | \tilde{e}_+ \uparrow \rangle}{\gamma_s B_\perp^{\text{ac}}} = R_- \approx -\frac{\alpha}{\lambda} , \tag{2.54}$$

where the minus sign in the small-strain expansion reflects the strain sign convention discussed in Sec. 2.1.2.

So far, we have restricted the discussion to the driving response of the system in the absence of an applied off-axis magnetic field. In the next section, we incorporate both the interaction with a time-dependent (ac) magnetic field and the effect of an off-axis dc magnetic field, closely following the approach of Ref. [80].

The coupling to an ac magnetic field $B^{\text{ac}}(t)$ is described by introducing a gyromagnetic tensor $\hat{\mu}$, which relates the electron spin to the applied field according to

$$\hat{H}_{\text{ac}} = \boldsymbol{S} \cdot \hat{\mu} \cdot \boldsymbol{B}^{\text{ac}}(t) . \tag{2.55}$$

The total Hamiltonian describing the combined effect of the dc magnetic field and the ac driving field then reads

$$\hat{H}_{\text{drive}} = \hat{\omega} + \boldsymbol{S} \cdot \hat{\mu} \cdot \boldsymbol{B}^{\text{ac}}(t) \,. \tag{2.56}$$

Projecting this Hamiltonian onto the eigenbasis $\mathcal{B}^{jt}$ and using the qubit splitting Δ_q derived in the previous section yields

$$\hat{H}^{jt}_{\text{drive}} = -\frac{\Delta_q}{2}\hat{\sigma}_z - \boldsymbol{S} \cdot \hat{\mu} \cdot \boldsymbol{B}^{\text{ac}} = \left(-\frac{\Delta_q}{2} + \tilde{B}^{\text{ac}}_z\right)\hat{\sigma}_z + \tilde{B}^{\text{ac}}_x(t)\hat{\sigma}_x + \tilde{B}^{\text{ac}}_y(t)\hat{\sigma}_y \,, \tag{2.57}$$

where $\tilde{B}^{\text{ac}}_{x,y,z}$ denote the components of the ac magnetic field multiplied with an effective gyromagnetic ratio along each cartesian orientation[1] defined by the transformation

$$\tilde{B}^{\text{ac}}_i = \hat{\mu} \cdot \boldsymbol{B}^{\text{ac}}_i \,. \tag{2.58}$$

Here, $\tilde{B}^{\text{ac}}_i$ has units of energy rather than magnetic field.

To further simplify the Hamiltonian, we transform into a rotating reference frame defined by the unitary operator

$$\hat{U} = \exp\left[-i\left(\frac{\Delta_q}{2} - \tilde{B}^{\text{ac}}_z\right)\hat{\sigma}_z\right] \,. \tag{2.59}$$

The rotated Hamiltonian is then given by the unitary transformation

$$\hat{H}'_{\text{drive}} = \hat{U}\hat{H}_{\text{drive}}\hat{U}^\dagger - i\hat{U}\dot{\hat{U}}^\dagger \,. \tag{2.60}$$

The resulting operator products involve matrix exponentials of Pauli operators, which can be evaluated in a particularly simple way without explicitly using their commutation relations[2]. Instead, one may directly apply the operators to the spin eigenstates and read off the operator form from the resulting matrix element. As an example, we find

$$\exp\left(-i\frac{\Delta_q}{2}t\hat{\sigma}_z\right)\hat{\sigma}_x \exp\left(i\frac{\Delta_q}{2}t\hat{\sigma}_z\right)|\uparrow\rangle = \exp\left(i\Delta_q t\right)|\downarrow\rangle \,, \tag{2.61}$$

$$\exp\left(-i\frac{\Delta_q}{2}t\hat{\sigma}_z\right)\hat{\sigma}_x \exp\left(i\frac{\Delta_q}{2}t\hat{\sigma}_z\right)|\downarrow\rangle = \exp\left(-i\Delta_q t\right)|\uparrow\rangle \,. \tag{2.62}$$

Consequently, the resulting operator identity can be written as

$$\hat{\sigma}_x \exp\left(i\Delta_q t\hat{\sigma}_z\right) = \exp\left(-i\Delta_q t\hat{\sigma}_z\right)\hat{\sigma}_x \,. \tag{2.63}$$

Applying this relation to the rotated driven Hamiltonian yields

$$\hat{H}'_{\text{drive}} = \tilde{B}^{\text{ac}}_x(t) \exp\left(-i\left(\Delta_q - 2\tilde{B}^{\text{ac}}_z\right)t\hat{\sigma}_z\right)\hat{\sigma}_x + \tilde{B}^{\text{ac}}_y(t) \exp\left(-i\left(\Delta_q - 2\tilde{B}^{\text{ac}}_z\right)t\hat{\sigma}_z\right)\hat{\sigma}_y \,. \tag{2.64}$$

[1] I thank Gregor Pieplow for pointing out the split up of the driving Hamiltonian into each individual cartesian direction and the insightful discussions on the derivation.

[2] I thank Prof. Shnirman for presenting this method in his lecture on the Physics of Quantum Information, summer semester 2019.

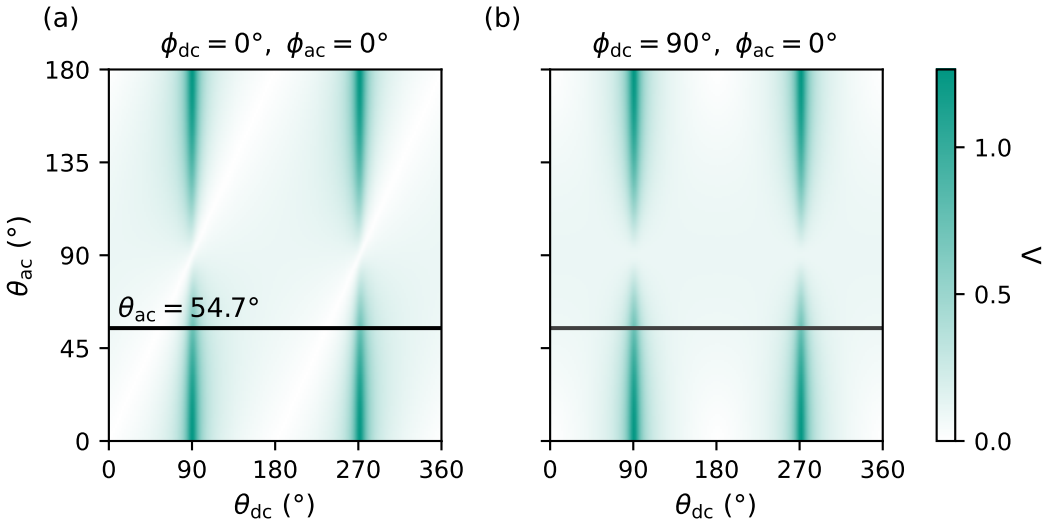

Figure 2.5.: Simulation of the dimensionless parameter Λ describing the angle-dependent response of the SnV center to an ac drive field for a simultaneous sweep of the dc magnetic field and the ac drive field. The strain of the SnV center is chosen to match the value of the emitter investigated in this thesis, $\alpha = 41.3$ GHz. For certain combinations of magnetic-field orientations, Λ is maximized. In particular, it reaches its maximum when the external dc magnetic field is perpendicular to the SnV center's quantization axis, i.e. $\theta_{dc} = 90°$. Values of $\Lambda > 1$ arise from the contribution of the orbital Zeeman term [80]. (a) Λ calculated for rotations in the $\phi_{dc} = 0°$ plane of the SnV center. The black line indicates the ac-field angle used in our experimental configuration. (b) Same calculation for a $\phi_{dc} = 90°$ rotation scan.

Since the energy modulation induced by the longitudinal ac field $2B_z^{ac}$ is much smaller than the total qubit splitting Δ_q, the corresponding dynamics occurs on a slower timescale and we can simplify by introducing $\hat{b}(t) = \exp\left(2i\tilde{B}_z^{ac} t\hat{\sigma}_z\right)$ leading to the more compact form

$$\hat{H}'_{drive} = \hat{b}(t)\left(\tilde{B}_x^{ac}(t)\hat{\sigma}_x + \tilde{B}_y^{ac}(t)\hat{\sigma}_y\right)\exp\left(i\Delta_q t\hat{\sigma}_z\right) . \tag{2.65}$$

Introducing the explicit time-dependence of the ac magnetic fields

$$\tilde{B}_x^{ac}(t)\hat{\sigma}_x = \tilde{B}_x^{ac}\cos(\omega t)\hat{\sigma}_x = \frac{1}{2}\tilde{B}_x^{ac}\left(\exp(i\omega t) + \exp(-i\omega t)\right)\left(\hat{\sigma}_+ + \hat{\sigma}_-\right) , \tag{2.66}$$

$$\tilde{B}_y^{ac}(t)\hat{\sigma}_y = \tilde{B}_y^{ac}\cos(\omega t)\hat{\sigma}_y = \frac{1}{2i}\tilde{B}_y^{ac}\left(\exp(i\omega t) + \exp(-i\omega t)\right)\left(\hat{\sigma}_+ - \hat{\sigma}_-\right) , \tag{2.67}$$

setting the driving frequency to resonance, $\omega = \Delta_q$, and performing the rotating wave approximation (RWA), rapidly oscillating terms proportional to $\exp(\pm 2i\Delta_q t)$ can be neglected. This yields the effective driven Hamiltonian

$$\hat{H}'_{drive,\,RWA} = \frac{1}{2}\hat{b}(t)\left(\tilde{B}_x^{ac}\hat{\sigma}_x + \tilde{B}_y^{ac}\hat{\sigma}_y\right) \equiv \hat{b}(t)\Omega\boldsymbol{n}\cdot\hat{\boldsymbol{\sigma}} , \tag{2.68}$$

where we introduced the rotation axis

$$\boldsymbol{n} = \frac{1}{2\Omega}\left(\tilde{B}_x^{ac}, \tilde{B}_y^{ac}, 0\right)^T , \tag{2.69}$$

describing rotations on the Bloch sphere. These can be described by the rotation matrix

$$R_{\boldsymbol{n}}(t) = \exp(i\theta_{\mathrm{Rabi}}(t)\boldsymbol{n}\cdot\hat{\boldsymbol{\sigma}})\,, \tag{2.70}$$

where the angle of rotation is given by $\theta_{\mathrm{Rabi}}(t) = \Omega\int_0^t b(\tau)d\tau$. Comparing both sides of Eq. 2.69, one finds that the normalization of $\boldsymbol{n}$ defines two times the Rabi frequency

$$\Omega = \frac{1}{2}\sqrt{\left(\tilde{B}_x^{\mathrm{ac}}\right)^2 + \left(\tilde{B}_y^{\mathrm{ac}}\right)^2}\,, \tag{2.71}$$

and only depends on the effective transverse driving fields. These fields can be expressed in terms of the gyromagnetic tensor defined in Eq. 2.58 and explicitly evaluated using its matrix representation. To do so, one may exploit the fact that, at the level of the spin Hamiltonian, there is no fundamental distinction between static and time-dependent magnetic fields apart from their explicit time dependence. The interaction with the ac magnetic field can therefore be derived directly from Eq. 2.38 by replacing the dc field components with the corresponding ac field amplitudes and expressing the result in the eigenbasis of the dc Hamiltonian.

Comparing the resulting Hamiltonian with the general form given in Eq. 2.55 and matching the coefficients associated with each ac field component allows the gyromagnetic tensor $\hat{\mu}$ to be determined completely. Each of its entries has the dimension of a gyromagnetic ratio. This approach provides direct access to the effective coupling coefficients and, consequently, to the angle-dependent Rabi frequency. The explicit derivation of the individual components of $\hat{\mu}$ is presented in Appendix A.1.

Expressing both the dc and ac magnetic fields in spherical coordinates with respect to the quantization axis of the SnV center allows the Rabi frequency to be written in the compact form

$$\Omega = \frac{1}{2}\sqrt{\left(\tilde{B}_x^{\mathrm{ac}}\right)^2 + \left(\left(\tilde{B}_y^{\mathrm{ac}}\right)^2\right.} \equiv \gamma_s B_{\mathrm{ac}}\Lambda\,, \tag{2.72}$$

where Λ is a dimensionless parameter. It is given by

$$\Lambda = \sin(x)\sqrt{\sin(\phi_{\mathrm{ac}}-\phi_{\mathrm{dc}})^2\sin(\theta_{\mathrm{ac}})^2 + \frac{\chi(\phi_{\mathrm{ac}},\phi_{\mathrm{dc}},\theta_{\mathrm{ac}},\theta_{\mathrm{dc}})^2}{\sin(\theta_{\mathrm{dc}})^2\zeta(x)^2+\cos(\theta_{\mathrm{dc}})^2}}\,, \tag{2.73}$$

where

$$\chi = \cos(\theta_{\mathrm{dc}})\cos(\phi_{\mathrm{ac}}-\phi_{\mathrm{dc}})\sin(\theta_{\mathrm{ac}}) - \cos(\theta_{\mathrm{ac}})\sin(\theta_{\mathrm{dc}})\,, \tag{2.74}$$

and

$$\zeta(x) = \frac{\gamma_s\sin(x)}{\gamma_s + 2\gamma_l(\delta + f\cos(x))}\,. \tag{2.75}$$

This expression makes explicit that the Rabi frequency is governed not only by the amplitude of the ac magnetic field, but also by the strain magnitude and the relative orientations of the dc and ac magnetic fields with respect to the quantization axis of the SnV center. In particular, strain modifies the effective spin-ac-field coupling through $\sin(x)$ and $\zeta(x)$,

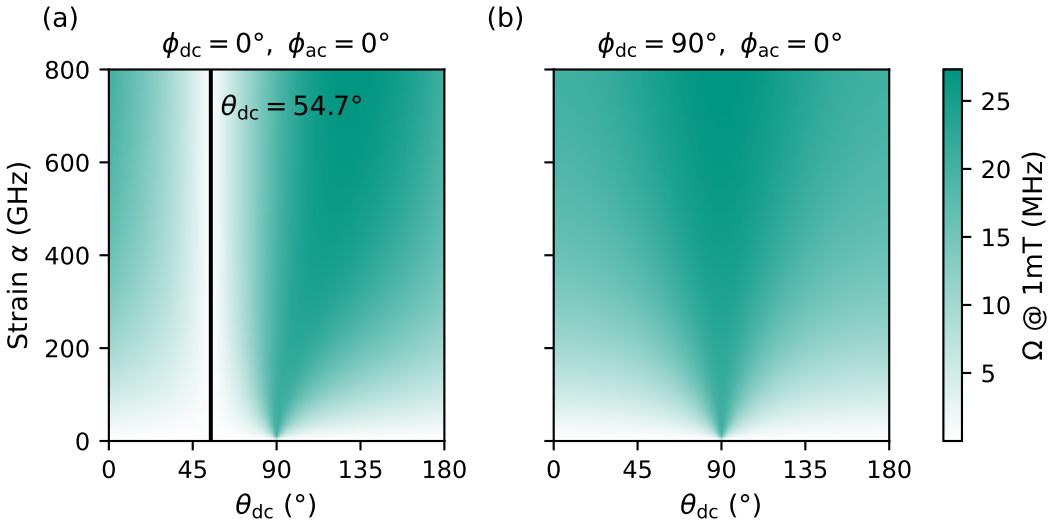

Figure 2.6.: Dependence of the Rabi frequency on the orientation of the external dc magnetic field for a varying strain magnitude α. The orientation of the ac magnetic field with respect to the SnV center's quantization axis is chosen as in the experiment, i.e. $\theta_{ac} = 54.7°$. As the strain increases, the angular dependence diminishes and the Rabi frequency approaches the free-electron value defined in the main text. (a) The magnetic field is aligned in an $\phi_{dc} = 0°$ configuration in the SnV frame, meaning that the ac and dc magnetic fields lie within the same plane. At an angle of $\theta_{dc} = 54.7°$, the two fields are parallel and the Rabi frequency vanishes. (b) For a $\phi_{dc} = 90°$ configuration, the ac and dc magnetic fields maintain a fixed relative angle, resulting in a symmetric dependence of the Rabi frequency on the dc polar angle.

while the angular dependence reflects the projection of the transverse driving field onto the qubit eigenbasis.

Figure 2.5 shows the dependence on the orientations of the dc magnetic field and the ac driving field. For the experiments discussed later, the coplanar-waveguide geometry fixes the ac-field orientation to $\theta_{ac} = 54.7°$ with respect to the SnV-center quantization axis. A detailed description of the SnV axis relative to the surrounding ac-field geometry, together with a visual representation of the dc and ac fields, is given in Sec. 2.3.2, in particular in Fig. 2.8.

It is useful to fix the angle $\phi_{ac} = 0°$, which aligns the x axis of the ac-field coordinate system with the x axis of the dc-field coordinate system. For the dc magnetic field, $\phi_{dc} = 0°$ means that the ac and dc magnetic fields lie in the same plane. Consequently, for certain combinations of θ_{ac} and θ_{dc}, the ac and dc magnetic fields become parallel, resulting in a vanishing Rabi drive. This is visible as the white diagonals in Fig. 2.5(a). In contrast, in Fig. 2.5(b), the ac and dc magnetic fields cannot become parallel for any combination of polar angles. Instead, they retain a finite relative angle, resulting in a nonzero global minimum $\Lambda > 0$. As the strain magnitude increases, the dependence on the angular orientation of the external magnetic fields decreases, as shown in Fig. 2.6, and the Rabi frequency approaches the value expected for a free electron spin. However, no Rabi drive is possible when both the ac driving field and the dc magnetic field are aligned parallel to the quantization axis of the SnV center as shown in Fig. 2.6(b).

2.3. Experimental platform and measurement techniques

Before discussing the optical and magneto-optical properties of the SnV center, we briefly introduce the experimental platform used throughout this work. The measurements are performed on single SnV centers embedded in diamond membranes and cooled down in a dilution cryostat. Optical excitation and detection are used for photoluminescence, photoluminescence-excitation spectroscopy, and spin-selective readout, while microwave and radio-frequency fields provide coherent control of the electronic and nuclear spin transitions. This section summarizes the relevant aspects of the sample, cryogenic setup, optical detection path, and control hardware needed to interpret the measurements presented in the following sections and chapters.

2.3.1. Cryogenic sample environment

The sample used throughout this thesis is a $1\,\mathrm{mm} \times 1\,\mathrm{mm} \times 26\,\mu\mathrm{m}$ diamond membrane containing single SnV centers. The fabrication process is described in detail in Appendix A.3. A scanning confocal microscope image of the sample at room temperature is shown in Fig. 2.7(a). An off-resonant excitation power of 1 mW at a wavelength of 532 nm is used. The fluorescence is filtered using a 532 nm notch filter and 600 nm and 620 nm long-pass filters to remove the Raman peaks of diamond. The confocal microscope used here is a home-built microscope used for pre-characterization of samples. As this is not the cryogenic setup used for the later experiments, we refer to Ref. [91] for a description of the setup. The bright green spots in Fig. 2.7(a) show individual SnV centers, indicating a dense but spatially separable distribution of SnV centers.

For implementation into the cryogenic confocal setup, the diamond membrane is glued onto a 4×4 mm undoped silicon wafer with a thin layer of UV-curing adhesive (NOA63, *Norland*) to mitigate background fluorescence. The adhesive layer is intentionally kept much thinner than in previous measurements [70] to reduce induced strain and thereby aim for higher optical cyclicity (see Sec. 2.5.2). Figure 2.7(b) shows a microscope image of the glued diamond sample, where the sample sits on top of the UV-curing adhesive.

The coplanar waveguide fabrication was performed by Ioannis Karapatzakis. The photoresist AZ5214E is used in a photolithography process to pattern the waveguide structure, followed by electron-beam evaporation of a 50 nm-thick niobium layer. Lift-off of the residual photoresist is performed in acetone, followed by a final cleaning step in water. For details on the waveguide fabrication, we refer to the PhD thesis of Ioannis Karapatzakis [72]. Figure 2.7(c) shows a microscope image of the sample during waveguide fabrication.

All measurements were performed in a home-built table-top dilution refrigerator with an inverted design, designed and built by Wolfgang Wernsdorfer. In this configuration, the millikelvin plate is placed at the top of the setup to allow optical access from above through windows. The concept for integrating optical access and the design of the millikelvin plate used in this work were realized by Marcel Schrodin. The system reaches temperatures

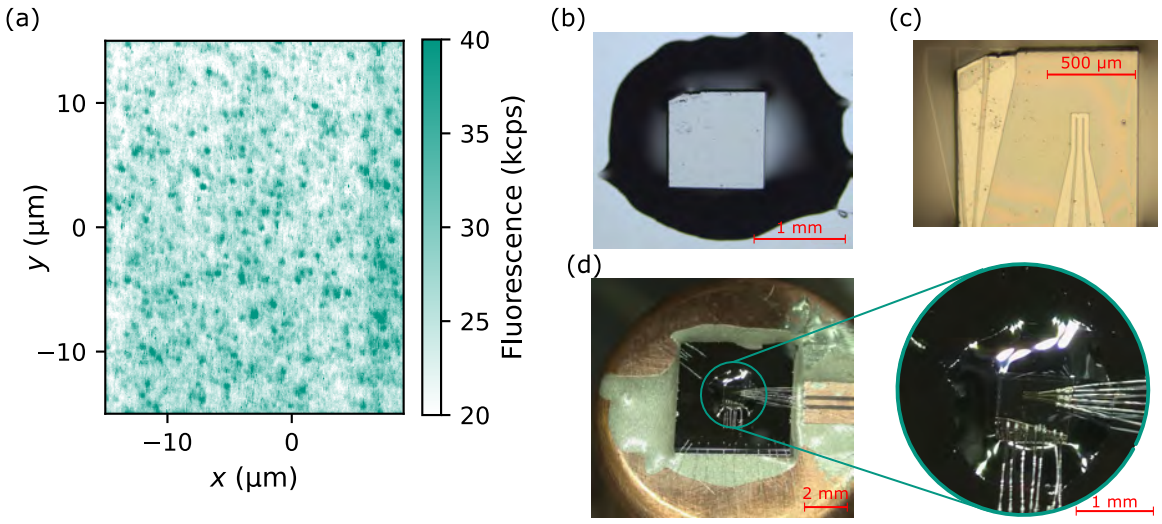

Figure 2.7.: Overview of the sample used within this thesis. (a) Scanning confocal microscope image at room temperature showing the distribution of SnV centers inside the sample. (b) Microscope image of the sample glued to a silicon wafer using UV-curing glue. (c) Microscope image of the sample during waveguide fabrication performed by Ioannis Karapatzakis [72]. (d) Image of the sample installed on the cold finger with wire bonds for microwave delivery and thermalization.

below 100 mK and contains a superconducting 3D vector magnet mounted on the 4 K stage, surrounding the microscope objective and the sample. Two closed-loop cooling circuits are used: a pulse-tube refrigerator precools the system with ^{4}He gas to approximately 4 K, while a ^{3}He/^{4}He loop enables further cooling into the millikelvin regime. For a detailed description of the working principle of a similar cryostat, we refer to Ref. [92].

To incorporate the sample into the cryostat, the silicon wafer is glued to a copper cold finger using silver epoxy, as shown in Fig. 2.7(d). The cold finger is mounted on piezoelectric steppers (2× ANPx101/RES/LT, 1× ANPz101/RES/LT, ANC300 controller, *Attocube*), which allow the sample to be moved in all three spatial dimensions. In addition, the cold finger is thermalized to the millikelvin plate using silver braids.

The superconducting waveguide on the diamond is connected to the microwave delivery line using aluminum wire bonds. More specifically, these wire bonds connect the waveguide to a custom-made coplanar waveguide fabricated on a flexible printed circuit board, featuring 18 µm-thick copper conductors and a 100 µm-thick polyimide dielectric, which is connected to the SMA connector of the microwave delivery line of the cryostat. Additional wire bonds are added to the second, unused waveguide structure and to the silicon wafer to improve thermalization of the sample. The wire bonding was performed by Ioannis Karapatzakis.

An important feature of the setup is the 3D vector magnet and its alignment with respect to the SnV center. This is important because, as discussed above, the properties of the SnV center depend on the orientation of the external dc magnetic field with respect to the SnV-center quantization axis, as well as on the ac magnetic field provided by the superconducting waveguide. Therefore, we discuss here the geometry of the SnV center with respect to the vector magnet used throughout this thesis. For the experimental procedure

used to determine the quantization axis of the SnV center, we refer to Sec. 2.5.1. For now, we assume that the direction of the SnV center is known and discuss the implications of its orientation with respect to the magnetic fields.

The SnV center is oriented along one of the crystallographic ⟨111⟩ directions of the diamond lattice. For the SnV center studied here, this orientation corresponds to a direction parallel to the $-X_{\mathrm{lab}}$ axis in the laboratory coordinate system defined by the dc vector magnet coils. This assignment follows from the gluing geometry of the sample, the ⟨110⟩ edge cuts of the diamond membrane and the random choice of one of the four ⟨111⟩ directions. The resulting geometry is shown in Fig. 2.8(a).

The ac magnetic field is generated by the coplanar niobium waveguide and forms a fixed angle of $\theta_{\mathrm{ac}} = 54.7^\circ$ with respect to the SnV-center quantization axis Z_{SnV}, as shown in Fig. 2.8(a). This geometry arises from the close proximity of the SnV center to the diamond surface, approximately 20 nm, compared to the waveguide gap of 5 µm, which creates an ac magnetic field solely along the Z_{lab} direction in the laboratory frame [72].

Figure 2.8(a) shows an XZ scan in the laboratory frame. Such a scan corresponds to rotating the dc magnetic field from the X_{lab} direction, where only the X coil is turned on, towards the Z_{lab} direction by increasing the current in the Z coil while decreasing the current in the X coil. This procedure is continued until the desired angular range is covered. To keep the magnetic-field strength constant throughout the scan, the current-to-magnetic-field conversion was calibrated beforehand. For further details, we refer to our earlier work [70].

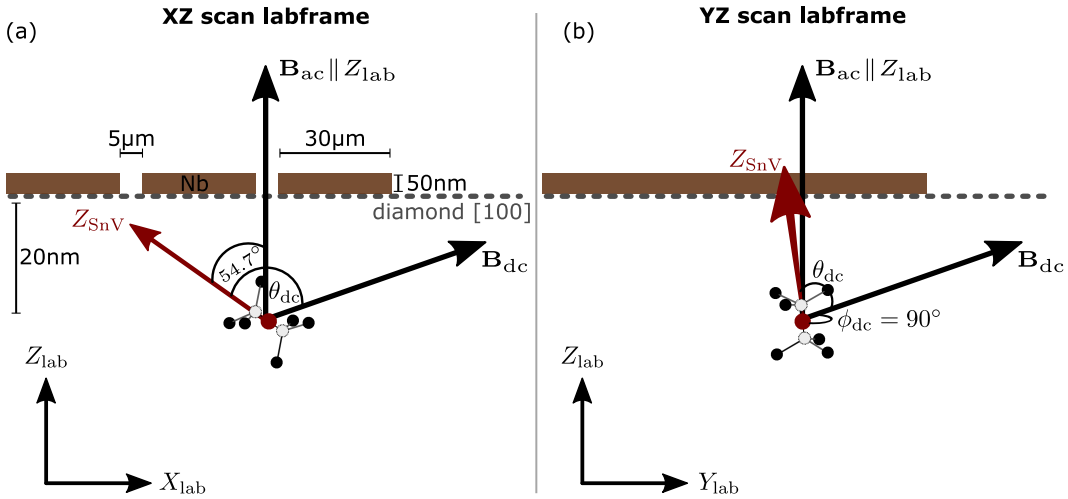

Figure 2.8.: Geometry of the dc and ac magnetic fields for the SnV center used throughout this thesis. The SnV-center quantization axis is denoted by Z_{SnV}. The ac magnetic field is generated by the coplanar niobium waveguide and has a fixed angle of $\theta_{\mathrm{ac}} = 54.7^\circ$ with respect to Z_{SnV}. (a) XZ scan in the laboratory frame. In this configuration, the dc magnetic field $\boldsymbol{B}_{\mathrm{dc}}$, the ac magnetic field $\boldsymbol{B}_{\mathrm{ac}}$, and the SnV quantization axis Z_{SnV} lie within the same plane. (b) YZ scan in the laboratory frame. In this case, the dc magnetic field has an azimuthal angle of $\phi_{\mathrm{dc}} = 90^\circ$ in the SnV-center frame.

In the configuration of the laboratory-frame XZ scan, the dc magnetic field $\boldsymbol{B}_{\mathrm{dc}}$, the ac magnetic field $\boldsymbol{B}_{\mathrm{ac}}$, and the SnV quantization axis Z_{SnV} lie within the same plane. In contrast, Fig. 2.8(b) shows a YZ scan in the laboratory frame, where this is not the case.

We define the X_{SnV} axis of the SnV center to point along the Y_{lab} axis. This choice is allowed because the g tensor is axially symmetric around the SnV quantization axis. Although this convention may seem counterintuitive, it was already used in our earlier work [70, 71] and is therefore kept here for consistency. With this definition, a YZ scan in the SnV-center frame corresponds to a configuration in which both magnetic fields and the quantization axis lie within the same plane, and thus to an azimuthal angle of $\phi_{\mathrm{dc}} = 0°$ for the dc magnetic field. This geometric consideration becomes important, for example, when analyzing the response of the electron spin under microwave driving, as discussed in Sec. 2.2. This should not be confused with the YZ scan in the laboratory frame shown in Fig. 2.8(b). In the convention used here, a XZ scan in the laboratory frame covers the same plane spanned by a YZ scan in the SnV-center frame.

2.3.2. Optical excitation and detection

The optical setup is described in detail in the thesis of Ioannis Karapatzakis [72]. We therefore do not reproduce the full description here, but refer the reader to his work. For convenience, the optical setup is shown in Fig. A.3, and we briefly summarize the most important components below, following the description of the setup in Ref. [70].

Resonant laser pulses are generated from a tunable continuous-wave laser source (C-WAVE VIS, *Hübner*), locked to a wavemeter (WS7, *HighFinesse*), using an acousto-optic modulator (3200-1214, *G&H*) in a double-pass configuration. The trigger signals are generated using fast transistor-transistor logic (TTL) electronics (ADwin-Pro II, *Jäger*). Charge repumping of the SnV center is performed using a continuous-wave 532 nm laser (Ventus MPC6000, *Laser Quantum*), which is gated using TTL logic (ADwin Gold II, *Jäger*). The coordination of the TTL electronics with the overall measurement protocols is discussed in the next section.

The excitation laser is focused onto the sample using a microscope objective with NA = 0.9 (MPLN100X, *Olympus*), which is mounted inside the vector magnet and thermalized to the 4 K stage. The laser is scanned spatially using a galvo mirror system (GVS212, GPS011 power supply, *Thorlabs*). The fluorescence is separated by a 90:10 beam splitter (BSN10, *Thorlabs*) and filtered using additional filters (BLP01-532R-25, FF01-593/LP-25, LP01-633R-25, *Semrock*). Finally, the signal is focused through a pinhole onto an avalanche photodetector (APD) (SPCM-AQRH-16, *Excelitas*). Photoluminescence spectra are recorded using a fiber-coupled spectrometer (SP-2500i, *Princeton Instruments*).

2.3.3. Microwave and radio-frequency control

The experimental control setup is shown in Fig. 2.9(a). A central PC coordinates the data acquisition, display and evaluation. The main control device, an ADwin-Pro II (*Jäger*), handles the triggering of all devices during pulsed measurements and photoluminescence-excitation (PLE) measurements. For PLE measurements, the ADwin-Pro II scans the cavity of the resonant laser using its analog output together with a high-voltage amplifier (E-836.1G, *Physik Instrumente*).

A second ADwin-Gold II (*Jäger*) handles slower tasks, such as gating the green excitation path mentioned above. In addition, the ADwin-Gold II provides stable voltages to the galvo-mirror system for focusing on the spatial position of the emitter, as well as to the current sources supplying the 3D vector magnet.

The measurement sequences are prepared as scripts and uploaded to the ADwin. Before the experiment, all pulses are generated as a single waveform in Python and uploaded to the arbitrary waveform generator (AWG) (AWG70001A, *Tektronix*) with a sampling rate of 50 GS/s for microwave pulses and 1 GS/s for radio-frequency pulses, unless stated otherwise. During the measurement, the AWG plays these waveforms upon being triggered by the ADwin-Pro II.

The TTL pulses from the APD are converted to timestamps using a TimeTagger (*Swabian Instruments*), which is triggered by the ADwin-Pro II.

For the pulsed nuclear spin measurements, the AWG output in the RF path is first attenuated by 10 dB (BW-S10-2W263A+, *Mini-Circuits*) to reduce noise leaking from the AWG. The signal is then amplified using a fixed-gain amplifier (ZX60-100VH+, *Mini-Circuits*), filtered using a narrow bandpass filter (SBP-21.4+, *Mini-Circuits*), and attenuated again by 10 dB (BW-S10-2W263A+, *Mini-Circuits*). The microwave path consists of a microwave source (N5183B, *Keysight*), which runs in pulsed mode and is triggered by the ADwin-Pro II via TTL signals. The microwave signal is filtered using a high-pass filter (VHF-2700A+, *Mini-Circuits*) and attenuated by 16 dB (BW-S6-2W263A+ and BW-S10-2W263A+, *Mini-Circuits*). The two paths are then combined using a combiner (ZX10-2-183-S+, *Mini-Circuits*) and high-pass filtered using a DC block (BLK-89-S+, *Mini-Circuits*). Implementing a narrow bandpass filter around the RF transition, a dc block after the combiner, and a high-pass filter in the microwave line led to a significant reduction of noise, as reflected in the nuclear coherence measurements discussed in Sec. 5.4.3. We emphasize the use of large attenuation as the last step before the combiner: these absorb reflections from inside the cryostat, i.e. from the shorted superconducting waveguide, and from the filters, which would otherwise bounce back and forth. With these attenuators, circulators are not required. For the ODMR and ODNR measurements, neither an amplifier nor a bandpass filter was used in the MW/RF path.

For the electron spin control measurements, the RF path was reconfigured to deliver the microwave pulses. A fixed-gain amplifier (ZHL-16W-43-S+ or ZVA-183-S+, *Mini-Circuits*) was used, depending on the qubit transition frequency, with the corresponding attenuation to achieve the desired power levels. No additional filtering was applied in the adapted

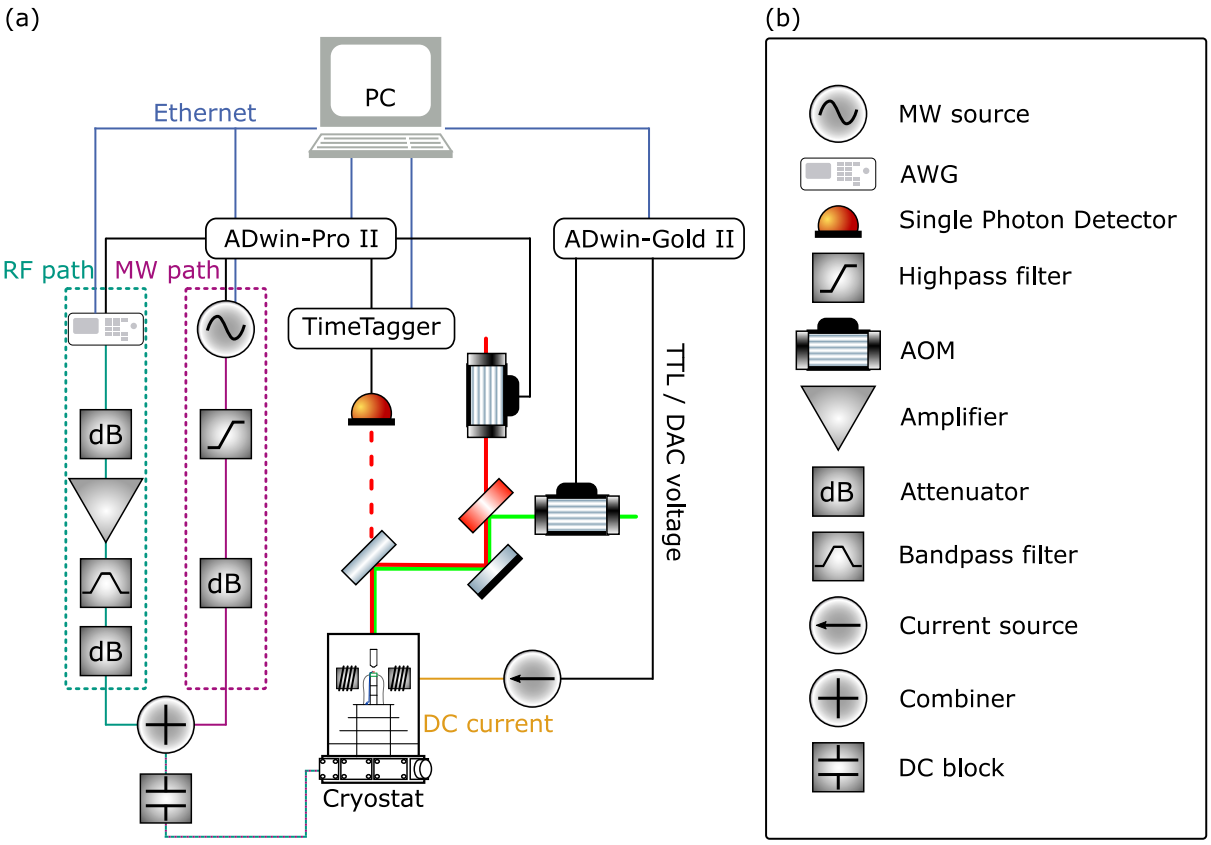

Figure 2.9.: Experimental setup for the pulsed nuclear spin control measurements performed in this thesis. (a) Simplified schematic of the experimental setup. (b) Legend of the components used. Some of the component graphics are from the ComponentLibrary by Alexander Franzen [93] and from the thesis of Ioannis Karapatzakis [72]. The schematic was inspired by Stas *et al.* [65].

pulsed microwave path. The microwave source path and combiner configuration remained unchanged.

All losses of the signal paths before the input of the cryostat were measured using a spectrum analyzer (N9323C, *Keysight*). The input return loss (S_{11}) of the microwave lines together with the sample inside the cryostat was measured at the input port of the cryostat using a vector network analyzer (E5071C, *Keysight*), as shown in Fig. 2.10. A local return-loss minimum is located at 3.7 GHz, which corresponds to the splitting of the electron-spin sublevels for a magnetic field of 106 mT aligned parallel to the SnV-center axis.

2.4. Photoluminescence and spectral stability

After introducing the experimental platform and measurement techniques, we now turn to the optical properties of the SnV center. We first discuss photoluminescence and photoluminescence-excitation spectroscopy before analyzing the linewidths and spectral stability of the optical transitions.

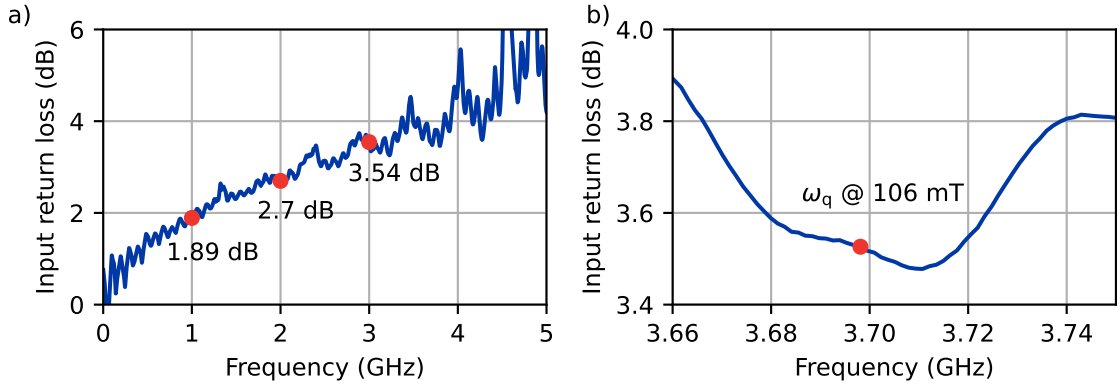

Figure 2.10.: Microwave losses inside the cryostat. (a) Input return loss of the microwave lines together with the sample measured at the input port of the cryostat. (b) The electron-spin resonance is tuned to the local minimum of the input return loss by adjusting the magnetic dc field. The figure is taken from Ref. [71].

Since the SnV center is embedded in the diamond lattice, its electronic and vibrational energy structures are coupled. In general, different charge configurations in the electronic ground and excited state lead to a shift in the equilibrium positions of the nuclei. However, for the SnV center, the charge distribution remains centrosymmetric in both the ground and excited state due to its inversion symmetry, resulting in a negligible change in equilibrium position.

Vibrational excitations can be described by harmonic-oscillator wavefunctions in the corresponding harmonic potentials. In this picture, the overlap between the vibrational ground states of the electronic ground and excited states is maximized when their equilibrium positions coincide. This explains the strong zero-phonon-line (ZPL) emission of the SnV center compared to the NV center, which lacks inversion symmetry and therefore exhibits a more pronounced phonon sideband.

The vibrational substructure also enables off-resonant excitation of the SnV center using green laser light. At room temperature, the resulting photoluminescence (PL) spectrum shows a strong ZPL accompanied by a phonon sideband, as shown in Fig. 2.11(a). Upon cooling to cryogenic temperatures, only two transitions, i.e. the C and D transitions, remain [68, 79], giving rise to narrow spectral lines, see Fig. 2.11(b).

The ratio of ZPL emission to the total optical emission is quantified by the Debye-Waller factor. For the SnV center, this factor is $\beta_{\mathrm{DBW}} = 0.57$ [79], significantly larger than the value of $\beta_{\mathrm{DBW}} = 0.03$ reported for the NV center [94].

The position of the first phonon sideband can be estimated as

$$\Delta E_{\mathrm{PSB}} = \sqrt{\frac{m}{3(M-m)}}\omega_D\,, \tag{2.76}$$

where $m = 12$ and $M = 116$ are the atomic masses of carbon and tin, respectively, and $\omega_D = 150\,\mathrm{meV}$ is the Debye energy of diamond [95]. This yields an energy shift of $\Delta E_{\mathrm{PSB}} \approx 29\,\mathrm{meV} \approx 7\,\mathrm{THz}$. This is much larger than the ground-state splitting, i.e. the

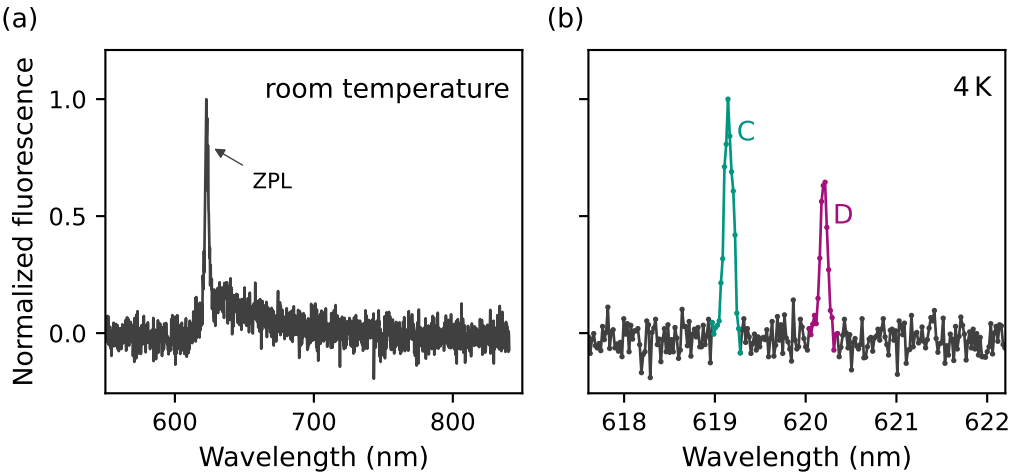

Figure 2.11.: Photoluminescence spectra of SnV centers at room and cryogenic temperatures. (a) Room-temperature photoluminescence spectrum of an arbitrary emitter, showing the zero-phonon line at ~ 620 nm together with the phonon sideband. (b) Photoluminescence spectrum of an unstrained emitter at $T = 4\,\mathrm{K}$, resolving the C (green) and D (purple) transitions, which correspond to decay from the lowest excited state to the two orbital ground states. Panel (b) was adapted from Ref. [70].

separation between the C and D transitions, which is approximately 1 THz, as shown in Fig. 2.11(b).

Photoluminescence excitation spectroscopy. To probe the electronic structure of the C transition and its associated states, we perform PLE spectroscopy by scanning a resonant laser across the transition while detecting emission in the phonon sideband. Examples of such PLE measurements, both with and without applied magnetic fields, are presented in the following section.

At a ZPL frequency of 484.193 THz, the sideband shift corresponds to a wavelength shift of $\Delta\lambda_{\mathrm{PSB}} \approx 9\,\mathrm{nm}$. Consequently, scattered laser photons used for resonant excitation of the C transition can be efficiently separated from phonon-sideband photons using, for example, a 633 nm long-pass filter.

The number of photons that can be scattered during a PLE measurement is determined by the excited-state lifetime τ_{SnV} and the relative excitation power $s = p/p_{\mathrm{sat}}$, as given in Eq. 2.94. In the strong-driving limit, i.e. for $p \gg p_{\mathrm{sat}}$, the scattering rate saturates at $\gamma/2 = 1/(2\tau)$ photons per second for unit collection efficiency. Here, τ denotes the lifetime of the electronic excited state of the SnV center, and $\gamma = 1/\tau$ is the corresponding radiative decay rate.

A saturation measurement, as e.g. shown in Fig. 2.12, can be analyzed by fitting the detected count rate I as a function of the applied laser power p via

$$I(p) = I_{\mathrm{sat}} \frac{s}{1+s} + n_{\mathrm{bgr}} p\,, \tag{2.77}$$

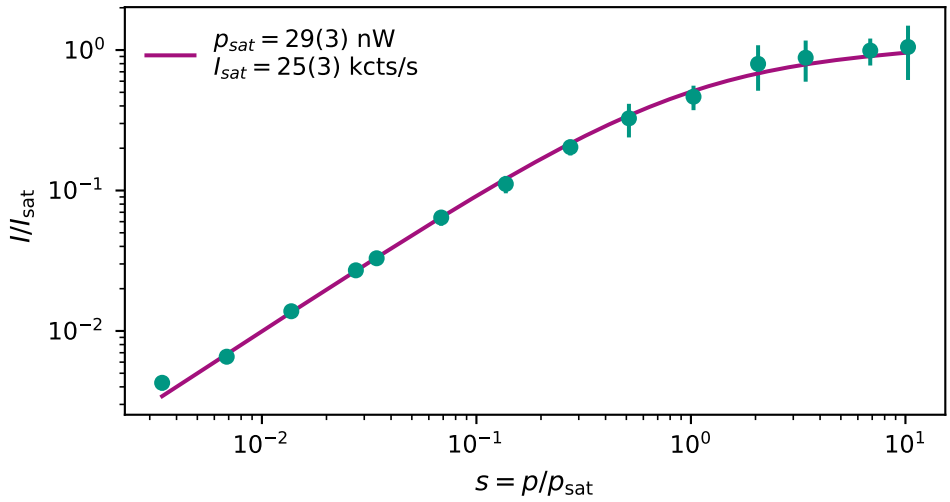

Figure 2.12.: Saturation photoluminescence excitation measurement of the C transition without an applied external magnetic field. The x and y axes are rescaled by the saturation power $p_{\mathrm{sat}} = 29(3)\,\mathrm{nW}$ and the saturation count rate $I_{\mathrm{sat}} = 25(3)\,\mathrm{kcts/s}$, respectively.

where I_{sat} is the saturation count rate and n_{bgr} accounts for a linear background.

Typical saturation powers lie in the range of 10 to 50 nW, with saturation count rates on the order of tens of kcts/s, depending on the emitter and the exact spatial position of the optical focus.

An example saturation curve of the C transition of the SnV center used in this work is shown in Fig. 2.12. From the fit, we obtain a saturation power of $p_{\mathrm{sat}} = 29(3)\,\mathrm{nW}$ and a saturation count rate of $I_{\mathrm{sat}} = 25(3)\,\mathrm{kcts/s}$. Estimating the beam waist at the position of the emitter as $w_0 = \lambda/[\pi \arcsin(\mathrm{NA})]$ [96], with an objective numerical aperture of $\mathrm{NA} = 0.9$, yields a saturation intensity of $4p_{\mathrm{sat}}/(\pi w_0^2) = 1.19\,\mu\mathrm{W}\,\mu\mathrm{m}^{-2}$.

Comparing the measured saturation count rate with the expected emission rate of $\eta_{\mathrm{QE}}/(2\tau_{\mathrm{SnV}}) \approx 80\,\mathrm{Mcts/s}$, where $\eta_{\mathrm{QE}} = 0.8$ is the quantum efficiency [68], yields a collection efficiency of approximately 0.02%. This value is in excellent agreement with the collection efficiency inferred from the cyclicity analysis discussed in Sec. 2.5.2.

Spectral stability. A detailed analysis of the spectral stability of SnV centers, including charge stability, spectral diffusion, and a workflow for identifying optically stable emitters, has been presented by Ioannis Karapatzakis in his PhD thesis [72]. Here, we provide only a concise overview to complete the discussion of the optical properties.

Spectral diffusion can be induced by fluctuating charges in the vicinity of the defect, which generate time-dependent electric fields at the emitter's position. The resulting energy shift of the optical transition is governed by the Stark effect, given to second order by $\Delta U(t) = -\boldsymbol{\Delta p} \cdot \boldsymbol{E}(t) - \frac{1}{2}\Delta\alpha \boldsymbol{E}^2(t)$, where $\boldsymbol{\Delta p}$ denotes the change in dipole moment between electronic ground and excited states, $\Delta\alpha$ the difference in polarizability, and $\boldsymbol{E}(t)$ the fluctuating local electric field at the emitter's position [97, 98]. Consequently, defects

that exhibit a non-zero difference in dipole moment between their electronic ground and excited states, like the NV center in diamond, are particularly sensitive to electric-field noise.

In solid-state systems, electric-field noise mainly arises from fluctuating charge traps. These are typically located near the surface, due to defects or dangling bonds, and form acceptor-like states within the bandgap. By capturing and releasing electrons, they create a fluctuating charge environment. This acceptor-like behavior close to the surface also leads to a band bending of the chemical potential, which can transfer emitters into their neutral charge state. To mitigate surface-induced spectral diffusion, the defect should ideally be located sufficiently far from the surface. This requirement poses challenges for defects based on non-abundant elements in diamond, which are commonly introduced by ion implantation [68]. Additionally, micro-structured surfaces, as required for optical cavities to enhance collection efficiency, tend to increase spectral diffusion due to the higher density of surface charge traps [46, 99].

Moreover, ion implantation introduces local lattice damage, i.e. defects in the lattice, and higher strain and thus additional charge traps around the emitter, which can further contribute to spectral diffusion [77, 99, 100]. One approach to mitigate this issue is high-temperature annealing, which can reduce lattice damage and lead to less spectral diffusion [68, 77].

For inversion-symmetric defects like the SnV center, the permanent electric dipole moment vanishes by symmetry due to the centrosymmetric charge distribution in both the ground and excited states, resulting in $\boldsymbol{p} = 0$ and therefore $\boldsymbol{\Delta p} = 0$. Quantitatively, differences in dipole moment and polarizability for the SnV center are found to be approximately four orders of magnitude smaller than for the NV center in diamond [97, 98, 101, 102]. This substantially reduces spectral diffusion and enables the use of nanostructures without severe degradation of optical stability. However, the finite polarizability of the SnV center, combined with the high density of charge traps introduced by heavy-ion implantation, can make the optical transition sensitive to nearby charge fluctuations. Such fluctuations lead to electric-field shifts with a $1/r^4$ dependence [100]. Charge hopping between nearby traps can therefore give rise to discrete spectral jumps of the emitter line, as also observed and discussed by Ioannis Karapatzakis [72].

In the following we present the spectral properties of the SnV center used throughout this work. To probe these properties without power broadening the transition or inducing charge-state transitions, we operate at excitation powers well below the saturation power of the emitter. In Fig. 2.13(a), repeated PLE scans of the C transition are shown, performed at zero magnetic field at a temperature of $T = 50\,\mathrm{mK}$ and a power of $p = 0.6\,\mathrm{nW}$, corresponding approximately to $p_{\mathrm{sat}}/50$. Technically, the scan is performed by tuning the laser cavity of the resonant laser over a voltage range of 4 V. For the laser used (see Sec. 2.3.2) and wavelength regime, a scan voltage of 10 V corresponds to a frequency sweep of approximately 2.5 GHz. In Fig. 2.13(a), we use an integration time of 60 ms per point to ensure sufficient counting statistics. If spectral diffusion were present, it would manifest itself as an increased linewidth. In such a case it would be advantageous to scan faster than the characteristic spectral diffusion time in order to separately resolve the homogeneous

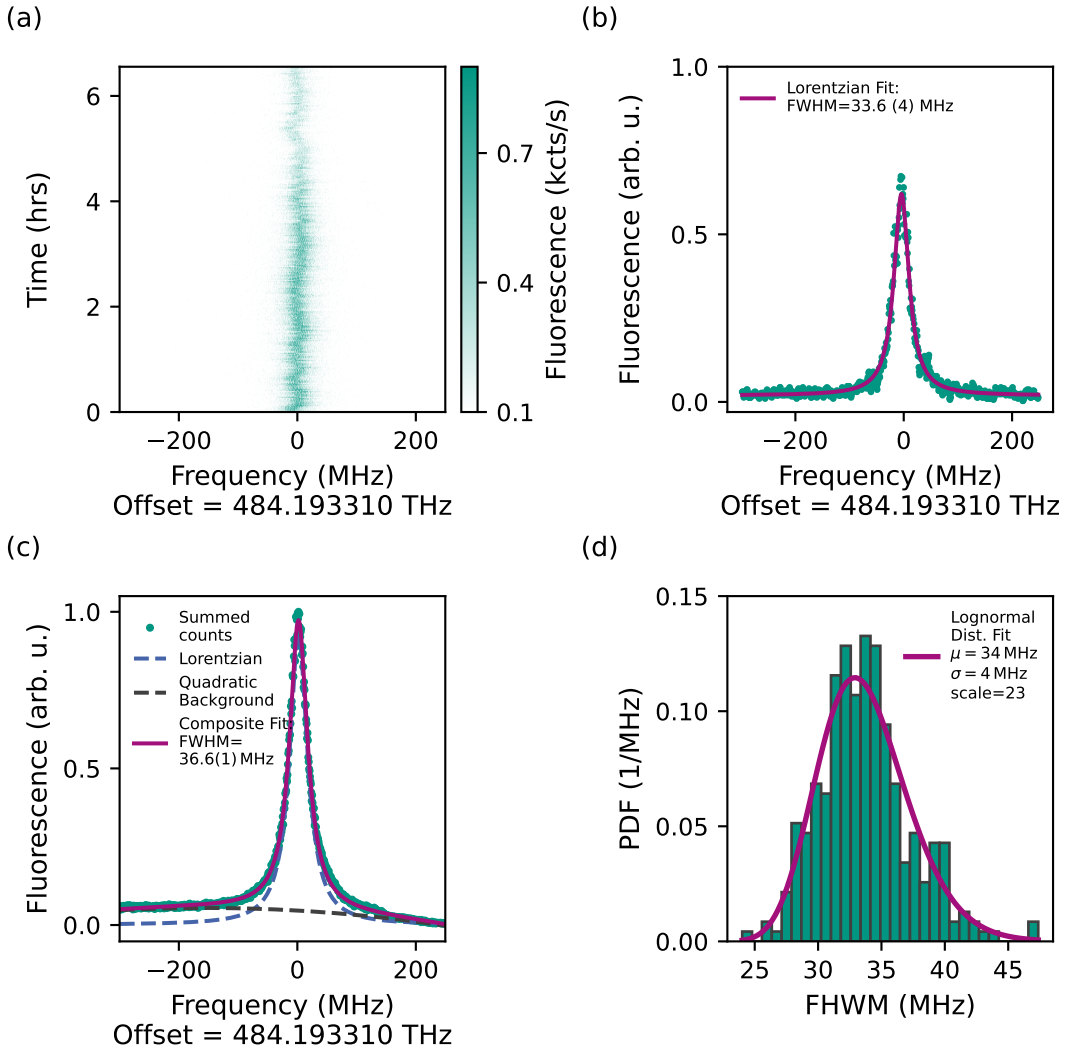

Figure 2.13.: Photoluminescence excitation spectroscopy and spectral diffusion. (a) Repeated PLE scans of the C transition performed at zero magnetic field at a temperature of 50 mK with an excitation power of $p = 0.6\,\mathrm{nW} \approx p_{\mathrm{sat}}/50$. (b) Single line sweep. A Lorentzian fit yields a FWHM of 33.6(4) MHz. (c) Lorentzian fit to the sum of all individual scans shown, resulting in a linewidth of 36.6(1) MHz. (d) Individual Lorentzian fits to each scan yield a linewidth of 34(4) MHz, in good agreement with the summed PLE scans. Since these values are also consistent with the single-scan linewidth, we conclude that slow spectral diffusion is negligible.

linewidth and the spectral broadening. The total measurement time for the repeated scans shown here is approximately 6 h. During this time we observe negligible spectral diffusion of the optical transition and no charge-state switching. This makes the emitter particularly promising for optical initialization and readout experiments, as neither charge repumping nor resonance checks are required during measurement sequences.

A single line scan yields a linewidth of 34(4) MHz, as shown in Fig. 2.13(b) and (d). Summing all recorded scans and fitting the resulting spectrum with a Lorentzian yields a linewidth of 36.6(1) MHz without any observable Gaussian contribution. Since no significant broadening is observed, this value is expected to be close to the Fourier-limited

linewidth determined by the excited-state lifetime of the emitter. Using this linewidth, we estimate a lifetime of $\tau_{\mathrm{SnV}} = 4.7(6)$ ns. This value is approximately 30% and 10% smaller, respectively, than previous lifetime measurements on other emitters in the same sample (performed during different cooldowns) which yielded 6.7(1) ns and 5.2(2) ns, respectively [70, 72]. Slightly shorter lifetimes have also been reported for ensembles of SnV centers located at similar depths below the diamond surface [79]. Since the excited-state lifetime of this particular emitter was not measured directly, and some emitter-to-emitter variation is expected, estimating the lifetime from the inverse Lorentzian linewidth provides a reasonable approximation for this system.

2.5. Magneto-optical response of the tin-vacancy center

As discussed in Sec. 2.1, the response of the SnV center to external magnetic fields depends on the field orientation with respect to its quantization axis. Here, we move beyond the general theoretical treatment and focus on the specific emitter investigated in this thesis, providing explicit parameters extracted from the experimental data.

2.5.1. Angle-dependent Zeeman spectroscopy

To gain a comprehensive insight into the optical and magnetic properties of the SnV center, we exploit the angular dependence by sweeping a dc magnetic field at fixed amplitude and recording the optical transitions as a function of the magnetic-field angle via repeated PLE scans.

This measurement is typically performed at elevated temperatures of $4 - 8$ K, where the electron spin lifetime is sufficiently short to allow population of both spin states while sweeping the laser across the spin-conserving transitions (see Appendix A.3 for further details). In Fig. 2.14, the two spin-conserving transitions A1 and B2 are shown. The magnetic-field orientation is given by the polar angle within the respective coordinate frame shown in the lower left corner. The magnetic-field amplitude is fixed at $|\boldsymbol{B}| = 200$ mT. The radial axis corresponds to the swept frequency and spans a range of $4.44 - 5$ GHz, depending on the respective sweep.

The blue-colored sweeps are taken with respect to the laboratory coordinate system, in the following also denoted shortly as lab frame, defined by the dc vector magnetic-field coils. From these measurements, the orientation of the SnV center's quantization axis can be determined. For this, we acquire two rotation maps, for example a XZ and a XY rotation map, as shown for the first two lab frame rotation maps in Fig. 2.14. Taking a closer look at the XZ scan in the lab frame, two key features can be observed. For orientations close to the polar angles $\theta = 0$ and $\theta = \pi$, the splitting between the two spin-conserving transitions is maximal. This corresponds to a dc magnetic field that is aligned as parallel as possible, within this plane, to the quantization axis. The observed splitting is proportional to the external magnetic-field amplitude as well as to the difference between the orbital

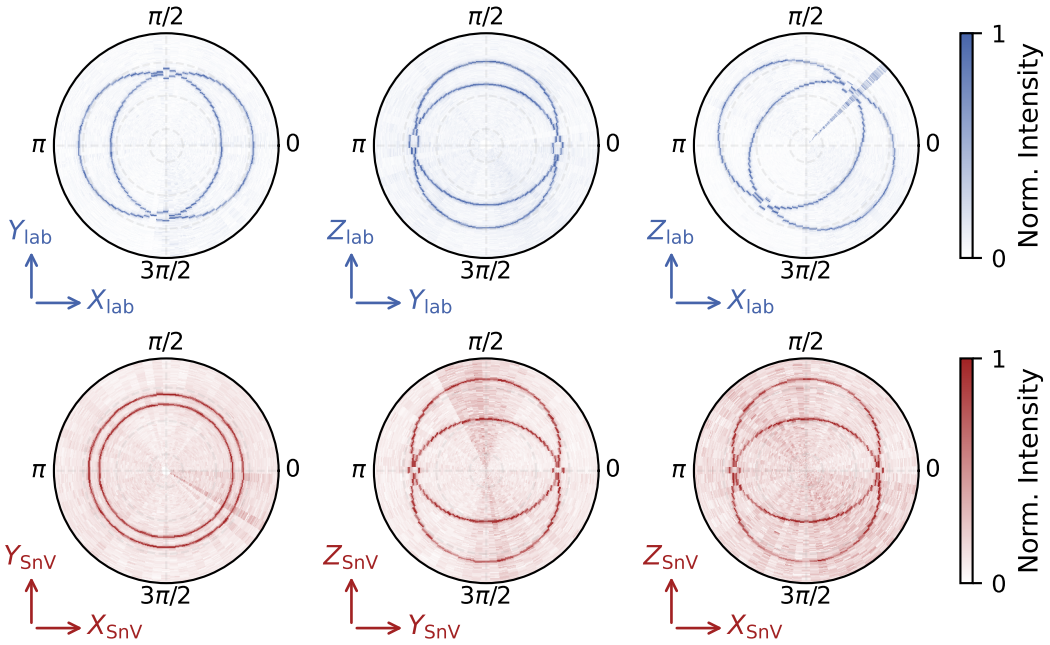

Figure 2.14.: Photoluminescence excitation spectra for different magnetic field sweeps. The amplitude of the magnetic field is set constant to $|\boldsymbol{B}| = 200\,\mathrm{mT}$. Top row: Sweeps in the lab frame indicated by the arrows on the bottom left of each subplot. Bottom row: Sweeps in the frame of the SnV center after changing the respective frame by using the angles found in the top row. All scans were deducted over a varying frequency range for each subplot, spanning in total between $4.44 - 5\,\mathrm{GHz}$.

quenching factors in the electronic ground and excited states, $f^g_{3/2}$ and $f^e_{3/2}$, as indicated in Fig. 2.3.

For magnetic-field orientations perpendicular to these directions, we observe an approach of both transitions, followed by a crossing and a subsequent splitting. The magnitude of this splitting depends on the strain of the emitter, as shown in Eq. 2.46. For a completely unstrained emitter, no splitting is observed [70]. This behavior allows us to determine the strain of the emitter, provided that the spin-orbit coupling λ is known. Using an unstrained emitter and measuring the energy difference between the C and D transitions of the lower and upper orbital ground states, respectively, we extract a ground-state spin-orbit coupling of $\lambda_g = 822(1)\,\mathrm{GHz}$ [70]. This value is consistent with measurements on deeply implanted SnV centers, located approximately 3 µm below the surface, that were subsequently treated by high-temperature annealing at 2100 °C. Both deep implantation and high-temperature annealing contribute to suppressing strain [77].

To determine the orientation of the SnV center within the lab frame, we simultaneously fit the Hamiltonian to the measured transition frequencies. Specifically, we use the qubit splittings Δ^g_q and Δ^e_q, defined in Eq. 2.39, and fit the difference between the corresponding allowed optical transition frequencies, including a variable angular offset. The tangent of this offset angle yields the ratio of the magnetic-field components parallel to the quantization axis of the SnV center, $Z_{\mathrm{SnV}} = (x_{\mathrm{lab}},\ y_{\mathrm{lab}},\ z_{\mathrm{lab}})^T$.

For the XY lab-frame scan, we obtain an angle of $\theta_{XY} = 91.1(1)^\circ$, while for the XZ lab-frame scan, we find $\theta_{XZ} = -54.1(1)^\circ$. This results in $x_{\mathrm{lab}}/y_{\mathrm{lab}} = \tan(91.1^\circ) = -53.4$ and $x_{\mathrm{lab}}/z_{\mathrm{lab}} = \tan(-54.1^\circ) = -1.4$. The vector parallel to the SnV-center quantization axis is therefore

$$\boldsymbol{Z}_{\mathrm{SnV}} = \begin{pmatrix} -0.810 \\ 0.015 \\ 0.586 \end{pmatrix}. \tag{2.78}$$

We can now also introduce the axes orthogonal to the SnV-center quantization axis, defining the new direction SnV frame, as

$$\boldsymbol{X}_{\mathrm{SnV}} = \begin{pmatrix} 0 \\ 0.999 \\ -0.025 \end{pmatrix}, \; \boldsymbol{Y}_{\mathrm{SnV}} = \begin{pmatrix} -0.586 \\ -0.021 \\ -0.809 \end{pmatrix}. \tag{2.79}$$

This set of vectors allows us to transform into the frame of the SnV center. Performing scans in the SnV frame, in particular in the XY plane of the SnV frame, provides a validation of this transformation. In the lower row of Fig. 2.14, the XY scan in the SnV frame is shown, revealing two circles corresponding to the two spin-conserving transitions. The presence of perfect circles is expected, as the polar angle between the dc magnetic field and the quantization axis is fixed at $\theta_{\mathrm{dc}} = 90^\circ$. This is, however, only possible if the absolute magnitude of the magnetic field remains constant for all orientations. Therefore, a calibration was performed in our previous work [70], where the response of the ^{13}C nuclear spin bath, i.e. its Larmor precession frequency, was measured at a given magnetic-field amplitude for two different orthogonal field orientations. From these measurements, correction factors were derived, and we obtain the magnetic-field components along the three different coil axes as

$$\begin{aligned} \text{Coil axis: X} &= -45.7(2)\,\mathrm{mT\,A^{-1}}, \\ \mathrm{Y} &= 61.5(3)\,\mathrm{mT\,A^{-1}}, \\ \mathrm{Z} &= 133.5(6)\,\mathrm{mT\,A^{-1}}. \end{aligned}$$

As the measured A1 and B2 transitions for the XY-SnV-frame scan in Fig. 2.14 form perfectly circular patterns without observable deviations, we conclude that the magnetic-field calibration is accurate.

The separation between the two circles is determined by the strain of the SnV center, yielding $\alpha^g = 41.3(8)$ GHz for the ground state and $\alpha^e = 65.5(3)$ GHz for the excited state. A more detailed description of the fitting procedure can be found in our previous work [70]. All parameters describing the full Hamiltonian of this SnV center are listed in Tab. 2.1.

2.5.2. Optical cyclicity and spin-selective transitions

Furthermore, in addition to the two allowed transitions A1 and B2, the two nominally forbidden transitions A2 and B1 become visible when the magnetic field is aligned perpendicular to the SnV quantization axis. This occurs as a result of spin mixing under these

conditions. This mixing can be treated using perturbation theory [72] or, as done in the following, by explicitly expanding the eigenvectors of the combined Hamiltonian.

For simplicity, we follow Refs. [69, 72] and consider spin mixing in the absence of strain and DJT contributions, leaving the Hamiltonian in the form $\hat{H} = \hat{H}_{\mathrm{SO}} + \hat{H}_{\mathrm{Z}}$. In the spin-orbit basis, the first term $\hat{H}_{\mathrm{SO}}$ is diagonal by construction. The Zeeman contribution can be written in the block form introduced in Eq. 2.26.

Assuming a purely transverse magnetic field $B_\perp$, only the off-diagonal elements of the sub-matrix $\hat{\Omega}$ remain finite in the Zeeman Hamiltonian. To first order in $B_\perp$, this leads to new eigenstates of the form

$$|e_- \downarrow\rangle' \approx |e_- \downarrow\rangle - \frac{\gamma_s B_\perp}{2\lambda} |e_- \uparrow\rangle \ , \tag{2.80}$$

$$|e_+ \uparrow\rangle' \approx |e_+ \uparrow\rangle - \frac{\gamma_s B_\perp}{2\lambda} |e_+ \downarrow\rangle \ . \tag{2.81}$$

As this effect originates from the off-diagonal elements of $\hat{\Omega}$, it follows that the electron spin of the lower orbital branch is mixed with the electron spin of opposite projection from the higher orbital branch of same orbital character. This can also be directly seen from the new eigenstates given above. Consequently, an off-axis magnetic field induces spin mixing without mixing the orbital degrees of freedom. As the mixing depends on the ratio between the off-axis magnetic field and the spin-orbit coupling constant, the spin mixing for a given magnetic field amplitude is stronger in the ground state than in the excited state. This is illustrated in Fig. 2.15(a) by the tilted arrows representing a tilted quantization axis of the spin levels in the excited state with respect to the ground state.

This has direct implications for the optical excitation of the SnV center under an applied external magnetic field. Due to the tilted quantization axes in the ground and excited states, only a finite number of spin-conserving excitation cycles are possible before the electron spin flips probabilistically. An important figure of merit is therefore the average number of spin-conserving cycles that can be driven. This quantity is characterized by

Table 2.1.: Fitted strain for the ground and excited state of the SnV center used withing this thesis with the relevant Hamiltonian parameters taken from [70]. The table is reprinted from Ref. [71].

Parameter	Value	Source
λ^{g} (GHz)	822	[70]
Υ^{g} (GHz)	41.3(8)	fitted
λ^{e} (GHz)	3000	[55, 79]
Υ^{e} (GHz)	65.5(34)	fitted
f_{12}^{g}	0.251	[70]
f_{32}^{g}	0.268	[70]
f_{12}^{e}	0.5	[70]
f_{32}^{e}	0.486	[70]
$B_\parallel$ (mT)	200	fixed
$B_\perp$ (mT)	200	fixed

the cyclicity, defined as the ratio between the probability of an electron spin-conserving decay P_{ec} and that of an electron spin-flipping decay P_{ef} [103]. This leads to the cyclicity given as

$$\Lambda_{\mathrm{e}} = \frac{P_{\mathrm{ec}}}{P_{\mathrm{ef}}} \,, \tag{2.82}$$

where we follow the notation of the indices introduced in our Ref. [71].

In order to simulate the cyclicity, the system can be reduced to an effective three-level system formed by the states $|1\rangle, |2\rangle, |A\rangle$ shown in Fig. 2.15(a). A comprehensive study of the cyclicity based on a master-equation approach has been presented e.g. by Ioannis Karapatzakis [72]. This framework enables both analytical and numerical simulations of the cyclicity using experimentally determined parameters.

Here, however, we aim to provide an intuitive picture of how the cyclicity depends on the off-axis magnetic field, following closely the discussion in Ref. [104]. We therefore consider the dipole operator of the SnV center, which acts only on the orbital part of the eigenstates and leaves the electron spin unchanged. Its components connect orbitals in the ground and excited states. In the following, we use the spin-orbit basis introduced in Ref. [73]. In this basis, the components of the dipole operator are given by

$$\hat{p}_x = \hat{\sigma}_x \otimes \hat{1}_2 \,, \qquad \hat{p}_y = \hat{\sigma}_y \otimes \hat{1}_2 \,, \qquad \hat{p}_z = 2\,\hat{1}_2 \otimes \hat{1}_2 \,. \tag{2.83}$$

The factor of two represents an empirical scaling of the dipole component $\hat{p}_z$ relative to the transverse components $\hat{p}_x$ and $\hat{p}_y$ [73]. This expression is adapted to our basis notation by permuting the rows and columns.

For simplicity, the excited state is for now assumed to be a pure spin-orbit eigenstate, i.e. $|A\rangle = |e_-^u \downarrow\rangle$, because its opposite-spin admixture is smaller than that of the ground state. For the qubit states, we use the mixed eigenstates introduced above, $|1\rangle = |e_-^g \downarrow\rangle'$ and $|2\rangle = |e_+^g \uparrow\rangle'$.

Following Ref. [104], the cyclicity can be estimated from the ratio of the spin-conserving to the spin-flipping transition strength. For completeness, we repeat the derivation here:

$$\Lambda_{\mathrm{e}} \propto \frac{|\langle A|\,\hat{p}\,|1\rangle|^2}{|\langle A|\,\hat{p}\,|2\rangle|^2} \,. \tag{2.84}$$

For the spin-conserving transition, we obtain

$$|\langle A|\,\hat{p}\,|1\rangle|^2 = \left| \underbrace{\langle e_-^u \downarrow|\,\hat{p}\,|e_-^g \downarrow\rangle}_{=2} - \frac{\gamma_s B_\perp}{2\lambda^g} \underbrace{\langle e_-^u \downarrow|\,\hat{p}\,|e_-^g \uparrow\rangle}_{=0} \right|^2 = 4 \,. \tag{2.85}$$

For the spin-flipping transition, we find

$$|\langle A|\,\hat{p}\,|2\rangle|^2 = \left| \underbrace{\langle e_-^u \downarrow|\,\hat{p}\,|e_+^g \uparrow\rangle}_{=0} - \frac{\gamma_s B_\perp}{2\lambda^g} \underbrace{\langle e_-^u \downarrow|\,\hat{p}\,|e_+^g \downarrow\rangle}_{=1-i} \right|^2 = \left(\frac{\gamma_s B_\perp}{\sqrt{2}\lambda^g} \right)^2 . \tag{2.86}$$

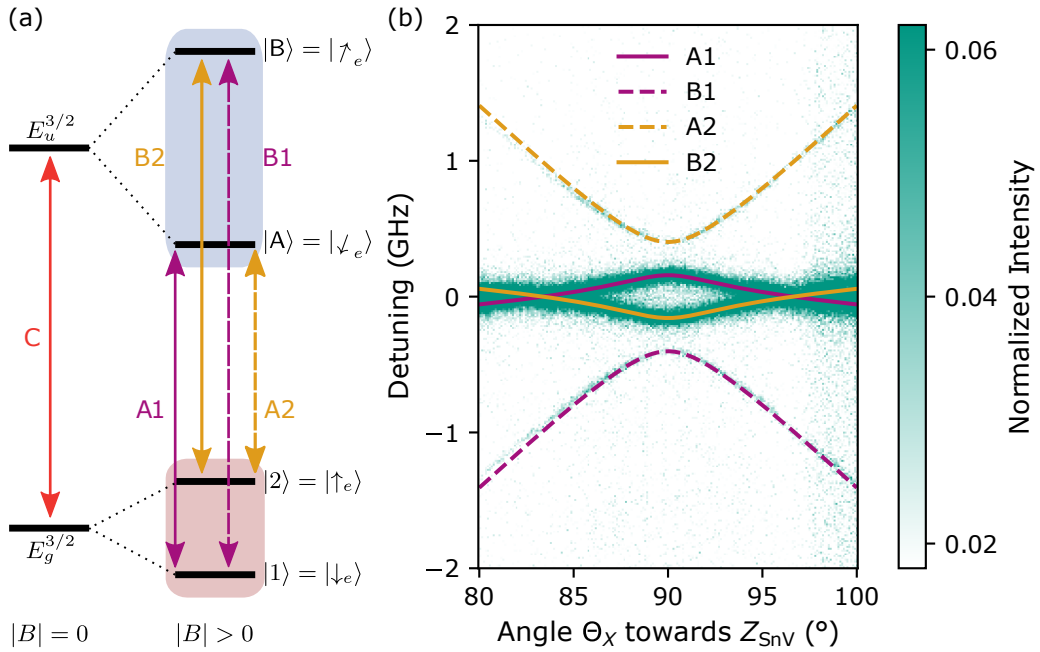

Figure 2.15.: Spin-conserving and spin-flipping transitions under off-axis magnetic fields. (a) Level scheme showing the Zeeman splitting of the ground (excited) state of the lowest orbital branch $E_g^{3/2}$ ($E_u^{3/2}$) under an external magnetic field. The C-transition splits into a total of four transitions, where two are spin-conserving and two spin-flipping transitions. (b) Photoluminescence excitation spectra using a magnetic field of $|\boldsymbol{B}| = 200\,\mathrm{mT}$ around the X-axis of the SnV center. The central bright lines are the spin allowed transitions, the faint lines the spin-flipping forbidden transitions. The analytical lines are reproduced by using Equation 2.39 and the Hamiltonian fit in Table 2.1. The transitions are labeled such, that they reproduce the commonly used name of the transitions for a field alignment parallel to the SnV center quantization axis as shown in (a).

This gives a cyclicity

$$\Lambda_\mathrm{e} \propto \left(\frac{2\lambda^g}{\gamma_s B_\perp}\right)^2, \tag{2.87}$$

showing that, for small off-axis field magnitudes, the cyclicity decreases quadratically with the perpendicular magnetic field component $B_\perp$.

This behavior is reflected in the weak increase of the nominally forbidden transitions A2 and B1 in Fig. 2.15(b), indicated by the dashed lines. However, due to the low count rate of these transitions in this scan, their angular dependence cannot be fitted reliably. The quadratic dependence is observed more clearly for other SnV centers, as shown in the PhD thesis of Ioannis Karapatzakis, Fig. 2.9(c) [72].

Therefore, achieving high cyclicity requires aligning the external magnetic field as parallel as possible to the quantization axis of the SnV center.

Modeling the cyclicity. There are multiple approaches to model the cyclicity and fit it to experimentally obtained data. In general, we follow Refs. [103, 105] and use the reduced three-level system introduced above, which is optically driven by a laser with optical Rabi

frequency Ω_{opt}. The resulting coherent Hamiltonian for driving the spin-conserving A1 transition is given by

$$H = \Delta_{\text{opt}} |A\rangle \langle A| + \frac{\Omega_{\text{opt}}}{2} \left(|1\rangle \langle A| + |A\rangle \langle 1| \right) , \tag{2.88}$$

where Δ_{opt} denotes the detuning of the laser from the spin-conserving transition. In addition, spontaneous emission into the ground states $|1\rangle$ and $|2\rangle$ occur. This can be implemented by introducing the spin-conserving decay rate γ_{A1} and the spin-flipping decay rate γ_{A2}. Using the definition of the cyclicity Λ_{e} given in Eq. 2.82, these rates can be re-expressed in terms of the cyclicity and the total spontaneous emission rate γ [103], yielding

$$\gamma_{\text{A1}} = \gamma P_{\text{ec}} = \gamma \frac{\Lambda_e}{\Lambda_e + 1} , \tag{2.89}$$

$$\gamma_{\text{A2}} = \gamma P_{\text{ef}} = \gamma \frac{1}{\Lambda_e + 1} . \tag{2.90}$$

These rates can be used to create a set of master equations, to solve the dynamics of the three-level system under these conditions. By imposing that the spin-conserving transition rate is much larger than the spin-flipping transition, one can set the time-derivatives of the coherences to zero and ends up with quasi-stationary solutions of the master equations [105]. For the populations of lowest ground state $|1\rangle$ and for the excited state $|A\rangle$ one obtains [105]

$$\dot{\rho}_{11} = -W\rho_{11} + (W + \gamma_{\text{A1}})\rho_{\text{AA}} , \tag{2.91}$$

$$\dot{\rho}_{\text{AA}} = W\rho_{11} - (W + \gamma)\rho_{\text{AA}} , \tag{2.92}$$

where W is the rate

$$W = \frac{\Omega_{\text{opt}}^2 \gamma}{4\Delta_{\text{opt}}^2 + \gamma^2} . \tag{2.93}$$

As the fluorescence signal is directly proportional to the population of the excited state ρ_{AA}, the cyclicity can be extracted by solving the corresponding differential equations and fitting the result to experimentally measured data.

Usually, the optical Rabi frequency is not known, but it is related to the saturation parameter $s = p/p_{\text{sat}}$ of the spin-conserving transition via the relation $s = 2\Omega_{\text{opt}}^2/\gamma^2$ [88]. The total decay rate γ is determined by the excited-state lifetime or, equivalently, by the full width at half maximum (FWHM) of the Lorentzian linewidth obtained from PLE measurements of the C transition.

Starting from the optical pumping rate R from $|1\rangle$ into the excited state $|A\rangle$, one can derive an effective rate model that captures the essential features of the spin initialization dynamics [103]. The rate R is given by [103]

$$R = \frac{\gamma}{2} \frac{s}{1 + s + \left(\frac{\Delta_{\text{opt}}}{\gamma/2} \right)^2} . \tag{2.94}$$

The spin polarization rate into the state $|1\rangle$ is given by $\Gamma_p = \frac{R}{\Lambda_e+1}$, resulting in an exponential decay of the population $\rho_{11}(t) = \rho_{11}(0)e^{-\Gamma_p t}$ and, correspondingly, an exponential decay of the observed fluorescence [103]. The same spin polarization rate can be recovered by performing a Taylor expansion of the solutions of the model introduced before in the limit of small spin-flipping rates [105].

An important feature becomes immediately apparent: for a finite cyclicity, initialization into the state $|1\rangle$ is possible by pumping exclusively the A1 transition, since the spin-flipping probability is non-zero. Furthermore, the cyclicity determines the mean number of photons, emitted before initialization into the opposite spin state occurs, as reflected by the polarization rate. Assuming that photons are emitted only via the cycling transition - which is generally justified, since the splitting between the two transitions is much larger than the emitter linewidth, we can extract the mean number of photons emitted before a spin flip occurs as $\langle N_{\mathrm{ph}}\rangle = \Lambda_e + 1$ [103]. Consequently, a higher cyclicity results in a longer initialization time at fixed pump power, but also in the emission of a larger number of photons per initialization, which is an important requirement for the single-shot readout of the spin state [41, 60, 103, 106].

If one aims to include more complex dynamics or extend the model to additional levels, it is often advantageous to describe the system using a simple rate-equation model rather than solving the full master equation and subsequently enforcing the vanishing of coherences.

For n ground states and m excited states we obtain rate equations of the ground state populations

$$\dot{N}_i^g = \sum_{j=1}^{m} (b_{ji}\gamma + R_{ji})N_j^e - R_{ji}N_i^g\,, \tag{2.95}$$

where we introduced the branching into the ground states by the $m \times n$ matrix $\hat{b}$. Similarly, the optical pumping processes are represented by the $m \times n$ matrix $\hat{R}$, which connects the ground and excited states. For the populations of the excited states, we obtain

$$\dot{N}_i^e = \sum_{j=1}^{n} \left[R_{ji}N_i^g - (R_{ji} + \gamma)N_i^e\right]\,. \tag{2.96}$$

If we set $n = 2$, $m = 1$ and choose $\hat{b} = (P_{\mathrm{ec}},\ P_{\mathrm{ef}})$ and $\hat{R} = (W, 0)$, we recover the model given in Eq. 2.91. However, we now have a framework that allows us to solve these rate equations efficiently and allows to include additional rates or energy levels as required, without significantly increasing the computational overhead.

A comparison of both the rate model, which can be solved numerically and the above introduced analytical model is shown in Fig. 2.16. The parameters in the figure are chosen to match the order of magnitude of the experimental values used in this thesis. The saturation parameter is set to $s = 1/3$, the spontaneous emission rate to $\gamma/2\pi = 34\,\mathrm{MHz}$, and the optical detuning to $\Delta_{\mathrm{opt}} = \gamma/2\pi$. The cyclicity is set to the experimentally determined value of $\Lambda_e = 6000$ for this emitter, resulting in a decay on the millisecond timescale. Apart from the visible population transfer into ρ_{AA} for the rate model, both models show perfect

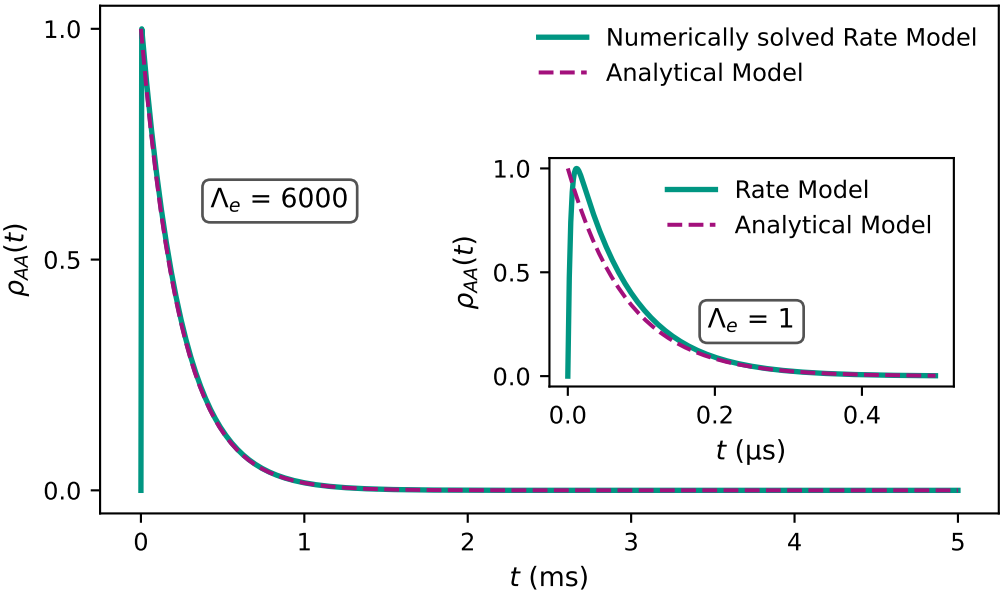

Figure 2.16.: Comparison of the excited-state population ρ_{AA} obtained from the rate model introduced in Eq. 2.96 and the analytical model presented in Refs. [103, 105]. The parameters are chosen to match the order of magnitude of the experimental values used in this thesis. The saturation parameter is set to $s = 1/3$, the spontaneous emission rate to $\gamma/2\pi = 34\,\mathrm{MHz}$, and the optical detuning to $\Delta_{\mathrm{opt}} = \gamma/2\pi$. The cyclicity is chosen as $\Lambda_{\mathrm{e}} = 6000$, resulting in a decay on the millisecond timescale. Apart from the visible population transfer into ρ_{AA} for the rate model, both models show perfect agreement. If the cyclicity is reduced, as indicated in the inset (here $\Lambda_{\mathrm{e}} = 1$), deviations become apparent at short timescales.

agreement. If the cyclicity is reduced, as indicated in the inset in Fig. 2.16 (here $\Lambda_{\mathrm{e}} = 1$), deviations become apparent at short timescales. Such small cyclicity occur under magnetic fields aligned perpendicular along the SnV quantization axis as presented in Ref. [72]. Such small cyclicity lead to faster initialization times at the cost of reduced photon counts per initialization. This reduced amount of data can be circumvented by increasing the number of measurement cycles. Of course this is only suitable for measurements that are time-wise only limited by the initialization time and not some other time, e.g. a waiting time.

We can also consider the initialization process from a statistical perspective and ask: what is the probability that a spin flip with probability $p = P_{\mathrm{ef}}$ requires n independent spin-conserving excitations with probability $1 - p = P_{\mathrm{ec}}$? Such a process is described by the geometric distribution [41] as

$$P(N = n) = (1 - p)^{n-1} p\,, \tag{2.97}$$

where N denotes the number of trials, i.e. the number of photons emitted before a spin flip occurs. The expectation value of this distribution is

$$E(N) = \frac{1}{p} = \frac{1}{P_{\mathrm{ef}}} = \Lambda_{\mathrm{e}} + 1\,, \tag{2.98}$$

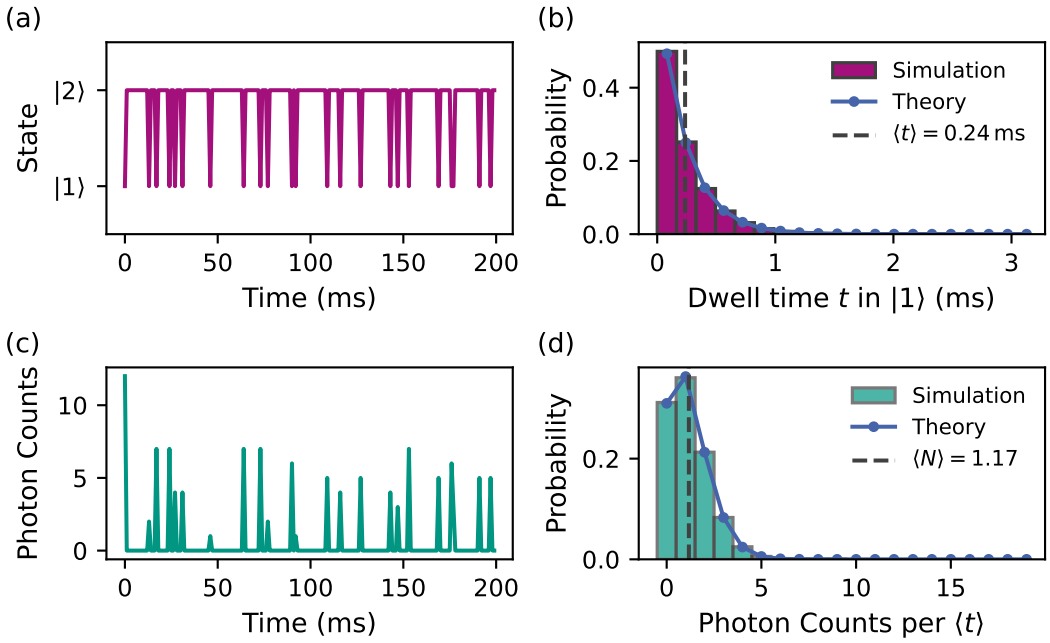

Figure 2.17.: Simulation of random telegraph switching between states $|1\rangle$ and $|2\rangle$ under optical pumping and finite spin relaxation time T_1. (a) Simulated telegraph-like switching between the states assuming polarization rates $\Gamma_{12} = \Gamma_p + 1/T_1$ and $\Gamma_{21} = 1/T_1$. (b) Histogram of the dwell times results in the characteristic exponential decay with a mean dwell time of 0.24 ms. (c) Time trace of detected photons assuming that each event results in a Poisson-distributed number of scattered photons. (d) Binning the detected photon counts leads to a Poisson distribution with a mean photon number per dwell time of approximately $\eta\Lambda_e$, where η is the overall collection efficiency of the optical setup. Simulation parameters are found in Tab. 2.2.

yielding the same expected result as derived above. This means that we can estimate the overall collection efficiency of our setup by measuring the mean number of detected photons per initialization sequence, i.e. flipping the spin, and dividing it by the cyclicity.

If we instead consider the dwell time of being either in state $|1\rangle$ or $|2\rangle$ as a function of time, we expect an exponential distribution for the waiting time between spin flips,

$$P(t, \Gamma) = \Gamma e^{-\Gamma t}, \tag{2.99}$$

characterized by the switching rate Γ [107]. For leaving the state $|1\rangle$, the rate is given by $\Gamma_{12} = \Gamma_p + 1/T_1$, while for leaving the state $|2\rangle$ it is $\Gamma_{21} = 1/T_1$, where T_1 denotes the relaxation time of the states $|1\rangle$ and $|2\rangle$ or any other rate connecting these two states. This switching results in a telegraph-noise like behavior as shown in Fig. 2.17(a). The autocorrelation function of the random telegraph noise is given by [108]

$$\langle s(t)s(0)\rangle \propto e^{-(\Gamma_{12}+\Gamma_{21})t}. \tag{2.100}$$

This defines a correlation time $\tau_c = 1/(\Gamma_{12} + \Gamma_{21})$. Under the reasonable assumption that $1/T_1 \ll R$, we obtain

$$\tau_c \approx 1/\Gamma_p = \frac{(\Lambda_e + 1)}{R}. \tag{2.101}$$

Thus, the cyclicity can alternatively be extracted by analyzing the autocorrelation of a telegraph-noise time trace. In the opposite limit of weak optical pumping, $R \ll 1/T_1$, the same approach can be used to determine the relaxation time T_1.

The number of photons emitted during one dwell time t is determined by the emission rate R and follows a Poisson distribution

$$P(N(t) = n) = \frac{(Rt)^n}{n!} e^{-Rt}, \tag{2.102}$$

which describes the probability of detecting n photons within a time interval t, given an average emission rate R [88, 103]. For the spin-conserving transition considered here, we use R given in Eq. 2.94.

Using all parameters listed in Tab. 2.2, we simulate the telegraph-like switching between the states $|1\rangle$ and $|2\rangle$, as shown in Fig. 2.17(a). We find an optical pump rate of $R \approx 25\,\mathrm{MHz}$ and a polarization rate $\Gamma_p \approx 4\,\mathrm{kHz}$.

Assuming that each event results in a Poisson-distributed number of scattered photons yields the time trace displayed in Fig. 2.17(c), which is in good agreement with the raw time traces observed in the experiment. Histogramming the dwell times results in the characteristic exponential decay expected from the model introduced above. We obtain a mean dwell time of 0.24 ms. Binning the detected photon counts shown in Fig. 2.17(c) leads to a Poisson distribution with a mean photon number per dwell time of approximately

$$\langle N \rangle = \eta \Lambda_\mathrm{e}, \tag{2.103}$$

which is independent on the optical pump rate R. It depends solely on the cyclicity and the collection efficiency. For the collection efficiency, we use values obtained for our setup (see Sec. 5.2), which is in good agreement with reported values for bulk samples [60].

Table 2.2.: Simulation parameters used for the results shown in Fig. 2.17. The implementation of these parameters within the respective probability distributions is described in the main text. The parameters were chosen to mimic the experimentally observed values and are the same parameters used in Fig 2.16.

Parameter	Symbol	Value
Spontaneous emission rate	$\gamma/2\pi$	34 MHz
Saturation parameter	s	1/3
Optical detuning	Δ_opt	$\gamma/2\pi$
Cyclicity	Λ_e	6000
Collection efficiency	η	0.02%
Spin relaxation time	T_1	10 ms
Binwidth Fig. 2.17(a) and (c)	-	1 ms
Total simulated time Fig. 2.17(a) and (c)	-	200 ms
Sample size Fig. 2.17(b) and (d)	-	100 000

Role of the second orbital ground state. So far, we have assumed a simplified three-level system. However, as discussed in Sec. 2.1, the SnV center possesses a higher orbital ground state into which the system can relax from the excited state with a probability of approximately $20 - 25\%$ [109, 110]. After such a decay event, the system remains in the upper orbital branch for a characteristic lifetime τ_{ub} before relaxing back into the lowest orbital branch. Consequently, the optical pumping rate R could in principle be limited by the lifetime of the upper orbital branch, i.e. $R \leq 1/\tau_{\mathrm{ub}}$ [60].

The relaxation rate to the lower orbital branch is given by the phonon emission rate

$$\gamma_- = 2\pi\chi\rho_0\Delta_{\mathrm{GS}}^3(n_{\mathrm{th}}(\Delta_{\mathrm{GS}}, T) + 1)\,, \tag{2.104}$$

where χ denotes the phonon scattering cross section, ρ_0 a proportionality constant related to the phonon density of states, and n_{th} the thermal phonon occupation given by the Bose-Einstein distribution [58, 69, 111]. The scattering cross section χ and the phonon density ρ_0 can be calculated theoretically and show reasonable agreement with experimentally obtained values [90, 111].

In the following, we use the experimentally determined parameters reported by Jahnke *et al.* [58]. They fitted data from a SiV center with a ground-state splitting of 50 GHz and obtained the rate

$$\gamma_-^{\mathrm{SiV}} = \frac{1}{101}(n_{\mathrm{th}}(50\,\mathrm{GHz}, T) + 1)\,\mathrm{GHz}\,. \tag{2.105}$$

Using the scaling approach of Ref. [60], this result can be rescaled to the ground-state splitting of the SnV center as

$$\gamma_- = \gamma_-^{\mathrm{SiV}}\left(\frac{50\,\mathrm{GHz}}{\Delta_{\mathrm{GS}}}\right)^3\,. \tag{2.106}$$

In addition, the lifetime of the upper orbital branch of an SnV center with a ground-state splitting of 830 GHz was measured to be $\tau_{\mathrm{ub}} \approx 30\,\mathrm{ps}$ at 4 K in Ref. [112]. Substituting the ground-state splitting value into Eq. 2.106 yields $1/\gamma_- \approx 22\,\mathrm{ps}$, in reasonable agreement with the reported lifetime. The deviation can be attributed to the scaling assumption that SnV and SiV centers have the same phonon scattering cross section χ and phonon density ρ_0. While this assumption is reasonable for the phonon density, theoretical work predicts a scattering cross section that is approximately three times smaller for the SnV center than for the SiV center [111].

Due to the large ground-state splitting of the SnV center and the low temperatures considered here, i.e. $k_{\mathrm{B}}T/h\Delta_{\mathrm{GS}} \ll 1$, this rate is effectively temperature independent. Consequently, the orbital lifetime can be assumed to be the same for the experiments performed in this work.

We therefore conclude that $R \ll \gamma_-$ and that the optical pumping rate is not limited by branching into the upper orbital branch. However, as discussed in Ref. [60], this effect becomes relevant for unstrained SiV centers, where the corresponding rate is approximately four orders of magnitude smaller than for the SnV center.

Cyclicity as a function of strain and magnetic field. In general, the cyclicity should diverge for a perfectly aligned magnetic field, independent of the strain magnitude or the externally applied dc magnetic field. This can be directly simulated using Eq. 2.85 and Eq. 2.86 without introducing additional simplifications.

Assuming a conservative misalignment of 1° at a magnetic-field magnitude of 100 mT for an emitter with a strain of $\alpha^g = 43\,\mathrm{GHz}$ and $\alpha^e = 63\,\mathrm{GHz}$, one would expect a cyclicity of approximately 10^6. This value is significantly larger than the cyclicity measured in our experiments and about one order of magnitude higher than the cyclicity achieved for low-strain SiV centers [60], which is surprising as we would expect a higher spin-orbit coupling to create a common quantization axis in ground and excited state [104]. Reducing the cyclicity to the experimentally observed value would require an unrealistic misalignment of several degrees or the presence of a constant stray magnetic field on the order of 50 mT, both of which would be clearly visible in our measurements and much larger than any hyperfine interactions observed. A similarly limited cyclicity has also been reported for strained SnV centers [90].

We simulate the cyclicity for a magnetic-field amplitude of $|B| = 200\,\mathrm{mT}$ while varying the strain α, normalized to the ground-state splitting, and the angle between the external dc magnetic field and the SnV quantization axis, as shown in Fig. 2.18.[3] For the strain in the excited state, we assume the approximate relation for the SnV center $\alpha^e \approx 1.7\alpha^g$.

In addition, we plot reported cyclicity values for SnV centers and, for broader context, also include values obtained for SiV and GeV centers. Most measurements performed with an aligned magnetic field yield significantly lower cyclicity values than predicted by the model. The trend of decreasing cyclicity with increasing misalignment angle at constant strain can be observed, for example, in the measurements by Ref. [103][4] or our Ref. [70]. The prediction of a rising cyclicity for perpendicular alignment has not been observed, even in our earlier work [70], where the model would predict a broad range around 90° to show this increase. We find that for a fixed angle, which can be arbitrary small, but larger than zero, the cyclicity will decrease with increasing strain (for similar simulations see also Refs. [82, 84, 104]).

Also, even for aligned fields, the experimentally observed cyclicity remains much smaller than the theoretically expected value. We therefore conclude that additional effects not captured by this model must contribute to a finite spin mixing, thereby limiting the cyclicity to values smaller than those predicted by the simplified theory.

[3] I want to thank Mohamed Elshorbagy for pointing out the importance of keeping track of the varying ordering of eigenvectors during the angular sweep.

[4] The code for converting the magnetic field angles in Ref. [103] to the SnV frame was done by Mohamed Elshorbagy during his master's thesis under my supervision.

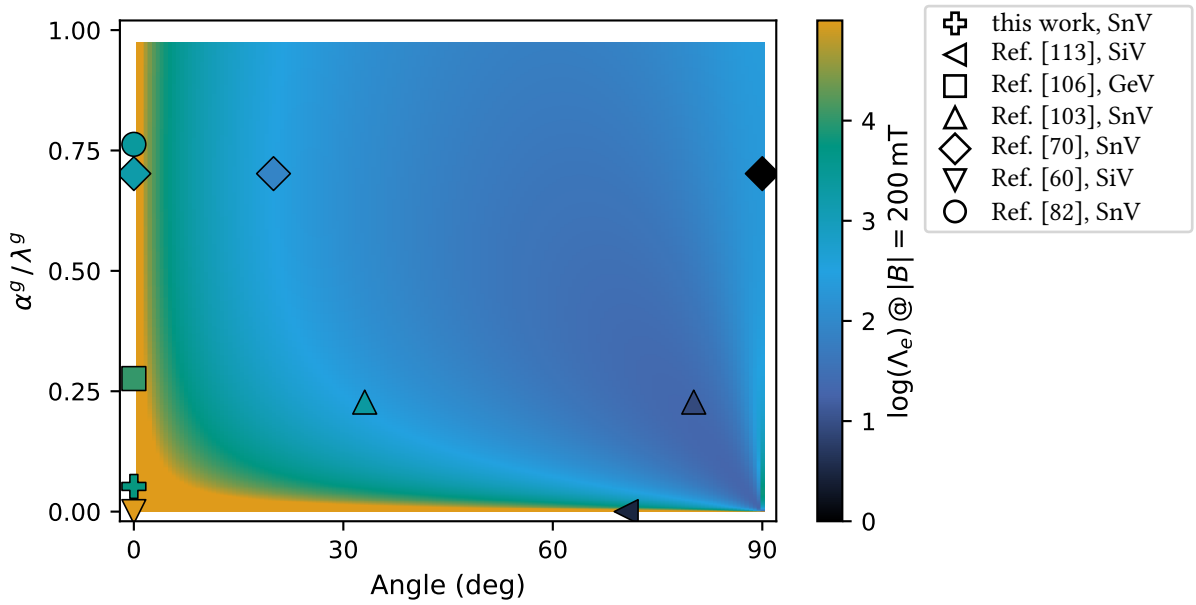

Figure 2.18.: Simulation of the cyclicity at a magnetic field amplitude of $|B| = 200\,\mathrm{mT}$ for varying strain α normalized to the ground state splitting and angles between the external dc magnetic field and the SnV quantization axis. For the excited state strain we assume the coarse relation for the SnV center of $\alpha^e \approx 1.7\alpha^g$. Most of the measurements with aligned magnetic field yield significantly lower cyclicity values. The trend of increasing angle at constant strain can be seen for e.g. Ref. [103] or Ref. [70].

2.6. Summary

In this chapter, we developed a comprehensive description of the SnV center, linking its electronic Hamiltonian to experimentally observable quantities. Starting from the effective Hamiltonian, including spin-orbit coupling, dynamical Jahn-Teller interaction, strain, and external magnetic fields, we established the level structure and qubit splittings relevant for this work. Based on this framework, we derived a theoretical description of the microwave-driven spin dynamics. In particular, we introduced an effective Rabi frequency that captures the response of the SnV center to an oscillatory magnetic field. This model reveals a strong dependence on both strain and magnetic-field geometry and shows how strain-induced orbital mixing enables magnetic dipole transitions between spin states that would otherwise be forbidden.

We also introduced the experimental platform and measurement techniques used throughout this thesis, including the cryogenic sample environment, optical excitation and detection, and microwave and radio-frequency control. Angle-dependent PLE measurements enabled the extraction of the emitter's orientation within the laboratory frame.

Further, the optical properties of the SnV center were characterized via PLE spectroscopy, revealing narrow linewidths close to the Fourier limit and negligible spectral diffusion.

Finally, we analyzed the cyclicity using both analytical and rate-equation models. While the theoretical framework predicts very high cyclicity for ideal conditions, the experimentally

observed values are significantly lower, indicating the presence of additional spin-mixing mechanisms beyond the simplified model.

Overall, this chapter establishes the SnV center as a well-understood quantum system and provides the essential foundation required for its use in the following spin initialization, control, and readout experiments.

3. Coherent control and decoherence mechanisms

A qubit in general can be any energetically isolated quantum mechanical two-level system. Here we consider the Zeeman-split spin sublevels of the lowest ground state of the SnV center as our qubit. For simplicity we denote the ground state as $|e_+ \downarrow\rangle = |0\rangle$ and the excited state $|e_- \uparrow\rangle = |1\rangle$, such that $|0\rangle$ and $|1\rangle$ form the two eigenstates of the qubit.

If we want to describe arbitrary superposition states of such a qubit, we can use a complex superposition of the two basis states, leading to a state

$$|\Psi\rangle = a_1 e^{i\phi_1} |0\rangle + a_2 e^{i\phi_2} |1\rangle \ , \tag{3.1}$$

where we introduced the four real numbers $a_1,\ a_2,\ \phi_1$ and ϕ_2. For this state to be a pure state, it must be normalized to one. We can further neglect a global phase, as we are only interested in phase differences between the two eigenstates. These restrictions leave two independent real numbers, which can be depicted by two angles, one polar and one azimuthal, to describe the qubit state. Doing so leads to

$$|\Psi\rangle = \cos(\theta/2) |0\rangle + \sin(\theta/2) e^{-i\phi} |1\rangle \ . \tag{3.2}$$

These states are usually represented as points on the Bloch sphere. In Fig. 3.1, the ground state ($\theta = 0$) is shown in green residing on the north-pole of the sphere. The state can be also written as a Bloch-vector pointing along the $+z$ axis of the Bloch sphere. In purple, an arbitrary superposition state with $\theta = -\pi/2$ and $\phi = -3\pi/4$ is shown. We can directly see that the ground and excited states carry no phase information ϕ. Superposition states in contrast are sensitive to the relative phase or also called coherence between the two eigenstates.

The relevant question is not only whether the SnV center spin or a proximal nuclear spin can form a qubit, but also whether they constitute a useful qubit. There are seven criteria that are widely used as a standardized measure to assess different qubit platforms: five criteria for quantum computing and two for quantum networking. These are known as the DiVincenzo criteria [114].

First, a scalable physical system with well-defined qubits is required. The theoretical basis for this is provided in Chapter 2, while Chapter 4 and Chapter 5 present the corresponding experimental implementations. The second criterion requires that the qubits can be initialized into a known and controllable state. In our system, this can be achieved by exploiting the finite cyclicity under optical illumination (see Sec. 2.5.2).

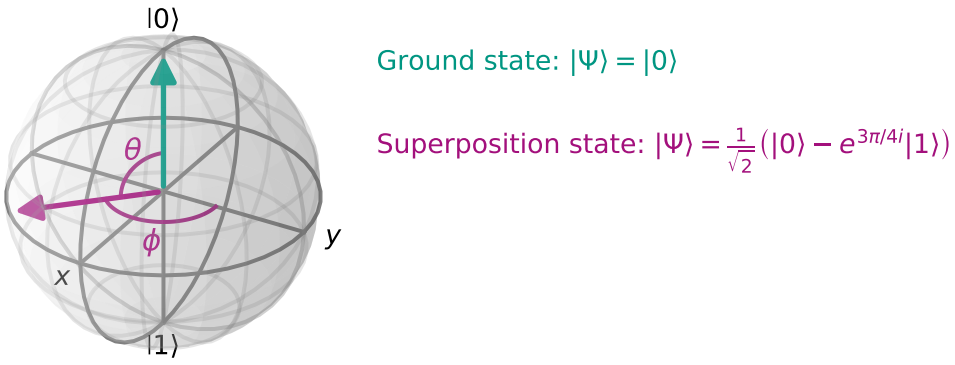

Figure 3.1.: Representation of a qubit using the Bloch-sphere, where $|0\rangle$ is the ground state and $|1\rangle$ the excited state of the qubit. Exemplarily, the ground state and a superposition state are shown, illustrating the role of the polar and azimuthal angles θ and ϕ.

Third, the coherence time of the qubit must be long compared to the gate operation time. The theoretical requirements for this condition will be discussed in the following sections. The fourth and fifth criteria require that a universal set of gates can be implemented on the qubit and that individual qubits can be measured with high fidelity. In this work, we demonstrate high-fidelity single-qubit gates on a proximal nuclear spin and perform qubit readout via its interaction with the electron spin in Chapter 5.

The characterization of two-qubit gates constitutes a natural next step but is not addressed in this thesis.

3.1. Coherent spin driving

As discussed in Sec. 2.2, we can drive the qubit by applying an oscillatory magnetic field, which leads to coherent oscillations between the ground and excited states with a Rabi frequency Ω. The exact amplitude of this Rabi frequency for the SnV center, including the effects of external magnetic fields and strain, can be found in the referenced section.

Here, we write this in the form of a simple two-level Hamiltonian

$$H = -\frac{1}{2}\Delta_q \sigma_z - \frac{1}{2}\Omega \cos(\omega t + \varphi)\sigma_x \,, \tag{3.3}$$

where Δ_q is the qubit splitting, ω the drive frequency, and φ the drive phase. Applying a frequency close to the qubit splitting, i.e. $\omega \approx \Delta_q$, leads to oscillations as shown in Fig. 3.2(a), where a so-called π-pulse is performed. Due to the qubit splitting being much larger than the Rabi frequency, this results in fast Larmor oscillations around the z-axis of the Bloch sphere.

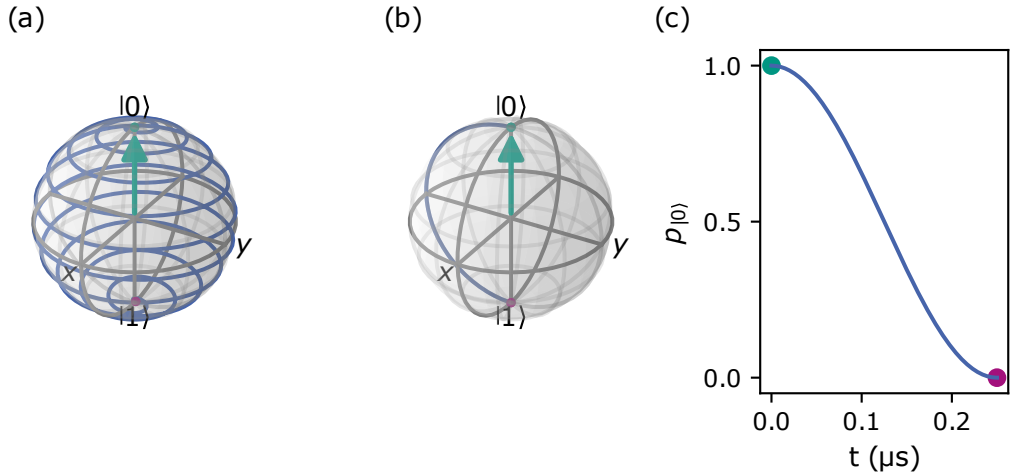

Figure 3.2.: Rabi oscillations on the Bloch sphere. (a) Example of a Rabi oscillation the lab-frame. A Larmor precession much faster than the Rabi frequency lead to a fast rotation around the z-axis in addition to the population transfer. (b) The same Rabi oscillation in a rotating reference, which rotates alongside the Larmor precession. (c) Population transfer of the Rabi oscillations is the same for both reference frames.

To avoid this trivial oscillation, we move to the rotating reference frame using Eq. 2.60 with the unitary operator $U = \exp(-i\omega t\sigma_z/2)$. This yields the Hamiltonian

$$H_{\text{rot}} = -\frac{1}{2}\delta\sigma_z - \frac{1}{2}\Omega\left(\cos(\varphi)\sigma_x + \sin(\varphi)\sigma_y\right), \tag{3.4}$$

where $\delta = \Delta_q - \omega$ is the detuning between the qubit splitting and the driving frequency. For vanishing detuning, this leads to the much simpler Rabi oscillations shown in Fig. 3.2(b). If a finite detuning δ is present, it manifests as a slow precession around the z-axis of the Bloch sphere.

In both the lab frame and the rotating frame, if we consider only the populations associated with σ_z, i.e. $p_{|0\rangle} = (1 + \langle\sigma_z\rangle)/2$, this results in the same population transfer from $|0\rangle$ to $|1\rangle$, as shown in Fig. 3.2(c). By adjusting the duration of the Rabi pulse and the phase φ, we can create any superposition state of the qubit.

This will become important in the experimental section, where the phase of the driving pulse is changed by $\pi/2$ during the sequence. This leads to rotations around the x- and y-axes of the Bloch sphere and is therefore referred to as X- and Y-pulses.

3.2. Phonon-induced decoherence

As we are in the solid state, interactions with the environment lead to decoherence of the qubit. These interactions can originate from various sources, including electron spins [115], nuclear spins [115], electric or strain field fluctuations [60], and phonons [111].

The relevant figures of merit characterizing decoherence are the spin relaxation time T_1 before the spin reaches an equilibrium state, the dephasing time T_ϕ, and the coherence time T_2 [116].

In order to simulate the interaction with the environment, or sometimes also called the bath, we consider the time evolution of the density matrix ρ. It is given by a 2×2 matrix, where the diagonal elements represent the populations of the qubit states and the off-diagonal elements the coherences between them

$$\rho = \begin{pmatrix} \rho_{00} & \rho_{01} \\ \rho_{10} & \rho_{11} \end{pmatrix} . \tag{3.5}$$

We can also express this in terms of a scalar product as

$$\rho = \frac{1}{2}(1_2 + \vec{r} \cdot \vec{\sigma}) , \tag{3.6}$$

where $\vec{r}$ is the so-called Bloch vector with components $\vec{r} = (\langle \sigma_x \rangle , \langle \sigma_y \rangle , \langle \sigma_z \rangle)$. A Bloch vector of unit length thus defines a pure state on the Bloch sphere, while a Bloch vector with $|\vec{r}| < 1$ corresponds to a partially mixed state inside the Bloch sphere.

To model the time evolution of the density matrix in the presence of a bath, we can use a master equation that extends the von Neumann equation by dissipative terms. This leads to the so-called Lindblad equation

$$\dot{\rho} = -i[H, \rho] + \sum_k \gamma_k \left(L_k \rho L_k^\dagger - \frac{1}{2}\{L_k^\dagger L_k, \rho\} \right) , \tag{3.7}$$

where γ_k are the dissipation rates and L_k the collapse operators [117]. Arriving at this form of the master equation requires the assumption that the memory time of the bath is much shorter than the characteristic timescale of the system dynamics and that the interaction with the bath is weak, i.e. the so-called Born-Markov approximation [117]. Such a short bath memory time is reasonable when modeling interactions with phonons, as they form a continuum of modes, which is cutoff sharply at the Debye frequency ω_D [118] thus leading to a rapid decay of bath correlations[1]. Below this cutoff the spectral density of an infinite bath of phonons is $\propto \omega^3$, which comes from the phonon density being $\propto \omega^2$ and the strain-mediated coupling strength $\propto \omega$ [58]. The bath correlation time is then on the order $\tau_c \sim 1/\omega_\mathrm{D}$ [119], which is much smaller than the time scales of the spin system.

In general, however, this assumption does not hold when describing the interaction of the electron spin with for example a surrounding nuclear spin bath.

[1] The cutoff of the spectral density plays the important role here of introducing the short memory time. Thanks a lot to Mohamed Belhassen pointing this out!

3.2.1. Spin relaxation and T_1

For the spin relaxation time, acoustic phonon scattering is the dominant mechanism due to the presence of the second orbital ground state [58, 111, 120]. Spin cross-relaxation would require that transitions in the spin bath match the qubit splitting [121], which are strongly detuned for the nuclear spin bath. For the electron spin bath, this matching is also suppressed due to the orbital Zeeman effect and the fixed quantization axis of the SnV center. Off-resonant cross-relaxation rates for electron spins are known from the NV center and are on the order of mHz [121]. These rates are therefore negligible for the SnV center.

Different electron-phonon mechanisms dominate in different temperature regimes [69, 122]. For temperatures where $k_\mathrm{B}T \approx \Delta_g$, with Δ_g being the splitting between the orbital ground states as defined in Eq. 2.18, a resonant two-phonon (Orbach) process dominates. For much lower temperatures, only the direct (single-phonon) process is relevant, while for much higher temperatures a Raman process involving two phonons and a virtual state becomes dominant. A key feature is that the Orbach process, which is typically the most limiting, is exponentially suppressed with increasing ground-state splitting Δ_g at a given temperature. Thus, the SnV center, with its much larger ground-state splitting, can be operated at higher temperatures compared to the SiV and GeV centers.

An extensive study of the temperature, strain, and magnetic-field dependence of these phonon processes for the SnV center used in this work has been presented by Ioannis Karapatzakis, see Sec. 2.5 of Ref. [72]. Therefore, these processes are not discussed in detail here. In summary, the spin lifetime is ultimately limited by single-phonon processes at a

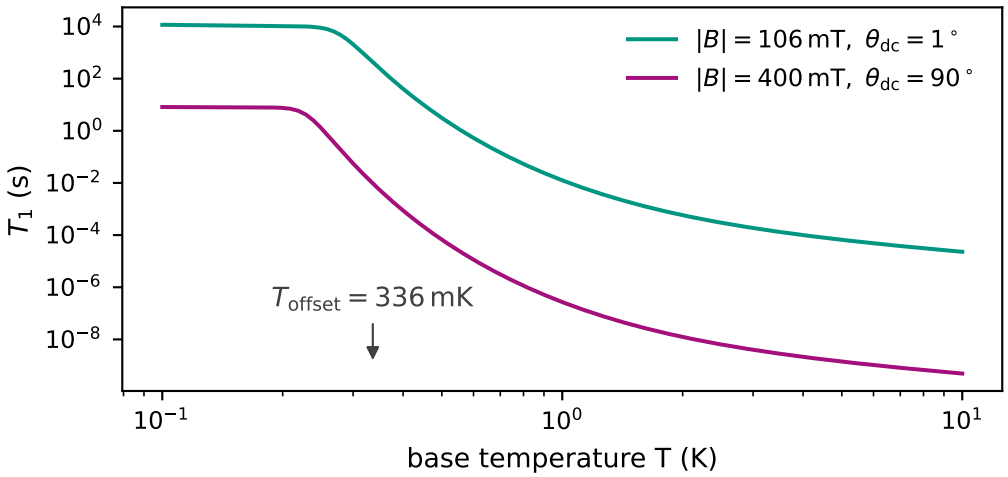

Figure 3.3.: Expected spin lifetime of the investigated SnV center as a function of temperature. The simulations use the parameters obtained by Ioannis Karapatzakis for the same emitter [72]. The lifetime is ultimately limited by single-phonon processes at an effective temperature of approximately 300 mK, above the dilution-refrigerator base temperature of 50 mK. The two curves correspond to experimentally relevant external dc magnetic-field configurations for a parallel external dc magnetic field (green) and a perpendicular configuration (purple). The larger perpendicular field compensates for the anisotropic g tensor.

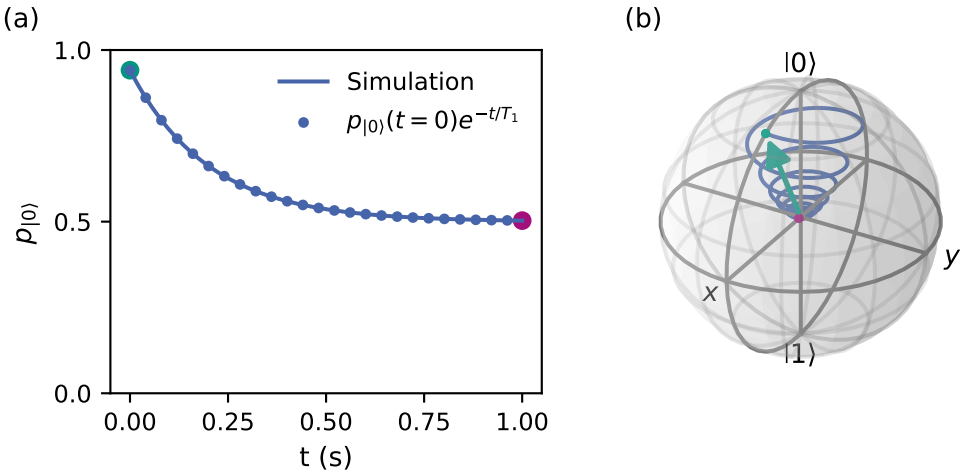

Figure 3.4.: Example of the relaxation of an arbitrary superposition state with a relaxation time $T_1 = 200\,\text{ms}$. (a) The mono-exponential decay of the population $p_{|0\rangle}$ simulated and given by the analytical expression. (b) Trajectory on the Bloch sphere assuming a finite detuning.

temperature of approximately 300 mK. This temperature exceeds the dilution-refrigerator base temperature of 50 mK, most likely due to heating from the surrounding 4 K shield.

Using the parameters obtained by Ioannis Karapatzakis [72], the resulting achievable spin lifetimes for the SnV center investigated in this thesis are shown in Fig. 3.3 for two external dc magnetic fields used experimentally. The perpendicular field is larger because the anisotropic g tensor requires higher magnetic-field amplitudes to achieve sizable qubit splittings.

For completeness, we simulate the relaxation of a qubit in an arbitrary superposition state with an arbitrary $T_1 = 200\,\text{ms}$ in Fig. 3.4. We set the collapse operators to be the raising and lowering operators σ_+ and σ_- with the corresponding rates $\gamma_+ = \sqrt{\frac{\pi}{T_1}}$ and $\gamma_- = \sqrt{\frac{\pi}{T_1}}$, respectively.

Solving this numerically using the Python package QuTiP [123], we find a mono-exponential decay of the population $p_{|0\rangle}$ as shown in Fig. 3.4(a). If we represent this evolution on the Bloch sphere, including an additional detuning for better visualization, we find that the Bloch vector precesses around the z-axis with a decaying magnitude until it reaches the completely mixed state at the center of the Bloch sphere.

3.2.2. Pure dephasing

We can think of dephasing as the loss of phase coherence, which on the Bloch sphere can be understood as a randomization of the azimuthal angle ϕ due to fluctuations in the

Larmor precession in the lab frame. We can therefore write the Hamiltonian of the qubit including dephasing as

$$H(t) = \frac{1}{2}\Delta_q \sigma_z + \frac{1}{2}\beta(t)\sigma_z\,, \tag{3.8}$$

where $\beta(t)$ incorporates the random fluctuations of the Larmor precession, leading to a finite, time-dependent but random detuning.

For the dephasing mechanisms of the electron spin, three main contributions are relevant: the interaction with the nuclear spin bath, the electron spin bath, and phonon-induced dephasing. The phonon-induced dephasing arises from the fact that the higher orbital ground state has a different orbital Zeeman splitting compared to the lower orbital ground state. As this process again requires an Orbach mechanism, the corresponding dephasing scales exponentially with temperature and the ground-state splitting. For the SnV center, it becomes relevant at temperatures around 3 – 4 K, depending on the strain of the emitter [82, 84, 111].

In the case of phonon-induced dephasing, we can treat the process in the Born-Markov approximation by introducing the dephasing operator $L_\phi = \sigma_z$ with the rate $\gamma_\phi = \sqrt{\frac{\pi}{T_\phi}}$, where T_ϕ is the pure dephasing time [116]. As shown in Fig. 3.5(b), this does not change the populations of the qubit, but only affects the coherences. For a finite detuning, we observe oscillations of the coherence, plotted in the figure as a population-like quantity, together with a decay of the Bloch vector length characterized by the dephasing time T_ϕ.

The timescale on which the coherences decay in the presence of relaxation is given by

$$\frac{1}{T_2} = \frac{1}{2T_1} + \frac{1}{T_\phi}\,. \tag{3.9}$$

This is why T_2 is referred to as the coherence time of the qubit.

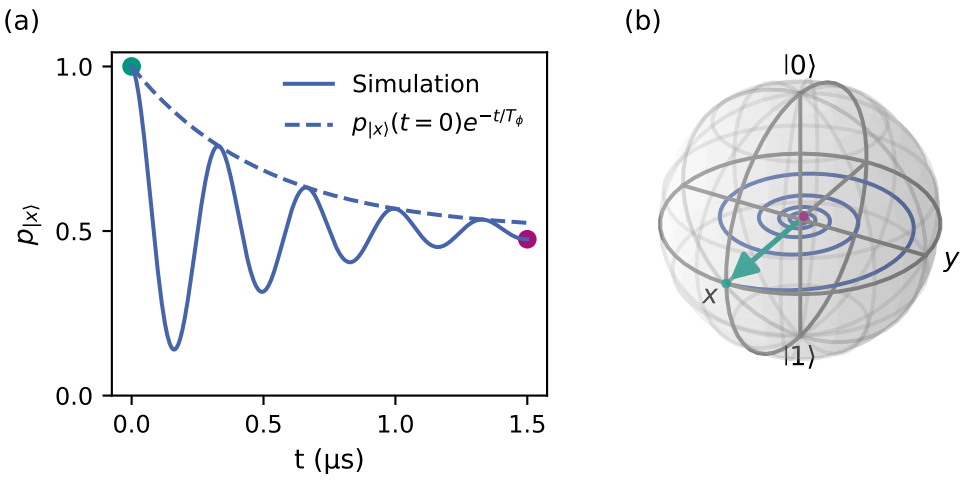

Figure 3.5.: Example of the dephasing of an superposition state with a dephasing time $T_\phi = 0.5\,\mu s$. (a) The mono-exponential decay of the coherence $p_{|x\rangle}$ simulated and given by the analytical expression. (b) Trajectory on the Bloch sphere assuming a finite detuning.

3.3. Decoherence due to spin-bath coupling

At low temperatures, the coherence time commonly does not follow the phonon- or temperature-limited trend and instead saturates [82, 84, 111]. This behavior arises from the previously mentioned magnetic noise of the spin bath surrounding the SnV center, which typically has long correlation times in contrast to the phonon bath. As a result, the coherence time can be extended using dynamical decoupling techniques in this slow magnetic noise limit [60, 84]. Modeling such a spin bath can be done analytically [108, 124, 125]. Here, we follow the derivations in Ref. [108] and Ref. [124].

We assume that there is no cross-relaxation with the surrounding spins and that only pure dephasing is present, allowing us to use the Hamiltonian in Eq. 3.8. We further assume that the quantity β arises from dipole-dipole interactions (see Sec. 5.1) with all surrounding spins and is given by

$$\beta(t) = \sum_k v_k \xi_k(t)\,, \tag{3.10}$$

where v_k is the individual coupling strength and $\xi_k(t) = \pm 1$ is a fluctuating random telegraph signal describing the flipping of an individual bath spin. This sum results in a static but random effective field experienced by the qubit during each measurement. We can therefore treat $\beta(t)$ as a random but classical variable that follows an Ornstein-Uhlenbeck process [125].

The correlation function of the Ornstein-Uhlenbeck process is given by

$$S(t) = \langle \beta(0)\beta(t)\rangle = b^2 e^{-t/\tau_c}\,, \tag{3.11}$$

where b^2 is the characteristic coupling strength (i.e. the variance of β) of the qubit to the bath, and τ_c is the correlation time of the bath, which is determined by intra-bath couplings [125]. This can be understood by comparison with the autocorrelation of the random telegraph noise used in Eq. 2.100 to derive the cyclicity, where the correlation time is given by the total relaxation rate between the two states, i.e. here the flip-flop rate of the bath spins.

If we now consider the phase ϕ acquired by the qubit under this classical random noise until a time t, we find that the coherences obtain a phase factor

$$\langle \sigma_x(t)\rangle = \sigma_x(0)\left\langle \exp\left(-i\int_0^t \beta(t')f(t'),dt'\right)\right\rangle \equiv \sigma_x(0)\,\langle \exp(-i\phi(t))\rangle\,, \tag{3.12}$$

where $\langle\cdots\rangle$ denotes the average over all experimental realizations and $f(t')$ describes the pulse sequence applied during the dephasing [108]. As the fluctuations β are Gaussian for an Ornstein-Uhlenbeck process [108, 124], we can simplify this expression to

$$\langle \exp\left(-i\phi(t)\right)\rangle = \exp\left(-\frac{1}{2}\left\langle (\phi(t))^2\right\rangle\right)\,. \tag{3.13}$$

This implies an exponential decay of the form

$$W(t) = e^{-\chi(t)}\,, \tag{3.14}$$

where the quantity $\chi(t)$ captures all relevant contributions, and can be computed analytically for various pulse sequences; see e.g. Refs. [124–128].

For the free-induction (FID) or Ramsey decay, one finds [127] the expression

$$\chi_{\mathrm{FID}}(t) = b^2\tau_c^2\left(\frac{t}{\tau_c} - 1 + e^{-t/\tau_c}\right). \tag{3.15}$$

In the limit of short correlation times $\tau_c \ll t$, we recover the mono-exponential decay from the Lindblad formalism with

$$\chi_{\mathrm{FID}}(t) \approx b^2\tau_c t\,, \tag{3.16}$$

while for the opposite case $\tau_c \gg t$, we find

$$\chi_{\mathrm{FID}}(t) \approx \frac{b^2}{2}t^2\,, \tag{3.17}$$

which is the commonly observed decay for spin baths coupled to a central spin [126], often referred to as Gaussian decay in this context [125]. The timescale $\sqrt{2}/b$ of this decay is commonly called the inhomogeneous dephasing time T_2^* [116]. Interestingly in the short correlation time case $\tau_c \ll t$, with a finite coupling $b > 0$, the dephasing time would go $T_2^* = 1/(b^2\tau_c) \to \infty$. This is called motional narrowing [65, 128] and has observed e.g. for nuclear spins coupled to NV centers in diamond, when the NV center undergoes rapid optical excitation and decays [129], as well as in the increase in coherence with increasing temperature of ^{29}Si host nuclear spins of SiV centers [65].

Another important pulse sequence is the Hahn-echo sequence, which corresponds to a free-induction decay with an intermediate π-pulse applied to the qubit during the free evolution. One finds [124]

$$\chi_{\mathrm{HE}}(t) = b^2\tau_c^2\left(\frac{t}{\tau_c} + 4\exp\left(-\frac{t}{2\tau_c}\right) - \exp\left(-\frac{t}{\tau_c}\right) - 3\right). \tag{3.18}$$

In the limit of short correlation times $\tau_c \ll t$, we recover the same decoherence decay as for the free-induction case in Eq. 3.16,

$$\chi_{\mathrm{HE}}(t) \approx \chi_{\mathrm{FID}}(t)\,, \tag{3.19}$$

which is expected, as there is no refocusing effect if the bath is already uncorrelated, as discussed previously for the phonon bath. In contrast, for a spin bath with $\tau_c \gg t$, one finds [125]

$$\chi_{\mathrm{HE}}(t) \approx \frac{b^2t^3}{12\tau_c}\,, \tag{3.20}$$

or correspondingly the commonly used Hahn-echo coherence time or homogeneous spin dephasing time [116]

$$T_2^{\mathrm{HE}} = \left(\frac{12\tau_c}{b^2}\right)^{1/3}, \tag{3.21}$$

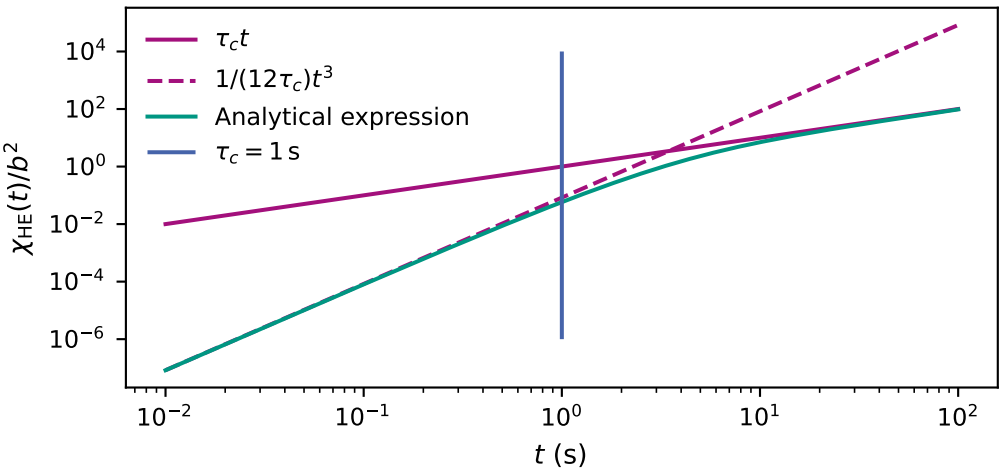

Figure 3.6.: Decoherence function for the Ornstein-Uhlenbeck process for a Hahn-echo. The analytical expression is given in Eq. 3.18. A correlation time for a nuclear spin bath of 1 s is chosen [70, 130] and normalized by b^2. Plotting the decoherence function on a loglog-scale allows to determine the slopes and thus the different regimes. Usually $t \ll \tau_c$ and we find a decoherence scaling with t^3.

which will lead to a stretched exponential decay of the coherence with a stretching factor of 3.

A comparison of both regimes in addition to the full analytical expression in the case of a correlation time of $\tau_c = 1\,\mathrm{s}$ are shown in Fig. 3.6. If a Gaussian FID decay is observed, one can use the measured T_2^* time to estimate the coupling to the bath via $b = \sqrt{2}/T_2^*$. Using a simple Hahn-echo measurement, one can then afterwards determine the bath correlation time by

$$\tau_c = \frac{b^2}{12}\left(T_2^{\mathrm{HE}}\right)^3 . \tag{3.22}$$

3.3.1. Filter-function formalism

As we often describe the bath in terms of its spectral density, e.g. in the context of spin-phonon coupling, we can also express the quantity $\chi(t)$ using the corresponding Fourier transforms, leading to

$$\chi(t) = \frac{1}{\pi}\int_0^\infty S(\omega)\frac{F(\omega t)}{\omega^2}\,d\omega\,. \tag{3.23}$$

The filter functions $F(\omega t)$ can be calculated and are given for the FID and Hahn-echo sequences as [108, 128]

$$F_{\mathrm{FID}}(\omega t) = 2\sin^2\left(\frac{\omega t}{2}\right), \tag{3.24}$$

$$F_{\mathrm{HE}}(\omega t) = 8\sin^4\left(\frac{\omega t}{4}\right). \tag{3.25}$$

The spectral density of the Ornstein-Uhlenbeck model is given by a Lorentzian

$$S(\omega) = 2\pi \frac{b^2}{\pi} \frac{\tau_c}{1 + \omega^2 \tau_c^2} \,. \tag{3.26}$$

The factor of 2π in contrast to e.g. Ref. [115] ensures that the decoherence function in Eq. 3.23 reproduces the analytical expression derived in the previous section.

The advantage of this formalism is that we are no longer limited to a single Ornstein-Uhlenbeck bath, but can include multiple spin baths or other environments for which the spectral density is known. This is particularly relevant for the SnV center, where not only the ^{13}C nuclear spin bath, but also an additional electron spin bath contributes [60, 70, 84].

A frequently used pulse sequence to extent the coherence is the Carr-Purcell-Meiboom-Gill (CPMG) decoupling sequence. Instead of a single π-pulse in the center of the free-induction decay, as in the Hahn-echo sequence, multiple 90° phase-shifted π-pulses are applied, separated by an inter-pulse spacing τ. The 90° phase-shift prevents the accumulation of pulse errors. For this sequence the total evolution time is then given by $t = 2N\tau$, and the corresponding filter function reads

$$F_{\mathrm{CPMG}}(\omega t) = 8 \sin^4\left(\frac{\omega t}{4n}\right) \frac{\sin^2\left(\frac{\omega t}{2}\right)}{\cos^2\left(\frac{\omega t}{2n}\right)} \,, \tag{3.27}$$

where n is an even number of applied pulses. For an odd number of pulses the nominator just needs to be replaced by a $\cos^2(\omega t/2)$ term [108].

If we examine these filter functions at a constant total evolution time t, as shown in Fig. 3.7, we observe that the filter functions shift to higher frequencies $\omega_0 = \pi n/t$ [115]. They appear to decrease in width due to the semi-logarithmic scale; however, the total width of the filter function is determined solely by the total evolution time t and is given by $\delta\omega = \pi/t$ [115], corresponding to a FWHM of $2\pi/t$.

As the spin bath noise follows a Lorentzian spectrum, it decreases monotonically with increasing frequency. The lower part of Fig. 3.7 shows an example of a normalized spectrum for a correlation time of $\tau_c = 100\,\mu\mathrm{s}$. This also means that, for a pulse sequence with a large number of pulses n, the filter function samples the noise spectrum at progressively higher frequencies, where the noise amplitude is smaller. As a result, the coherence time can increase with n. This is in contrast to white noise, for which the sampled noise amplitude is independent of frequency and therefore does not decrease with increasing pulse number.

Another important point is that we can vary the number of pulses n with a long but fixed total evolution time t, thereby enabling fine sampling of the noise spectrum and even the identification of individual spins that couple to the central spin. This approach has been extensively used for the NV center in diamond; see, e.g., Ref. [35]. For the SnV center, whose electron spin forms a spin-1/2 system, the dynamics are less sensitive to individual surrounding nuclear spins besides the nuclear spin bath [131]. Therefore, correlation spectroscopy methods were proposed [106, 131].

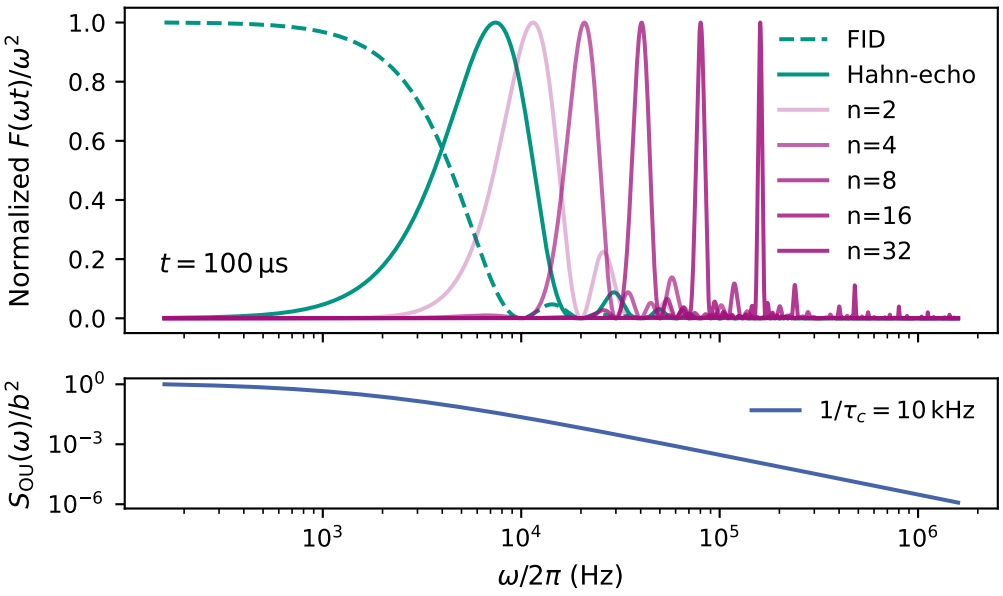

Figure 3.7.: Upper part: Normalized filter functions $F(\omega t)/\omega^2$ for different pulse sequences at a fixes total evolution time t. With increasing pulse number n the filter functions shift to higher frequencies. Lower part: Normalized Ornstein-Uhlenbeck noise spectrum for a correlation time of $\tau_c = 100\,\mu s$. The noise spectrum monotonically decreases with increasing frequency.

If we now measure a decoherence decay, we can invert Eq. 3.23 using the known filter function to recover the noise spectrum. Inspired by the work of A. Stramma [90], we follow his derivation based on Refs. [115, 132].

The filter functions can be approximated by a δ-function as

$$\frac{1}{t}\frac{F(\omega t)}{\omega^2} \approx \delta(\omega - \omega_0),, \tag{3.28}$$

where the factor of $1/t$ arises from the integration over the filter function [108], and $\omega_0 = n\pi/t$ is the position of the main lobe of the filter function. Substituting this into Eq. 3.23 yields the spectral density

$$S_\delta(\omega) \approx \pi\frac{\chi(t)}{t},. \tag{3.29}$$

This approximation neglects the higher-order lobes at larger frequencies. Assuming a monotonically decreasing noise spectrum, these lobes contribute less than the main lobe and can be subtracted. This leads to the following expression for the i-th spectral noise point:

$$S(\omega_i) \approx \pi\frac{\chi(t_i)}{t_i} - \frac{1}{t_i}\int_{\omega_i}^{\infty}\tilde{S}(\omega)\frac{F(\omega t_i)}{\omega^2}, d\omega,, \tag{3.30}$$

where $\tilde{S}(\omega)$ denotes the previously reconstructed noise spectrum for all frequencies $\omega > \omega_i$. This means that the noise spectrum is corrected iteratively in a descending manner by

subtracting contributions from the higher-order lobes. The integration is performed numerically with a higher sampling rate $\propto n$ to correctly sample the higher-order lobes of the filter function [132]. Only values $\chi(t)$ around the decay should be considered for this algorithm as the saturated values for full or zero coherence contain no information and will lead to artifacts in the reconstructed spectral density for the associated frequencies.

3.3.2. Dynamical decoupling

So far, we have focused on measuring the coherence and characterization of the noise bath; however, we are also interested in extending the coherence time. In practice, dynamical decoupling sequences such as the previously mentioned CPMG sequence are employed. For such sequences, as shown in Fig. 3.7, only the high-frequency tail of the Lorentzian noise spectrum is relevant and can be approximated by $S(\omega) \propto 1/\omega^2$. For a spectral density following a power law $S(\omega) \propto \omega^{-\alpha}$, the decoherence function takes the form [133]

$$\chi(t) = \left(\frac{t}{T_2}\right)^{\alpha+1}, \tag{3.31}$$

which recovers the cubic scaling for the Hahn-echo measurement in the long bath correlation time limit discussed in the previous section.

The coherence time as a function of the number of pulses follows a scaling determined by this exponent of the noise spectral density and is given by

$$T_2(N) = T_2(N=1)N^{\alpha/(\alpha+1)}, \tag{3.32}$$

which yields a $2/3$ scaling for a Lorentzian noise spectrum [133]. For frequency-independent (white) noise, this scaling predicts no extension of the coherence time and the mono-exponential decay as discussed for phonon-induced decoherence.

These findings are important, as they show that the bath can already be characterized by analyzing the exponents in both the decay function and the scaling behavior under dynamical decoupling without the need to employ a full noise spectroscopy.

3.4. Randomized benchmarking

So far, we have discussed coherent control, such as Rabi oscillations, and the coherence properties of the qubit. While it is desirable to achieve as long a coherence time as possible, it is equally important to operate the qubit with sufficiently low gate errors. One intuitive approach is to first consider the quality of the Rabi oscillations for example by introducing a quality factor, defined as the number of π-rotations before the Rabi contrast decays to $1/e$ of its initial value [134].

For very low Rabi frequencies, the dynamics are limited by shot-to-shot detuning of the driving frequency, and thus the quality factor depends strongly on T_2^* [60, 84, 104, 134].

To mitigate this, faster and therefore spectrally broader Rabi oscillations can be used. In this regime, the oscillations are instead limited by the qubit lifetime T_1 and drive-induced heating [60, 84]. In between these two regimes, when the Rabi frequency matches the Larmor precession frequency of the ^{13}C nuclear spin bath (the so-called Hartmann-Hahn condition), cross-relaxation can occur [135], which further reduces the quality factor of the Rabi oscillations [134].

In general, not only π-rotations are applied, but also arbitrary rotations around different axes and with different rotation angles. This leads to a finite probability of occupying superposition states during gate operations, and thus the dynamics remain sensitive to T_2^* even in the limit of fast driving [84].

To accurately quantify the error per gate, sequences of varying length are applied, and the resulting decay of fidelity is analyzed [136, 137]. At the end of each sequence, the inverse operation is applied, and the fidelity with respect to the initial state is measured, allowing extraction of the average gate infidelity. Typically, gates from the Clifford group are used [82, 84, 136–139], ensuring that the sequence can be efficiently inverted using Pauli operations [136].

The randomization of the gate sequences is essential to average over errors that may be correlated with specific pulses or subsequences of pulses [136]. Therefore, for a fixed sequence length, multiple random realizations are generated, measured, and averaged to obtain a reliable estimate of the gate error.

From an experimental perspective, it is often more practical to implement randomized benchmarking using the native, or primitive, gates of the qubit rather than the full Clifford gates directly. The Clifford group also contains operations such as rotations around the z axis and the Hadamard gate, which are typically not implemented as elementary pulses in the experiment. Instead, Clifford gates can be decomposed into combinations of primitive gates, here restricted to rotations around the x and y axes with angles $\pi/2$ and π, together with the identity [136, 138, 140]. If a primitive gate fidelity F_P is determined, it can be converted to a Clifford gate fidelity F_C, since a single Clifford gate consists, on average, of 1.875 primitive gates [138, 140].

3.5. Summary

We have shown that the Zeeman-split two-level system of the SnV center forms a qubit and can be visualized on the Bloch sphere. Using Rabi driving, we can implement arbitrary pulses by varying the duration and phase of the drive. The decoherence is characterized by the lifetime T_1, the dephasing time T_2^*, and the coherence time T_2.

As discussed, the phonon bath can be treated in the memoryless (Markovian) limit and analyzed using a master equation approach. In contrast, the spin bath has a finite correlation time and can be modeled as stochastic magnetic noise acting on the qubit, which

can be treated using decoherence functions. This leads to stretched-exponential decays of coherence, where the stretching exponent reflects the spectral properties of the noise.

Hahn-echo and CPMG pulse sequences suppress low-frequency noise and thereby extend the coherence time. The filter-function formalism directly links the spectral density of the bath to the coherence function, enabling reconstruction of the noise spectral density from decoherence measurements.

Finally, the overall gate fidelity depends on both the applied Rabi pulses and the noise environment, and can be reliably quantified using randomized benchmarking.

4. Coherent control of the electron spin of a low-strain SnV center

With the understanding of the spin Hamiltonian developed in Chapter 2 and the theoretical framework for operating a spin qubit in a noisy spin environment discussed in Chapter 3, we now focus on the experimental implementation of coherent spin control of the SnV center electron spin. In recent studies, both optical [104, 141] and microwave [82, 84] spin control have been demonstrated. For microwave-based control, drive-induced heating has been identified as a limiting factor, arising directly from the electron-phonon coupling discussed in Sec. 3.2.1.

There are several approaches to deliver microwave fields to the SnV center, such as wires spanned over the diamond [84, 130], on-chip coplanar waveguides (CPWs) in a transmission geometry [82], or shorted CPWs [60]. These waveguides are typically fabricated from gold, which introduces Ohmic losses and thus heating of the sample at high driving powers. Such high powers are required to achieve π-pulses that are much shorter than the dephasing time of the spin T_2^*, as needed for high-fidelity gate operations (see Sec. 3.4).

The limitations due to Ohmic losses were investigated in our Ref. [70] and studied in more detail by Ioannis Karapatzakis [72] using a shorted gold CPW fabricated on top of the diamond sample, with a low-strain SnV center located approximately 10 µm away from the inner conductor.

Even for moderate input powers around 0 dBm, significant heating occurs when applying an off-resonant 10 ms long pulse, accompanied by a reduction of the electron spin lifetime T_1. For simple spectroscopy measurements such as optically detected magnetic resonance (ODMR, see Sec. 4.2), which operate at powers as low as −20 dBm, such waveguides can still be used for low-strain emitters. However, coherent measurements such as Rabi oscillations require powers that are three to four orders of magnitude higher. Despite the short pulse durations in the µs regime, only a few Rabi cycles have been observed in our measurements, which is attributed to a direct reduction of T_1 upon application of the microwave drive.

To circumvent these limitations, one approach is to use high-strain SnV centers, which can be operated at elevated temperatures [82, 84]. However, this comes at the cost of reduced cyclicity of the spin-conserving transition and thus fewer photons per readout (see Fig. 2.18 and Refs. [82, 84, 104]). Another approach is to apply an external magnetic dc field perpendicular to the SnV quantization axis, which increases the Rabi frequency even for low-strain emitters, but also reduces the cyclicity.

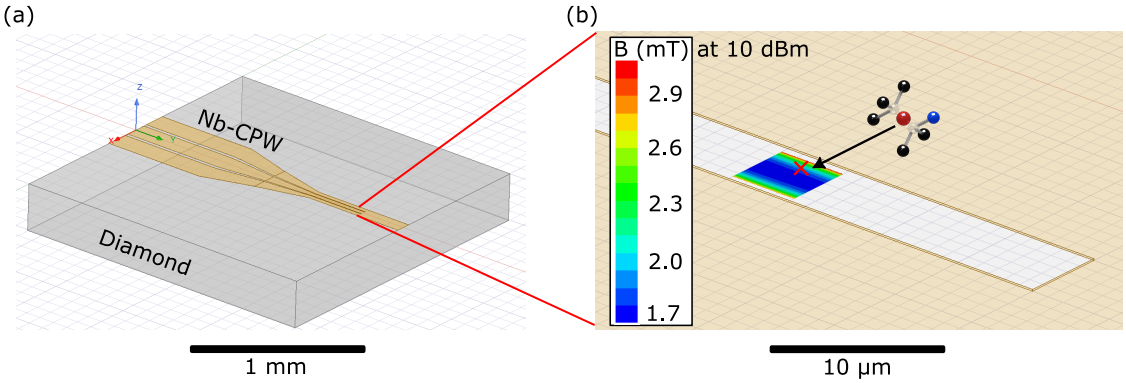

Figure 4.1.: Simulation of the waveguide structure used in this work. (a) Geometry of the niobium coplanar waveguide (CPW) on a diamond substrate, modeled in Ansys HFSS. (b) Simulated magnetic-field strength of the alternating microwave field for an input power of 10 dBm. The simulation yields a field amplitude of 1.7 mT along the z_{lab} axis. The simulation was performed by Ioannis Karapatzakis. The figure is reprinted from Ref. [71]

In this work, we build upon our Refs. [70, 71] and employ a superconducting coplanar waveguide (SC-CPW) made of niobium. The design and fabrication were carried out by Ioannis Karapatzakis, and a comprehensive discussion of the SC-CPW properties can be found in his PhD thesis [72]. Here, we provide a brief description for completeness. The device is a shorted CPW with an impedance-matched geometry, fabricated by optical lithography followed by electron-beam evaporation of 50 nm niobium directly onto the diamond substrate. The impedance matching results in gaps of 5 µm between the central conductor and the two ground planes, and conductor widths of 30 µm, as shown in Fig. 2.8. These dimensions are smaller than those used in our Ref. [70], where 24 µm gaps were used, leading to higher microwave field strengths within the gap at the expense of a reduced number of accessible SnV centers.

Towards the edges of the diamond, the conductor width and gap size increase to allow wire bonding of aluminum wires from the SC-CPW to a flexible CPW cable, which connects to the SMA microwave delivery line at the mK stage. The niobium films have a critical temperature of approximately 9.2 K [142] and are therefore superconducting at the operating temperature in this work. Karapatzakis has shown that, at $B = 0$, superconductivity breaks down upon application of a 2 GHz tone at an input power of around 17 dBm. This threshold decreases for higher base temperatures, stronger external dc magnetic fields, and higher microwave frequencies, but is still high enough to allow coherent control of the electron spin.

Throughout the following sections, all stated microwave powers refer to the insertion power at the input of the cryostat. This value already accounts for losses introduced by the microwave and radio-frequency filters, the combiner, and the room-temperature coaxial cabling. Inside the cryostat, however, the attenuation is strongly frequency-dependent, increasing toward higher frequencies. Typical values for the input return loss, which corresponds to twice the one-way loss toward the sample, are 1.89 dB at 1 GHz, 2.7 dB at 2 GHz, and 3.54 dB at 3 GHz (see Fig. 2.10). The internal loss reaches a minimum near

3.7 GHz, which motivates our choice of a dc magnetic field of 106 mT. At this field and for a parallel orientation of the magnetic field with respect to the SnV center's symmetry axis, the qubit splitting coincides with this low-loss frequency.

A three-dimensional model of the niobium coplanar waveguide was simulated in Ansys HFSS by Ioannis Karapatzakis and is shown in Fig. 4.1. The simulation yields an ac magnetic field of 1.7 mT along the laboratory z-axis for an input power of 10 dBm at the waveguide at a frequency of 20 MHz, with only sub-percent variation up to 3 GHz. At the surface of the diamond, the B_{ac} field is oriented perpendicular to the diamond surface. Since the diamond is aligned to the laboratory z-axis to within approximately 0.1°, as defined by the dc magnetic-field coils, the B_{ac} field is effectively directed purely along the laboratory z-direction. Given that the SnV center is located in close proximity to the surface, at a depth of approximately 20 nm, we assume the same B_{ac}-field orientation at its position.

4.1. Electron-spin initialization

As a first step, the initialization of the electron spin is achieved by resonantly driving one of the spin-conserving optical transitions, either A1 or B2, due to the finite cyclicity of these transitions. As derived in Sec. 2.5.2, we expect a mono-exponential decay depending on the ratio of the optical pump rate and the cyclicity.

The optical cyclicity is particularly high for a magnetic field aligned parallel to the SnV axis, yielding a high readout signal but also increasing the initialization time. The latter can be tuned by adjusting the excitation power of the resonant laser beam. We will fit counts collected during such an initialization curve by

$$I(t) = A \exp(-\Gamma_p t) + C(B)\,, \tag{4.1}$$

where A is the initial count rate at $t = 0$, Γ_p the polarization rate, and C an offset due to dark counts of the single photon detector B and a steady state background photon scattering rate [104], which we attribute to fluorescence in the sample. While fitting we weight each data point with $\sqrt{N+1}$ to account for Poisson noise statistics and get reliable uncertainties on the fit parameters. The +1 is chosen here to attribute a finite uncertainty to bins with zero photon counts.

In order to record such an initialization curve one needs multiple experimental runs due to the probabilistic nature of the process. Due to the long spin lifetime one needs to somehow pump back the population into the probed state. This can be done by waiting much longer than the spin lifetime T_1, which is completely unreasonable, or by using, e.g., the other spin-conserving transition to pump back into the desired initial state. In this work, we simply apply a Rabi π-pulse on the electron spin transition at the end of the initialization sequence bringing the population back into the initial state.

The initialization infidelity is defined by the ratio of the offset counts C and the initial counts A [104, 143]. In addition, as we can distinguish between the steady state counts C and the dark counts by the detector by just integrating these counts without applying

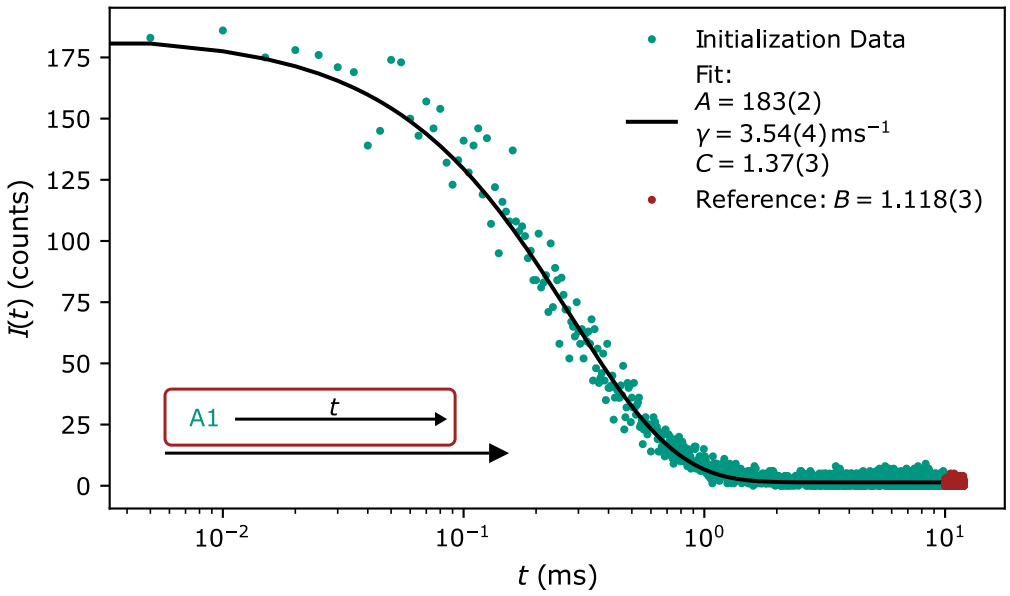

Figure 4.2.: Time-resolved fluorescence during driving the spin-conserving optical A1 transition showing an exponential decay. The fit is shown as a black line. The reference level (red) indicates the background dark count rate after the laser is turned off. The resulting fit parameters are given in the legend, for the calculation of the initialization fidelity we refer to the main text.

any laser, we use the dark count corrected background for the initialization fidelity [104]. Thus, we get

$$F_{\text{init}} = 1 - \frac{C - B}{A - B}\,. \tag{4.2}$$

To calculate the uncertainty of the initialization fidelity we define $C' = C - B$ and $A' = A - B$, and the fidelity as $F = 1 - C'/A'$. Further, we define the functions $g = A' - C'$ and $h = A'$, such that the fidelity can be written as $F_{\text{init}} = g/h$. The uncertainties of g, h, and F_{init} are obtained by considering their partial derivatives, correlations ρ, and uncertainties σ in standard correlated error propagation. Since a higher background leads to higher counts, we assume correlations $\rho_{AB} = 1$ and $\rho_{CB} = 1$, while the correlation coefficient ρ_{AC} can be determined by the fit of the initialization curve. We further assume a correlation $\rho_{gh} = 1$.

Figure 4.2 shows such a representative electron-spin initialization curve on a semilogarithmic scale, which also includes the appended reference dark count measurement at $t > 10\,\text{ms}$. The fit uses Eq. 4.2 and the resulting fit parameters and their uncertainty are given in the figure legend. If we compute the background-corrected initialization fidelity we obtain $F_{\text{init}} = 99.862(3)\%$ in good agreement with our results in Ref. [70]. If we did not perform this background correction, we would obtain a fidelity of $F_{\text{init}} = 99.25(1)\%$. Not performing the Poisson weighting leads to reduced uncertainties and also to lower fidelity, but only on the sub-% level.

As discussed in Sec. 2.5.2 from the decay rate Γ_p we can calculate the cyclicity from this initialization curve by

$$\Lambda_e = R/\Gamma_p - 1\,, \tag{4.3}$$

where R is the optical pumping rate in Eq. 2.94. The initialization in Fig. 4.2 was measured with a saturation parameter of $s = 0.24$ and an optical detuning of 23 MHz. The spontaneous emission rate for this emitter was found to be $\gamma = 2\pi \times 36.6(1)$ MHz (see Fig. 2.13). Plugging these numbers in, we find a cyclicity of $\Lambda_e = 6090(20)$ in good agreement to the master equation fit used in our Ref. [71] on the exact same initialization curve. The main source of uncertainty here is the total decay rate γ, which is inferred from the PLE linewidth rather than a lifetime measurement.

In addition, we can count the number of photons acquired during this measurement. For the curve in Fig. 4.2 the cycle was repeated 14116 times. We get a mean count rate per repetition of 1.39(1). Using the previously obtained cyclicity we find a collection efficiency of 0.0231(3)%, which is 10% higher than reported in our Ref. [71]. This can be attributed to changes in emitter position in the axial position towards the microscope objective or different fogging of the objective aperture due to gas leakage inside the cryostat. This change is rather small and shows the robustness of our setup, as this measurement and the measurement of collection efficiency in Ref. [71] are 6 months and multiple warm-ups and cooldowns apart, indicating the reproducibility of these measurements.

4.2. Optically detected magnetic resonance of the SnV electron spin

The ability to optically initialize the SnV center electron spin into a specific sub-state enables the determination of the spin qubit resonance frequency via optically detected magnetic resonance (ODMR). Driving transition A1 prepares the system in the upper spin state $|\uparrow\rangle$, making the SnV center off-resonant with the laser frequency as discussed in the previous section. Applying a microwave pulse at the qubit transition frequency can partially restore the population in the lower spin state $|\downarrow\rangle$, thereby allowing continuous photon detection through repeated excitation cycles.

In pulsed-ODMR, the microwave π-pulse following the optical initialization pulse, allows full recovery of the spin population. This yields a maximized count rate per cycle and minimizes power broadening. A prerequisite for this approach, however, is prior knowledge of the spin transition frequency. While the electron-spin resonance frequencies of the SnV center can in principle be calculated for arbitrary magnetic fields from its known Hamiltonian parameters, this is often impractical for uncharacterized defects, whose Hamiltonian parameters must first be determined experimentally. In particular, the strong sensitivity of the qubit frequency to strain makes prediction unreliable when the strain is unknown. Furthermore, the superconducting coplanar waveguide shifts the effective magnetic field experienced by the SnV center, displacing the resonance frequency by several

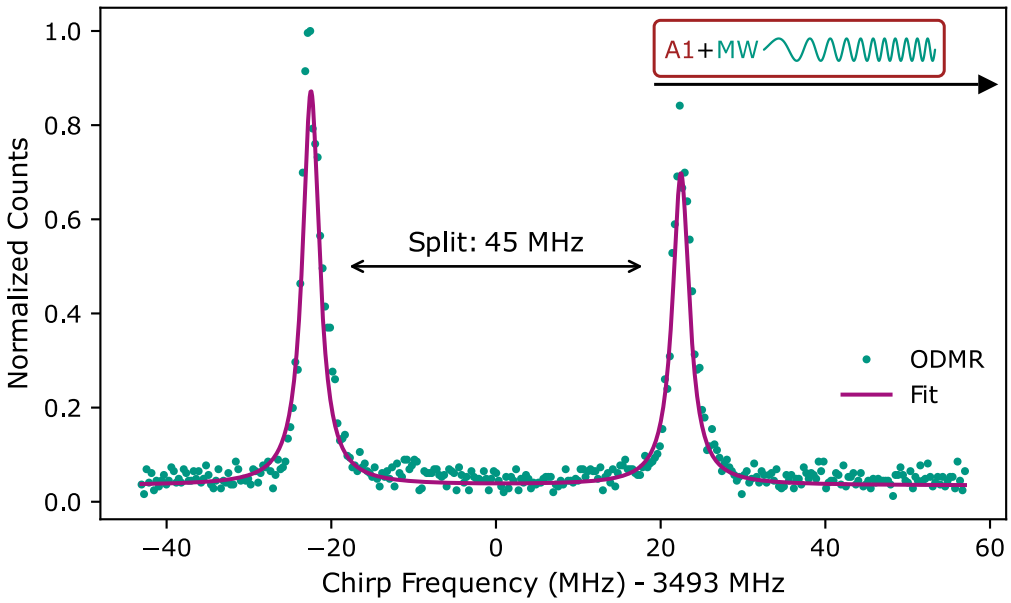

Figure 4.3.: ODMR measurement using continuous wave excitation using −27 dBm of mw power and an external dc magnetic field of $B_{\mathrm{dc}} = 100\,\mathrm{mT}$ parallel to the SnV centers quantization axis. Two resonances are observed due to a hyperfine splitting of the electron-spin transition due to the ^{13}C nuclear spin, yielding two microwave transitions. The purple line corresponds to a double Lorentzian fit with a center frequency of 3493 MHz. The whole data set is shifted by this center frequency.

MHz. To achieve a stable frequency over time we repeatedly break the superconductivity many time with 19 dBm pulses of 1 ms duration with 10% duty cycle.

A simplified continuous ODMR measurement meets the need for a fast and reliable screening of the transition frequency. In this approach, a continuous microwave chirp spanning the target frequency range is applied while simultaneously driving the spin-conserving optical transition A1 and collecting phonon sideband fluorescence. The chirp duration and power are chosen according to the required frequency span and spectral resolution. In a typical measurement, the microwave frequency is swept over a fixed interval of $10 - 20\,\mathrm{ms}$ under continuous resonant optical excitation at low laser powers of a few nanowatts. Care must be taken to keep the optical power high enough that the optical polarization rate Γ_p remains higher than the inverse sweep duration; otherwise, the observed transitions exhibit skewed lineshape artifacts.

When covering large frequency spans, a higher microwave power ensures efficient detection of the qubit during the short window in which the chirp passes through resonance. The sequence is repeated until sufficient signal-to-noise ratio is obtained. For high spectral resolution, the microwave amplitude is reduced and the chirp span narrowed accordingly.

Fig. 4.3 shows an exemplary continuous-wave ODMR scan of the SnV electron spin, recorded at a microwave insertion power of −27 dBm and an external dc magnetic field of $B_{\mathrm{dc}} = 100\,\mathrm{mT}$ aligned parallel to the SnV center's quantization axis. Two resonances are

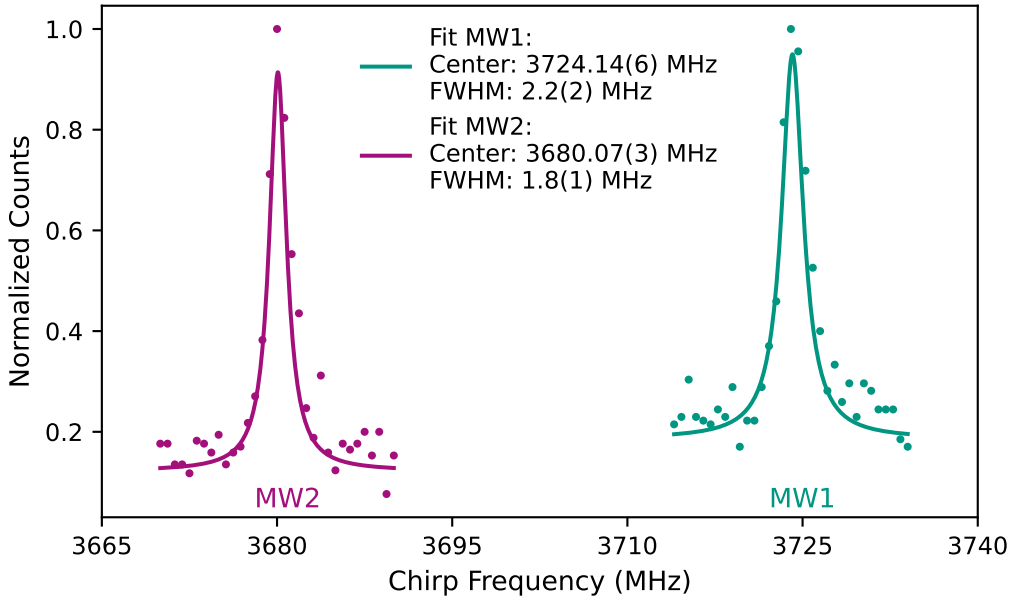

Figure 4.4.: ODMR measurement using continuous wave excitation using −23 dBm of mw power and an external dc magnetic field of $B_{dc} = 106$ mT parallel to the SnV centers quantization axis. For each resonance the ^{13}C nuclear spin is initialized into one of its sub-states, yielding one detectable microwave transition.

visible, arising from the hyperfine interaction between the electron spin and a proximal ^{13}C nuclear spin. The ^{13}C being a spin 1/2 system, each resonance corresponds to one of the two possible nuclear-spin projections. A double-Lorentzian fit, indicated by the purple line in Fig. 4.3, yields a center frequency of 3493.04(3) MHz and a mean full width at half maximum (FWHM) of 2.48(8) MHz. The exact linewidth is not relevant here, but will discussed later on ODMR on the single transitions. The two transitions also differ in amplitude, which originates from a slight detuning of the laser frequency with respect to the midpoint between the two microwave transitions. Tuning the laser to lower frequencies enhances MW1, while shifting it to higher frequencies favors MW2. A total laser frequency shift of approximately 30 MHz is sufficient to transfer the full ODMR contrast from one transition to the other.

To resolve the intrinsic linewidth of a single transition, we first initialize the nuclear spin into a specific sub-state and then chirp over the corresponding microwave transition at low optical and microwave power. This nuclear-spin initialization procedure will be discussed in detail in Sec. 5.2. Fig. 4.4 presents the result of such a measurement, performed at −23 dBm microwave power with an external field of $B_{dc} = 106$ mT parallel to the quantization axis. By preparing the ^{13}C nuclear spin in either of its sub-states, only a single microwave transition remains detectable in each case: MW2 corresponds to the nuclear spin in $|\downarrow_n\rangle$, while MW1 corresponds to $|\uparrow_n\rangle$. Across all our ODMR measurements, MW1 consistently appears broader than MW2, which we attribute to a coupling of a second nuclear spin to the electron spin whose strength depends on the state of the first nuclear spin. A similar asymmetry is observed in the radio-frequency transitions of the nuclear spin.

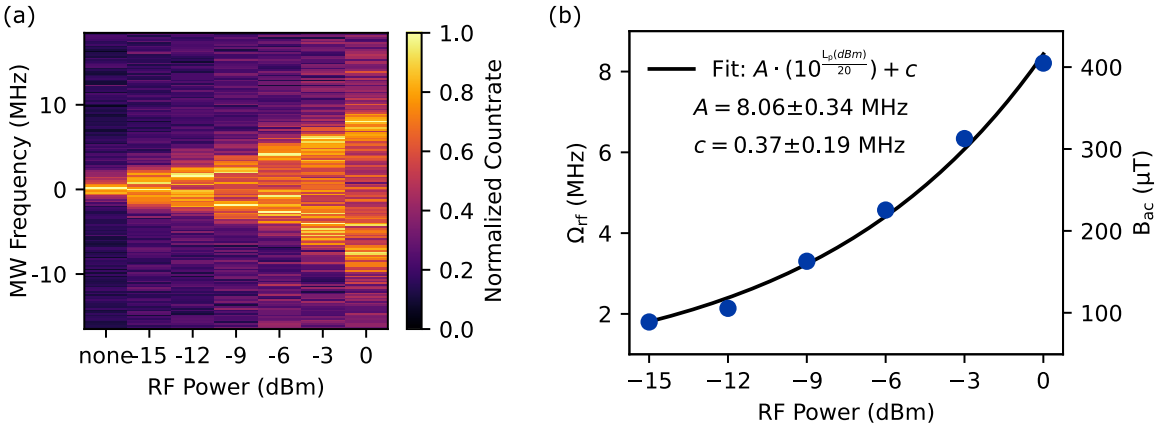

Figure 4.5.: Electron-spin transition under two-tone driving. A weak microwave signal drives the electron-spin transition, while a low-frequency rf signal at 10 kHz simultaneously modulates the qubit transition. (a) Microwave spectrum of the electron-spin transition as a function of the applied rf power under two-tone driving. (b) Frequency-modulation amplitude as a function of the applied rf power with the corresponding inferred ac magnetic field amplitude. The figure is adapted from Ref. [71].

Nuclear-spin initialization prior to electron-spin manipulation is essential in this system, as the hyperfine splitting of 44.93(3) MHz far exceeds the Rabi frequencies attainable with the present waveguide geometry and a low-strain SnV center. This stands in contrast to our earlier work [70], where the observed hyperfine splitting was only about 4 MHz, allowing the electron spin to be driven irrespective of the nuclear-spin projection.

Beyond the electromagnetic simulation of the waveguide, the microwave transition itself can be used to experimentally probe the ac magnetic field at the location of the SnV center using ODMR. This calibration measurement was carried out by Ioannis Karapatzakis and is described in detail in our Ref. [71]. In this approach, the electron-spin transition MW2 is driven with a weak microwave signal of −26 dBm, while a stronger (−15 − 0 dBm) rf tone at 10 kHz is applied simultaneously to modulate the qubit transition frequency. In the rotating frame of the qubit, the slowly varying B_{ac} field acts as an approximately static contribution during a single shot of the measurement sequence. Consequently, while probing the spin transition, the qubit splitting Δ_q assumes a random value between $\Delta_q - \Omega_{ac}$ and $\Delta_q + \Omega_{ac}$, following an arcsine probability distribution. Here, Ω_{ac} denotes the maximum amplitude of the sinusoidal modulation of the qubit transition frequency. The resulting spread of the electron-spin transition is shown in Fig. 4.5(a).

Since both the direction of the ac field and the crystallographic orientation of the SnV center within the diamond are known, the amplitude of the frequency modulation can be expressed as $\Omega_{ac} = \gamma_{SnV}(54.7°)\, B_{ac} = 20.27\,\mathrm{MHz\,mT^{-1}}\, B_{ac}$, which corresponds to a g-factor of $g = 0.72$ as can also be seen in Fig. 2.4.

As shown in Fig. 4.5, each spectral line can be fitted with an arcsine distribution convolved with a Lorentzian lineshape. The observed splitting scales as $\propto 10^{L_p(\mathrm{dBm})/20}$. Extrapolating to an rf power of 10 dBm, we extract a magnetic-field amplitude of $B_{ac} \approx 1.26$ mT, which is roughly 30% lower than the simulated value. This discrepancy can be accounted for by additional losses not captured in the simulation: the SMA connectors at the millikelvin plate

introduce approximately 0.5 – 0.7 dB of reflection loss, and the bonding wires connecting to the CPW on the diamond contribute a further return loss of about 0.4 dB. These losses are not accessible through the simple insertion loss measurements discussed above, as the low phase change of reflected signals at kilohertz frequencies prevents their extraction [71].

4.3. Microwave control of the electron spin

Having established the ability to initialize both the nuclear and electron spin into well-defined sub-states, we can proceed to coherent control of the electron spin. In order to do so, a resonant microwave pulse of variable duration is applied on either the MW1 or MW2 transition, driving Rabi oscillations. An exemplary electron-spin Rabi oscillation measured at an angle of $\theta_{dc} = 70°$ and a microwave power of $P = 8.3$ dBm is shown in Fig. 4.6. From the measurement, we extract a Rabi frequency of $\Omega = 0.730(6)$ MHz. The pulse sequence, shown in the inset, consists of electron-nuclear spin initialization, a microwave pulse, and a subsequent initialization pulse used for readout. As discussed in Sec. 2.2, the Rabi frequency depends sensitively on the angle between the external dc and ac magnetic fields. This is encoded in the coupling parameter Λ, which quantifies the interaction strength of the ac field with the electron spin. Fig. 4.7 presents the measured angular dependence of Λ for two different planes.

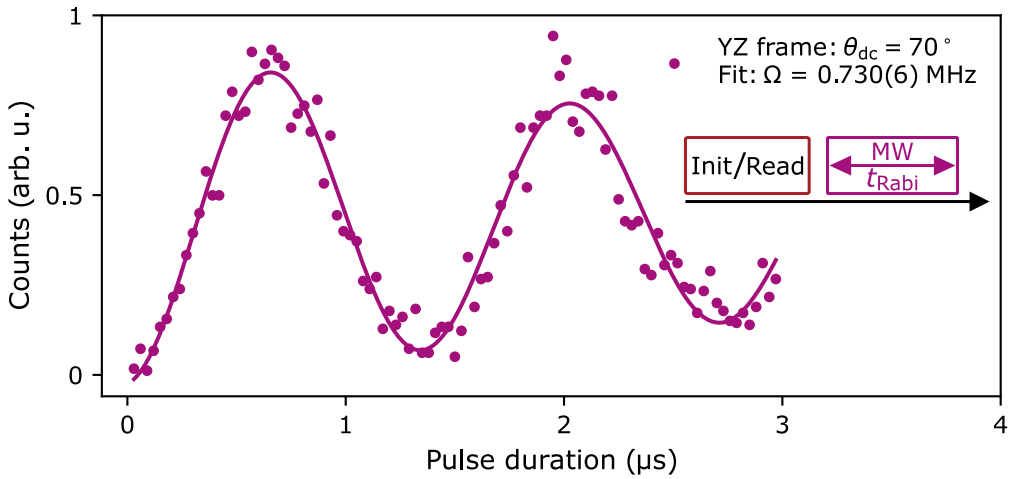

Figure 4.6.: Rabi oscillation of the electron spin for a dc magnetic field angle of $\theta_{dc} = 70°$ using a microwave power of $P = 8.3$ dBm. This results in a Rabi frequency of $\Omega = 0.730(6)$ MHz. The pulse sequence is shown in the inset and consists of electron-nuclear spin initialization and a microwave pulse. The subsequent initialization pulse is used for readout.

To account for the different microwave powers used at each driving frequency, we convert the applied power to an effective ac driving field. Using the calibration in Fig. 4.5(b), the effective driving field as a function of input power P reads

$$B_{\mathrm{ac}}^{\mathrm{eff}}(P) = \frac{1}{\gamma_{\mathrm{SnV}}(54.7°)} \left(A\, 10^{P[\mathrm{dBm}]/20} + C \right) . \tag{4.4}$$

The frequency-dependent losses of the passive components preceding the cryostat are measured independently and the input power P is corrected accordingly. Since these measurements are performed at gigahertz frequencies, whereas the power calibration is carried out at kilohertz frequencies, we additionally account for the measured insertion losses between the cryostat input and the sample, as shown in Fig. 2.10.

Each measured Rabi oscillation is fitted by a sine function to extract its frequency, which is then normalized by the free-electron gyromagnetic ratio $\gamma_s = 28\,\mathrm{MHz\,mT^{-1}}$ and the effective driving field $B_{\mathrm{ac}}^{\mathrm{eff}}$ divided by 2, yielding the parameter Λ as defined in Eq. 2.73.

The solid lines in Fig. 4.7 represent the theoretical prediction of Λ with the SnV center's strain as the only parameter, fixed to the independently measured value of $\alpha_{\mathrm{g}} = 41\,\mathrm{GHz}$. The maximum value found here, $\Lambda \approx 0.75$, originates from the fixed ac-field orientation of $\theta_{\mathrm{ac}} = 54.7°$. The good agreement between theory and experiment, including the prediction of the asymmetric behavior under rotations in different planes relative to the experimental geometry, confirms the robustness of the preceding characterizations. The remaining deviations can be explained by additional frequency-dependent losses inside the cryostat and uncertainty of the ac field calibration earlier.

As we will measure in Chapter 5 mostly with external dc magnetic fields aligned parallel to the SnV center's quantization axis, we will look into the electron spin properties under this configuration in more detail. In addition to Rabi measurements we also perform Ramsey measurements to determine the dephasing T_2^* time of the electron spin. The results of these measurements are presented in Fig. 4.8, where the same color coding as in Fig. 4.4 is used, such that MW1 is colored green and MW2 purple.

Table 4.1.: Measurement parameters used in Fig. 4.7. The angle θ_{dc} describes the tilt of the external dc magnetic field towards the SnV quantization axis. The frame yields the plane chosen in which the external magnetic field is rotated, i.e. the angle ϕ_{dc}. From the input power at the cryostat the ac magnetic field can be calculated using Eq. 4.4. Together with the fitted Rabi frequency the parameter $\Lambda_{\mathrm{exp}} = 2\Omega/(\gamma_s B_{\mathrm{ac}})$ can be calculated. A comparison with the theoretical values from Eq. 2.73 is given.

$\theta_{\mathrm{dc}}(°)$	**Frame**	**Input power (dBm)**	B_{ac} **along** z_{lab} **(mT)**	Ω **(MHz)**	Λ_{exp}	Λ_{theo}
70	XZ	8.9	0.80	1.61	0.14	0.18
110	XZ	8.3	0.75	1.60	0.15	0.18
110	YZ	8.3	0.75	2.22	0.21	0.23
70	YZ	8.3	0.75	0.73	0.07	0.08
90	YZ	8.3	0.75	7.82	0.74	0.73
0	-	15.5	1.70	1.59	0.07	0.08
180	-	10.6	0.98	0.90	0.07	0.08

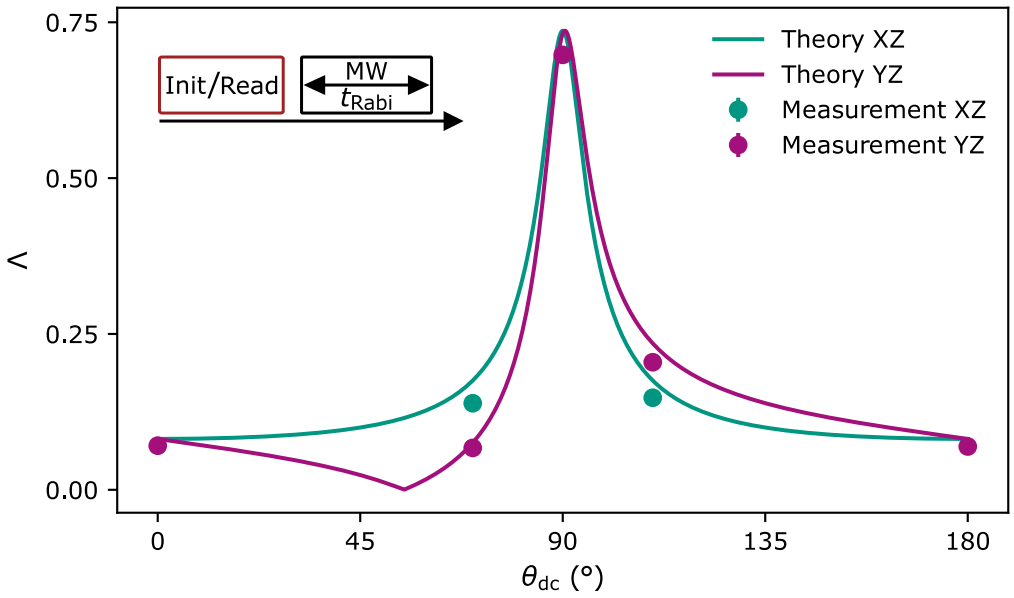

Figure 4.7.: Measured parameter Λ as a function of the dc magnetic field angle θ_{dc}. The theoretical curves use the strain as the only parameter, set to the measured value $\alpha_g = 41$ GHz. Experimental values for Rabi frequencies and corresponding driving powers are given Table 4.1. The asymmetry between the XZ and YZ scans arises from the orientation of the plane of rotation relative to the ac magnetic field, i.e. whether the ac magnetic fields lies in-plane or out-of-plane.

The Rabi oscillation in Fig. 4.8(a) was measured using a power of $P_{mw} = 15.5$ dBm at a driving frequency of $\omega_{MW1} = 3712.4$ MHz. This yields a Rabi frequency of $\Omega = 1.59(1)$ MHz and a theoretical π-pulse duration of $t_\pi = 314$ ns, where in the Ramsey measurement a pulse duration of 300 ns is chosen. Due to the power being close to the critical power of the SC-CPW at gigahertz frequencies, we observe heating during the Rabi measurement and the Rabi oscillations can not be described by a pure sine function. For long pulse durations t_{Rabi}, the overall contrast decreases and the baseline of counts increases. Similar behavior has been reported for GeV centers and also attributed to heating effects [144]. In addition, we suspect a change of the nuclear spin populations due interaction with the electron spin during manipulation of the electron spin to lead to a gradual depopulation of the resonant level. This will be discussed further in Sec. 5.4.4. To account for this in these measurements, we fit the oscillation with an additional exponential damping term and a linearly increasing baseline.

For the MW1 Ramsey measurement, a detuned drive offset by 3 MHz is used as shown in Fig. 4.8(c). As shown in the figure the Ramsey measurements consists out of an initialization pulse, two $\pi/2$-pulses separated by the free induction time τ and a readout pulse. In the experimental implementation there is no initialization pulse, as each readout pulse is also a initialization pulse. In addition, the sequence is repeated twice. The sequence is performed twice: once with the second $\pi/2$ pulse in phase with the first $\pi/2$ pulse, and once with the

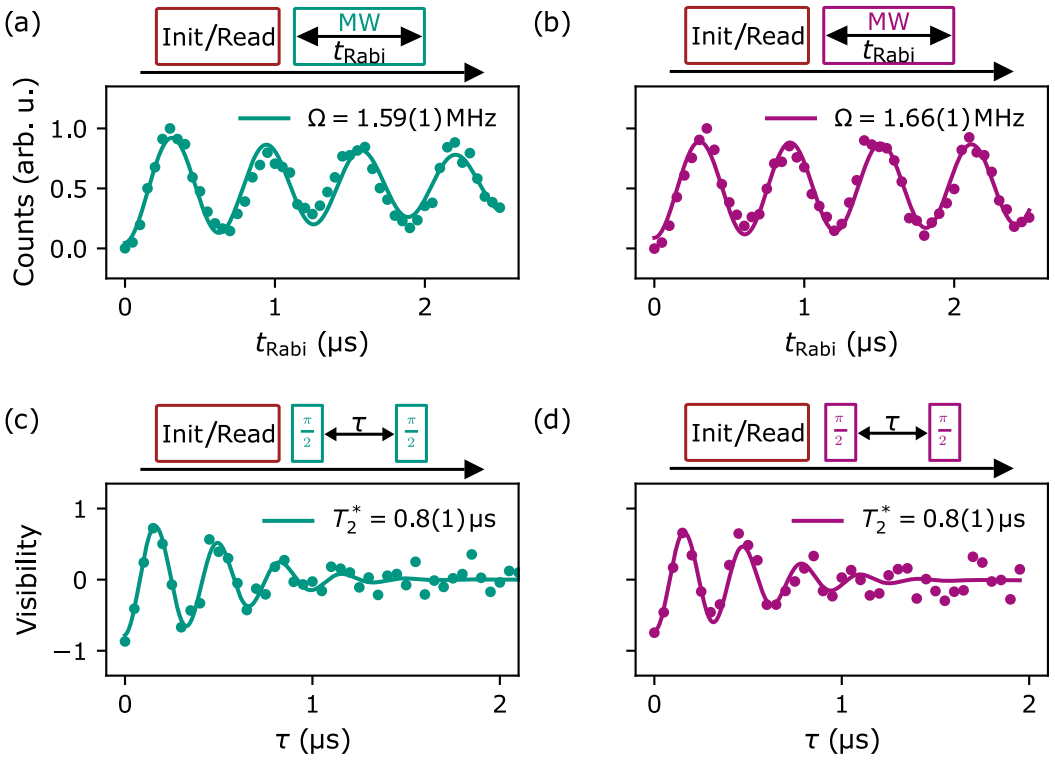

Figure 4.8.: Rabi and Ramsey measurements of the electron spin under an external magnetic dc field aligned parallel to the SnV centers quantization axis. (a) Single oscillation with a Rabi frequency of $\Omega = 1.59(1)$ MHz at 15.5 dBm power for transition frequency MW1. (b) Single oscillation with a Rabi frequency of $\Omega = 1.66$ MHz at 13.5 dBm power for transition frequency MW2. (c) Ramsey decay of MW1 for a fixed detuning yielding a coherence time $T_2^* = 0.8(1)$ μs. (d) Ramsey decay of MW2 for a fixed detuning yielding the same coherence time as expected.

second pulse shifted by 180°, corresponding to a $-\pi/2$ pulse. This projects the state onto the opposite spin state. A visibility is then calculated as

$$V = \frac{S_0 - S_{180}}{S_0 + S_{180}}, \tag{4.5}$$

where S indicates the counted fluorescence of the readout pulse on each of the two measurement cycles. This cancels out fluctuations in the count rate from the laser intensity or spatial emitter drifts. Since this is only a measurement detail, it is not shown in Fig. 4.8(c) and (d) in order to keep the figure readable. However, in all following figures in this chapter and the next chapter, whenever a visibility is reported, it refers to exactly this inversion of the final projection pulse.

As we expect the nuclear spin bath to be the main contribution to dephasing, we fit the oscillation of the visibility with a Gaussian decay

$$V_{\text{Ramsey}} = A\cos(2\pi f + \varphi_0)e^{-(t/T_2^*)^2}, \tag{4.6}$$

and obtain a dephasing time of $T_2^* = 0.8(1)$ μs. For comparison, dephasing times in the range of $0.4 - 2.4$ μs have been reported for SnV centers in natural-abundance diamond,

where the dephasing is dominated by the ^{13}C nuclear-spin bath [66, 70, 84]. For isotopically purified diamond, values of 2.5 µs have been reported [82]. As we can fit the stretching exponent well with a value of 2, we are confident that the dephasing arises from slow fluctuations of the nuclear spin bath. Thus we can use Eq. 3.17 to calculate the bath coupling strength as $b = \sqrt{2}/T_2^* = 2\pi \times 291(3)$ kHz, which is in the same order of magnitude to what was found in our previous work in Ref. [70] and for GeV centers [130].

A dephasing time of $T_2^* = 0.8(1)$ µs would give us an expected ODMR linewidth of $\sqrt{2}/(\pi T_2^*) = 0.60(9)$ MHz [145], which is still much lower than what we observed. This discrepancy will be addressed in more detail when the echo decay of the electron spin is discussed.

For MW2, performing the same measurements yields a Rabi frequency of $\Omega_{\mathrm{MW2}} = 1.66(1)$ MHz at a driving power of $P_{\mathrm{mw}} = 13.5$ dBm and a driving frequency of $\omega_{\mathrm{MW2}} = 3665.5$ MHz. As shown in Fig. 4.8(d), a Ramsey measurement with a detuning of again 3 MHz yields the same dephasing time as for MW1, as expected.

Since we expect the nuclear spin bath to be the main source of noise, the coherence can be extended using dynamical decoupling or, as a starting point, a Hahn-echo sequence. We perform an echo measurement in parallel field alignment, initializing the electron spin via the spin-conserving transition B2 and subsequently manipulating it using an echo sequence with MW1 at a power of 11 dBm. We perform the same repeating of the sequence with an inverted final projecting pulse as described for the preceding Ramsey measurements and calculate the visibility according to Eq. 4.5.

As shown in Fig. 4.9, the echo signal is strongly modulated and exhibits a characteristic beating frequency. This beating arises from the coupling of nearby ^{13}C nuclear spins to the electron spin, whose coupling strengths can significantly exceed those of the surrounding nuclear spin bath [130, 146].

For the present emitter, the modulation indicates the presence of a second strongly coupled ^{13}C nuclear spin. Although this spin is not directly resolved in the ODMR measurements, signatures of its coupling are observed in later nuclear-spin measurements, see Sec. 5.3.

For a single ^{13}C nuclear spin, the Hamiltonian in the secular approximation, i.e. neglecting the electron-flipping terms [128], and for a magnetic field aligned along the SnV center's quantization axis is given by

$$H = \Delta S_z + (\gamma_n B_{\mathrm{dc}} + A_{zz} S_z) I_z + A_{zx} S_z I_x \,, \tag{4.7}$$

where Δ is the detuning from the qubit resonance, γ_n is the gyromagnetic ratio of the ^{13}C nuclear spin, and A_{zz} and A_{zx} are the remaining non-zero hyperfine parameters [131]. For more details on the hyperfine parameters we refer to Chapter 5. The echo signal of such a coupled ^{13}C nuclear spin can be calculated, yielding

$$V_{\mathrm{Echo}} = \left[1 - 2k^2 \sin\left(\frac{\omega_0 \tau}{2}\right)^2 \sin\left(\frac{\omega_1 \tau}{2}\right)^2\right] e^{-\left(\frac{2\tau}{T_2^{\mathrm{HE}}}\right)^3} \,, \tag{4.8}$$

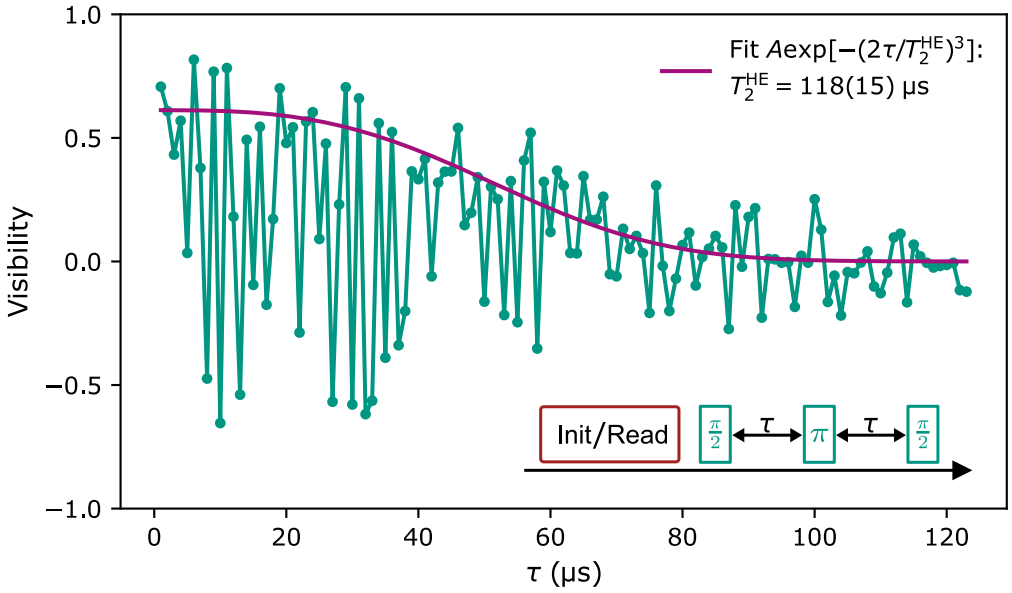

Figure 4.9.: Hahn-echo measurement of the electron spin. Visibility of the spin echo as a function of the total evolution time $t = 2\tau$. The green points show the experimental data strongly modulated by proximal nuclear spins. The magenta curve is a fit to a stretched exponential with cubic stretching for a nuclear spin bath yielding a Hahn-echo coherence time of $T_2^{\mathrm{HE}} = 118(15)\,\mu\mathrm{s}$. The inset shows the corresponding pulse sequence.

where $k = \frac{\omega_L A_{zx}}{\omega_0 \omega_1}$ is the modulation contrast and ω_0 and ω_1 are the precession frequencies of the coupled nuclear spin for the two electron spin orientations $m_s = +\frac{1}{2}$ and $m_s = -\frac{1}{2}$, respectively [131]. These effective Larmor frequencies are related to the hyperfine coupling via [131]

$$\omega_0 = \sqrt{(\omega_L + A_{zz}/2)^2 + (A_{zx}/2)^2}\,, \tag{4.9}$$

$$\omega_1 = \sqrt{(\omega_L - A_{zz}/2)^2 + (A_{zx}/2)^2}\,. \tag{4.10}$$

The Larmor frequency is given by $\omega_L/2\pi = \gamma_{^{13}C} B_{dc} = 1.135\,\mathrm{MHz}$, using $\gamma_{^{13}C} = 10.71\,\mathrm{MHz\,T^{-1}}$. It should be noted that the repeatability of this measurement was very low due to the limited signal quality and strong modulation from this nuclear spin. Moreover, the signal is under-sampled: the Larmor precession period of the nuclear spins is of the same order of magnitude as the inter-pulse spacing of the echo sequence, which affects the observed hyperfine modulation. The nuclear bath contribution becomes apparent at times $\tau \approx (2p + 1/4)\tau_L$[66], where $\tau_L = 2\pi/\omega_L = 0.88\,\mu\mathrm{s}$, which is close to our fixed inter-pulse spacing of $\tau_0 = 1\,\mu\mathrm{s}$. The effective Larmor frequencies ω_0 (ω_1) are split around the bare Larmor frequency and shift to higher (lower) values as the hyperfine coupling increases. A finer sampling than the Larmor precession period would therefore be required to make a quantitative statement about these frequencies.

To gain an insight on the order of magnitude of this coupling we can compare these observations with the broadening of our observed ODMR linewidth. The expected ODMR

splitting of such a strongly coupled nuclear spin is given by $\sim A_{zz}$ [86], which provides an upper limit on the hyperfine coupling. Since we observe a broadening of the ODMR linewidth beyond the expected T_2^*-limit, we can assume that a second nuclear spin couples within this MHz range. Simulating two T_2^*-limited Lorentzian transitions with a hyperfine splitting of $A_{zz}/2\pi = 0.75\,\mathrm{MHz}$ produces a single unresolvable peak with a resulting linewidth of 1.8 MHz, in good agreement with the experimentally observed value. Since the effective hyperfine splittings are predominantly governed by A_{zz}, we expect such strong coupling to also cause large deviations of the effective Larmor precession from the free Larmor precession. Furthermore, the strong modulation contrast suggests a sizable A_{zx} coupling. Because $\omega_\mathrm{L} \not\gg A_{zz}, A_{zx}$, the typical simplifications regarding the echo dip positions [66, 131] do not hold, and a quantitative analysis would require fitting a finely sampled trace of this echo. This is left for future work. Consequently, we do not take these oscillations into account and only provide a rough estimate of the spin bath properties.

Nuclear spin bath. We can only consider the envelope of the echo decay to make assumptions about the nuclear spin bath [130]. The echo decay yields a decay time of $T_2^\mathrm{Echo} = 119(1)\,\mu\mathrm{s}$. It is worth noting that in Fig. 4.9 the single precession time τ is plotted, but the total precession time, which determines the decoherence time, is given by $t = 2\tau$. As this decay stems from the interaction with the ^{13}C nuclear spin bath, we can estimate the bath correlation time τ_c using Eq. 3.22. We find $\tau_c = 0.5(1)\,\mathrm{s}$, roughly a factor of six smaller than reported in our previous work [70]. As noted there, such a coherence time is smaller than what we would expect from the pure ^{13}C nuclear spin bath alone. To gain an intuitive understanding, we follow Ref. [89] and discuss the predictions under the assumption of a pure ^{13}C nuclear spin bath.

As discussed in Sec. 3.3, the coupling of the nuclear spins to the electron spin of the SnV center can be described by the variance of magnetic fields produced by these nuclear bath spins, as well as their intra-bath dynamics. The square root of the magnetic field variance for a given ^{13}C density n_c is given by [147]

$$\sigma_0 \approx \sqrt{\frac{2\pi}{3}} \frac{\mu_0}{4\pi} n_c \hbar \gamma_{^{13}\mathrm{C}} \,. \tag{4.11}$$

The spin density can be calculated by considering the 1.1% probability of one of the 8 carbon atoms in the cubic unit cell of diamond being a ^{13}C nuclear spin. With the diamond lattice constant of $a_\mathrm{d} = 0.36\,\mathrm{nm}$, this gives a concentration $n_c = 1.94\,\mathrm{nm}^{-3}$. Plugging this into Eq. 4.11 yields a field of $\sigma_0 \approx 2\,\mu\mathrm{T}$. From this we obtain a coupling of the electron spin to the bath via $b = \gamma_e \sigma_0 = 2\pi \times 55\,\mathrm{kHz}$ and thus a inhomogeneous dephasing time $T_2^* = \sqrt{2}/b = 4\,\mu\mathrm{s}$, as similarly presented in Refs. [128, 147].

The internal dynamics of the bath spins are governed by the dipolar interactions between the bath spins and the resulting flip-flops [125, 148]. It is worthwhile to distinguish between bath spins, which undergo free evolution and the bath spins in the proximity of the SnV center, as the latter experience a hyperfine coupling and thus an energy shift in their Larmor precession. This also means that these nuclear spins have different Larmor precession frequencies not only to the "free" bath spins, but also from one another, which

hinders flip-flop transitions [149, 150]. This results in a so-called frozen core [149] around the SnV center. The radius of this core is given by $r = [(\gamma_e/\gamma_n)^{1/4}]a$, where a is the statistical mean distance between two neighboring ^{13}C nuclear spins [149, 150]. The mean distance a is related to the spin density via $a = 0.554 n_c^{-1/3} = 0.44\,\text{nm}$ [149, 151], yielding a frozen core radius of $r_{\text{core}} = 3.2\,\text{nm}$. The number of ^{13}C nuclear spins in this core can be calculated by multiplying the volume of the frozen core $V_{\text{core}} = 4/3\pi r_{\text{core}}^3$ with the average concentration n_c, yielding approximately $\sim$ 260 ^{13}C nuclear spins contributing to this core. Summing over all nuclear spins in the the nuclear spin bath gives the quasi-static contribution. During a measurement sequence this remains constant, but between each measurement the value changes by the variance described above, i.e. shot-to-shot noise, and thus leading to the inhomogeneous dephasing time T_2^*.

Flip-flop transitions will mostly occur for nuclear spins at the border of the frozen core and beyond. Randomly distributed pairs of spins will create the fluctuations seen by the SnV center electron spin via the hyperfine interaction [128]. Nuclear spins far out will not only couple more weakly to each other but also share the same Larmor frequency, and thus only create a modulation of the echo without leading to a decay of coherence [147, 152]. Pairs of nearest-neighbor nuclear spins located around the frozen core will have the strongest impact due to their strong dipole coupling [128]. The decoherence rate $1/T_2$ scales approximately as the geometric mean of the average nuclear-nuclear dipolar interaction and the electron-nuclear hyperfine interaction, and therefore increases linearly with the nuclear spin density n_c [152, 153]. For natural abundance, this yields a theoretical coherence time of $T_2 \approx 400\,\mu\text{s}$ [147], in good agreement with experimentally reported values [70, 130, 153].

Electron spin bath. The nuclear spin bath is not the only bath that can be present in the vicinity of the SnV center. Due to the implantation process, nearby charge traps can create an electron spin bath [66, 84], and so can the diamond surface in close proximity [63, 154].

Flips of bath electron spins create a fluctuating magnetic field at the position of the SnV center. For a finite refocusing-pulse bandwidth, the refocusing pulse can flip not only the spin qubit but also bath electron spins, thereby changing the local magnetic field [86]. This effect is known as instantaneous diffusion and can strongly reduce the efficiency of the refocusing pulse [155].

The electron spin bath is therefore expected to contribute significantly to decoherence when the g factor of the SnV center is close to the free-electron value. This can occur for strongly strained SnV centers or for suitable magnetic-field orientations, and can also enable flip-flop processes between bath electron spins and the spin qubit [86]. Instantaneous diffusion has been found to limit the coherence of moderately strained SnV centers under small-amplitude off-axis magnetic fields with $\theta_{\text{dc}} \approx 30°$ and at low magnetic-field amplitudes [84]. For a large magnetic field amplitude aligned along the quantization axis, the orbital Zeeman effect shifts the qubit far from the free electron spins, making instantaneous diffusion negligible.

Nevertheless, the fluctuating magnetic field created by electron spin bath still contributes, mainly affecting the observed coherence time T_2, while T_2^* is limited by the nuclear spins surrounding the defect. Such an electron spin bath follows a Lorentzian noise spectral density [154] and can be incorporated into bath simulations, as done in our previous work in Ref. [70], reducing the coherence time by roughly a factor of 3. This is in good agreement with the coherence time observed in Fig. 4.9. As we did not perform extensive coherence measurements on the SnV center's electron spin here, we will not discuss the relevant parameters for the electron spin bath but refer to Refs. [66, 84, 90], our work in Ref. [70], and the thesis of Karapatzakis [72], where this is discussed in more detail in the direct context of the SnV center.

4.4. Summary and outlook

We have shown in this chapter that we can coherently control the electron spin of a low-strain SnV center. After initializing the electron spin and measuring the microwave transition frequencies via ODMR, we quantify the theoretical dependence of the Rabi frequency on the angle of the external off-axis field. For parallel magnetic field configurations, we have demonstrated Rabi and Ramsey measurements of both microwave transitions (MW1 and MW2), yielding Rabi frequencies of around 1.6 MHz and dephasing times of $T_2^* \approx 0.8\,\mu s$.

The Hahn-echo measurement reveals a strong modulation from a second nearby coupled ^{13}C nuclear spin. Due to the poor signal quality of the echo, only rough estimates are possible. Comparing the observed ODMR linewidth broadening beyond the expected T_2^*-limit suggests a hyperfine coupling on the order of $\sim$ 1 MHz. As this coupling is comparable to the Larmor frequency of the bath, a strong modulation is observed.

Considering only the echo envelope, a coherence time of $T_2^{HE} = 119\,\mu s$ is measured. Estimating from a randomly distributed nuclear spin bath around the SnV center yields a theoretical coherence time of $T_2^{HE} \sim 400\,\mu s$. The observed T_2 is shorter than this prediction, which is attributed to an additional electron spin bath created by charge traps from the ion implantation and the diamond surface.

Since in our echo measurements the Rabi π-pulse duration is on the same order of magnitude as T_2^*, we expect a high accumulation of infidelity during the coherent control of the SnV center's electron spin. This will limit the dynamical decoupling efficiency, making it hard to quantify the phenomena described above in qualitative manner. Furthermore, the strong coupling of two individual ^{13}C nuclear spins complicates the control and needs to be accounted for, e.g. by initialization of both nuclear spins at the same time before coherent control of the electron spin.

We chose the configuration of low strain and parallel magnetic dc field, despite it being the most inefficient for Rabi driving, to maximize the cyclicity and the number of collected photon counts for the nuclear spin measurements in Chapter 5. If one were to use a nano-structured diamond with a higher collection efficiency, these constraints would be

relaxed and one could move to off-axis fields or employ higher strains, where we showed dynamical decoupling using SC-CPWs [70]. As shown in Fig. 4.7, applying an off-axis field would provide about a 9-fold improvement in Rabi frequency for this low-strain emitter, enabling high-fidelity manipulation to extend the coherence time of the electron spin further.

Using such high-fidelity decoupling, one can identify coupled ^{13}C nuclear spins surrounding the SnV center by analyzing the dips in the coherence signal. For more weakly coupled nuclear spins, the resonances ω_0 and ω_1 approach the Larmor frequency and the sensitivity scales with $(A_{zx}/\omega_L)^2$ [66, 131]. In contrast to the spin-1 system of the NV center, this makes it much more difficult to distinguish individual spins from the nuclear spin bath. If they couple strongly enough, they can still be resolved, as recently shown [66]. Such nuclear spins can be controlled either by timed dynamical decoupling protocols or by direct rf driving using DDRF protocols, as has been demonstrated [66].

Another approach is correlation spectroscopy, which is not limited by the finite coherence time of the system but by the lifetime of the electron spin [131]. The main idea is to perform a Hahn-echo-like pulse sequence on the electron spin, creating coherence in the surrounding nuclear spins [86]. Afterwards, the coherence of the electron spin decays and the nuclear spins undergo free induction decay governed by one of the two effective Larmor frequencies [131] $\omega_0,\ \omega_1$ given in Eq. 4.9. This leads to a phase accumulation on the nuclear spins during the free evolution. Since the electron spin is de-phased during the free induction decay of the nuclear spins, this sequence is limited only by the electron lifetime. A second echo measurement at the end maps this phase contrast onto the electron spin, which can then be read out. This technique has recently been applied successfully to the GeV center in diamond [106].

5. Coherent control of a single strongly coupled ^{13}C nuclear spin

5.1. Hyperfine interaction with a proximal nuclear spin

As we already have seen in the previous chapter, in addition to the single electron spin of the SnV center, there can also be nuclei with non-zero nuclear spins, such as the ^{13}C isotope. The total Hamiltonian of the combined system can be written as a sum of the individual contributions

$$\hat{H} = \hat{H}_0 + \hat{H}_{\mathrm{HF}} + \hat{H}_{\mathrm{NZ}} + \hat{H}_{\mathrm{NQ}} + \hat{H}_{\mathrm{NN}}\,, \tag{5.1}$$

where $\hat{H}_0$ captures the electron spin and the effects discussed in Chapter 2 and Chapter 4. The term $\hat{H}_{\mathrm{HF}}$ describes the hyperfine coupling between the electron and the nuclear spins, and $\hat{H}_{\mathrm{NZ}}$ accounts for the nuclear Zeeman effect. For nuclear spins with spin $I > 1/2$, the nuclear quadrupole term $\hat{H}_{\mathrm{NQ}}$ becomes relevant [86]. In addition, if multiple nuclear spins are present, nuclear-nuclear interactions may also become relevant, summarized by the term $\hat{H}_{\mathrm{NN}}$ [86]. As ^{13}C has a natural abundance of 1.1% in diamond, nuclear spins with $I = 1/2$ are the most relevant, and the nuclear quadrupole term $\hat{H}_{\mathrm{NQ}}$ will not be discussed further here. Due to the higher mass of nuclei, their gyromagnetic ratios are orders of magnitude smaller, which leads to typical nuclear-nuclear interactions in the kHz regime as discussed in Sec. 4.3 (see also e.g. Ref. [128]). Thus, the dominant additional terms in the Hamiltonian are the hyperfine coupling and the nuclear Zeeman term, which lead to energies in the MHz range [86]. In the following section, we will discuss both effects in more detail.

Nuclear Zeeman effect. The nuclear Zeeman effect can be described, in direct analogy to the electron Zeeman effect, by the interaction of the nuclear spin with an externally applied magnetic field as

$$\hat{H}_{\mathrm{NZ}} = -\gamma_n \hat{\boldsymbol{I}} \boldsymbol{B}\,. \tag{5.2}$$

The gyromagnetic ratio for a ^{13}C nuclear spin is $\gamma_{^{13}\mathrm{C}} = 10.71\,\mathrm{kHz\,mT^{-1}}$. For the magnetic fields used in this thesis, on the order of $60 - 400\,\mathrm{mT}$, this corresponds to energy scales in the single MHz regime.

For nuclear spins that only weakly couple to the electron spin ($E_{\mathrm{HF}} \ll E_{\mathrm{NZ}}$), this Zeeman interaction dominates the dynamics, and the nuclear spins precess around a quantization axis defined by the direction of the external magnetic field, with a unique Larmor frequency

of $|\omega_L| = \gamma_n B$. As a result, the nuclear spins generate an effective oscillating magnetic field at the position of the electron spin. This oscillating field imprints a characteristic modulation onto the electron spin dynamics, for example observed in the decoherence signal measured in a Hahn-echo-like experiment. See e.g. Ref. [146] or Sec. 4.3.

As this gives just a classical field oscillation with no effects by the electron spin itself [152], this effect can therefore be exploited to accurately calibrate the external magnetic field of the vector magnetic field coils. This has been done in our previous work in Ref. [70] to calibrate the 3D vector magnet (see also Sec. 2.5.1).

We expect hyperfine couplings in the range of tens to single MHz and thus the nuclear Zeeman effect is not negligible when estimating hyperfine coupling parameters.

Hyperfine coupling. In the following we will focus on the hyperfine interaction of single nuclear spins coupled to the SnV center's electron spin. We will first give a theoretical introduction to the hyperfine coupling in general, before introducing the coupling to a nearest-neighbor ^{13}C nuclear spin, which is the relevant case for the studies presented in this work. We begin with estimations from DFT calculations, providing a first order of magnitude of the expected hyperfine coupling. In the next subsection we will use these numbers to develop the relevant level structure of the electro-nuclear coupled system.

The hyperfine interaction is mediated by the hyperfine tensor and can be written in general as

$$\hat{H}_{\mathrm{HF}} = \hat{\boldsymbol{S}}\hat{A}\hat{\boldsymbol{I}}\,. \tag{5.3}$$

The tensor $\hat{A}$ can be decomposed into an isotropic Fermi contact interaction A_{FC} and an electron-nuclear dipole-dipole coupling term $\hat{\boldsymbol{A}}_{\mathrm{DD}}$ [86]. The Fermi contact contribution is described by the scalar parameter

$$A_{\mathrm{FC}} = \frac{2}{3}\gamma_s\gamma_n|\psi_0(0)|^2\,, \tag{5.4}$$

where $|\psi_0(0)|^2$ denotes the electron spin density at the position of the nucleus, i.e. the difference in density between spin-up and spin-down electrons [86, 156].

The dipole-dipole coupling can be described as

$$\hat{A}_{\mathrm{DD}} = \frac{1}{4\pi}\gamma_s\gamma_n\left\langle\left[3\frac{\left(\boldsymbol{r}\hat{\boldsymbol{S}}\right)\left(\boldsymbol{r}\hat{\boldsymbol{I}}\right)}{r^5} - \frac{\hat{\boldsymbol{S}}\hat{\boldsymbol{I}}}{r^3}\right]\right\rangle\,, \tag{5.5}$$

where $\boldsymbol{r}$ is the vector connecting the electron and nuclear spin [86], and $\langle\ldots\rangle$ denotes the averaging over the electron wavefunction [86, 90, 146]. For nuclear spins at distances $r > 0.25\,\mathrm{nm}$, this coupling can be well approximated by the interaction of two point dipoles [86].

Within the point-dipole approximation, only three independent non-zero parameters remain [146]. The hyperfine tensor is then axially symmetric and described by the parallel

hyperfine coupling $A_{\parallel}$, the perpendicular hyperfine coupling $A_{\perp}$ and the angle θ between the hyperfine quantization axis and the applied external field [86, 157]. If there is no Fermi-contact contribution, the dipolar coupling strength and the angle θ are the only two independent parameters [86, 145]. Having a finite angle θ leads to a pseudo-secular coupling $\sim A_{zx} S_z I_x$ [86], which is often also represented by the quantity $A_{\perp}$ [66, 67, 158] despite being not exactly the same per se. For a nuclear spin located at the inversion symmetry point of the defect, such as a host Sn nuclear spin, the dipole coupling tensor is diagonal in the frame of the SnV center parameter [111, 157].

For a proximal ^{13}C nuclear spin, however, the dipole coupling cannot be approximated by point-dipoles, and the corresponding tensor in the frame of the SnV center is generally not diagonal. Nevertheless, averaging over the spatial electron distribution yields a symmetric and traceless dipole coupling tensor, resulting in six independent non-zero parameters of the total hyperfine tensor in the frame of the SnV center [86, 146]. Rotating the external magnetic field away from the SnV center's quantization axis allows in principle for the determination of these six parameters.

Following for example Gali *et al.* [159], the hyperfine tensor can in general be diagonalized into its principal axis frame, in which the hyperfine tensor is purely diagonal. The principal axis frame does not necessarily coincide with the symmetry axis of the SnV center nor with the orientation of the external magnetic field [86]. However, performing this transformation theoretically yields the so-called principal values, or hyperfine constants, A^p_{xx}, A^p_{yy}, and A^p_{zz}. The Fermi-contact term is given by one-third of the trace of the hyperfine tensor,

$$A_{\mathrm{FC}} = \frac{1}{3} \sum_i A_{ii} \,. \tag{5.6}$$

This is physically intuitive, as the Fermi-contact contribution corresponds to an isotropic (diagonal) term.

To gain insight into the order of magnitude of the expected hyperfine coupling of such a nearest-neighbor ^{13}C nuclear spin, we consider DFT calculations from the literature. Using the values obtained by Kuate Defo *et al.* [160] and Mohseni *et al.* [157], we can extract the expected Fermi-contact and dipole-coupling terms. Both references note that one could expect two sets of hyperfine couplings, since the spin density is anisotropically distributed over the nearest neighbors due to lattice distortions caused by the large Sn nucleus. This is in contrast to the SiV center, where six equivalent carbon sites were simulated [160, 161] and also experimentally observed [162].

We distinguish the obtained hyperfine parameters by writing them in the form site 1(site 2). Using the values by Kuate Defo *et al.* [160], one expects Fermi-contact terms of $A_{\mathrm{FC}} = 18 - 25\,\mathrm{MHz}(92 - 129\,\mathrm{MHz})$. The overall interaction strength can be estimated as $A_{\mathrm{mean}} = 21 - 28\,\mathrm{MHz}(103 - 137\,\mathrm{MHz})$ [146] for this lowered symmetry.

Mohseni *et al.* [157] also calculate the expected hyperfine coupling in the case of the full D_{3d} symmetry and finds a hyperfine tensor in the frame of the SnV center of

$$\hat{A}_{\mathrm{DFT}} = \begin{pmatrix} 70.1 & 0 & 14.6 \\ 0 & 28.3 & 0 \\ 14.6 & 0 & 33.4 \end{pmatrix} \mathrm{MHz}\,. \tag{5.7}$$

Diagonalizing this tensor yields the principal values $A^p_{xx} = 28.3\,\mathrm{MHz}$, $A^p_{yy} = 33.4\,\mathrm{MHz}$, $A^p_{zz} = 70.1\,\mathrm{MHz}$, a Fermi-contact term of $A_{\mathrm{FC}} = 43.9\,\mathrm{MHz}$ and a mean interaction strength of $A_{\mathrm{mean}} = 48\,\mathrm{MHz}$ [146]. This is much closer to our observed values in Fig. 4.3 and thus the full D_{3d} symmetry might be retained in our system and we will use this hyperfine tensor as a first order of magnitude model in the following subsection.

Level structure with a single strongly coupled proximal nuclear spin. The previous discussion provides the magnitudes of the hyperfine interaction, but not the expected level structure. This level structure is required to describe the transition frequencies observed in our measurements. Since the hyperfine interaction is much smaller than the electron Zeeman splitting, we first write the eigenstates as product states, $|{\downarrow_e}{\downarrow_n}\rangle$, $|{\downarrow_e}{\uparrow_n}\rangle$, $|{\uparrow_e}{\downarrow_n}\rangle$, and $|{\uparrow_e}{\uparrow_n}\rangle$ [86, 163].

To gain an intuitive understanding of the expected transition frequencies, we take a closer look at the hyperfine tensor in Eq. 5.7. The zero entries are readily understood from symmetry considerations. Similar to the treatment of a nearest-neighbor ^{13}C nuclear spin coupled to an NV center by Rao and Suter [164], the number of independent non-zero parameters of the hyperfine tensor can be reduced by considering the symmetry of the combined system. Since the nuclear spin is expected to be located at one of the six nearest-neighbor lattice sites, the symmetry is reduced from D_{3d} to C_s. This point group contains only a single mirror plane, which is spanned by the SnV quantization axis and the vector connecting the SnV center to the chosen nearest-neighbor lattice site, $\boldsymbol{r}_{^{13}\mathrm{C}}$ [164].

Since the g tensor is axially symmetric, we define the x-axis of the coordinate system to be in the plane spanned by $\boldsymbol{r}_{^{13}\mathrm{C}}$ and the SnV center's quantization axis. This reduces the hyperfine tensor in the SnV frame to four independent non-zero parameters, yielding the hyperfine interaction [164]

$$\hat{H}_{\mathrm{HF}} = \sum_{i=x,y,z} A_{ii}\hat{S}_i\hat{I}_i + A_{zx}\left(\hat{S}_x\hat{I}_z + \hat{S}_z\hat{I}_x\right)\,. \tag{5.8}$$

Following Ref. [86], the ground-state electron spin Hamiltonian is first diagonalized by rotating into the principal-axis frame of the g tensor of the SnV center. This yields eigenvalues $\Delta^g_q m_s$ for the electron Zeeman interaction. The resulting four eigenvalues of the combined electron-nuclear spin system are given by [86]

$$E(m_s, m_I) = \Delta^g_q m_s + c(m_s) m_I\,. \tag{5.9}$$

The allowed electron spin resonance transitions are those with $\Delta m_s = 1$ and unchanged nuclear quantum number, while the opposite holds for the nuclear spin resonance transitions [86, 87]. This gives four allowed transitions: two in the GHz regime, referred to as MW transitions, and two in the MHz regime, referred to as RF transitions in this work. The two MW transitions are separated by the value of $c(m_s)$. This can be seen in Fig. 5.1(a), where the two Zeeman sublevels of the electron spin split into four levels, with the two nuclear spin-conserving microwave transitions labeled MW1 and MW2. The color scheme is chosen to match that used in Chapter 4. The two electron spin-conserving nuclear transitions are labeled RF1 and RF2. In addition, Fig. 5.1(a) illustrates the electron Zeeman splitting in the excited state to indicate the spin-conserving optical transitions A1 and B2. The Zeeman splitting in the excited state is larger due to the less quenched orbital contribution for a magnetic field aligned along the SnV quantization axis, leading to A1<B2. A schematic representation of the SnV center within the diamond lattice is also shown, where black spheres denote ^{12}C atoms, white spheres vacancies, the red sphere the tin atom, and the blue sphere the ^{13}C nuclear spin. The position of the ^{13}C atom is chosen arbitrarily among the nearest-neighbor sites.

For simplicity, one can assume an isotropic hyperfine tensor, i.e. $\hat{A} = A$, because the Fermi-contact contribution is expected to be larger than the anisotropic dipolar coupling when comparing the DFT values of the Fermi-contact contribution with the off-axis coupling term. This approximation has, for example, been used for nearest-neighbor ^{13}C nuclear spins coupled to an NV center [165]. For comparison, nearest-neighbor couplings of a ^{13}C nuclear spin to an NV center in diamond with hyperfine coupling strengths of ~ 150 MHz have been reported [152, 165–168]. If one further neglects the nuclear Zeeman splitting, the eigenvalues are given by $c(m_s) \approx A/2$ [86]. From this, we find that the splitting between the allowed MW transitions is approximately $\Delta\omega_{\mathrm{MW}} \approx A$. For arbitrary magnetic-field orientations, the RF transitions are given by $\omega_{\mathrm{RF}} = c(m_s) \approx A/2$ [86]. Thus, the RF transition frequencies are expected to be approximately half the splitting of the MW transitions, with corrections arising from the nuclear Zeeman interaction and pseudo-secular terms. Using the measured ODMR spectrum in Fig. 4.3, we find $A \approx 45$ MHz in agreement with the Fermi-contact value reported by DFT calculations [157]. The nuclear Zeeman term can be calculated from the external dc magnetic field and is given by $\omega_{\mathrm{L}} \approx -1$ MHz for a field of 100 mT. Assuming an isotropic hyperfine coupling, we find $\omega_{\mathrm{RF}} = A/2 - 2m_s\omega_{\mathrm{L}}$. The nuclear Zeeman term therefore increases the RF frequency of the $|{\downarrow_{\mathrm{e}}}\rangle$ state, denoted RF1, and decreases that of the $|{\uparrow_{\mathrm{e}}}\rangle$ state, denoted RF2. This agrees well with the observed asymmetry in the RF splittings as shown in Fig. 5.1(a).

For a magnetic field aligned along the z-direction of the SnV center or for an isotropic g tensor, i.e. a high-strain SnV center, we can have a simplified look at the Hamiltonian of the hyperfine interaction. Under this assumption one can neglect the off-diagonal electron spin operators, i.e. the non-secular terms $\hat{S}_x$ and $\hat{S}_y$ [86, 128]. This is the so-called secular approximation, which is commonly applied to an electron spin 1/2 coupled to a nuclear spin 1/2 [86]. Under this approximation, the hyperfine Hamiltonian reduces to

$$\hat{H}_{\mathrm{HF}} = A_{zz}\hat{S}_z\hat{I}_z + A_{zx}\hat{S}_z\hat{I}_x\,, \tag{5.10}$$

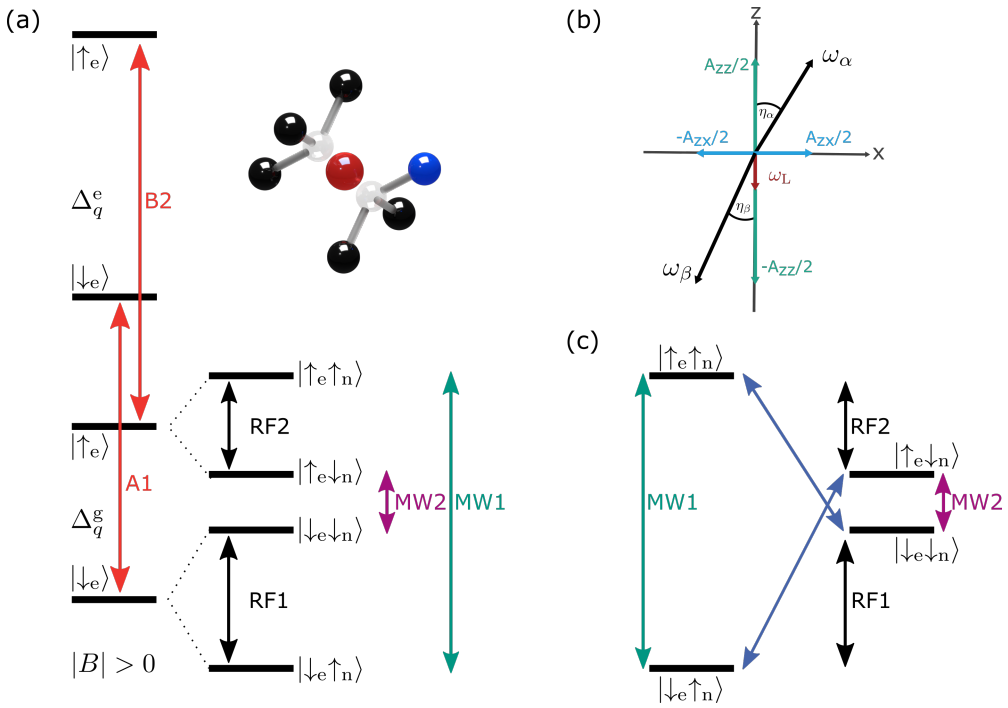

Figure 5.1.: Level scheme of the hyperfine coupling between the electron spin of the SnV center and a proximal ^{13}C nuclear spin. (a) The two Zeeman sublevels of the electron spin split into four levels. In addition, the electron Zeeman splitting in the excited state is shown to indicate the spin-conserving optical transitions A1 and B2. A depiction of the SnV center's symmetry inside the carbon lattice is also shown, with black spheres indicating ^{12}C atoms, white spheres vacancies, the red sphere the tin atom, and the blue sphere the ^{13}C nuclear spin. The position of the ^{13}C is arbitrarily chosen among the nearest neighbors. (b) Nuclear precession axis ω_α and ω_β for the two different electron states respectively. The length of these vectors give the nuclear transition frequencies RF1 and RF2. (c) Allowed and forbidden transitions for a strongly coupled nuclear spin. The forbidden transitions are shown in blue. Figure (a) is adapted from Fig. 1 in Ref. [71]. Figure (b) and (c) are adapted from figures 3.5.1 and 3.5.2 in Ref. [86].

where the term containing A_{zz} is referred to as the secular hyperfine coupling, while A_{zx} is the pseudo-secular hyperfine coupling [86]. From this expression, it becomes clear that all elements of the hyperfine tensor can only be determined by applying off-axis magnetic fields and considering the full tensor with four independent parameters. Since the hyperfine tensor in Eq. 5.7 is not axially symmetric, it is not possible to introduce the parameters $A_\parallel$ and $A_\perp$. The Hamiltonian above corresponds to the same hyperfine interaction discussed in Eq. 4.7 in the context of echo modulations induced by proximal nuclear spins.

Using this Hamiltonian, together with the nuclear Zeeman interaction, the nuclear transition frequencies are given by

$$|\omega_{\alpha,\beta}| = \sqrt{\left(\omega_L \pm \frac{A_{zz}}{2}\right)^2 + \left(\frac{A_{zx}}{2}\right)^2}. \tag{5.11}$$

Using the DFT values in Eq. 5.7, namely $A_{zz} = 33.4\,\mathrm{MHz}$ and $A_{zx} = 14.6\,\mathrm{MHz}$, we obtain $\omega_\alpha = 17.2\,\mathrm{MHz}$ and $\omega_\beta = 19.27\,\mathrm{MHz}$. As discussed above, we assign ω_β to the $|{\downarrow_\mathrm{e}}\rangle$ state (RF1) and ω_α to the $|{\uparrow_\mathrm{e}}\rangle$ state (RF2).

To determine the ODMR splitting shown in Fig. 4.3, we follow Ref. [86] and introduce the angles

$$\eta_{\alpha,\beta} = \arctan\left(\frac{-A_{zx}}{A_{zz} \mp 2\omega_\mathrm{L}}\right) . \tag{5.12}$$

This allows the nuclear transition frequencies to be rewritten as

$$\omega_\alpha = \left(\omega_\mathrm{L} + \frac{A_{zz}}{2}\right)\cos\eta_\alpha - \frac{A_{zx}}{2}\sin\eta_\alpha\,, \tag{5.13}$$

$$\omega_\beta = \left(\omega_\mathrm{L} - \frac{A_{zz}}{2}\right)\cos\eta_\beta + \frac{A_{zx}}{2}\sin\eta_\beta\,. \tag{5.14}$$

Fig. 5.1(b) shows the relevant precession axes, derived in a geometrical manner by adapting the figure 3.5.1 from Ref. [86] to our situation.

The difference between the two allowed electron spin transitions is given by $\Delta_\mathrm{alw} = \omega_\alpha - \omega_\beta \approx 36\,\mathrm{MHz}$, which is smaller than the experimentally observed splitting of $\sim 45\,\mathrm{MHz}$. For the forbidden transitions, one obtains $\Delta_\mathrm{frb} = \omega_\alpha + \omega_\beta \approx -2\,\mathrm{MHz}$. The relative strengths of these transitions are given by

$$\frac{I_\mathrm{alw}}{I_\mathrm{frb}} = \frac{\cos^2\left(\frac{\eta_\alpha - \eta_\beta}{2}\right)}{\sin^2\left(\frac{\eta_\alpha - \eta_\beta}{2}\right)} \gg 1\,, \tag{5.15}$$

and therefore the forbidden transitions can be neglected in ODMR experiments at low driving power. This is in good agreement with the observations shown in Fig. 4.3. For high power ODMR measurements, i.e. powers of roughly -10 to $-4\,\mathrm{dBm}$, yield a broadened central peak, which we attribute to the forbidden transitions.

In Fig. 5.1(c) the derived transitions are shown, where we adapted the figure 3.5.2 from Ref. [86] to our notation. The forbidden transitions are shown in blue and one can see directly from geometry, that they are close to equal in transition frequency. Note that the nuclear spin ordering is reversed in the $|{\uparrow_\mathrm{e}}\rangle$ manifold due to the strong hyperfine coupling [86].

As given in Refs. [86, 165], the new eigenvectors are not the bare product states anymore but superpositions of opposing nuclear spin projections along the quantization axis of the SnV center. The mixing depends on the strength of A_{zx} relative to A_{zz} in the strong coupling case as considered here. For the DFT values used above we find an 5% admixture of the opposite nuclear spin state. Thus we denote the states as pure product states [86] in Fig. 5.1(a) and (c).

With this level scheme, we have sufficient understanding to describe the phenomena observed in Sec. 5.2 through Sec. 5.4.3.

5.2. Initialization via microwave-assisted optical pumping

Before the nuclear spin can serve as a qubit, it needs to be prepared into one of its sublevels. While methods such as SWAP gates [144], spin-echo resonances [63, 66], or Hartmann-Hahn cross-polarization [135] exist for this purpose, the low electron Rabi frequency of low-strain SnV centers, when the magnetic field is aligned along the SnV quantization axis, makes these approaches impractical here. Instead, an optical pumping protocol can be used.

The initialization scheme works by simultaneously driving a microwave transition incoherently and a spin-conserving optical transition, for instance MW1 together with A1. The A1 transition is chosen such that it excites the electron spin state $|\downarrow_e\rangle$ regardless of the nuclear spin orientation. This can be verified by comparing the ODMR contrast of both microwave transitions: As shown in Fig. 4.3, these should be of equal height for this condition to be satisfied. As soon as an electron flip occurs due to the finite cyclicity of A1, the microwave drive MW1 creates an incoherent mixture of both electron spin projections, provided the nuclear spin is in the $|\uparrow_n\rangle$ state. This leads again to excitation via A1, until only population in $|\uparrow_e\downarrow_n\rangle$ remains. This state is off-resonant with all drive fields and forms a dark state. The population transfer can be traced by the observed fluorescence, which decays exponentially as population accumulates in the dark state. Analogous pumping schemes using MW2 and/or B2 can populate any of the four sublevels.

Since only an incoherent mixture of the electron spin is needed, microwave powers as low as $P = -16\,\mathrm{dBm}$ can be used. Typically, a short laser-only pulse is appended at the end of the nuclear initialization sequence to provide a reference of the background fluorescence level, as already discussed in Sec. 4.1. Using the same formulas presented in that section, one can calculate the initialization fidelity. Due to the high cyclicity of the electron spin of ~ 6000 (see Sec. 4.1), this initialization takes roughly $5 - 10\,\mathrm{ms}$ depending on the optical and microwave power as can be seen in Fig. 5.2(a).

In order to model the initialization, one has to consider all four ground-state levels as well as the two hyperfine levels in the excited state connected to the electron-spin-conserving transition being probed. Solving the master equations obtained from a Hamiltonian similar to the one in Eq. 2.88 is rather tedious, as the energy scales of the electron spin transitions and nuclear spin transitions differ by three orders of magnitude. Even if one dephases the coherences very quickly, a naive approach of numerically solving the time evolution requires long computing times. However, we can benefit from using the rate models in Eq. 2.95 and Eq. 2.96. Assuming microwave pumping with MW1, we obtain for the four ground-state levels a rate equation

$$\dot{N}_i^g = \sum_{j=1}^{m=2} (b_{ji}\gamma + R_{ji}) N_j^e - R_{ji} N_i^g + W_{\mathrm{MW1}}(\xi_{14}\delta_{i1} + \xi_{41}\delta_{i4})\,, \tag{5.16}$$

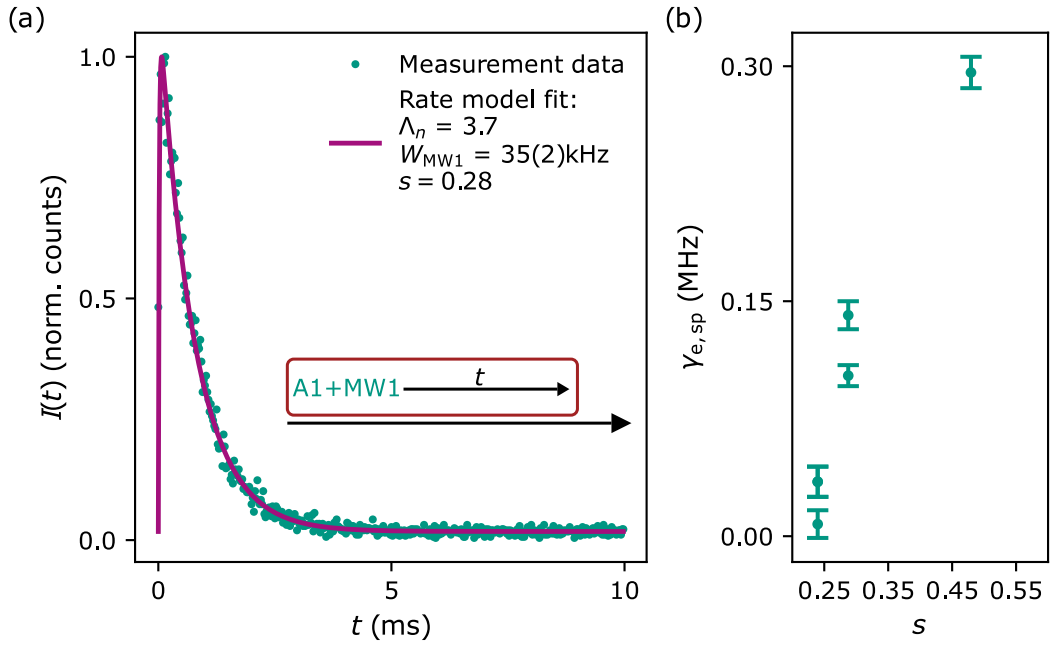

Figure 5.2.: Initialization into a single electron-nuclear sub-state using incoherent microwave pumping of the MW1 transition while optically driving the optical A1 transition. (a) Time-resolved fluorescence decay. Fitting to the rate model in Eq. 5.16 and Eq. 5.17 yields a pump rate of $W_{\mathrm{MW}} \sim 35(2)$ kHz. The measurement was performed under similar conditions as the electron initialization in Fig. 4.2, with a saturation parameter of $s = 0.28$, using a π-pulse on the RF2 transition after initialization to repopulate, and was repeated 10^4 times. (b) Effective linewidth of the spin transition observed during optical pumping. Higher optical powers broaden the effective microwave transition.

where $\xi_{ij} = (N_i^g - N_j^g)$ is the difference between the ground-state populations i and j, and i runs from 1 to 4. As we consider two excited states, we set $m = 2$. For the excited state we obtain

$$\dot{N}_i^e = \sum_{j=1}^{n=4} \left[(R_{ji} N_i^g - (R_{ji} + \gamma) N_i^e \right] , \tag{5.17}$$

where i runs from 1 to 2 and $n = 4$ accounts for all ground-state levels. The rate W_{MW1} describes the incoherent microwave pumping and connects the lowest level $N_1^g = |{\downarrow_{\mathrm{e}}}{\uparrow_{\mathrm{n}}}\rangle$ with the $N_4^g = |{\uparrow_{\mathrm{e}}}{\uparrow_{\mathrm{n}}}\rangle$ level, as shown in Fig. 5.1. The matrix b_{ji} gives the probabilities to flip or conserve the nuclear and/or electron spin during a spontaneous emission decay. We indicate this by labeling the probabilities with indices: for example, electron-conserving is denoted by the index ec and nuclear-flipping by nf, and so on. This leads to the matrix

$$b = \begin{pmatrix} P_{\mathrm{ec}}P_{\mathrm{nc}} & P_{\mathrm{ec}}P_{\mathrm{ef}} & P_{\mathrm{ef}}P_{\mathrm{nf}} & P_{\mathrm{ef}}P_{\mathrm{ec}} \\ P_{\mathrm{ec}}P_{\mathrm{ef}} & P_{\mathrm{ec}}P_{\mathrm{nc}} & P_{\mathrm{ef}}P_{\mathrm{nc}} & P_{\mathrm{ef}}P_{\mathrm{ef}} \end{pmatrix} , \tag{5.18}$$

obtained by considering all possible decay transitions from the excited state to the ground-state levels. We can define these probabilities in analogy to the cyclicity derived in Sec. 2.5.2. This introduces the quantity Λ_{n}, which quantifies after how many random electron-spin flips the nuclear spin becomes depolarized. This quantity is thus closely related to the pseudo-secular terms in the hyperfine interaction. Stronger pseudo-secular terms should

lead to a smaller Λ_n, making the nuclear spin more susceptible to random electron-spin flips. The probabilities can then be written as

$$P_{ec} = \Lambda_e/(1+\Lambda_e)\,, \tag{5.19}$$
$$P_{ef} = 1/(1+\Lambda_e)\,, \tag{5.20}$$
$$P_{nc} = \Lambda_n/(1+\Lambda_n)\,, \tag{5.21}$$
$$P_{nf} = 1/(1+\Lambda_n)\,. \tag{5.22}$$

For driving A1, the optical pump rate R connects only the $|\downarrow_e\rangle$ sublevels in ground and excited state and is assumed to be nuclear spin-conserving, and is thus given simply by

$$R = \begin{pmatrix} W & 0 & 0 & 0 \\ 0 & W & 0 & 0 \end{pmatrix}, \tag{5.23}$$

where W is the optical pump rate defined in Eq. 2.93. While this rate can be determined from a saturation measurement and the lifetime of the emitter, e.g. via a Fourier-limited PLE measurement, the incoherent microwave pump rate W_{MW1} cannot be measured easily. In a naive approach, one could simply scale down the Rabi frequency at high powers to a slow, attenuated Rabi frequency via $\Omega_{att} = \Omega \times 10^{att/20}$, where a typical Rabi frequency is $\Omega = 1\,\text{MHz}$ and a typical attenuation is $att = -30\,\text{dB}$. As the resulting Rabi frequency is lower than the linewidth of the spin transition $\gamma_{e,sp}$, we need to consider an incoherent pump rate with a finite detuning from the resonance frequency. In analogy to the optical pump rate defined in Eq. 2.93, we define

$$W_{MW} = \frac{\Omega_{att}^2 \gamma_{e,sp}}{\gamma_{e,sp}^2 + 4\Delta_{MW}}\,. \tag{5.24}$$

However, directly measuring this dark spin pump rate is not possible, as $\Omega_{att} \ll \gamma_{e,sp}$. This yields only a contribution to the fluorescence signal when the electron spin is resonant with the microwave tone. The resulting rates, in the $10 - 100\,\text{Hz}$ range, are too small to be quantified reliably. Furthermore, during the initialization process the optical pumping broadens the spin resonance by the optical Rabi frequency, making the incoherent spin pump rate under these driving conditions not directly accessible.

If we take the nuclear cyclicity obtained in Sec. 5.4.4 of $\Lambda_n = 3.7(9)$ and the Rabi frequency of $\Omega = 1.59(1)\,\text{MHz}$ for MW1 at a driving power of 15.5 dBm as a reference, we can fit the nuclear initialization curve in Fig. 5.2(a).

For this measurement, an attenuation of $-27\,\text{dB}$ is used, which leads to an estimated incoherent pump rate of $W_{MW} \sim 10\,\text{kHz}$. Fitting yields a pump rate of $W_{MW} \sim 35(2)\,\text{kHz}$, in reasonable agreement with our estimate. The measurement was performed under similar conditions as the electron initialization in Fig. 4.2, with a saturation parameter of $s = 0.28$ and a excited state decay rate of $2\pi \times 36\,\text{MHz}$. Statistics were created using a π-pulse on the RF2 transition after initialization to repopulate and repeating the sequence 10^4 times.

If we assume that only the measurement cycles contribute in which the microwave is exactly on the spin resonance, $\Delta_{MW} = 0$, we can extract the effective spin transition

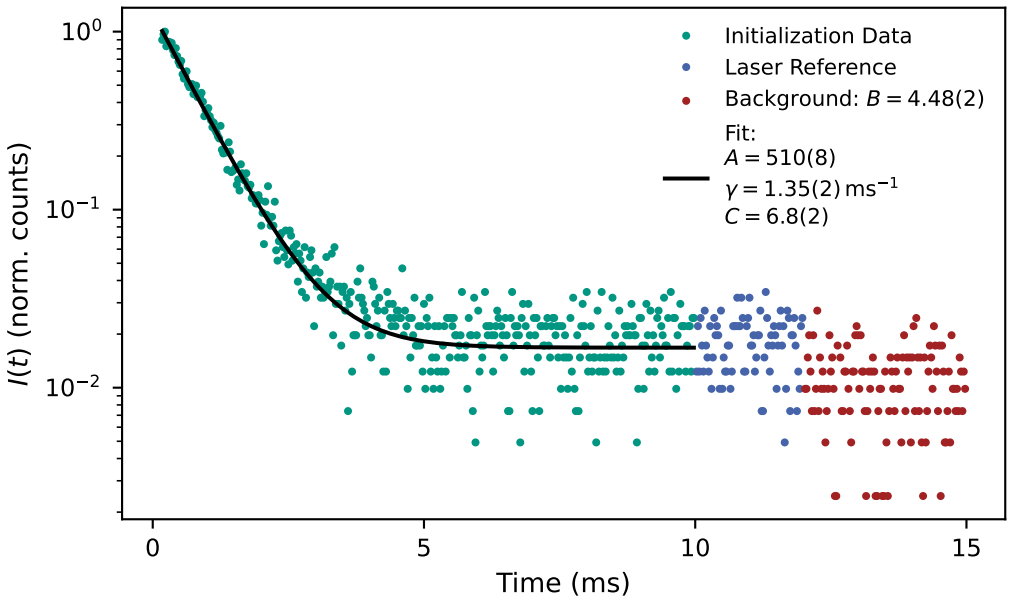

Figure 5.3.: Initialization into a single electron-nuclear sub-state showing a time-resolved fluorescence decay. In addition to incoherent microwave pumping on the MW1 transition the system is optically pumped via the A1 spin-conserving transition. The green data points mark the initialization data, the blue points the laser-induced background counts and the red points the dark counts by the single photon detector. Fitting the data with a mono-exponential decay yields an initialization fidelity of $F_{\mathrm{init}} = 99.539(5)\%$, obtained from the fitted amplitude A and the remaining counts C after correcting for the dark counts B. Without this background correction, the initialization fidelity is $F_{\mathrm{init}} = 98.66(2)\%$.

linewidth $\gamma_{\mathrm{e,sp}}$ during optical pumping. As can be seen in Fig. 5.2(b), this linewidth increases with the optical power, given by the saturation parameter $s = p/p_{\mathrm{sat}}$. For low powers, the effective spin transition linewidth $\gamma_{\mathrm{e,sp}}$ is lower than the T_2^*-limit, as only processes in which the spin is on resonance with the transition contribute, due to the very low Rabi frequency $\Omega_{\mathrm{att}} \ll 1/\sqrt{T_2^*}$. The increase in the effective spin transition linewidth follows the optical pump rate $R(s)$ in Eq. 2.94. The exact determination of the parameters and pump rates involved should be addressed in further studies, but the present analysis provides a qualitative model of how the initialization process works.

In order to calculate the initialization fidelity, we follow the procedure in Sec. 4.1 step by step and perform a mono-exponential fit of the form $Ae^{-\gamma t} + C$ to the falling edge of the initialization curve. The result is shown in Fig. 5.3. As in our work in Ref. [71], we measure the laser-induced background counts, marked as laser reference, as well as the dark counts of the single-photon detector. From this we can calculate a non-background-corrected initialization fidelity of $F_{\mathrm{init}} = 98.66(2)\%$, or, if we account for the background, a fidelity of $F_{\mathrm{init}} = 99.539(5)\%$, in good agreement with the values reported in Ref. [71]. The measurement shown here was taken a year after the measurement presented in Ref. [71], demonstrating the reproducibility of the reported values. The deviation in fidelity at the sub-percent level stems from the varying laser background and the measurement noise. The measurement here was optimized to give the most clear initialization contrast.

5.3. Optically detected nuclear magnetic resonance of a single strongly-coupled ^{13}C nuclear spin

As discussed in Sec. 5.1, nuclear-spin transitions are expected around 20 MHz. Their exact frequencies can be measured using optically detected nuclear magnetic resonance, referred to here as ODNR [169]. For this, one optical transition, either B2 or A1, is continuously pumped together with one microwave transition, either MW1 or MW2, while an rf field is swept across the expected nuclear-spin transition range. The corresponding driven transitions are shown in Fig. 5.1(a) and (c).

The combination of optical and microwave pumping continuously initializes the system into a dark state and depopulates all other levels, as described in the previous section. As soon as the nuclear transition is hit, a small fraction of population is transferred to the bright states and immediately pumped away. The detection of the initialization fluorescence as a function of the applied RF frequency then allows the detection of the nuclear resonance. In this sense, the measurement can also be viewed as a transition saturated by the simultaneous microwave and optical drive that is desaturated by the RF drive. This means we perform optically read-out electron-nuclear double resonance (ENDOR) spectroscopy [86].

Figure 5.4 shows the ODNR transitions RF1 and RF2, recorded at a magnetic field of $B_{\mathrm{dc}} = 60\,\mathrm{mT}$ for qualitative characterization. A change to $B_{\mathrm{dc}} = 106\,\mathrm{mT}$ leads only to a shift in Zeeman energy of $\sim 0.5\,\mathrm{MHz}$, which is much less than the hyperfine coupling. Over many cooldowns, the RF2 transition frequency of the nuclear spin varied in a range from 20.53 MHz to 21.13 MHz at the constant field of $B_{\mathrm{dc}} = 106\,\mathrm{mT}$ used for each measurement. This variation amounts to roughly 1% of the hyperfine coupling; its origin cannot be explained by variations in the external field but must rather stem from the hyperfine interaction itself. The cause of this remains unclear and needs to be investigated further.

To examine the substructure of these transitions, it suffices to consider the measurement at $B_{\mathrm{dc}} = 60\,\mathrm{mT}$. The measurement is carried out by chirping the radio frequency across the resonance at −23 dBm while continuously driving MW1 at −19 dBm together with the spin-conserving optical transition B2 (for RF1) or A1 (for RF2) at low optical powers to avoid power broadening. Fitting RF1 to a pair of Lorentzian curves gives a FWHM of 1.6(2) kHz and a splitting of $\Delta = 3.89(6)\,\mathrm{kHz}$ — a signature of coupling to an additional ^{13}C nuclear spin. RF2, by contrast, is well described by a single Lorentzian, showing no evidence of such coupling, even with a lower broadening of the resonance at the same powers. For this reason, all subsequent experiments are carried out on the RF2 transition. The physical picture behind this asymmetry is that the two electron-spin states $|\uparrow_{\mathrm{e}}\rangle$ and $|\downarrow_{\mathrm{e}}\rangle$ reorient the electron's dipolar field and thereby rotate the total magnetic field experienced by the second ^{13}C nuclear spin. This shifts its quantization axis in a state-dependent way [170], such that the nuclear-nuclear coupling is effectively present only in the $|\downarrow_{\mathrm{e}}\rangle$ configuration and absent in $|\uparrow_{\mathrm{e}}\rangle$. The splitting Δ of the RF1 transition is larger than the maximal dipole coupling of two nearest neighbor dipole coupled ^{13}C nuclear spins. We attribute this to the enhancement of the gyromagnetic ratio due the strong hyperfine coupling of the first

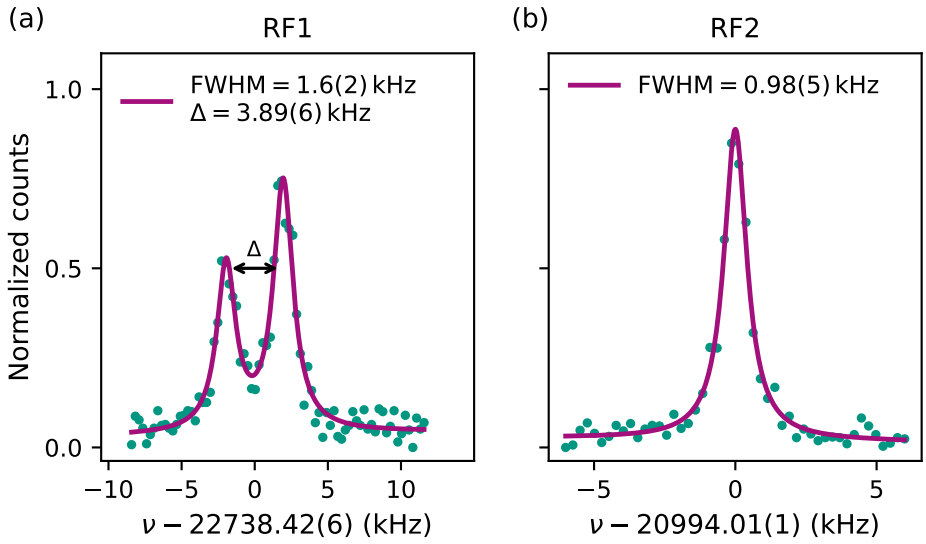

Figure 5.4.: Optically detected nuclear magnetic resonance spectra measured at an external dc magnetic field of $B_{dc} = 60\,\text{mT}$ along the quantization axis of the SnV center. The measurement is carried out by chirping the RF frequency across the resonance at −23 dBm while continuously driving MW1 at −19 dBm together with the spin-conserving optical transition B2 (for RF1) or A1 (for RF2). RF1 shows a signature of coupling to an additional ^{13}C nuclear spin, as described in the main text.

^{13}C with the SnV center's electron spin [146], which can increase the bare dipole-dipole coupling by several times [152, 171]. This effect will be discussed in more detail in the following section.

5.4. Radio-frequency control of the nuclear spin

The ability to initialize into a single electro-nuclear spin sub-state, combined with knowledge of its transition frequency, allows for coherent control of the nuclear spin. In this chapter we closely follow the work presented in our Ref. [71]. We begin by performing Rabi and Ramsey measurements on the RF transition in Subsection 5.4.1. To quantify the quality of the coherent control, randomized benchmarking is performed in Subsection 5.4.2. Finally, the coherence time of the nuclear spin is characterized: first under dark conditions in Subsection 5.4.3, and then under optical illumination in Subsection 5.4.4, to evaluate its suitability as a quantum memory while probing the electron spin.

5.4.1. Rabi and Ramsey measurements

Figure 5.5(a) displays a Rabi chevron pattern centered at a frequency of $\omega_{rf} = 20.998\,\text{MHz}$. The measurement is performed by first initializing the system into $|\uparrow_e\uparrow_n\rangle$ via MW2, then driving the transition to the bright state $|\uparrow_e\downarrow_n\rangle$ with RF pulses at frequency RF2 of varying duration and detuning, under a magnetic field of $B_{dc} = 60\,\text{mT}$ aligned along the SnV axis.

At an RF input power of $P = 10\,\mathrm{dBm}$, a Rabi frequency of $\Omega = 12.93(7)\,\mathrm{kHz}$ is achieved. The pattern shows clean oscillations; the counts are normalized to the maximum count rate and the color range is limited to 80% of the maximum counts to ensure good readability.

In Fig. 5.5(b), a Ramsey sequence of the same nuclear transition is performed to characterize the coherence and frequency stability of the nuclear-spin transition, varying the detuning around 20.53 MHz.

For this and all subsequent measurements, a magnetic field of $B_{\mathrm{dc}} = 106\,\mathrm{mT}$ was chosen to further separate the optically allowed transitions and avoid cross-pumping. Nevertheless, we plot both measurements in one figure with a shared y-axis of the detuning to illustrate the physical connection between a Rabi and a Ramsey measurement. On resonance, corresponding to the middle continuous line in Fig. 5.5(b), the slowest Rabi oscillations with the highest contrast are observed. Further away from resonance, the Rabi oscillations become faster with decreasing contrast. However, even at the highest detunings shown, the contrast is still clearly visible. This depends on the strength of the Rabi frequency relative to the detuning. If the Rabi frequency is strong enough, one can select a $\pi/2$-pulse from the Rabi oscillation and measure Ramsey fringes even at larger detunings. As before, a visibility measurement provides a direct readout of the nuclear-spin state population: each sequence is repeated with a 180° phase shift on the second $\pi/2$ pulse, and the visibility is extracted in the same manner as described in Sec. 4.3. The full Ramsey chevron measurement spans a total acquisition time of four days and reveals no significant frequency jumps of the nuclear transition.

A sinusoidal frequency determination by fitting a Ramsey decay at a fixed detuning is much more accurate than the ODNR measurement discussed in Sec. 5.3 and much faster than searching for the slowest Rabi frequency. Thus, a typical measurement cycle after performing an ODNR measurement proceeds as follows: a Rabi measurement at the ODNR frequency is carried out to find a rough $\pi/2$-pulse duration, followed by a Ramsey measurement with an arbitrary detuning, e.g. 3 kHz above the ODNR frequency. After determining the exact transition frequency, a final Rabi measurement is performed to find the on-resonance π-pulse duration for all subsequent measurements.

Dephasing time T_2^*. In order to measure the coherence of the system, the free induction time τ during the Ramsey sequence is increased until the system completely dephases, i.e. the visibility goes to zero. This can be done for a single detuning or for all detunings as shown in Fig. 5.5(b). In fact, this figure is just a cutout of Fig. 5.6(a).

Each oscillation trace is fitted to a sinusoid multiplied by an exponential decay $\exp[-(t/T_2^*)^{\xi}]$, where here $t = \tau$, yielding the dephasing time T_2^*. As discussed in Sec. 3.2.2 and Sec. 3.3, the stretching factor provides insight into the bath correlation time. For short correlation times, e.g. frequency-independent white noise, one would expect a mono-exponential decay with $\xi = 1$. We do not expect phonons to couple directly to the nuclear spin [65, 172], as it has no quadrupole moment due to its spin 1/2 [86].

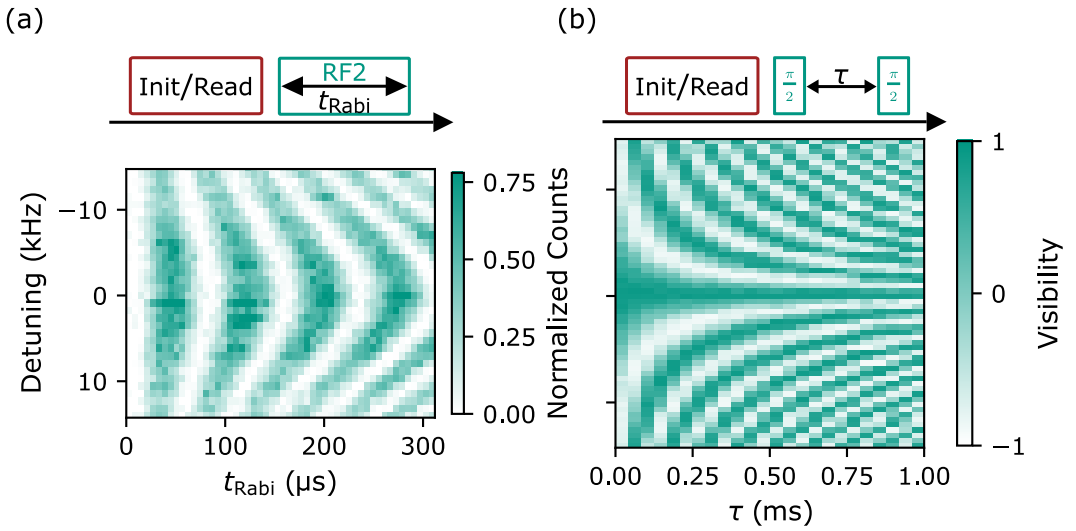

Figure 5.5.: Chevron patterns of the nuclear transition frequency RF2. (a) Chevron pattern of Rabi oscillations for various detunings at an external dc field of $B_{\mathrm{dc}} = 60\,\mathrm{mT}$ along the quantization axis of the SnV center. (b) Chevron pattern observed by detuned Ramsey measurements at $B_{\mathrm{dc}} = 106\,\mathrm{mT}$ showing the stability of the qubit frequency.

We also expect $\xi = 1$ for a single spin bath with short correlation times τ_c compared to the free evolution time t. For correlation times much longer than the free evolution time, we expect a Gaussian decay with $\xi = 2$. Electronic noise or paramagnetic surface spins give rise to $1/f$-noise, which also yields $\xi = 2$ [173]. We therefore restrict our stretching factor to the range between 1 and 2. We find an average stretching factor of 1.9(1) in good agreement to reported stretching factors [66]. Accordingly in our Ref. [71] all fits were performed with a fixed $\xi = 2$, as expected for slow shot-to-shot noise. Here, we retain the freedom to fit with a varying exponent.

In addition, we can treat the detuning differently. If we assume the detuning to be fixed, i.e. use the set parameters and do not allow it to vary in the fit, we find $\sim$ 12% smaller coherence times on average. However, as can be seen in Fig. 5.6(a), there are horizontal cuts visible that correspond to small jumps in frequency. These small deviations of the detuning over the course of the measurement are plausible, as the total measurement duration was approximately 100 h.

The shift in detuning might not be directly visible in the time-domain data, and we therefore plot the Fourier transform of the Ramsey data in Fig. 5.7 alongside the set detuning versus the frequency obtained from the Fourier transform. This yields straight lines, as one would expect. Fitting two linear slopes to both branches gives slopes close to unity, confirming that the oscillation frequency indeed scales linearly with the set detuning. The offset of each line of $\sim$ 200 Hz is simply a fixed offset from when the frequency range of the measurement was set up. More important are deviations from the linear slope, as these quantify the change in frequency relative to the expected detuning. Taking the standard deviation of the difference between the maximum of each row and the corresponding linear fit value, we find a mean deviation of $\sim$ 180 Hz. Tracking the frequency deviation for each sinusoidal fit yields the same mean deviation.

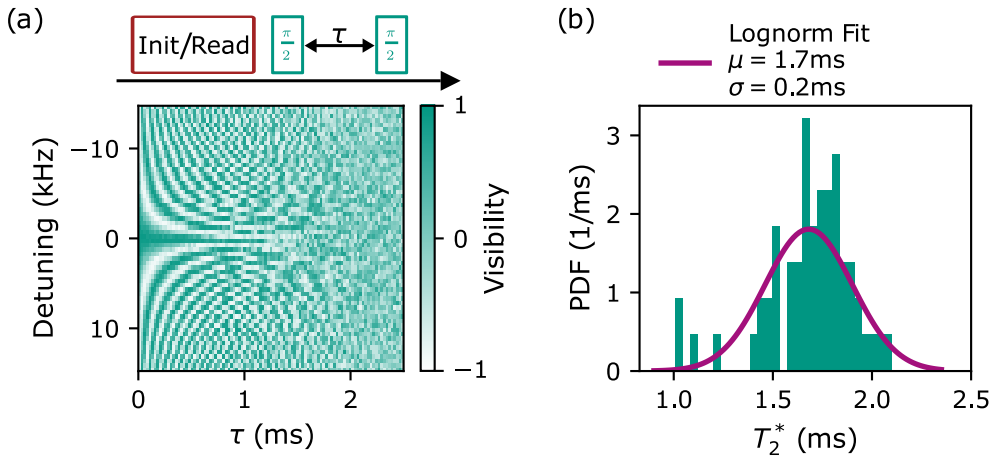

Figure 5.6.: Dephasing of the nuclear spin qubit. (a) Ramsey measurements of RF2 for varying detunings up to a waiting time of 2.5 ms. (b) Histogram of all coherence times for varying detunings leading to a mean coherence time of 1.7(2) ms.

Collecting the fitted coherence times across all detunings produces a histogram with a mean dephasing time of $\bar{T}_2^* = 1.7(2)$ ms as shown in Fig. 5.6(b). We use a log-norm distribution to include the skewed distribution of coherence times to smaller values. The mean value here is slightly higher due to the different fitting procedure, but is in the standard deviation of the reported value in our Ref. [71].

From this coherence time we can calculate the ODNR linewidth to be $\sqrt{2}/(\pi T_2^*) = 265(3)$ Hz [145], which is roughly a factor of four times smaller than the observed linewidth in Fig. 5.4(b).

The fitted scattering of detunings of $\sim$ 180 Hz, indicates slow frequency jumps from measurement to measurement over the course of hours. The width of each peak in Fig. 5.7, i.e. each peak in each row, reflect the shot-to-shot noise during a repeated Ramsey sequence and we find a width of $\sim$ 800 Hz, which agrees with the expect bath coupling of $b = \sqrt{2}/T_2^* = 830(97)$ Hz. This makes sense as the spectral resolution of the Fourier transform is limited by the total acquisition time, which is itself bounded by the coherence time T_2^* as the Ramsey signal decays on this timescale. Consequently, the FFT peak width scales with $1/T_{\text{max}} \sim 1/T_2^*$ and is approximately equal to the intrinsic T_2^* linewidth. So the FFT plot shows that our system behaves as expected, and the sinusoidal fit of each row gives us the reliable quantities of the system.

Extended Rabi driving. In order to study the power dependence of the Rabi frequency, we measure Rabi frequencies at varying driving powers. Using the power calibration from Eq. 4.4, we can convert the input power to the cryostat P to an ac magnetic field along the z-axis of the lab frame. For the electron spin this was sufficient, as all the angle dependence was captured by the parameter Λ defined in Eq. 2.73. Here we assume that the ac magnetic field perpendicular to the SnV center's quantization axis is driving the nuclear spin. More precisely, it should be the field perpendicular to the new eigen-axis of the hyperfine-coupled system. As discussed in Sec. 5.1, the tilt angle lies in the plane

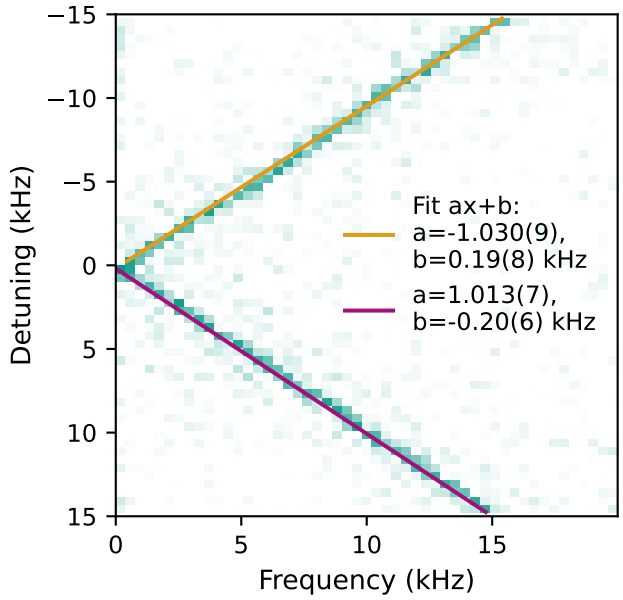

Figure 5.7.: FFT spectrum of individual Ramsey lines. Each row of the Ramsey fringe pattern was Fourier transformed independently. The peak frequency tracks the applied detuning linearly, with independent linear fits to the negative (orange) and positive (red) detuning branches yielding slopes consistent with unity.

spanned by the SnV center's quantization axis and the nuclear spin position. Since we do not know which of the six lattice sites the nuclear spin occupies, we cannot calculate the tilt angle with respect to the ac magnetic field. For small angles this does not change the result significantly; only if the nuclear spin were to tilt the new quantization axis heavily towards the z-lab axis would this lead to a large overestimation of the perpendicular field. The Rabi frequency for a given ac magnetic field is given by

$$\Omega = \frac{\gamma_{^{13}\mathrm{C}}}{2} \xi B_{\mathrm{ac},\perp}\,, \tag{5.25}$$

where ξ is an enhancement factor [146, 174]. The factor $1/2$ accounts for the linearly polarized microwave field, of which only the co-rotating circular component drives the nuclear spin.

This enhancement of the driving field arises due to the strong coupling to the electron spin. This effect was discussed for a ^{13}C nuclear spin strongly coupled to a NV center by Childress *et al.* [146]. The authors state that the non-secular terms as well as dipole interactions mix the electron-spin levels, introducing electronic character into the nuclear spin levels and thus enhancing the effective magnetic moment. They observed this effect as an enhanced nuclear Larmor precession for nearby ^{13}C nuclear spins. As the magnetic moment is also the quantity that couples to the ac magnetic field, an enhancement of the Rabi frequency compared to free ^{13}C nuclear spins is expected. They further state that this enhancement is anisotropic and maximal when the external dc magnetic field is aligned perpendicular to the quantization axis of the NV center. Since we operate with an aligned

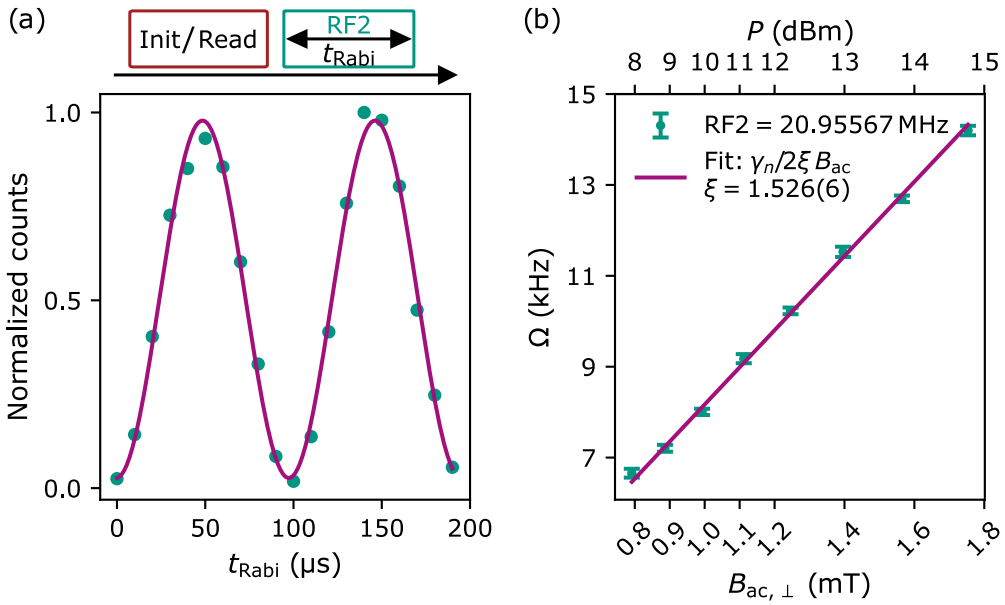

Figure 5.8.: Power dependence of the nuclear Rabi oscillations. (a) Single Rabi oscillation at a power of $P = 11.5\,\mathrm{dBm}$ showing a Rabi frequency of $\Omega/2\pi = 10.2(1)\,\mathrm{kHz}$. (b) Rabi frequency as a function of the applied ac magnetic field. The corresponding power is shown at the top label. These measurements were performed by Tim Bohn during his Master's thesis under the shared supervision of Ioannis Karapatzakis and myself.

magnetic field, the non-secular terms vanish, and we also expect the lowest enhancement in this field configuration.

Ref. [86] give a classical explanation for this phenomenon. The oscillating ac field is much slower than the Larmor precession of the electron spin, so that the electron spin follows the ac field adiabatically. This leads to a modulation of the hyperfine field generated by the electron at the RF driving frequency, which in turn produces an enhanced driving field. In general, this enhancement can be calculated if the hyperfine tensor is known. For an isotropic hyperfine coupling, one would expect an enhancement of $\sim A_{\mathrm{FC}}/\omega_{\mathrm{L}}$ [86].

We set the driving field to the component perpendicular to the SnV center's quantization axis, giving $B_{\mathrm{ac},\perp} = B_{\mathrm{ac,z-lab}}\cos(35.3°)$. As discussed above, varying this angle leads to different enhancements ξ for a fixed measured Rabi frequency Ω. One can immediately see that shifting this angle by $+54.7°$ leads to a divergence of the enhancement factor. However, as we expect the tilt of the quantization axis with respect to the lab-frame axis to be small, we proceed with this field orientation. We thus use our calibration of the ac magnetic field to estimate the enhancement.

Figure 5.8(a) shows an example Rabi measurement at a power of $P = 11.5\,\mathrm{dBm}$, resulting in a Rabi frequency of $\Omega/2\pi = 10.2(1)\,\mathrm{kHz}$. This measurement and the subsequent measurements shown in Fig. 5.8 were performed by Tim Bohn during his Master's thesis under the shared supervision of Ioannis Karapatzakis and myself. Varying the power leads to a linear increase of the Rabi frequency with the ac field. The deviation of the linear fit from the bare gyromagnetic ratio of $\gamma_{^{13}\mathrm{C}} = 10.71\,\mathrm{kHz\,mT^{-1}}$ (see Eq. 5.25) yields

an enhancement factor of $\xi = 1.526(6)$. This measurement is much more precise than the single-oscillation estimation in our Ref. [71] but agrees with the reported value at a much smaller uncertainty. This value is much smaller than enhancement factors reported for proximal ^{13}C nuclear spins coupled to NV centers in diamond were weak external magnetic fields perpendicular to the nuclear spins quantization axis were used [146, 175].

In order to quantify how long we can drive the nuclear spin without heating the system, we measure Rabi oscillations with as many π-rotations as possible. For these long-duration Rabi measurements, a visibility metric is employed to compensate for slow drifts of the emitter over the course of the acquisition. This is achieved by recording two interleaved Rabi traces with different pulse lengths: the second trace uses a pulse duration extended by exactly one additional π-pulse length, effectively introducing a 180° phase shift. The visibility is then computed as $V = (S_0 - S_{180})/(S_0 + S_{180})$, where S denotes the integrated fluorescence collected during the readout pulse for each of the two sequences. As shown in Fig. 5.9(a), high-quality Rabi oscillations are sustained for up to 9.5 ms without any loss of contrast, corresponding to 138 π-pulses. This was limited only by the total measurement time and increasing noise in the visibility due to the slow spatial drift of the emitter out of the confocal focus, as the total acquisition time was 18 h. This can be easily mitigated by simple refocusing sequences. During the measurement, the emitter lost its charge state but was recovered by a 532 nm laser pulse. The qubit frequency remains close to its value before green-laser pumping, allowing it to be driven with the same applied microwave tone. This can be seen in the FFT in Fig. 5.9(b), where a single sharp resonance at $\sim$ 7.3 kHz is present. Fitting both Rabi oscillations separately yields a change in the fitted Rabi frequencies from 7.263(2) to 7.305(3) kHz, which can be attributed to a detuning of $\Delta = 826(30)$ Hz, on par with the slow spectral diffusion discussed above. We do not believe the green laser pulse itself causes the detuning, as we observe this also in measurements without a green laser pulse. We therefore expect slow spectral diffusion of this order of magnitude to be responsible for the detuning over the course of the measurement.

This preservation of the visibility contrast demonstrates that the superconducting waveguide can deliver extended continuous RF driving without introducing heating, which is a common limitation in many experimental platforms [63, 65, 144].

Here, a power of $P = 10.55$ dBm, corresponding to a field of $B_{\mathrm{ac},\perp} = 1.36$ mT, is used to drive the RF2 transition at $\omega_{\mathrm{rf2}} = 20.53$ MHz. This yields a notably smaller enhancement factor of $\xi = 1.23$ compared to the data in Fig. 5.8 at the same external magnetic field of 106 mT along the SnV quantization axis.

To determine whether this difference in enhancement correlates with the shift in resonance frequency or is simply due to measurement noise, we fit a large number of Rabi oscillations across multiple cool-downs, tracking both the resonance frequency and the enhancement factor. The results are compiled in Fig. 5.10. Each data point represents the mean of repeated measurements at a fixed frequency, with error bars obtained by adding the fit uncertainty and shot-to-shot scatter in quadrature. In total, 18 measurements spanning approximately 1.5 years are included. The dashed line and shaded band indicate the overall weighted mean and its uncertainty, shown for comparison with the value reported in

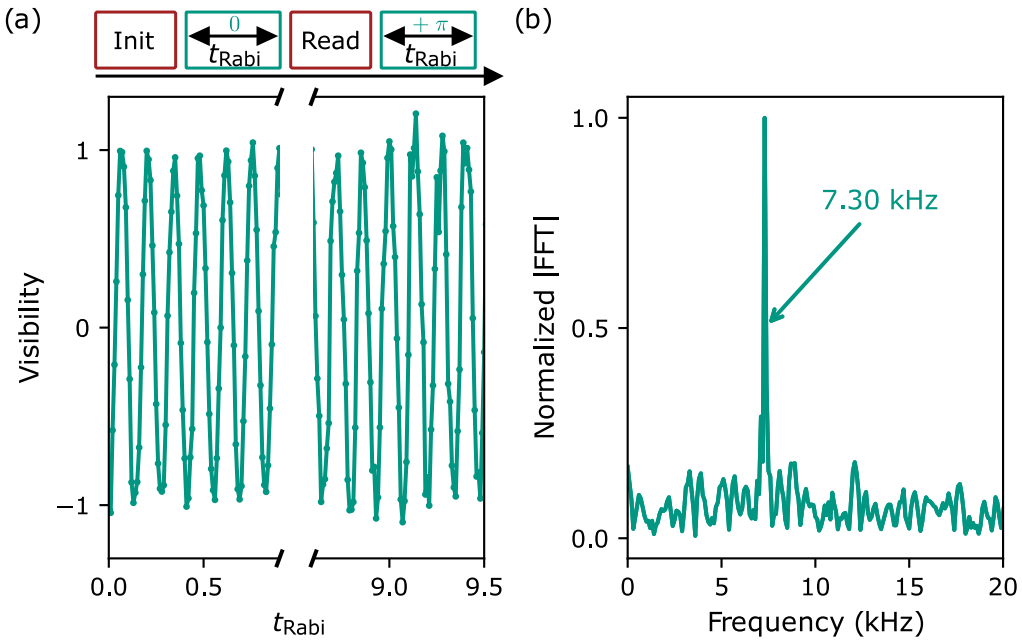

Figure 5.9.: Extended Rabi driving up to 138 π pulses. (a) Interleaved Rabi traces acquired with different pulse lengths. For the second trace, the pulse duration is increased by exactly one additional π-pulse length, effectively introducing a 180° phase shift. The visibility is then calculated as $V = (S_0 - S_{180})/(S_0 + S_{180})$, where S denotes the integrated fluorescence collected during the readout pulse for each sequence. The line breaks are added for better readability. During the measurement, the emitter lost its charge state but was recovered using a 532 nm repump pulse. (b) Fourier transform of the full Rabi trace, showing a single dominant frequency.

Ref. [71]. The two differ slightly owing to the different amount of data included in each mean value estimation.

As discussed above, the enhancement is governed by the relative orientation of the ^{13}C magnetic moment and the B_{ac} field. At the low dc fields used here, the pseudo-secular coupling to the electron spin dominates and sets the precession axis of the ^{13}C spin. In the limit of very strong dc fields, the Rabi frequency is expected to approach that of a free ^{13}C nuclear spin. To map out this behavior, we measure the enhancement as a function of dc magnetic field strength along the SnV quantization axis.

In contrast to Fig. 10 in Ref. [71], only data acquired during a single cooldown are used here to ensure consistency. These measurements were performed by Mohamed Elshorbagy during his Master's thesis under my supervision.

The Rabi frequency data shown in Fig. 5.11(b) are normalized to the applied ac field $B_{ac,\perp}$ using the same calibration as above, yielding an enhancement factor as a function of the external dc magnetic field. A maximum enhancement of the RF2 transition of $\xi(106\,\mathrm{mT}) \sim 1.9$ is observed, corresponding to a nuclear Rabi frequency roughly twice the free-spin value for a given ac magnetic field. This free-spin reference is indicated by the horizontal black line at $\xi = 1$. Notably, the enhancement at $B_{dc} = 106$ mT reaches this maximum when the resonance frequency coincides with the value obtained at $B_{dc} = 60$ mT,

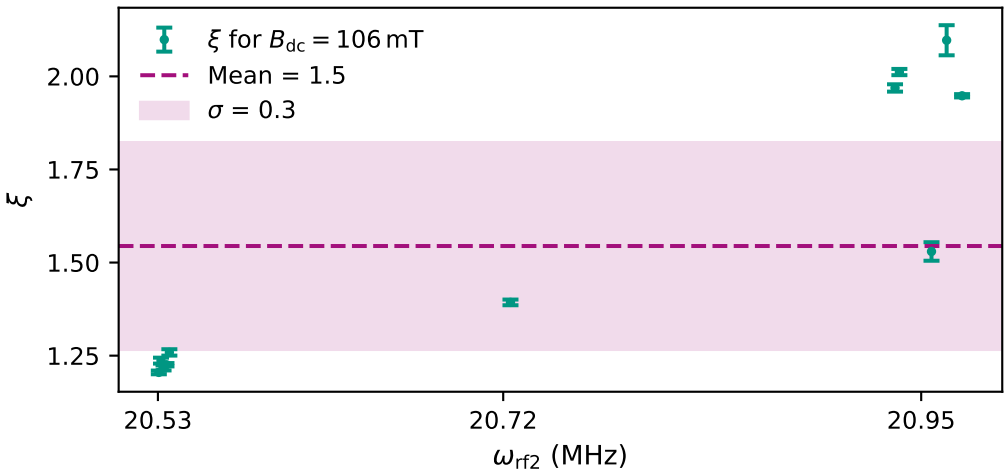

Figure 5.10.: Measured enhancement of the gyromagnetic ratio using the Rabi frequency as a function of RF drive frequency. Each point represents the mean over repeated measurements at a fixed frequency, with error bars combining the fit uncertainty and shot-to-shot scatter. The dashed line and shaded band indicate the overall weighted mean and its uncertainty to relate to the reported values in Ref. [71]. Overall 18 measurements over the course of 1.5 years are evaluated.

i.e. $\omega_{rf2} \sim 21\,\mathrm{MHz}$. A theoretical prediction for the enhancement, adapted from the NV center framework [174], is given by

$$\xi = \left(\frac{A_{\perp}^{\mathrm{enh}}}{\gamma_{^{13}\mathrm{C}} B_{\mathrm{dc}}} + 1 \right) \chi \,, \tag{5.26}$$

where $A_{\perp}^{\mathrm{enh}}$ is the hyperfine component relevant for the enhancement. The parameter $\chi = \cos(\theta_{\mathrm{HF}})$ describes an additional tilt of the nuclear spin quantization axis, with an arbitrary angle of $\theta_{\mathrm{HF}} = 54.7°$. Choosing a tilt angle different from the expected 35.3° allows for enhancement factors below unity, as the effective ac field is overestimated in the calculation of the enhancement factor.

In our Ref. [71], we described this behavior differently and noted that the nuclear Rabi frequency is determined by the relative orientation of the ^{13}C magnetic moment and the applied ac field B_{ac}. At low dc fields, the pseudo-secular hyperfine coupling dominates and defines the precession axis of the ^{13}C spin. With increasing dc field strength, this axis progressively tilts toward the external field direction, which in the present experiment coincides with the SnV quantization axis. Depending on the spatial position of the ^{13}C spin relative to the SnV center, this tilt can align the precession axis with the B_{ac} field orientation, producing a local minimum in the Rabi frequency at intermediate fields. Only in the limit of very strong dc fields is the Rabi frequency expected to converge to that of a free ^{13}C nuclear spin.

The resulting theoretical prediction for ξ following the first approach is shown as the light dashed line in Fig. 5.11(b) and shows reasonable agreement with the data, serving as a useful guide to the eye. Since the exact tilt of the nuclear spin's quantization axis in the lab

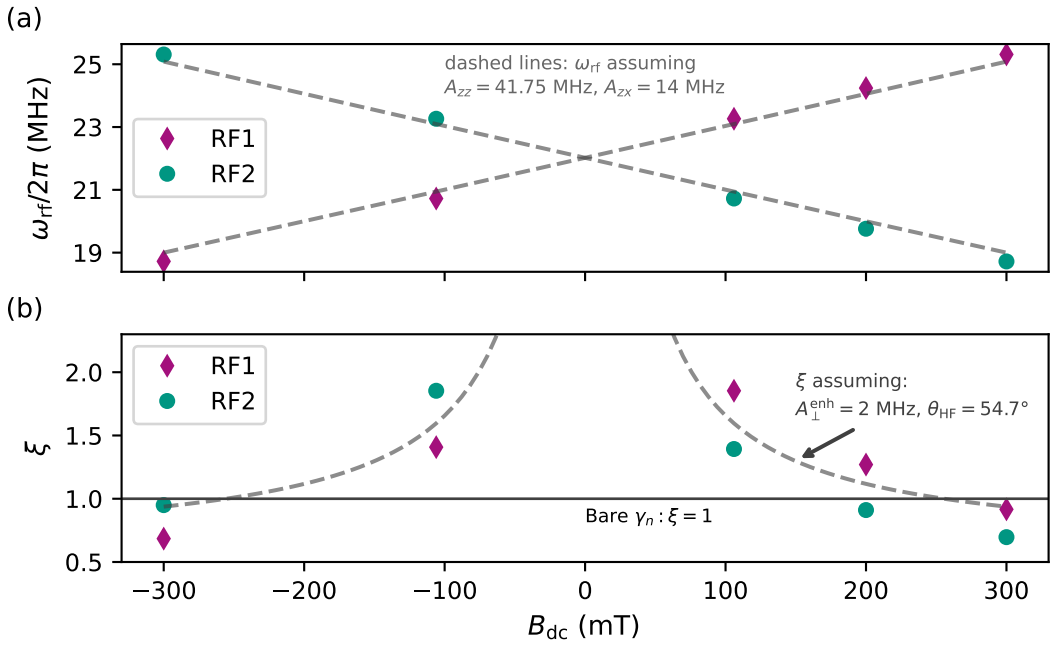

Figure 5.11.: (a) Radio-frequency transition frequencies $\omega_{rf}/2\pi$ for RF1 and RF2 as a function of the applied dc magnetic field B_{dc} along the SnV quantization axis. Dashed lines show the expected dependence following Eq. 5.13, assuming $A_{zz} = 41.75$ MHz and $A_{zx} = 14$ MHz. (b) Enhancement factor ξ of the nuclear Rabi frequency for both transitions as a function of B_{dc}. The horizontal line at $\xi = 1$ marks the bare ^{13}C gyromagnetic ratio, corresponding to the free-spin Rabi frequency. The dashed line shows a theoretical prediction adapted from the NV center framework, assuming $A_{\perp}^{enh} = 2$ MHz. A maximum enhancement of $\xi \sim 1.9$ is observed near $B_{dc} = 106$ mT, while the enhancement decreases below unity at higher fields as the nuclear precession axis tilts toward the external field direction. All data were acquired during a single cooldown.

frame, itself a function of A_{zz}, ω_L, and A_{zx}, is not independently known, the enhancement data alone cannot be used to fit the hyperfine parameters. Also, the parameter $A_{\perp}^{enh}$ describes the non-secular behavior of the hyperfine interaction (see Sec. 5.1) as it describes an electron spin flip followed by an electron-nuclear spin flip-flop [146, 174]. This is different to the pseudo-secular coupling A_{zx}, which only describes an nuclear-spin flip in the secular approximation.

As shown in Fig. 5.11(a), the two transition frequencies vary with the applied dc magnetic field following Eq. 5.13. Despite the data being collected within a single cooldown over the course of one month, we are unable to extract the hyperfine parameters from a fit, as the variation in the hyperfine coupling is of the same order of magnitude as the Larmor precession, a prerequisite for achieving reasonable fit uncertainties. We therefore assume the DFT value $A_{zx} = 14$ MHz (see Sec. 5.1) as a purely illustrative value to gain qualitative insight into the field-dependent behavior. However, adopting this value for A_{zx}, one can choose A_{zz} such that it reproduces the linear trend in Fig. 5.11(a). This choice also satisfies the relation $\Delta_{ODMR} = 45$ MHz $\approx \sqrt{A_{zz}^2 + A_{zx}^2}$ and we pick a value of $A_{zz} = 41.75$ MHz.

More generally, A_{zz} can be determined from the transition frequencies via the relation

$$\omega_{rf2}^2 - \omega_{rf1}^2 = -2\gamma_{^{13}C} A_{zz} B_{dc} . \tag{5.27}$$

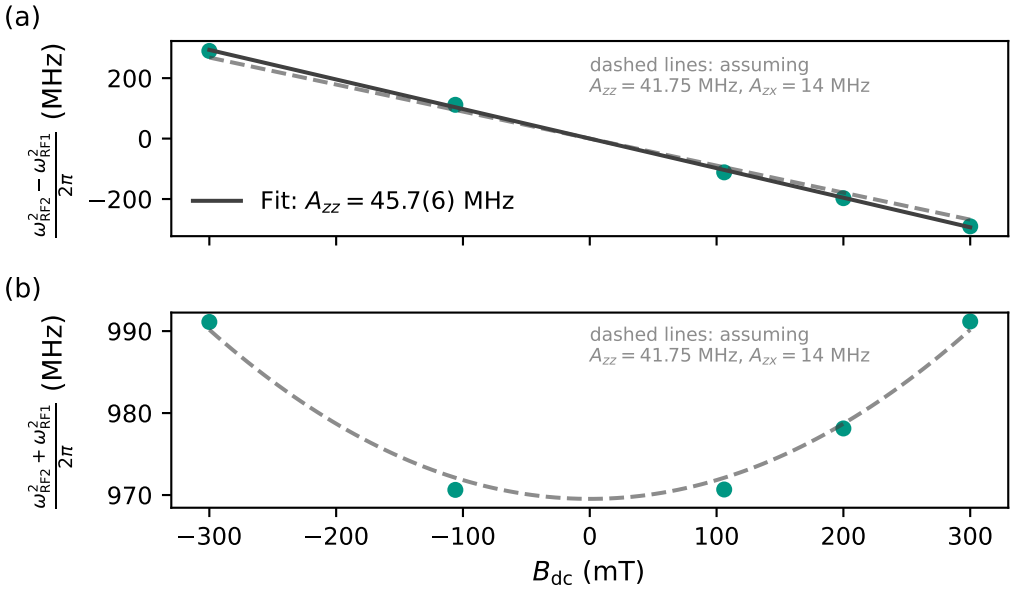

Figure 5.12.: Difference of the squared nuclear transition frequencies and their connection to the hyperfine parameters. (a) Difference of the squared transition frequencies $(\omega_{rf2}^2 - \omega_{rf1}^2)/2\pi$ as a function of the applied dc magnetic field B_{dc}. The linear dependence allows extraction of the secular hyperfine parameter via $\omega_{rf2}^2 - \omega_{rf1}^2 = -2\gamma_{^{13}C} A_{zz} B_{dc}$, yielding $A_{zz} = 45.7(6)$ MHz. (b) Sum of the squared transition frequencies $(\omega_{rf2}^2 + \omega_{rf1}^2)/2\pi$ as a function of B_{dc}. In both panels, dashed lines show the expected dependence assuming $A_{zz} = 41.75$ MHz and $A_{zx} = 14$ MHz. The parabolic minimum in (b) is sensitive to both A_{zz} and A_{zx}; however, a consistent fit of both parameters from (a) and (b) simultaneously is not achieved without assuming a nonphysical offset in the magnetic field calibration, likely due to the limited sensitivity of the measurements and higher-order contributions from the unknown A_{xx} and A_{yy} components.

By measuring the transition frequencies as a function of the applied dc field, the excess slope directly yields A_{zz}. This is shown in Fig. 5.12(a), where the fit gives $A_{zz} = 45.7(6)$ MHz. Using the complementary relation

$$\omega_{rf2}^2 + \omega_{rf1}^2 = 2\gamma_n^2 B_{dc}^2 + 2\left(\frac{A_{zx}}{2}\right)^2 + 2\left(\frac{A_{zz}}{2}\right)^2, \tag{5.28}$$

one can attempt to fit the data shown in Fig. 5.12(b). However, using the A_{zz} value obtained by the fit produces values that are too large to describe the minimum of the parabola even for a vanishing pseudo-secular component. Assuming a magnetic field calibration that is approximately 4% too high would allow both A_{zz} and A_{zx} to be fitted simultaneously with reasonable values. This offset is not supported by the data: comparing the measured electron spin splittings with the theoretical g factor (see Eq. 2.41) suggests that the field is, if anything, about 2% smaller than expected. Even incorporating data from additional cooldowns, the measurements are neither sufficiently sensitive nor well-calibrated enough to extract these parameters with meaningful precision. Furthermore, the unknown A_{xx} and A_{yy} components contribute to the transition frequencies at higher order [164], adding further uncertainty. By forcing $A_{zx} = 14$ MHz, we can fit A_{zz} to the parabola in Fig. 5.12(b) and thus obtain the value of $A_{zz} = 41.75$ MHz. As we can obtain similar matching data

for varying combination of hyperfine coupling strengths, we can therefore only provide a qualitative estimate.

A more systematic determination could be achieved by measuring ratios of transition probabilities as well as ratios of Rabi frequencies for the two transitions as a function of an off-axis dc magnetic field, which would provide additional constraints on the remaining hyperfine parameters. Such an approach was employed by Rao and Suter [164] for a nearest-neighbor ^{13}C nuclear spin coupled to an NV center in diamond. Adapting this method to the present system would require extending the second-order perturbation theory developed for a spin-1 system to the spin-1/2 case of the SnV center. By extending such measurements to three-dimensional angular dependence, this technique should enable a precise determination of the full hyperfine tensor between the SnV center and the proximal ^{13}C spin [146, 164]. While a complete quantitative extraction of the tensor components is beyond the scope of the present data, our measurements nonetheless allow qualitative conclusions regarding the effects of the hyperfine interaction, such that the enhancement factors are reasonable as long as the hyperfine quantization axis does not coincide with the lab z-axis, in which case much higher enhancement factors would result out of the measured data.

5.4.2. Single-qubit gate fidelity via randomized benchmarking

While achieving long coherence times T_2^* and fast Rabi frequencies is essential, it is equally important that qubit operations can be performed with sufficiently low gate errors. As discussed in Sec. 3.4, a first intuitive measure of gate quality is the Rabi quality factor, defined as the number of π-rotations before the Rabi contrast decays to $1/e$ of its initial value. However, this metric alone does not capture the full picture: since practical gate sequences involve arbitrary rotation angles and axes, the qubit transiently occupies superposition states during operations and thus maintains some sensitivity to T_2^* even in the fast-driving regime.

To rigorously quantify the average error per gate, we employ randomized benchmarking [136, 137]. In this protocol, sequences of randomly chosen gates of increasing length are applied, and after each sequence the corresponding inverse operation is appended. Measuring the fidelity with respect to the initial state as a function of sequence length then yields the average gate infidelity. The randomization over gate sequences is crucial, as it averages over errors that may be correlated with specific pulses or subsequences, providing an unbiased estimate of the gate error.

We work with the set of primitive gates $\mathcal{G} = \{I, \pm X, \pm Y, \pm X^2, \pm Y^2\}$, where X and Y denote 90°, i.e. $\pi/2$, rotations around the x- and y-axes of the qubit, X^2 and Y^2 are the corresponding 180° rotations, and I is the identity operation. The identity gate is implemented as a waiting period of equal duration to the X^2 pulse, mimicking the idle time that would occur during a nuclear-spin memory readout or state transfer in a practical quantum protocol.

For each sequence length N, a random selection of gates from $\mathcal{G}$ is drawn, and the inverse gate for the entire sequence is computed and appended as the final operation. For

simplicity, this is done in multiples of $N = 10n$ gates, where $n = 1, 2, ..., 15$. After each gate, an additional waiting time of $\tau_{\text{buf}} = 1\,\mu\text{s}$ is inserted; this is much shorter than all relevant timescales and can thus be neglected. The overall sequence starts with a delay of 5.12 µs as the AWG has a fixed minimum sample size for 1 GS/s. A larger buffer time between the gates would lead to higher dephasing errors, but can be used, if heating during the sequence becomes relevant [84]. As this is not the case for our system, we chose the buffer time to be very small. In contrast to Rosenthal *et al.* [84], our gates share not the exact amount of time $\tau_{\text{rmbm}} = \tau_{\text{gate}} + \tau_{\text{buf}} \neq \text{const.}$, but rather have two time sets $\tau_{\text{rmbm,1}} = \tau_\pi + \tau_{\text{buf}}$ or $\tau_{\text{rmbm,2}} = \tau_{\frac{\pi}{2}} + \tau_{\text{buf}}$ depending on wether an π-pulse or $\frac{\pi}{2}$-pulse was picked.

Once the full sequence is constructed, the inverse gate is calculated. For this we use a geometric approach based on Bloch-sphere tracking, following the ideas of Thomas Koch and Viktor Adam [138]: starting from a state vector at the north pole, each gate in the sequence is applied as a rotation around the corresponding axis. Since the final vector must point along one of the six cardinal directions of the Bloch sphere, determining which direction it points to immediately identifies the required recovery gate, which is a single primitive operation that returns the state to the north pole. This approach is computationally efficient, as it avoids the need to compute full matrix inversions.

To obtain a normalized visibility, each sequence is executed twice: once as constructed, and once with the phase of the final inverse gate shifted by 180°, effectively mapping the initial state to the south pole of the Bloch sphere. For each sequence length, 20 random realizations are generated in separate measurement runs to ensure a representative statistical distribution, i.e. a total of 24000 random gates, with each realization repeated 500 times to accumulate sufficient counting statistics. The resulting measurements are shown in Fig. 5.13(a) and were taken over the course of 10 h.

To ensure full traceability and enable post-hoc analysis, for instance, verifying the correctness of the computed inverse gate, the complete gate sequence for each randomized benchmarking run is stored alongside the measurement data. As a consistency check, the resulting distribution of gates shows a mean occurrence of 1/9 per gate, as expected from uniform random sampling (see Fig. 5.14). The peak at zero originates from pulse sequences in which the respective gate does not occur. This contribution is particularly pronounced for gate sets with a small total number of gates.

The mean visibilities, shown as data points in Fig. 5.13(a), are fitted by the function AP^N, where A is a constant pre-factor encoding the combined initialization and readout fidelity, P is the depolarizing parameter describing the fidelity per gate operation, and N is the number of gates. This assumes that we only have gate-independent errors [137]. We do not account for the error on the final inverse gate in P. Adding this gate, i.e. fitting to $N + 1$, does change the resulting fidelity per gate below the measurement uncertainty. Usually this inverse gate fidelity is absorbed into the constant pre-factor A [137]. The primitive gate fidelity is then extracted as

$$F_{\text{G}} = 1 - \frac{1 - P}{2}, \tag{5.29}$$

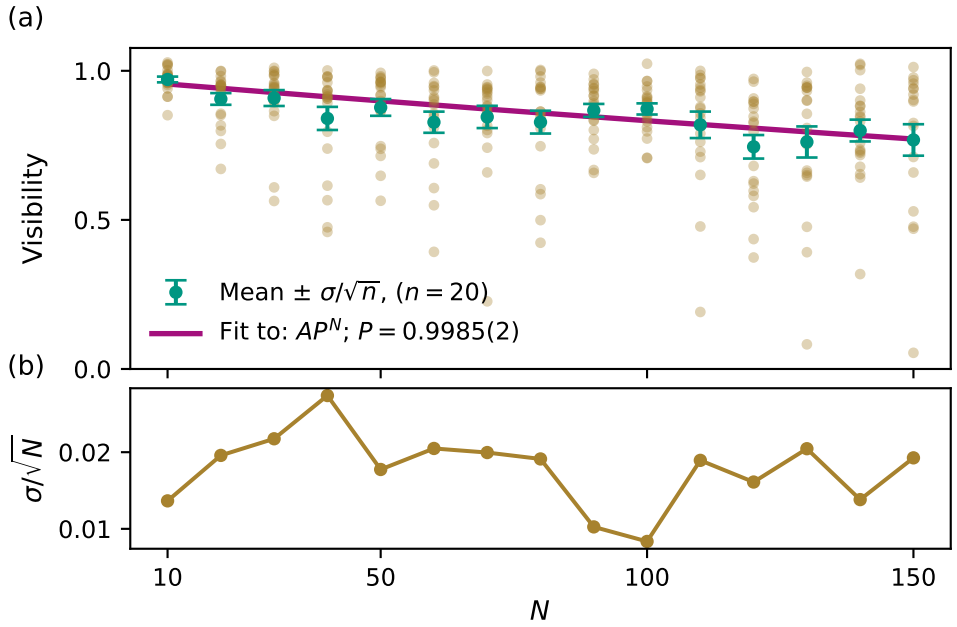

Figure 5.13.: Gate characterization. (a) Randomized benchmarking decay of the nuclear spin qubit. The visibility is plotted as a function of the number of primitive gates N. Individual randomized sequences are shown as faint points, while the mean over $n = 20$ sequences is indicated by markers with error bars denoting the standard error of the mean. The solid line shows a fit to AP^N, yielding a $P = 0.9985(2)$. (b) Standard deviation $\sigma/\sqrt{N}$ of the visibility across the randomized benchmarking sequences as a function of N showing no trend with increasing pulse number.

where the factor of $1/2$ accounts for the two sequences per visibility measurement [138]. The fit yields $A = 97(1)\,\%$ and $P = 99.85(2)\,\%$, resulting in an overall primitive gate fidelity of $F_\mathrm{G} = 99.92(1)\,\%$. The fidelity of A strongly depends on the background correction during the readout pulses and integration times. As the correlation between A and P is large, the fit is confirmed with A fixed to the initial visibility for 10 gates, yielding only differences smaller than the fit uncertainty. Not performing the background corrections of the readout leads to a reduced A but no significant change in P as expected.

Since a single Clifford gate consists, on average, of 1.875 primitive gates [138, 139], this can be converted to the more commonly reported single-qubit Clifford gate fidelity of $F_\mathrm{C} = 99.85(2)\,\%$.

The brown markers in Fig. 5.13(a) show individual randomized benchmarking sequences. The spread in visibility increases with the number of gates N, reflecting accumulated gate errors. To quantify this behavior, the standard deviation normalized by the square root of the number of gates, $\sigma/\sqrt{N}$, is plotted in Fig. 5.13(b). This quantity remains constant at increasing sequence lengths as expected of stochastic error accumulation, for which $\sigma \propto \sqrt{N}$, leading to $\sigma/\sqrt{N} \propto \sigma$.

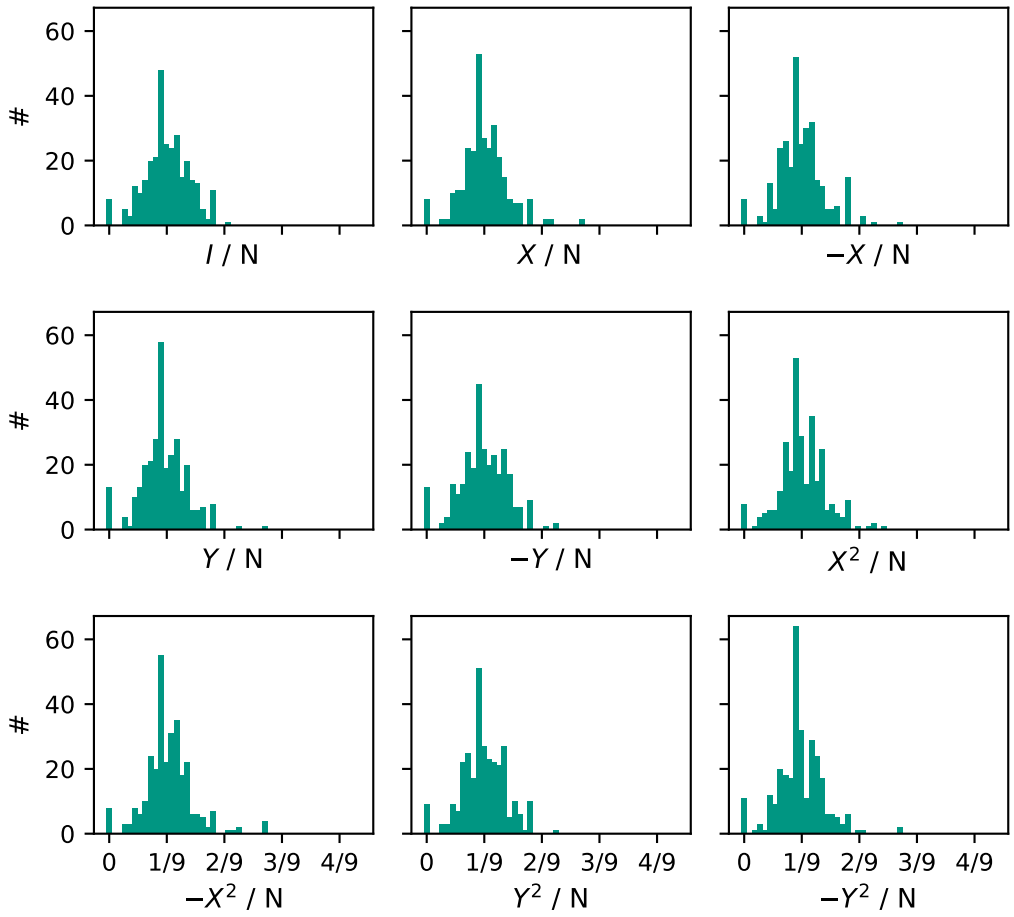

Figure 5.14.: Gate occurrences during the randomized benchmarking experiment. A total 24000 gates are performed by randomly picking from the primitive gate set. As this set contains out of 9 different possible gates, each subplot corresponds to the respective gate. Each gate is normalized by the total number of gates used in the sequence, such that the expectation value reflects the 1/9 probability to choose one of these gates. As can be seen in all subplots for each primitive gate a sufficient normal distribution around this theoretical expectation value is reached.

5.4.3. Dynamical decoupling of the nuclear spin

The high primitive gate fidelity of $F_G = 99.92(1)\,\%$ established above makes the nuclear-spin qubit a promising candidate for dynamical decoupling protocols, which rely on the repeated application of high-fidelity π-pulses to refocus environmental noise. As a first step, we employ a Hahn-echo sequence to probe the timescale of the dominant noise source. If the echo coherence time T_2 significantly exceeds the free-induction decay time T_2^*, this indicates that the dephasing is governed by slow, quasi-static fluctuations that can be effectively refocused, motivating the use of more advanced multi-pulse decoupling sequences.

As shown in Fig. 5.15, the Hahn-echo visibility decays following a stretched exponential $A\exp[-(t/T_2)^\xi]$, where $t = 2\tau$ is the total evolution time, A is the initial decoupling fidelity,

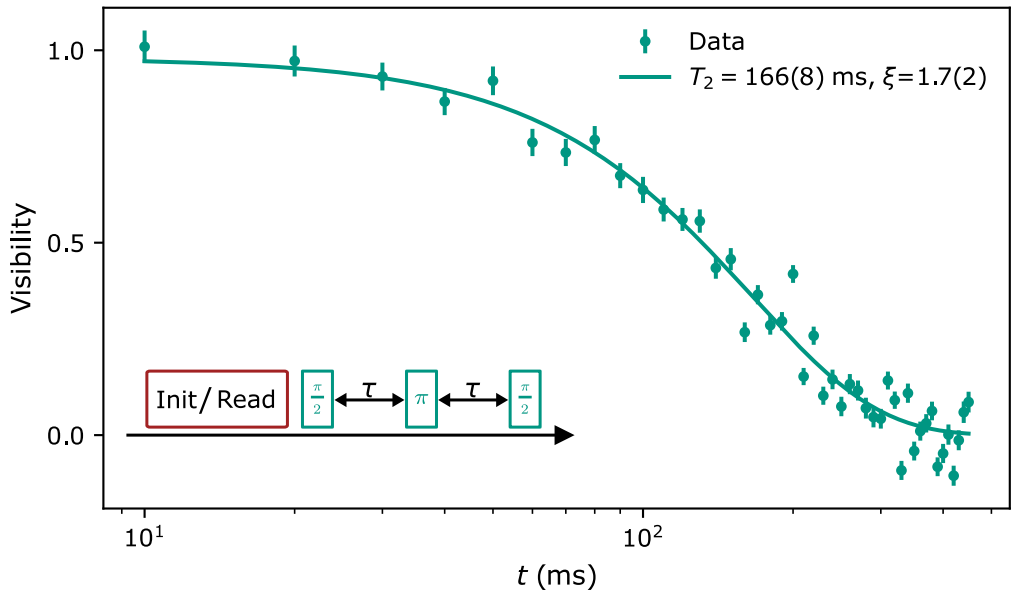

Figure 5.15.: Hahn-echo measurement of the nuclear-spin coherence time. The visibility decays following a stretched exponential yielding $T_2 = 166(8)$ ms and a stretching exponent $\xi = 1.7(2)$. The substantial improvement over the Ramsey dephasing time $T_2^* = 1.7(2)$ ms confirms that the dominant noise source consists of slow fluctuations that are effectively refocused by a single echo pulse. Within an Ornstein-Uhlenbeck model for the bath noise, these values correspond to a bath coupling strength of 830(97) Hz and a correlation time of $\tau_c = 260(70)$ s. The inset shows the pulse sequence.

T_2 is the coherence time, and ξ the stretching exponent. The fit yields $T_2 = 166(8)$ ms and $\xi = 1.7(2)$, representing a substantial improvement by two orders of magnitude over the Ramsey dephasing time of $T_2^* = 1.7(2)$ ms measured in Sec. 5.4.1. This confirms that the dominant noise source consists of slow fluctuations that are well refocused by a single echo pulse.

Assuming an Ornstein-Uhlenbeck model for the nuclear spin bath noise as discussed in Sec. 3.3, the coherence time yields a bath coupling strength of $\sqrt{2}/T_2^* = 830(97)$ Hz. The corresponding bath correlation time is $\tau_c = 260(70)$ s, which is lower than but comparable to recent results obtained for a single ^{13}C nuclear spin coupled to a GeV center [144].

Having established that the noise is predominantly slow, we extend the coherence further using a CPMG dynamical decoupling sequence, in which the decoupling π-pulses are phase-shifted by 90° relative to the initial $\pi/2$ pulse. For each number of decoupling pulses N, the interpulse delay τ is varied and the resulting visibility decay is fitted.

The coherence decay in Fig. 5.16 is well described by a stretched exponential with a mean stretching factor of $\xi = 2.0(1)$. In this figure, the total evolution time is given by $t = 2N\tau$. The variation of the stretching factor around its mean value is attributed to noise in the data. Fixing the stretching exponent to $\xi_{\text{fix}} = 2$ does not appreciably affect the quality of the fits or the extracted coherence times, and yields the same maximum coherence times.

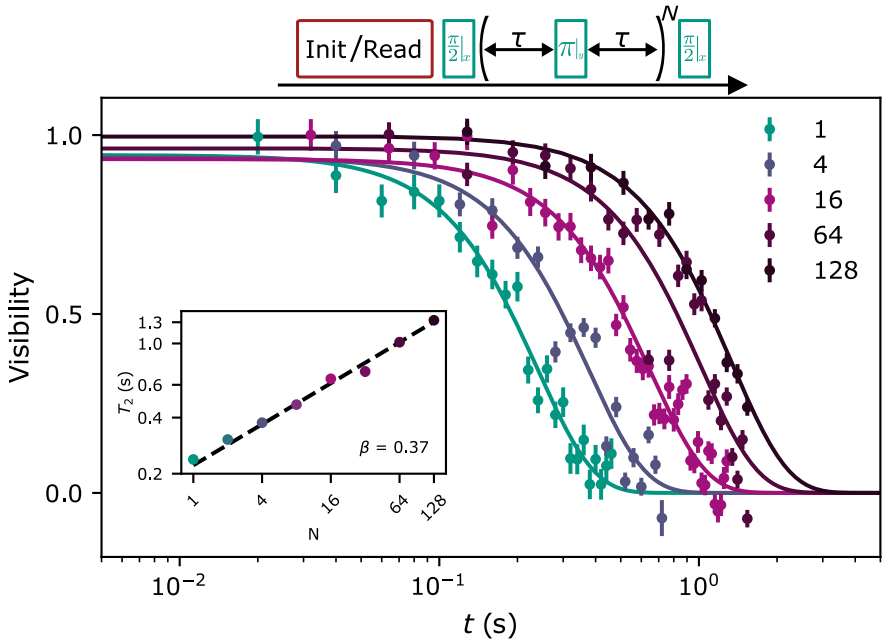

Figure 5.16.: CPMG measurement of the nuclear-spin coherence time. An initialization is followed by a $\pi_x/2{-}\tau{-}\pi_y{-}\tau{-}\pi_x/2$ sequence for a single refocusing pulse and subsequent readout. The visibility decays following a stretched exponential with a stretching factor of $\xi = 2$, yielding a maximum $T_2 = 1.35(3)$ s for $N = 128$ decoupling pulses. The inset shows the scaling of the coherence time with increase pulse number. The coherence follows the power law $T_2(1)N^{\beta}$, with $\beta = 0.37(2)$.

A single decoupling pulse yields $T_2(1) = 232(7)$ ms, and increasing the number of pulses progressively extends the coherence up to $T_2(128) = 1.35(3)$ s with 128 decoupling pulses. This value is not yet limited by the electron-spin lifetime. The electro-nuclear spin T_1 time was measured for a dc magnetic field aligned along the SnV axis using a simple pump-wait-probe sequence (see Sec. 5.4.4). No T_1-induced decay is observed on timescales up to 30 s, indicating that T_1 must be significantly longer. This is further supported by previous measurements reported in our Ref. [70], where an electron-spin $T_1 \sim 1$ s was measured at a temperature of $T = 1$ K for an unstrained emitter (Fig. 8(b) in that reference). Since the present experiment operates at slightly higher strain and a substantially lower temperature of $T = 50$ mK, we expect T_1 to exceed all timescales measured here by a wide margin.

The scaling of the coherence time with pulse number, shown in the inset of Fig. 5.16, follows a power law $T_2 \propto N^{\beta}$ with an exponent $\beta = 0.37(2)$. This is lower than the $\beta = 2/3$ scaling expected for a pure Ornstein-Uhlenbeck noise spectrum, which we attribute to the presence of additional noise baths, in contrast to bulk-embedded defects, our near-surface SnV center, and thus the ^{13}C nuclear spin, is subject to additional noise sources at the diamond surface. Importantly for the proof of concept, no reduction in visibility is observed with increasing pulse number, indicating that gate errors do not accumulate appreciably. The longest coherence time achieved in this work is limited by the programming capacity of the arbitrary waveform generator rather than by any intrinsic property of the system. Notably, neither a deviation from the power-law scaling nor a reduction of the initial

visibility is observed at large pulse numbers, suggesting that further coherence extension is readily achievable by increasing the number of decoupling pulses.

For comparison, Grimm *et al.* [144] report a similar starting coherence time of $T_2(1) = 274(16)$ ms for a single ^{13}C nuclear spin coupled to a GeV center, close to our value of $T_2(1) = 232(7)$ ms. However, their CPMG coherence time scales as $T_2 \propto N^{2/3}$, whereas we observe a significantly weaker scaling of $T_2 \propto N^{0.37}$, requiring a larger number of decoupling pulses to achieve comparable maximum coherence times. Our scaling exponent is more consistent with the results of Stas *et al.* [65], who use 256 decoupling pulses to reach a coherence time of approximately 1 s for a ^{29}Si nuclear spin and find a scaling exponent of $\beta = 0.53$. We attribute this difference in scaling to the distinct bath environments, as already discussed above. The GeV center studied by Grimm *et al.* is located several micrometers deep inside a diamond solid immersion lens and is much less coupled to the electron spin, i.e. the ^{13}C nuclear spin bath constitutes the dominant noise source. In contrast, our SnV center is situated at a depth of only 20 nm, placing it in close proximity to the diamond surface and thereby exposing it to additional noise channels that are not as efficiently refocused by the CPMG protocol, reducing the scaling exponent. Stas *et al.* model the coherence of the host ^{29}Si nuclear spin as consisting of three contributions: the depolarization rate of the electron spin $T_{1,\mathrm{e}}$, since the strong hyperfine coupling causes different phases to be acquired for the different electron spin projections, i.e. uncontrolled flips will lead to a fast dephasing of the nuclear spin [158]; a temperature-independent ^{13}C nuclear spin bath; and a bath of two-level systems with phonon-addressable transitions, making this last contribution temperature-dependent. Such a bath has, for example, been found at the oxide interface of silicon, leading to $1/f$-noise characteristics in certain temperature regimes [173]. For Stas *et al.*, this additional bath was important, as it described their observed initial increase in coherence time with increasing temperature. They attributed this to the effect of motional averaging, which we discussed in Sec. 3.3. The main idea is that for a short bath correlation time $\tau_c(T)$ compared to the total evolution time t and a fixed coupling strength b, increasingly fast fluctuations, i.e. smaller τ_c, cause the bath to average out more effectively, leading to an increase in coherence [65]. As we are also studying a spin-1/2 system with comparable hyperfine coupling, we can expect to be similarly affected by such phonon-addressable spins. Since we did not measure the nuclear spin coherence as a function of temperature, we do not fit a model here.

Another noise source is the RF and microwave signal generators themselves. These can have a significant impact, as our first measurements were performed without any filters or switches. The measured echoes were very noisy, with strong contributions at $f = 50$ Hz, $f = 200$ Hz, $f = 250$ Hz, and $f = 400$ Hz, and a maximum Hahn-echo coherence time of only ~ 30 ms. Implementing a narrow bandpass filter around the RF transition, a DC block after the combiner, and a high-pass filter in the microwave channel path led to a significant reduction of the noise (see Sec. 2.3.2 for details). At the same time, implementing the visibility measurement technique and increasing the magnetic field from $B_{\mathrm{dc}} = 60$ mT to $B_{\mathrm{dc}} = 106$ mT led to the coherence times reported here. As we do not have a dedicated switch in the microwave line but instead turn the microwave source off internally, some residual noise may leak into the system during the long waiting times; however, this would constitute only high-frequency noise. As the setup will be upgraded in the continuation of

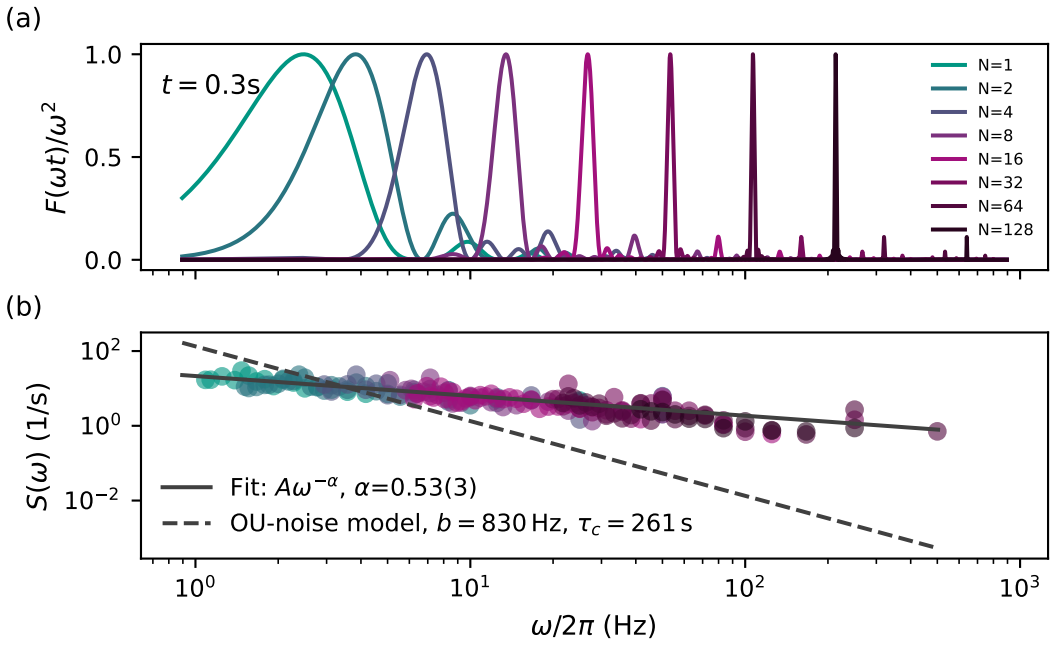

Figure 5.17.: Reconstruction of the noise spectrum of data in Fig. 5.16. (a) The corresponding CPMG filter functions for a total evolution time of $t = 0.3\,\mathrm{s} \approx T_2^{\mathrm{HE}}$ are shown to illustrate the width and frequency sensitivity. (b) Actual reconstruction of the noise spectrum. The corresponding free evolution time for each visibility data point is used. No correction for the higher-order lobes of the CPMG filters is applied, as it yielded a worse reconstruction. The spectral density $S(\omega)$ follows a power law with an exponent $\alpha = 0.53(3)$, as indicated by the black solid line. In addition, the predicted Ornstein-Uhlenbeck noise spectrum obtained from the echo fit is shown as a dashed line.

this work to allow multi-qubit control, incorporating a new AWG, IQ mixing, and switches, it will be interesting to see whether the coherence changes, i.e. is setup-limited, or remains the same, i.e. is sample-limited.

In order to gain more insight into the bath structure, we perform a reconstruction of the noise spectrum as described in Sec. 3.3.1. In Fig. 5.17(a), the corresponding CPMG filter functions for a total evolution time of $t = 0.3\,\mathrm{s} \approx T_2(1)$ are shown to illustrate the width and frequency sensitivity. In the actual reconstruction, the corresponding time for each visibility data point is used. No correction for the higher-order lobes of the CPMG filters is applied, as it yielded a worse reconstruction. The result of the reconstruction is shown in Fig. 5.17(b). The spectral density $S(\omega)$ follows a power law with an exponent $\alpha = 0.53(3)$, as indicated by the black solid line. The reconstructed bath exponent predicts a scaling of $T_2 \propto N^{0.35(1)}$, in good agreement with the experimentally observed exponent in Fig. 5.16. From this, we expect a stretching of the individual decay curves of $\xi = 1.53(3)$. Fitting the data in Fig. 5.16 with this stretching exponent only slightly changes the coherence times, yielding a maximum coherence time of $T_2(128) = 1.32(6)$ s. This value is in good agreement with the longest coherence times reported for nuclear spins coupled to group-IV centers. Grimm *et al.* observed a coherence time of 2.5 s for a ^{13}C nuclear spin coupled to a GeV center [144]. Similarly, coherence times of approximately 2 s were reported for ^{29}Si host nuclear spins coupled to SiV centers by Stas *et al.* and Knaut *et al.* on two independent

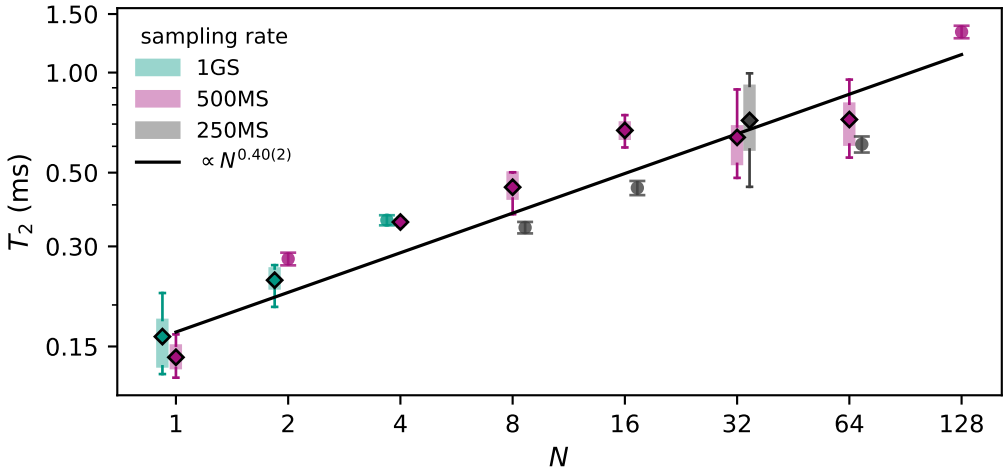

Figure 5.18.: Overview of all CPMG coherence times measured over the course of 72 days, comprising a total of 46 measurements. Data points are color-coded by the AWG sampling rate. For pulse numbers with more than one measurement, boxplots are shown: the black diamond marks the mean coherence time, the box spans the 50% quartile, and the capped lines indicate the maximum and minimum measured values. A power-law fit yields $\beta = 0.40(2)$, consistent with the result in Fig. 5.16.

SiV centers [31]. These works attribute the limited coherence time to phonon-induced fluctuations mediated by the electron spin.

In addition, the predicted Ornstein-Uhlenbeck noise spectrum obtained from the echo fit is shown as a dashed line. The reconstructed spectrum clearly deviates from this model. The crossing point with the reconstructed noise spectrum is determined by the choice of parameters from the echo fit. Reproducing the noise spectral density within the Ornstein-Uhlenbeck framework would require bath correlation times that increase as a function of the number of pulses, which is nonphysical and not experimentally observed [144]. As we observe no substructure in the noise spectrum, it is not possible to assign additional bath contributions beyond the baths discussed above with any justification. Adding white noise to the Ornstein-Uhlenbeck bath limits the noise spectral density at high frequencies but does not change the scaling exponent α in the relevant frequency region. As we deviate from the Ornstein-Uhlenbeck noise model significant, we can conclude we are not limited by the nuclear spin bath but one of the other noise sources discussed above. Similar scalings ~ 0.4 have been observed for NV centers in ^{12}C enriched samples [115], which also hints to other dominating noise sources.

To give an overview of all coherence times measured, we plot the observed coherence times with their respective pulse number N in Fig. 5.18. The data points are color-coded by the sampling rate of the AWG. Even for the lowest sampling rates, the coherence times show no systematic deviation. For pulse numbers with more than one measurement, boxplots are shown: the black diamond marks the mean coherence time, the box spans the 50% quartile, and the capped lines indicate the maximum and minimum measured values. The plot consists of a total of 46 measurements over the course of 72 days. The most frequently measured sequences are $N = 1$ and $N = 32$, with 11 and 15 repetitions,

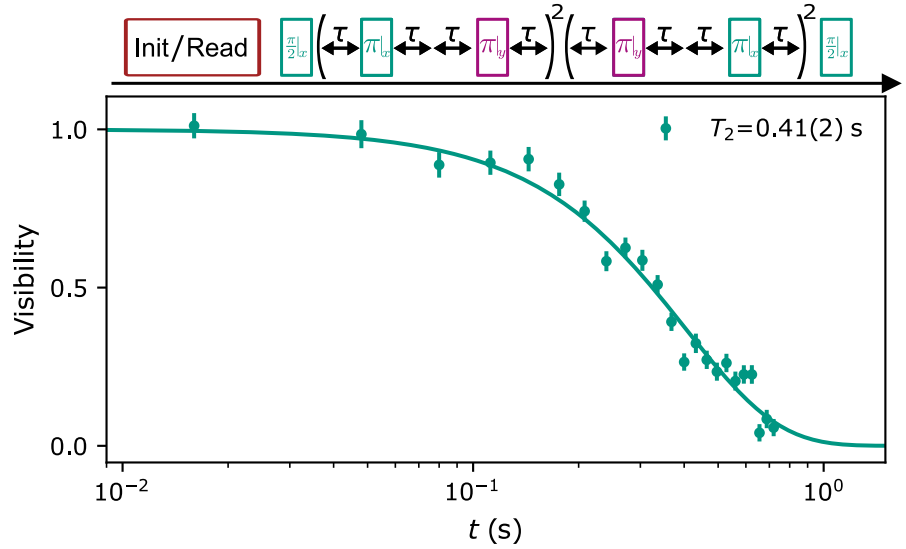

Figure 5.19.: XY8 measurement of the nuclear-spin coherence time. An initialization is followed by a the pulse sequence depicted for a single XY8-N sequence with $N = 1$. The visibility decays following a stretched exponential with a stretching factor of $\xi = 1.6(2)$, yielding a coherence time $T_2 = 0.41(2)$ s in good agreement with the CPMG-8 sequence shown in Fig. 5.16.

respectively. The $N = 32$ measurements were taken over the course of 11 different days. Fitting the coherence times to a power-law model yields $\beta = 0.40(2)$, in good agreement with the result in Fig. 5.16. We also observe a clustering of coherence times into two groups with the same scaling exponent but different absolute values. The origin of these two sets of initial coherence times is unknown, as all measurements were performed during a single cooldown and noise reconstruction did not lead to any substructure in the noise spectral density. In summary, this demonstrates that the reported CPMG parameters are reproducible over many repeated measurements and do not merely reflect handpicked best-case data.

In order to exclude pulse errors we also use the commonly XY8-sequence [31, 65, 144]. The sequence is shown in Fig. 5.19. A total waiting time for a single XY8-sequence is $t = 16\tau$. Fitting the visibility signal leads also to a stretched exponential decay with a coherence time of $T_2 = 0.41(2)$ s. As this coherence time matches the coherence time of the CPMG-8 sequence, we conclude that pulse errors were indeed negligible [144] and the discussion above sufficient.

5.4.4. Nuclear-spin coherence under optical excitation

An important consideration for the realization of quantum network nodes is the extent to which a proximal nuclear spin is affected by optical excitation of the electron spin. This is can be either during a spin-dependent reflection [64, 65] or when intermediate readouts of the electron spin is required [65, 158].

This question is twofold: first, how quickly does the nuclear spin depolarize due to electron-spin flips during optical cycling; and second, how much additional dephasing does the nuclear spin experience from the differing hyperfine coupling in the electronic ground and excited states. The first effect is sensitive to the pseudo-secular hyperfine coupling A_{zx}, while the second effect is also sensitive on the difference of the secular hyperfine coupling A_{zz} [176].

As a first step, we perform pump-probe measurements to quantify the depolarization of the nuclear spin under resonant optical excitation of the electron spin. The nuclear spin is initialized, after which the optical transition is driven for a variable duration, and the remaining nuclear-spin polarization is read out. To further investigate the coherence properties under optical illumination, we perform Hahn-echo measurements on the nuclear spin while the electron is optically excited, following the approach of Stas *et al.* [65], where analogous measurements were carried out on the host ^{29}Si nuclear spin of SiV centers.

Nuclear-spin depolarization under optical excitation. To quantify the depolarization of the nuclear spin induced by optical cycling of the electron spin, we perform pump-probe measurements. The system is initialized into the sub-state $|\uparrow_e\downarrow_n\rangle$ by pumping transitions A1 and MW1, followed by a variable waiting time t_{wait} and subsequent readout. For the bright (dark) readout, an RF2 π-pulse is applied (omitted) before the readout pulse, and the contrast is defined as the bright readout counts divided by the sum of bright and dark counts. The resulting contrast as a function of t_{wait} is shown in Fig. 5.20(a) as the blue curve, labeled C_1. No decrease in contrast is observed, confirming that the electron-spin lifetime T_1 does not measurably affect the nuclear-spin state on timescales up to 30 s.

To probe the nuclear-spin depolarization rate R_{dp}, the same pump-probe measurement is repeated with the laser kept continuously resonant with A1 during the waiting time t_{wait}. After initialization, the electron occupies the spin state whose resonant optical transition is B2, while the laser is tuned to A1. Excitation can therefore only occur off-resonantly via the Lorentzian tail of the A1 line overlapping with B2, leading to occasional excitation into the optically excited state. These off-resonant excitations can induce a flip of the nuclear spin. With increasing waiting time under this continuous A1 illumination, a decrease in the contrast is observed, labeled C2 in Fig. 5.20(a) (red curve).

In total a sequence consists of three cases, which are appended after each other

$$\text{Case 1 : Init} - \text{apply A1} - \pi_{\text{RF2}} - \text{Readout}, \tag{5.30}$$

$$\text{Case 2 : Init} - \text{wait} - \pi_{\text{RF2}} - \text{Readout}, \tag{5.31}$$

$$\text{Case 3 : Init} - \text{wait} - \text{do nothing} - \text{Readout}. \tag{5.32}$$

Each sequence Case 1 - Case 2 - Case 3 is repeated between 5000 and 250 times, depending on the difference in sequence duration, to accumulate enough statistics. The laser was aligned spectrally such that both nuclear spin resonances are driven with equal probability. For example C_1 in Fig. 5.20(a) is then defined as the ratio by of the signals obtained in Case 2 / (Case 2 + Case 3).

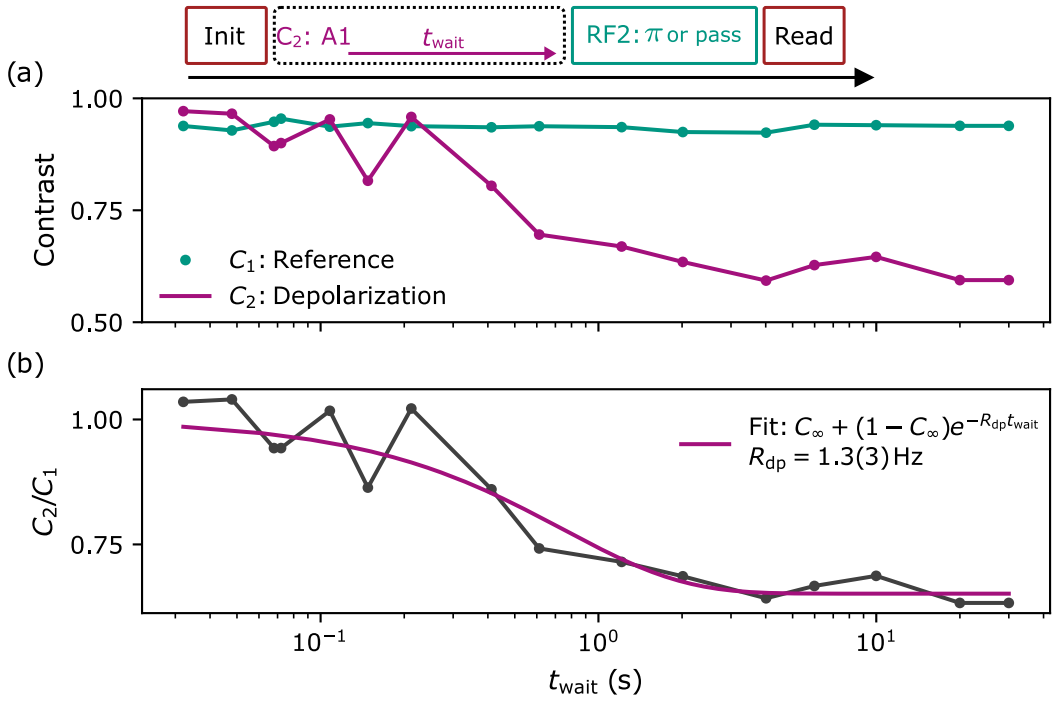

Figure 5.20.: Measurement of the electron-spin population and nuclear-spin depolarization. (a) Pump-probe measurement of the electron-spin population and nuclear-spin depolarization. The system is initialized into $|\uparrow_e\downarrow_n\rangle$, followed by a variable waiting time t_{wait}, an RF2 π-pulse, and subsequent readout. The contrast C_1 (green), measured without laser illumination during the waiting time, shows no decay up to 30 s, placing a lower bound on the electron-spin lifetime of $T_1 \gg 30$ s. When the laser remains resonant with A1 during the waiting time, the contrast C_2 (purple) decreases due to off-resonant excitation-induced nuclear-spin depolarization. Both contrasts are normalized using a reference sequence in which the RF2 π-pulse is omitted. (b) Ratio C_2/C_1, isolating the nuclear-spin depolarization from other effects. An exponential fit yields a depolarization rate of $R_{\text{dp}} = 1.3(3)$ Hz, corresponding to a nuclear cyclicity of $\Lambda_{\text{n}} = 3.7(9)$ electron-spin flips before depolarization.

Fitting the ratio C_2/C_1 to an exponential decay of the form

$$\frac{C_2}{C_1} = C_\infty + (1 - C_\infty)\, e^{-R_{\text{dp}}\, t_{\text{wait}}} \tag{5.33}$$

yields a depolarization rate of $R_{\text{dp}} = 1.3(3)$ Hz [see Fig. 5.20(b)].

To relate this depolarization rate to the number of optically induced electron-spin flips, we compare background-corrected count rates under off-resonant and far-detuned excitation. Specifically, we measure the difference in count rates between driving on A1 and illuminating with the laser detuned by −9.6 GHz, with a total integration time of 30 min for each setting as shown in Fig. 5.21. At a resonant laser power of 9.2 nW, we observe a count rate of $S_{\text{A1}} = 30.419(3)$ Hz on A1 and $S_{\text{det}} = 23.689(3)$ Hz when detuned, giving a difference of $S_{\text{A1}} - S_{\text{det}} = 6.730(4)$ Hz.

To convert this into an electron-spin-flip rate, we measure the electron-spin initialization under identical experimental conditions and obtain an average background-corrected photon count per electron initialization of $S_{\text{init}} = 1.37(1)$. This is performed in the

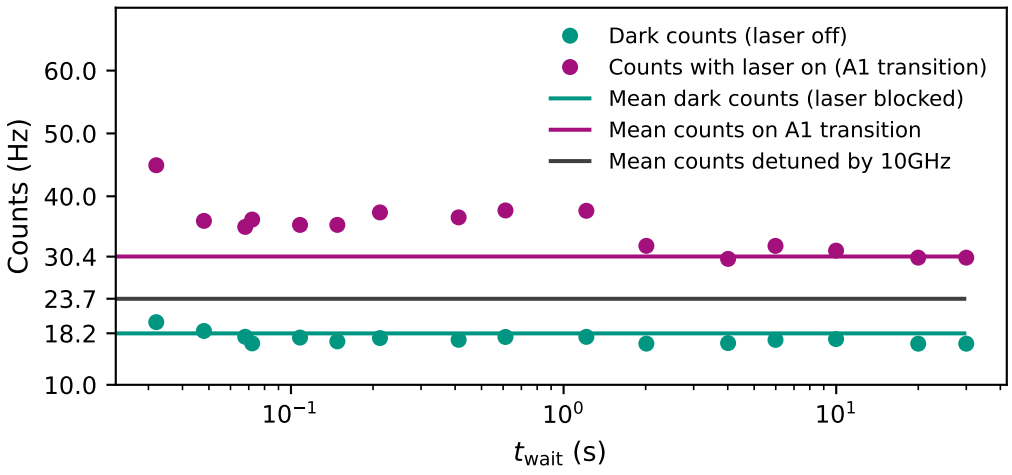

Figure 5.21.: Comparison of the background count rates under resonant and far-detuned excitation. Specifically, the difference in count rates between driving on A1 and illuminating with the laser detuned by −9.6 GHz. The measured count rates during the experiment in Fig. 5.20(a) (dots) are compared to cw measurements with a total integration time of 30 min for each setting (solid lines). At a resonant laser power of 9.2 nW, we observe a count rate of $S_{\mathrm{A1}} = 30.419(3)$ Hz on A1 and $S_{\mathrm{det}} = 23.689(3)$ Hz when detuned. We observe an increase in count rate for shorter waiting times, which we attribute to intensity fluctuations due to heating of the acousto optical modulator. As we are mostly in the long-time regime, the values obtained in the cw measurements, which provide lower statistical uncertainty, are used in the main text.

same manner as shown in Fig. 4.2, where a similar value for the mean photon counts per initialization was found. As the procedure and result are essentially identical, the corresponding plot is not reproduced here.

The electron-spin-flip rate is then

$$R_{\mathrm{flip}}(9.2\,\mathrm{nW}) = \frac{S_{\mathrm{A1}} - S_{\mathrm{det}}}{S_{\mathrm{init}}} = 4.9(4)\,\mathrm{Hz}\,. \tag{5.34}$$

Comparing this to the depolarization rate yields an estimate of the nuclear cyclicity,

$$\Lambda_{\mathrm{n}} = \frac{R_{\mathrm{flip}}}{R_{\mathrm{dp}}} = 3.7(9)\,, \tag{5.35}$$

indicating that the nuclear spin depolarizes after an average of approximately four random electron-spin flips.

In Fig. 5.22, we show the electron initialization together with the nuclear-spin repump applied before every repetition of the sequence. If the combination of an electron π-pulse followed by electron initialization did not affect the nuclear eigenstate, no additional fluorescence would be expected during the subsequent nuclear repump step. However, a clear fluorescence signal is observed. The integrated counts during this nuclear repump are approximately 20% smaller than those during the electron initialization. For comparison, a full nuclear repump, implemented by deliberately applying an RF2 π-pulse, produces

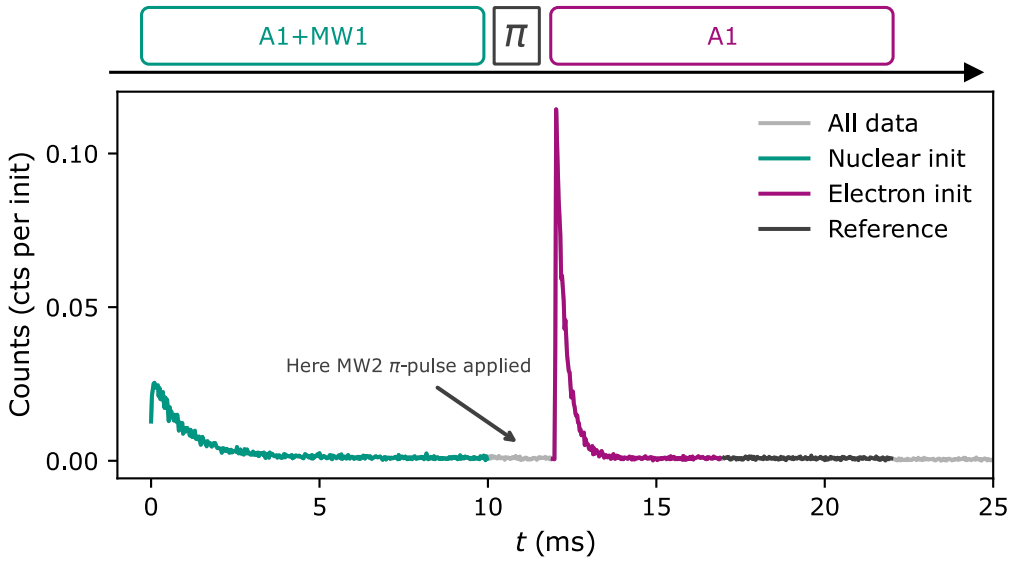

Figure 5.22.: Electron initialization with nuclear spin repump. The pulse sequence consists of a nuclear initialization phase (A1+MW1), followed by an MW2 π-pulse to flip the electron spin, and a subsequent electron initialization phase (A1). The green trace shows the fluorescence during the nuclear initialization, the purple trace the fluorescence during the electron initialization, and the dark gray trace a laser-only reference. The gray trace shows the total unused data. The integrated counts during the nuclear initialization are approximately 20% smaller than those during the electron initialization, indicating that the preceding electron manipulations partially disturb the nuclear spin state.

approximately 2.6 times more photons than electron initialization alone. From this calibration, the observed nuclear-repump signal corresponds to an admixture of the opposite nuclear branch of approximately 30%. Thus, after a single electron-spin flip followed by electron initialization, the nuclear-state contrast is reduced to approximately $C_{\mathrm{nuc}} \simeq 70\%$. Solving $C_{\mathrm{nuc}}^{\Lambda_{\mathrm{n}}} = 1/e$ gives an effective nuclear cyclicity of $\Lambda_{\mathrm{n}} = -1/\log C_{\mathrm{nuc}} \approx 3$ in reasonable agreement with the depolarization rate obtained above. Using $\Lambda_{\mathrm{n}} = 3.7$, we would find a remaining contrast of $C_{\mathrm{nuc}} \approx 76\%$. The fidelity is given by $F_{\mathrm{nuc}} = \frac{1}{2}(1 + C_{\mathrm{nuc}})$ [175], which yields $F_{\mathrm{nuc}} = 85\% - 88\%$ depending on the remaining contrast chosen.

The observed nuclear-state mixing can originate either from imperfect coherent electron manipulation or from the subsequent electron initialization either by the optical cycling of the electron spin or the electron-spin flip itself. The small effective nuclear cyclicity is consistent with the expected strong pseudo-secular hyperfine coupling of the proximal ^{13}C spin, which makes the nuclear eigenbasis sensitive to changes in the electron-spin configuration. This does not, by itself, imply that a selective microwave pulse randomly flips the nuclear spin. A coherent microwave pulse drives a well-defined transition between electro-nuclear eigenstates and can in principle be reversible. The situation is different for optical electron initialization. Although the electron is reset (flipped) only once, the reset is an incoherent and effectively sudden operation on the electro-nuclear system accompanied by many optical cycles between ground and excited state.

For ^{13}C nuclear spins strongly coupled to NV centers, it has been observed that the nuclear spin remains unaffected even after scattering a large number of optical photons, on the

order of $\sim 10^3$ [175]. They excluded that the electron spin-flipping transitions are the dominant process, but the spin-cycling transitions are the relevant effect [129]. This large number of possible scattered photons without depolarizing the nuclear spin allowed repetitive readout of the electron spin for an improved signal amplitude [171]. Special care needs to be taken to compare these results to our system. As the NV center is a spin-1 system, in the $m_s = 0$ state, which is optically cycled in their experiment, no hyperfine action is present [175]. For the $m_s = \pm 1$ a finite hyperfine action is present, which they assume to point along the z-axis of the NV center [171, 175].

Since we look at a spin-1/2 system, the pseudo-secular hyperfine interaction makes the nuclear quantization axis depend on the electron spin state with a finite hyperfine interaction for both electron spin states. If we take the DFT values from above (see Sec. 5.1 and Ref. [157]), we find a tilt angle of the hyperfine quantization axis away from the SnV centers quantization of $\xi = (\eta_\alpha + \eta_\beta)/2 = -24°$ [86]. Using the increased $A_{zz} = 41.75\,\mathrm{MHz}$ inferred from the behavior of the measured data in Fig. 5.12, we find a tilt of the hyperfine quantization axis of $\xi = -19°$, which the two nuclear precession vectors spanning an angle almost antiparallel of $\eta = 178°$ [86] (see Fig. 5.1(b) for the geometrical illustration). In addition, due to the different hyperfine coupling in the excited state the nuclear spin will precess around a different axis in the excited state, even if the electron is not flipped [129]. These fast oscillations will lead to high frequency noise, also possibly flip the nuclear spin [129]. The amount of photons, which can be scattered by the electron before the nuclear spin depolarizes is $\gamma^2/(\Delta\omega_\perp)^2$, in the limit that $\gamma \gg \Delta\omega_\perp$, where γ is the decay rate of the excited state and $\Delta\omega_\perp$ the perpendicular component of the hyperfine difference [129]. As we will see in the following section, we measure a hyperfine difference in the range of MHz and thus this ratio could become comparable to the cyclicity of the spin-conserving optical transition Λ_e, and thus a single electron initialization can already produce a sizable nuclear-state error. To mitigate this an initialization via the spin-flipping transition or decrease in the optical lifetime via the integration into optical cavities could be used.

A direct test would be a measurement analogous to Fig. 5.22, but with a nominal 2π-pulse instead of a π-pulse before the electron-only reset (only pumping the A1 transition) and a subsequent nuclear-repump step. The purpose of this measurement is to separate two pieces of information that are otherwise mixed together. The fluorescence in the electron-nuclear initialization only shows how much population is outside the dark state before the initialization pulse. Since the full electro-nuclear initialization pumps all bright electro-nuclear states back into the same dark state, this fluorescence signal does not tell us into which nuclear branch the population has ended. In contrast, applying only the electron reset first and then measuring the fluorescence during a following nuclear repump directly tests whether the electron reset has mapped population into the wrong nuclear branch. In addition, this should be done as a function of laser power and laser duration for both the spin-conserving and spin-flipping transition. For such measurements, to get reliable data, the electron Rabi frequency should be large compared with the electron dephasing rate, which is not the case for the present SnV center. This can be improved in emitters with larger strain, where stronger and cleaner electron-spin driving is possible, as we have shown previously [70].

These depolarization effects are in contrast with group-IV color centers using the host nuclear spin as the memory qubit. In that case, no pseudo-secular term is present in the hyperfine tensor in the ground and excited state [156]. This means the nuclear spin should dephase during initialization but not depolarize.

Also in the work with ^{13}C nuclear spins weakly coupled to NV centers, the main error source is dephasing due to the different Larmor precession for the two different electron spin states [67, 158, 177] and not a change in precession axes. This is due to the fact that the relation $\gamma_{^{13}\mathrm{C}} B \gg \sqrt{A_{zx}^2 + A_{zz}^2}$ holds and change in precession axis is suppressed [67]. This means a field of $B_{\mathrm{dc}} \gg 4\,\mathrm{T}$ would be needed to be applied for our system to reach this regime. As this is not possible, this also mean that we would not directly benefit of the encoding into decoherence free subspaces, as this copes only with dephasing of the nuclear spin states [67].

Nuclear-spin dephasing under optical excitation. To develop an intuitive understanding of the impact of the additional dephasing on the nuclear-spin memory when the electron spin is optically excited, we follow the analysis of Harris *et al.* [176] and Kalb *et al.* [158] and calculate the memory fidelity of the nuclear spin after n optical excitations. Consider an initial superposition state $|\psi_{\mathrm{n}}\rangle = \frac{1}{\sqrt{2}}(|\downarrow_{\mathrm{n}}\rangle + |\uparrow_{\mathrm{n}}\rangle)$. Upon optical excitation of the electron spin, the nuclear-spin state accumulates a differential phase, since the hyperfine interaction differs between the electronic ground and excited states due to their distinct wavefunctions and consequently different overlap at the nuclear site [129]. After a time t spent in the excited state, the nuclear-spin state evolves to $|\psi_{\mathrm{n}}\rangle = \frac{1}{\sqrt{2}}(e^{-i\Delta\omega_{\mathrm{hf}}t/2}\,|\downarrow_{\mathrm{n}}\rangle + e^{i\Delta\omega_{\mathrm{hf}}t/2}\,|\uparrow_{\mathrm{n}}\rangle)$, where $\Delta\omega_{\mathrm{hf}}$ is the difference in hyperfine splitting between the two electronic states.

At low excitation powers, the time spent in the excited state is random and follows an exponential probability distribution $p(t) = \frac{1}{\tau}e^{-t/\tau}$, where τ is the excited-state lifetime. The relevant quantity is then the absolute value of the expectation value of the acquired phase, which can be computed as

$$\left|\langle e^{i\phi}\rangle\right| = \left|\int_0^\infty p(t)\, e^{i\Delta\omega_{\mathrm{hf}}t}\,\mathrm{d}t\right| = \frac{1}{\sqrt{1 + (\Delta\omega_{\mathrm{hf}}\tau)^2}}\,. \tag{5.36}$$

After n excitations, the memory fidelity takes the form

$$F_{\mathrm{mem}}(n) = \frac{1}{2}\left(1 + |\langle e^{i\phi}\rangle|^n\right), \tag{5.37}$$

which yields $F_{\mathrm{mem}} = 1$ for $n = 0$ and decays to $F_{\mathrm{mem}} = 1/2$ for $n \gg 1$, since $|\langle e^{i\phi}\rangle| < 1$.

This expression immediately reveals two strategies for preserving nuclear-spin coherence during optical operations: either minimize the time spent in the excited state or ensure a small difference in hyperfine coupling between the ground and excited electronic states.

A useful experimental indicator for the magnitude of $\Delta\omega_{\mathrm{hf}}$ is the PLE spectrum of the defect. For low-strain emitters, if the hyperfine coupling exceeds the optical linewidth, typically tens of megahertz, a resolved splitting appears in the PLE transitions, corresponding to

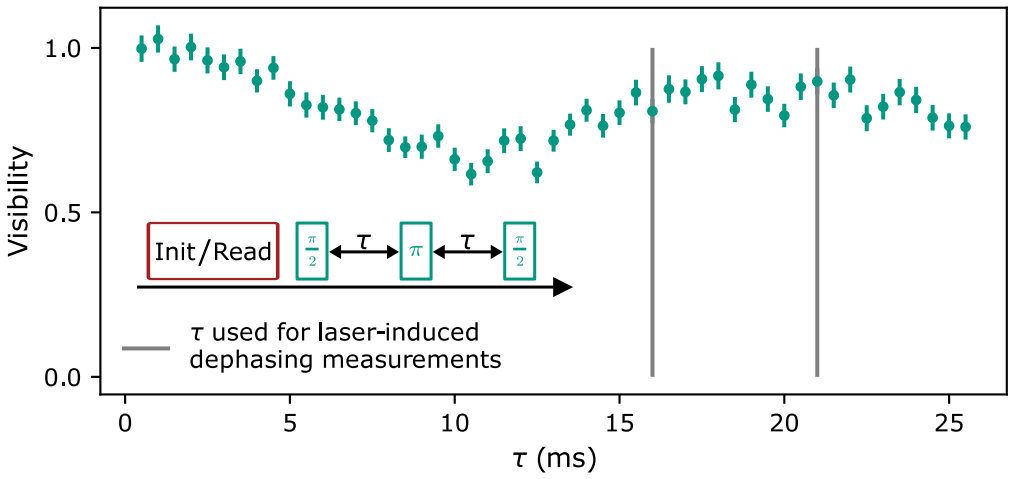

Figure 5.23.: Hahn-echo measurement with short time resolution. The visibility is plotted as a function of half the free evolution time τ. After an initial decrease, the echo visibility recovers. Two durations of high visibility are selected: $\tau = 21$ ms for Fig. 5.24(a) and $\tau = 16$ ms for Fig. 5.24(b), as indicated by the gray vertical lines.

half the difference between the ground- and excited-state hyperfine splittings [156]. This is indeed observed for host nuclear spins such as ^{29}Si [65], ^{73}Ge [156], or $^{117/119}$Sn [156]. In our case, however, the PLE spectra show a purely Lorentzian lineshape with no resolvable double structure, albeit with a linewidth somewhat broader than expected from the lifetime alone. This constrains the hyperfine difference to roughly $\Delta\omega_{\mathrm{hf}} < 10$ MHz, consistent with DFT calculations that predict $\Delta\omega_{\mathrm{hf}} \sim 5$ MHz. We also observe no angular-dependence of this behavior (see Fig. A.1 for more details).

To quantify this dephasing experimentally, we follow the approach of Ref. [65] and perform Hahn-echo-like measurements on the nuclear spin under optical illumination. The system is first initialized into $|\uparrow_e\downarrow_n\rangle$ by pumping A1 and MW1. An RF2 $\pi/2$-pulse then creates a nuclear-spin superposition. During a fixed nuclear-spin evolution time of $\tau = 21$ ms, a laser pulse resonant with A1 of variable duration t is applied. We note that in our Ref. [71] a waiting time of $\tau = 20$ ms was stated; this does not affect any of the results and can already be inferred from Fig. 14 in that reference, where the data points extend beyond the 20 ms mark. The free-evolution time is chosen such that the echo is maximally refocused, meaning that neither resonances in the echo signal nor the overall decay should be too pronounced. At the same time, the duration must be long enough for the expected oscillations to be observable. This is illustrated in Fig. 5.23, where the echo visibility is plotted as a function of half the free evolution time $t/2 = \tau$. After an initial decrease of the visibility, most likely due to coupling to nearby nuclear spins, the echo signal is fully recovered. Two durations of high visibility are selected: $\tau = 21$ ms for Fig. 5.24(a) and $\tau = 16$ ms for Fig. 5.24(b), as indicated by the gray vertical lines.

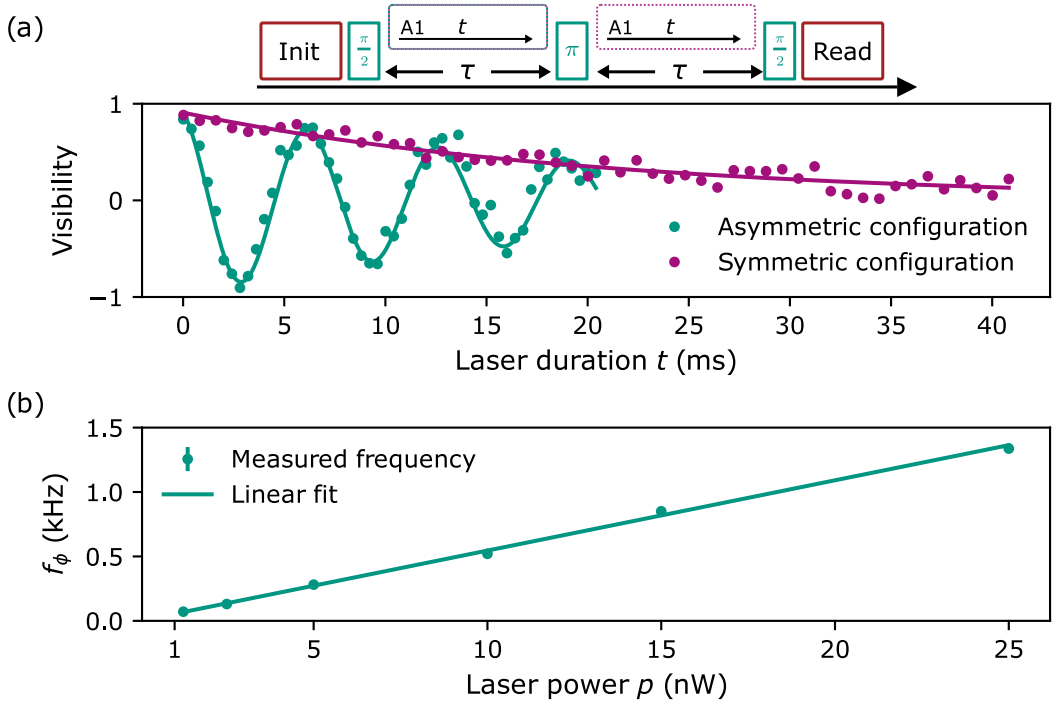

Figure 5.24.: (a) Hahn-echo measurement of the nuclear-spin coherence under optical excitation. A laser pulse of variable duration t is applied during the echo waiting time. In the asymmetric configuration (green), a single laser pulse is applied in the first waiting-time window, revealing both coherent phase oscillations and exponential decoherence. In the symmetric configuration (purple), equal laser pulses are applied in both windows, canceling the coherent phase accumulation and isolating the decoherence contribution. (b) Power dependence of the oscillation frequency extracted from the asymmetric measurements, corresponding to the differential Larmor precession between the electronic ground and excited states. Error bars denote the standard error of the fitted frequency.

After the first free evolution time under optical illumination, the nuclear spin is refocused with a π-pulse, followed by a second waiting interval of equal length and a final $\pi/2$-pulse that projects the state before readout.

If the laser is applied only during the first free evolution, this constitutes the asymmetric configuration, following the notation of Stas *et al.* [65], as shown in Fig. 5.24(a). To normalize the signal, the sequence is repeated with the phase of the final $\pi/2$-pulse shifted by 180°, and a visibility is calculated as usual.

The differing hyperfine interaction in the electronic ground and excited states leads to an electronic-state-dependent precession frequency of the nuclear spin, as observed in Fig. 5.24(a). In the asymmetric configuration, increasing the illumination time leads to more time spent in the excited state on average, and we expect to observe oscillations governed by the acquired phase $\phi = \Delta\omega_{\mathrm{hf}}\, t_{\mathrm{exc}}$ [176].

The time spent in the excited state, t_{exc}, is determined by the optical pump rate, i.e. the saturation parameter s [66, 88]. Because an electron-spin flip followed by re-initialization would involve many optical cycles under resonant excitation and immediately decohere the nuclear spin state, we apply off-resonant excitation during the free evolution and focus

on the off-resonant excitations that occur without inducing a spin flip. Specifically, driving A1 with the laser while the electron occupies states resonant with the B2 transition results in a very small effective saturation parameter, $s_{\text{eff}} = p_{\text{eff}}/p_{\text{sat}} \ll 1$. In this limit [66, 88],

$$t_{\text{exc}} = \frac{s_{\text{eff}}}{2s_{\text{eff}} + 1}\, t \approx s_{\text{eff}}\, t = \frac{p_{\text{eff}}}{p_{\text{sat}}}\, t\,. \tag{5.38}$$

This is important because it shows that the time spent in the excited state is linear not only in the applied power but also in the laser duration. Consequently, increasing the laser duration t at constant power yields a sinusoidal evolution of the visibility. Since the oscillation frequency in Fig. 5.24(a) is given by $f_\phi = \phi/t = \Delta\omega_{\text{hf}}\, s_{\text{eff}}$, a single oscillation trace could in principle be used to determine the difference in hyperfine splitting. To obtain a more precise measurement, we examine the power dependence of the oscillation frequency. The effective saturation parameter as a function of the applied power on A1 is given by

$$\frac{p_{\text{eff}}}{p_{\text{sat}}} = \frac{p}{p_{\text{sat}}} \frac{\Gamma^2}{\Gamma^2 + 4\Delta_{\text{opt}}^2}\,, \tag{5.39}$$

where Δ_{opt} is the detuning between the A1 and B2 transitions. The oscillation frequency is then

$$f_\phi = \Delta\omega_{\text{hf}} \frac{p}{p_{\text{sat}}} \frac{\Gamma^2}{\Gamma^2 + 4\Delta_{\text{opt}}^2}\,, \tag{5.40}$$

which yields the expected linear dependence on power. Fitting the linear trend measured in Fig. 5.24(b) gives a slope of $a = 54.9\,\text{Hz}\,\text{nW}^{-1}$. Using an optical splitting of $\Delta_{\text{opt}} = 647$ MHz, an emitter linewidth of $\Gamma = 34(4)$ MHz, and a saturation power of 32(2) nW inferred from the cyclicity measurement [71], we obtain a difference in hyperfine splitting of

$$\Delta\omega_{\text{hf}} = a\, p_{\text{sat}} \left(1 + \frac{4\Delta_{\text{opt}}^2}{\Gamma^2}\right) = 2\pi \times 2.6(6)\,\text{MHz}\,. \tag{5.41}$$

Despite propagating all uncertainties, this value depends on a number of parameters, and we therefore seek to confirm the result using as independently measured quantities as possible.

We perform count-rate measurements analogous to those in the previous section at a fixed excitation power of 10 nW. The excitation rate is inferred from the photon rate detected under continuous driving on A1, which is effectively off-resonant during the measurement, as the electron resides in the opposite spin state. Using the measured photon rate and the number of photons per electron initialization defined in the previous section, we extract the electron-spin-flip rate, obtaining $R_{\text{flip}}(10\,\text{nW}) = 8.1(1)$ Hz for this cooldown. This is then converted into an excitation rate via

$$R_{\text{exc}}(10\,\text{nW}) = \frac{1}{2}\,\Lambda_e\, R_{\text{flip}}(10\,\text{nW}) = 24.3(3)\,\text{kHz}\,. \tag{5.42}$$

The factor of 1/2 accounts for the fact that under continuous A1 driving, on average twice as many photons are detected per flip event: after an detected electron-spin flip, i.e.

on average after $1/\eta$ attempts, where η is the collection efficiency, the system becomes resonant with A1 and typically flips back rapidly (on the timescale of the measurement), producing a second photon burst. In the asymmetric echo measurement, by contrast, A1 is applied only for a short duration and at low effective saturation, so that electron-spin flips during the pulse are negligible. The observed oscillation therefore reflects phase accumulation from off-resonant excitations without this rapid flip-back process. The excitation rate inferred in this way is in excellent agreement with the theoretical excitation rate given by Eq. 2.94, which yields $R \sim 23.6\,\mathrm{kHz}$ for detuned pumping of a two-level system.

Measuring a single asymmetric echo configuration at this excitation power yields an oscillation frequency of $f_\phi = 253(3)\,\mathrm{Hz}$. Combined with the mean excited-state lifetime $\tau_{\mathrm{SnV}} = 1/(2\pi\Gamma) = 4.7(6)\,\mathrm{ns}$, this gives a differential hyperfine splitting of

$$\Delta\omega_{\mathrm{hf}} = \frac{f_\phi}{R_{\mathrm{exc}} \cdot \tau_{\mathrm{SnV}}} = 2\pi \times 2.3(3)\,\mathrm{MHz}, \tag{5.43}$$

in good agreement with the value obtained from the power-dependent measurements.

These oscillations are superimposed on an exponential damping envelope, reflecting the probabilistic distribution of times spent in the excited state due to the spontaneous emission process. When a second laser pulse of equal duration is applied in the second waiting-time window, i.e. the symmetric configuration in Fig. 5.24(a), the coherent phase accumulation cancels, isolating purely the decoherence contribution.

The decay of the echo visibility as a function of the optical excitation duration thus provides a direct measure of the optically induced nuclear-spin dephasing. Equation 5.36 describes the mean phase accumulated per optical excitation. In the low-excitation limit, the number of excitations is given by $n \approx R_{\mathrm{exc}}\, t$. The coherence should therefore decay as

$$C(t) = \left|\langle e^{i\phi}\rangle\right| = \left(\frac{1}{\sqrt{1 + (\Delta\omega_{\mathrm{hf}}\tau_{\mathrm{SnV}})^2}}\right)^{R_{\mathrm{exc}}\, t}. \tag{5.44}$$

Using the identity $a^x = \exp(x \ln a)$, we find

$$C(t) = \exp\left[-\frac{R_{\mathrm{exc}}}{2} \ln\left(1 + (\Delta\omega_{\mathrm{hf}}\tau_{\mathrm{SnV}})^2\right)\, t\right], \tag{5.45}$$

which allows us to introduce a decay time

$$T_{\mathrm{decay}} = \frac{2}{R_{\mathrm{exc}} \ln\left(1 + (\Delta\omega_{\mathrm{hf}}\tau_{\mathrm{SnV}})^2\right)}. \tag{5.46}$$

For small random phases per excitation, i.e. $\Delta\omega_{\mathrm{hf}}\tau_{\mathrm{SnV}} \ll 1$, this simplifies to $T_{\mathrm{decay}} \approx 2/[R_{\mathrm{exc}}(\Delta\omega_{\mathrm{hf}}\tau_{\mathrm{SnV}})^2]$. Here we find $\Delta\omega_{\mathrm{hf}}\tau_{\mathrm{SnV}} = 66(11)\,\mathrm{mrad}$, and this condition is indeed satisfied. From this we obtain an expected decay time of $T_{\mathrm{decay}} = 19(3)\,\mathrm{ms}$, in excellent agreement with the exponential decay time of $17(5)\,\mathrm{ms}$ extracted from the damping envelope of the echo, as shown in Fig. 5.24(a).

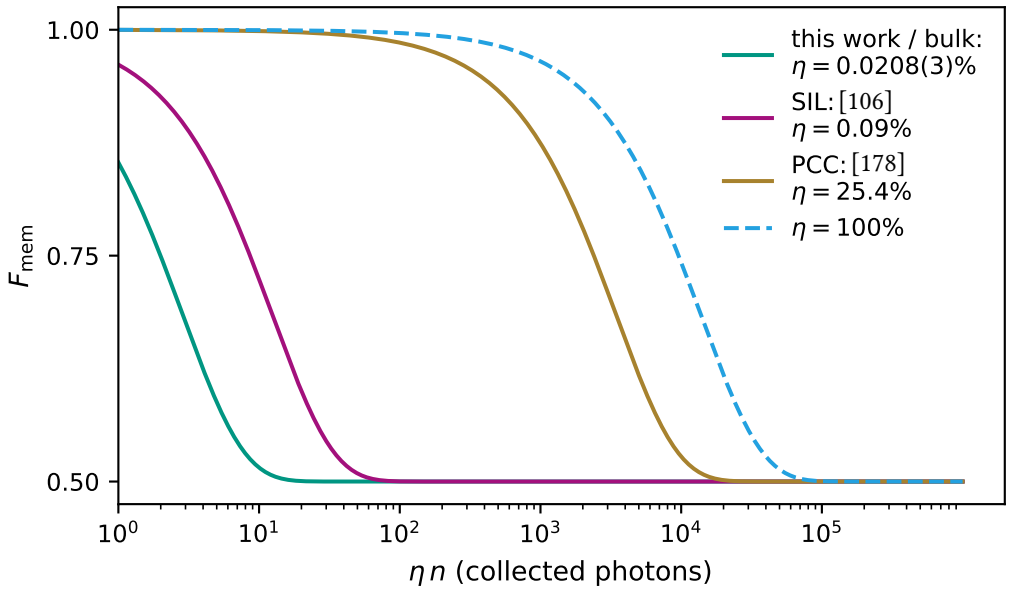

Figure 5.25.: Nuclear-spin memory fidelity F_{mem} as a function of the number of successfully collected photons ηn_π, calculated for different collection efficiencies η using the model of Harris *et al.* [176]. While the decay curves shift horizontally with η, they all correspond to the same underlying decoherence as a function of the total number of optical π-pulses n, shown as the dashed curve. Full decoherence of the nuclear spin is reached after approximately 5×10^4 optical π-pulses. Higher collection efficiencies, as achieved with photonic structures such as solid immersion lenses or photonic crystal cavities, yield significantly more collected photons before the nuclear-spin coherence is lost.

Knowing the differential hyperfine splitting between the ground and excited states allows us to estimate the reduction in nuclear-spin memory fidelity during network protocols that employ optical π-pulses. Following the model of Ref. [176], the number of optical π pulses required to reach a remaining coherence $\left|\langle e^{i\phi}\rangle\right|$ is

$$n_{\mathrm{th}} = \frac{2\,\ln\left(1/\left|\langle e^{i\phi}\rangle\right|\right)}{\ln[1 + (\Delta\omega_{\mathrm{hf}}\tau_{\mathrm{SnV}})^2]}\,. \tag{5.47}$$

For our parameters, we find that approximately $n_{\mathrm{th}} \approx 10^4$ optical π-pulses reduce the coherence to $\left|\langle e^{i\phi}\rangle\right|^{n_{\mathrm{th}}} = 1/e$, corresponding to a memory fidelity of $F_{\mathrm{mem}} = 68\,\%$. Since the total number of excitations required scales inversely with the collection efficiency η of the setup, it is instructive to express the memory fidelity as a function of the number of successfully collected photons, given by the product ηn_π, as shown in Fig. 5.25.

We estimate the collection efficiency from the ratio of the number of photons collected per initialization to the electron cyclicity $\Lambda_e = 5988$, the latter corresponding to the mean number of scattered photons during an initialization process. This yields $\eta = 0.0208(3)\,\%$. While this value is low, it is expected given that our SnV center is located in bulk diamond without photonic enhancement. For comparison, we plot the memory fidelity for the same differential hyperfine splitting but using the collection efficiencies reported for photonic

structures in diamond, specifically solid immersion lenses and photonic crystal cavities. As shown in Fig. 5.25, these enhanced collection efficiencies yield substantially higher fidelity for the same number of collected photons.

5.5. Summary

In this chapter, we have demonstrated full coherent control of a single ^{13}C nuclear spin strongly coupled to the electron spin of an SnV center in diamond. Starting from the theoretical framework of the hyperfine interaction, we identified the relevant level structure and used DFT calculations to estimate the expected coupling strengths, finding that our observed hyperfine coupling indicates a ^{13}C nuclear spin located at one of the nearest-neighbor lattice sites.

The nuclear spin is initialized into a single electro-nuclear sub-state via simultaneous incoherent microwave and optical pumping, achieving fidelities of up to $F_{\text{init}} = 99.5\,\%$. Optically detected nuclear resonance spectroscopy reveals the RF transitions around 20 MHz. The RF1 transition exhibits a doublet structure from coupling to a second ^{13}C nuclear spin, while RF2 remains a clean single Lorentzian most likely due to electron-state-dependent nuclear-nuclear coupling. All subsequent experiments were therefore performed on RF2.

Rabi measurements demonstrate clean oscillations sustained for 9.5 ms, corresponding to 138 π-pulses without any loss of contrast, confirming that the superconducting waveguide can deliver extended continuous RF driving without introducing heating. The Rabi frequency scales linearly with the ac magnetic field, yielding an enhancement factor of 1.526(6) over the bare gyromagnetic ratio attributed to hyperfine-mediated mixing of electronic character into the nuclear spin levels. Ramsey interferometry yields a dephasing time of $T_2^* \approx 1.7$ ms with a stretching exponent near 2, consistent with slow quasi-static noise, and a four-day chevron measurement confirms long-term frequency stability. Randomized benchmarking establishes a primitive gate fidelity of $F_{\text{G}} = 99.92(1)\,\%$ and a single-qubit Clifford gate fidelity of $F_{\text{C}} = 99.85(2)\,\%$.

The high gate fidelity enables effective dynamical decoupling. A Hahn-echo measurement yields $T_2 = 166$ ms, confirming that the dominant noise is slow and refocus-able. CPMG sequences progressively extend the coherence to $T_2(128) = 1.35$ s with 128 decoupling pulses, scaling as $N^{0.37}$, which is weaker than the $\beta = 2/3$ expected for a pure Ornstein-Uhlenbeck noise spectrum, which we attribute to additional noise channels. Noise spectral reconstruction confirms a power-law spectrum with exponent $\alpha = 0.53$, deviating from a single Ornstein-Uhlenbeck model. Importantly, neither a reduction in visibility nor a deviation from the power-law scaling is observed at large pulse numbers, indicating that the achieved coherence time is so far rather limited by the programming capacity of the arbitrary waveform generator rather than by any intrinsic property of the system.

Finally, we characterized the optical dephasing of the nuclear spin, which arises from the differing hyperfine interaction in the electronic ground and excited states. Asymmetric

Hahn-echo measurements under optical illumination reveal coherent phase oscillations superimposed on an exponential damping envelope. From both power-dependent and count-rate-based analyses, we extract a differential hyperfine splitting of $\Delta\omega_{\mathrm{hf}} \approx 2\pi \times 2.3 - 2.6\,\mathrm{MHz}$, in the same order of magnitude as DFT predictions and consistent with the absence of resolved splittings in the PLE spectrum. The measured decay times are in excellent agreement with a model based on the stochastic excited-state lifetime distribution, providing a quantitative understanding of the nuclear-spin memory performance during optical operations on the electron spin.

6. Conclusion and outlook

Summary of the main achievements. This thesis investigated the tin-vacancy center in diamond as a platform for optically addressable spin qubits, with a particular focus on the coherent control of its electron spin and of a nearby ^{13}C nuclear spin. As discussed in the introduction, quantum-network nodes require an efficient spin-photon interface, long-lived quantum memories, and high-fidelity control that remains compatible with cryogenic operation. The SnV center is a promising candidate in this context due to its inversion symmetry, leading to narrow optical transitions suitable for spin-photon interfaces, while its larger spin-orbit splitting compared to the SiV center can relax the requirements on operating temperature.

The work presented here addresses several of the corresponding challenges. Microwave control of a low-strain SnV center was investigated using superconducting coplanar waveguides, providing a route toward spin control with reduced Ohmic heating. Building on this, the coupling to a proximal ^{13}C nuclear spin was explored as a possible route toward a local quantum memory. The thesis thereby connects the microscopic physics of the SnV center, including spin-orbit coupling, strain, magnetic fields, and hyperfine interaction, to the experimentally observed spin control, coherence, and optical robustness of the coupled electron-nuclear system.

The main result is the high-fidelity coherent control of the single proximal ^{13}C nuclear spin coupled to an SnV center, together with a study of the mechanisms that limit its coherence and robustness under optical excitation. In the following, the main results of this thesis are summarized. These results are then compared to the current state of the art for group-IV color centers in diamond, followed by an outlook on possible future directions toward SnV-based quantum-network nodes.

Electron-spin control of a low-strain SnV center. In this work, coherent microwave control of a low-strain SnV center was demonstrated using superconducting coplanar waveguides, enabling strong drive fields while minimizing microwave-induced heating. The analysis builds on existing theoretical work on the angle-dependent Rabi frequency [80], reformulated in the notation used in our earlier work [70]. The measured angle dependence of the Rabi frequency is reproduced qualitatively using the strain of the SnV center as the only parameter. In particular, the observed asymmetry between scans in different angular planes confirms both the theoretical model and the geometry of the applied driving field.

Together with the optical cyclicity analysis, these measurements show that strain can be used as a tuning parameter of the SnV spin-photon interface. It determines the trade-off

between microwave drivability and optical cyclicity: stronger mixing can enhance spin driving, while at the same time modifying the spin selectivity of the optical transitions. This trade-off is an important design consideration for future SnV-based quantum-network nodes, where efficient spin control and high-fidelity optical initialization and readout have to be achieved simultaneously.

Identification and high-fidelity control of a proximal ^{13}C nuclear spin. A strongly coupled proximal ^{13}C nuclear spin was identified through the large hyperfine splitting of approximately 45 MHz observed in optically detected magnetic resonance. Because the hyperfine interaction is large compared with the nuclear Larmor frequency, the hyperfine parameters could not be determined independently from the measured transition frequencies, even within the secular approximation and using different external magnetic fields. Nevertheless, a consistent level scheme was assigned in analogy to the host ^{29}Si nuclear spin strongly coupled to the SiV center [65].

Using microwave-assisted optical pumping, the nuclear spin was initialized with high fidelity. The large electron-spin cyclicity of $\Lambda_e \sim 6000$ allows efficient electron-spin readout. Coherent radio-frequency control of the nuclear spin was demonstrated, with single-qubit gates reaching sub-percent error rates per gate. Finally, dynamical decoupling extended the nuclear-spin coherence time to above one second.

Decoherence of the nuclear spin under optical excitation. The difference between the hyperfine splittings in the electronic ground and excited states is comparatively small. Estimating the nuclear-memory fidelity as a function of the number of optical excitations, a full decay of the nuclear coherence is expected after approximately 10^4 optical excitation cycles. However, the collection efficiency of the optical setup is only $\eta = 0.0208(3)\%$, as extracted from the ratio of collected photons per initialization event to the electron-spin cyclicity. This low value is expected for an SnV center in bulk diamond without photonic enhancement. As a consequence, only a single-digit number of photons can be collected before the nuclear-spin state is expected to fully decohere. This highlights the need for photonic structures that enhance photon collection and light-matter interaction, such as solid-immersion lenses, photonic crystal cavities, or open microcavities. The latter approach has recently shown promising results within our group through the work of Kerim Köster, demonstrating coherent coupling of single SnV centers to a fiber-based microcavity with an extinction contrast of 81%.

Comparison to other existing platforms. The development of the SnV center could follow a similar path to the one established for the SiV platform, where deterministic spin-photon interfaces, telecom-band frequency conversion, and remote entanglement of nuclear-spin memories through deployed fiber have been demonstrated [23, 31, 61–64]. The larger ground-state splitting of the SnV center may relax the cryogenic requirements compared with the SiV center, even in a low-strain regime, and could therefore make future multi-node implementations more practical.

To place the results of this thesis in the context of the current state of the art, we compare the nuclear-spin memory performance of our system with that of Stas *et al.* [65], who used a host ^{29}Si nuclear spin coupled to a SiV center. Although our system is based on a proximal ^{13}C nuclear spin coupled to an SnV center, the comparison is useful for assessing both platforms as candidates for group-IV quantum-network nodes.

Since cavity experiments were not performed as part of this thesis, the comparison is based on a hypothetical scenario in which our emitter is placed in the same nanophotonic diamond cavity as used by Stas *et al.*. We therefore assume identical cavity parameters: a total cavity linewidth of $\kappa/2\pi = 250\,\mathrm{GHz}$, an in-coupling rate of $\kappa_{\mathrm{in}}/2\pi = 202\,\mathrm{GHz}$, an emitter-cavity coupling rate of $g/2\pi = 3.19\,\mathrm{GHz}$, and no out-coupling, $\kappa_{\mathrm{out}}/2\pi = 0$. The cavity detuning is chosen as $\omega_{\downarrow_e\uparrow_n} - \omega_c = 2\pi \times 150\,\mathrm{GHz}$. This detuning is larger than in Ref. [65], because the narrower emitter linewidth in our system, $\gamma_0/2\pi = 35\,\mathrm{MHz}$, requires a larger detuning to reach full reflection contrast. Using a hyperfine splitting of $\Delta\omega_{\mathrm{hf}} \simeq 3\,\mathrm{MHz}$, we then follow the approach of Ref. [65] and calculate the decoherence of the nuclear spin upon reflection of a photon from the cavity[1].

The exact photon-number requirements for the readout are not explicitly stated in Ref. [65]. We therefore infer from Figs. S6 and 1G of that work that a phase readout with 95% fidelity requires a mean photon number of approximately 20, whereas a resonant readout requires a mean photon number of approximately 5, assuming a coherent state reflected from the cavity. Using these values, we reproduce the behavior reported in Ref. [65] for their system, shown by the green curves in Fig. 6.1(b). Resonant readout on one of the spin transitions leads to a rapid decay of the nuclear memory fidelity. By contrast, phase readout, performed at a detuning on either side of the spin transition, causes substantially less decoherence because the scattered photons acquire less information about the nuclear-spin state [65].

Applying the same photon-number requirements to our SnV-^{13}C system yields the purple curves in Fig. 6.1(b). Two features are apparent. First, the resonant readout shows a similar decay despite the smaller difference between the ground- and excited-state hyperfine splittings. This is caused by the larger cavity detuning chosen to obtain sufficient reflection and phase contrast. Second, and more importantly, the phase readout shows a substantially improved memory fidelity. This improvement originates from the larger separation of the spin-conserving optical transitions in the low-strain SnV center compared with the high-strain SiV center, even though the magnetic field used here is four times smaller. Together with the narrower emitter linewidth, this larger optical separation improves the expected memory performance. This directly addresses one of the limitations identified by Stas *et al.*, namely that the optical transition separation in their SiV system limits the phase-readout performance, while increasing the magnetic field would push the qubit frequency into a regime where microwave control becomes increasingly lossy.

[1] I thank Kerim Köster for providing the scripts used to calculate the cavity reflection and scattering coefficients!

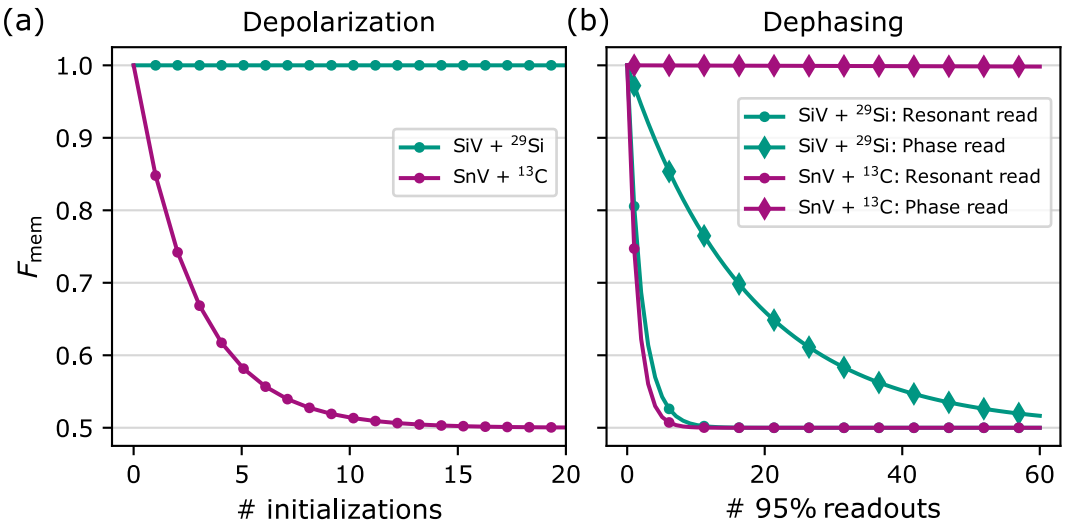

Figure 6.1.: Simulated comparison of nuclear-spin memory fidelity for the SnV center (purple) and the SiV center (Stas *et al.* [65], green). (a) Memory fidelity as a function of the number of electron-spin initializations for the SnV center, reflecting the depolarization of the ^{13}C nuclear spin using a remaining contrast $C_{\mathrm{nuc}} = 0.7$ per initialization. This effect is absent for the host ^{29}Si spin in the SiV system and thus unit fidelity is assumed. (b) Memory fidelity as a function of the number of photons scattered off a cavity, assuming identical cavity parameters for both systems. Circles correspond to a resonant readout scheme, diamonds to a phase readout. The SnV center benefits from more widely separated optical transitions and a narrower emitter linewidth, leading to significantly improved phase-readout performance. However, the nuclear-spin depolarization upon electron-spin initialization shown in (a) limits the overall memory fidelity.

However, the comparison must also include nuclear-spin depolarization during electron-spin initialization, which is an effect that is negligible in the case of a SiV center coupled to its host nuclear spin. In the system studied here, by contrast, the observed nuclear contrast decreases by approximately 30% per electron-spin initialization. We use this value as a reference and define the corresponding memory fidelity as $F_{\mathrm{mem}} = \frac{1}{2}\left(1 + C_{\mathrm{nuc}}^{n}\right)$, where n is the number of electron-spin initializations and $C_{\mathrm{nuc}} = 0.7$ is the remaining nuclear contrast per initialization, extracted from Fig. 5.22. [175]

This analysis reveals a rapid decay of the memory fidelity with the number of electron-spin initializations. For quantum-network applications, the overall performance will be limited by the smallest of the relevant fidelities. Under the assumptions used here, the proximal ^{13}C nuclear spin coupled to our SnV center would therefore be limited by initialization-induced depolarization, despite its favorable behavior under phase-readout. Moving to more weakly coupled nuclear spins could reduce the pseudo-secular hyperfine terms relative to the nuclear Zeeman energy and thereby suppress this limitation. In such a regime, the low-strain SnV center could benefit from the optical advantages discussed above, in particular the larger separation of the spin-conserving optical transitions and the narrower emitter linewidth. The coherent control of weakly coupled ^{13}C nuclear spins has recently been demonstrated by Beukers *et al.* [66], with dephasing times in the tens of milliseconds and coherence decay over hundreds of optical cycles, making these spins promising candidates for robust quantum memories.

Taken together, this work demonstrates coherent control of the electron spin of a low-strain SnV center and of a proximal ^{13}C nuclear spin coupled to it. A superconducting waveguide with reduced heating, careful magnetic-field alignment, and a qualitative model of the hyperfine interaction enabled control of both spins and characterization of the ^{13}C nuclear-spin decoherence under optical excitation. Future experiments can build on these results by combining the spin-control and coherence properties studied in this thesis with photonic integration. Improved photon collection and enhanced light-matter interaction will be important for assessing SnV-based systems under conditions closer to those required for quantum-network applications.

A. Appendix

A.1. Explicit representation of the gyromagnetic tensor $\hat{\mu}$

As discussed in Sec. 2.2, the interaction of the SnV center electron spin with the ac magnetic field can be derived from Eq. 2.38 by replacing the dc field components with the corresponding ac field components and expressing it in the eigenbasis of the dc magnetic field.

For this we need the eigenvectors of the static dc magnetic field Hamiltonian in Eq. 2.27. These can be computed as

$$\mathrm{EV}_{\mathrm{dc}} = \begin{pmatrix} \frac{\Phi_1 - i\Phi_2}{\sqrt{(\Delta+\Theta)^2+\Phi_1^2+\Phi_2^2}} & -\frac{\Delta+\Theta}{\sqrt{(\Delta+\Theta)^2+\Phi_1^2+\Phi_2^2}} \\ \frac{\Phi_1 - i\Phi_2}{\sqrt{(\Delta-\Theta)^2+\Phi_1^2+\Phi_2^2}} & \frac{\Delta-\Theta}{\sqrt{(\Delta-\Theta)^2+\Phi_1^2+\Phi_2^2}} \end{pmatrix}, \tag{A.1}$$

where the variables $\Phi_1 = \Phi(B_x^{\mathrm{dc}}, B_y^{\mathrm{dc}})$, $\Phi_2 = \Phi(-B_y^{\mathrm{dc}}, B_x^{\mathrm{dc}})$, $\Theta = \Theta(B_z^{\mathrm{dc}})$ and the splitting

$$\Delta = \sqrt{\Phi_1^2 + \Phi_2^2 + \Theta^2}, \tag{A.2}$$

can be derived from the variables Φ and Θ defined in Sec. 2.2.

Expressing the ac magnetic field Hamiltonian, by substituting the field components in Eq. 2.27 by ac fields, and representing it in the eigenbasis of the dc magnetic Hamiltonian using the eigenvectors above, gives

$$\hat{H}_{\mathrm{ac}} = \gamma_s \begin{pmatrix} H_{\mathrm{ac}}^{11} & H_{\mathrm{ac}}^{12} \\ H_{\mathrm{ac}}^{21} & H_{\mathrm{ac}}^{22} \end{pmatrix}, \tag{A.3}$$

where we defined the sub-matrices

$$H_{\mathrm{ac}}^{11} = -\frac{\Theta\Theta_{\mathrm{ac}} + \Phi_1\Phi_1^{\mathrm{ac}} + \Phi_2\Phi_2^{\mathrm{ac}}}{\Delta} \tag{A.4}$$

$$H_{\mathrm{ac}}^{12} = \frac{(\Theta^2 - \Delta^2)(-\Theta_{\mathrm{ac}}(\Phi_1^2 + \Phi_2^2) + \Theta(\Phi_1\Phi_1^{\mathrm{ac}} + \Phi_2\Phi_2^{\mathrm{ac}}))}{\Delta(\Phi_1^2 + \Phi_2^2)^{3/2}} + i\frac{\Phi_1^{\mathrm{ac}}\Phi_2 - \Phi_2^{\mathrm{ac}}\Phi_1}{\sqrt{\Phi_1^2 + \Phi_2^2}} \tag{A.5}$$

$$H_{\mathrm{ac}}^{21} = -\frac{(\Theta^2 - \Delta^2)(-\Theta_{\mathrm{ac}}(\Phi_1^2 + \Phi_2^2) + \Theta(\Phi_1\Phi_1^{\mathrm{ac}} + \Phi_2\Phi_2^{\mathrm{ac}}))}{\Delta(\Phi_1^2 + \Phi_2^2)^{3/2}} - i\frac{\Phi_1^{\mathrm{ac}}\Phi_2 - \Phi_2^{\mathrm{ac}}\Phi_1}{\sqrt{\Phi_1^2 + \Phi_2^2}} \tag{A.6}$$

$$H_{\mathrm{ac}}^{22} = \frac{\Theta\Theta_{\mathrm{ac}} + \Phi_1\Phi_1^{\mathrm{ac}} + \Phi_2\Phi_2^{\mathrm{ac}}}{\Delta}. \tag{A.7}$$

Using the general form of the interaction

$$\begin{aligned}\hat{H}_{\mathrm{ac}} = \boldsymbol{S}\cdot\hat{\mu}\cdot\boldsymbol{B}^{\mathrm{ac}} = -\frac{1}{2}\big[&(B_x^{\mathrm{ac}}\mu_{zx} + B_y^{ac}\mu_{zy} + B_z^{\mathrm{ac}}\mu_{zz})\sigma_z \\ &+(B_x^{\mathrm{ac}}\mu_{xx} + B_y^{\mathrm{ac}}\mu_{xy} + B_z^{\mathrm{ac}}\mu_{xz})\sigma_x \\ &-(B_x^{\mathrm{ac}}\mu_{yx} + B_y^{\mathrm{ac}}\mu_{yy} + B_z^{\mathrm{ac}}\mu_{yz})\sigma_y\big],\end{aligned}$$

and comparing each component of the two matrices yields the mediation matrix

$$\hat{\mu} = \begin{pmatrix} \frac{4\gamma_S^2 B_x \Theta \sin(x)}{|B_\perp|\Delta_q} & \frac{4\gamma_S^2 B_y \Theta \sin(x)}{|B_\perp|\Delta_q} & -\frac{4\gamma_S^2 \Theta |B_\perp| \sin(x)}{B_z \Delta_q} \\ -\frac{2\gamma_S B_y \sin(x)}{|B_\perp|} & \frac{2\gamma_S B_x \sin(x)}{|B_\perp|} & 0 \\ \frac{4\gamma_S^2 B_x \sin(x)^2}{\Delta_q} & \frac{4\gamma_S^2 B_y \sin(x)^2}{\Delta_q} & \frac{4\gamma_S^2 \Theta^2}{B_z \Delta_q} \end{pmatrix}. \tag{A.8}$$

A.2. Angular dependence of the spin-conserving transition linewidths

In order to check whether the difference in hyperfine coupling between the ground and excited states, as discussed in Sec. 5.4.4, has an angular dependence, we fit the data shown in Fig. 2.14. The resulting FWHM for all six frames measured is shown in Fig. A.1. As can be seen, the data show no additional angle-dependent broadening beyond the measurement uncertainty.

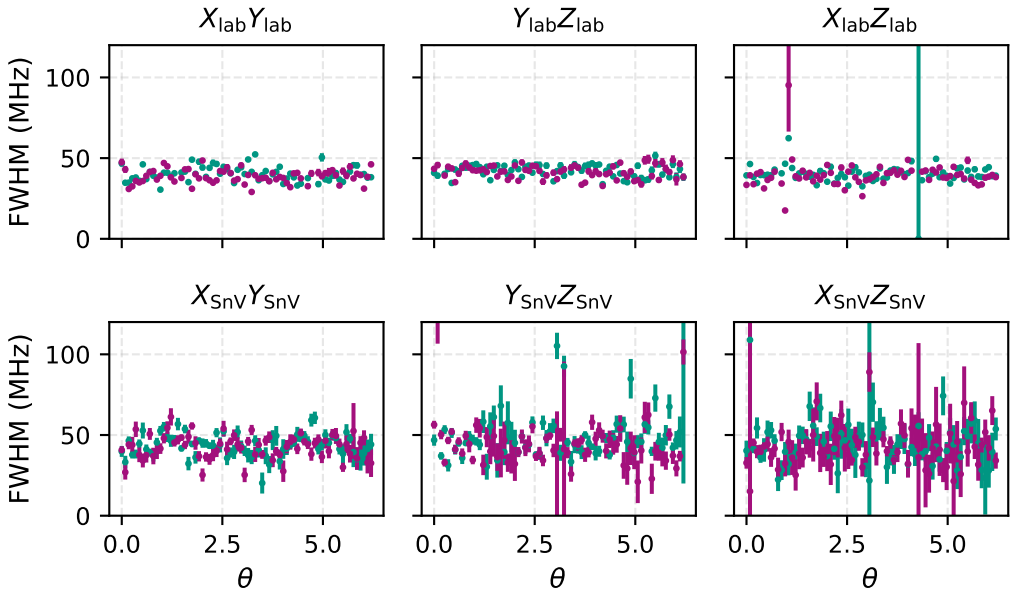

Figure A.1.: Angular dependence of the spin-conserving optical transition linewidths. FWHM of the two Lorentzians extracted from the dc magnetic angle-resolved spectra of Fig. 2.14, plotted as a function of the rotation angle θ for each of the six planes in either the lab- or SnV-frame. Markers in green and purple correspond to the lower- and higher-frequency branch, i.e. A1 and B2, respectively. Error bars are the standard deviations of the fit. Points near the branch crossing are omitted because the two Lorentzian transitions become unresolvable.

A.3. Diamond sample fabrication and further characterization

The diamond sample used in this work is an electronic-grade diamond membrane from *Element Six*, cut along the ⟨110⟩ directions with a (100) surface orientation. The initial dimensions are 2×2×0.04 mm, with a surface roughness of 4 nm (side A) and 2.3 nm (side B). To relieve residual strain from the manufacturing polish and reduce the surface roughness, both sides are etched by reactive ion etching by Philipp Fuchs (Saarland University) using the following procedures:

(i) Side A: 50 min Ar/Cl_2 + 5×(7 min Ar/Cl_2 + 13 min O_2),

(ii) Side B: 20 min Ar/Cl_2 + 5×(7 min Ar/Cl_2 + 15 min O_2) + 10 min Ar/Cl_2 + 15 min O_2.

For further details on this etching procedure, see Ref. [49]. In total, 7 µm of material is removed from each side, resulting in a final surface roughness of 3 nm (side A) and 2 nm (side B) measured by Julia Heupel (Kassel University) and confirmed by white-light-interferometry measurements, which yield a RMS surface roughness of $S_q = 0.5$ nm with a maximum peak-height of $S_p = 2.5$ nm over an area of 20 µm × 20 µm. The total final membrane thickness is 26 µm.

Side B, having the lower surface roughness, is used for ion implantation. The isotope ^{116}Sn is implanted at an energy of 65 keV with a fluence of 1×10^9 cm^{-2} by Michael Kieschnick at the Felix-Bloch-Institute for solid state physics (University Leipzig). Post-implantation, the sample is annealed at 1200 °C for 4 h at a pressure below 1×10^{-6} mbar by Philipp Fuchs. Surface cleaning is carried out by boiling in a tri-acid mixture (1:1:1, nitric acid:sulfuric acid:perchloric acid) at 400 °C.

The membrane is subsequently laser-cut into four pieces by *Diamond Materials*. All measurements were performed on SnV-F in sample SnV-2-B2 (see Karapatzakis [72] for comparison). The diamond piece used in this work is baked on a hotplate, which consists of a ramp-up from room-temperature to 450 °C over 2.5 h, a baking for 6 h and a final boil in piranha acid after cooldown.

Electron spin lifetime at elevated temperatures. As discussed throughout this thesis, the electron spin lifetime at the operating temperature of $T = 50$ mK is longer than all relevant experimental timescales. This regime was already studied in detail in our previous work [70], and a more extensive temperature- and field-dependent study was performed by Ioannis Karapatzakis [72]. Therefore, we do not repeat in presenting the electron spin lifetime measurements in greater detail here.

However, as mentioned in Sec. 2.5.1, the spin lifetime decreases significantly at elevated temperatures. To quantify this effect and to illustrate the measurement procedure, we show in Fig. A.2 an electron spin lifetime measurement performed by Ioannis Karapatzakis at $T = 3.6$ K. The system is initialized by resonantly pumping the A1 transition, followed by a variable waiting time t_{wait} and a second initialization pulse. The increase in fluorescence with increasing waiting time directly reflects the re-population of the initially depleted spin state and is used to extract the spin lifetime.

For the measurement shown in Fig. A.2, an external magnetic field of 400 mT is applied parallel to the quantization axis of the SnV center, i.e. $\theta_{\text{dc}} = 0°$. In the off-axis field configurations used for the angle-dependent Zeeman measurements in Sec. 2.5.1, and at the even higher temperatures used there, the spin lifetime is further reduced. This ensures that both spin states are populated during the measurement.

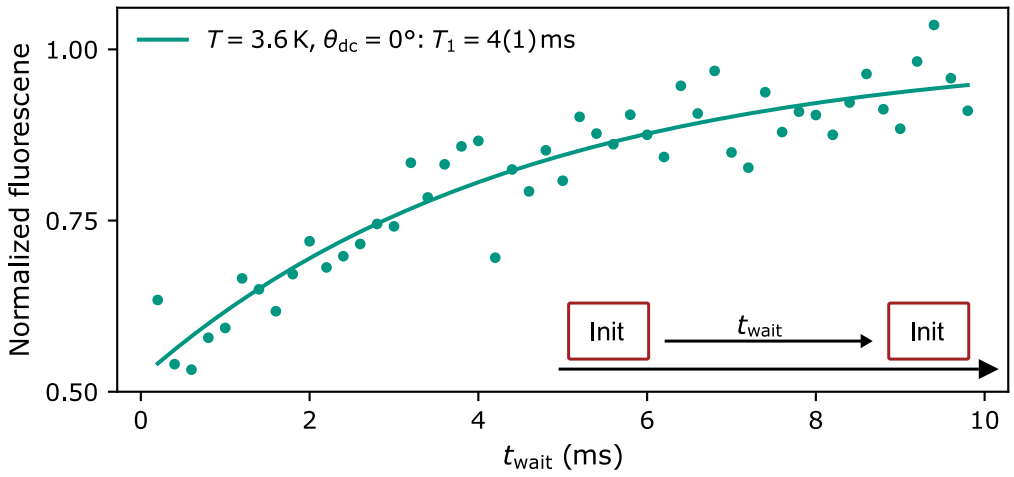

Figure A.2.: Electron spin lifetime measurement at $T = 3.6\,\mathrm{K}$. Normalized fluorescence as a function of the waiting time t_{wait} between two initialization pulses. The pulse sequence is shown schematically in the inset in the lower right. An external magnetic field of 400 mT is applied parallel to the quantization axis of the SnV center, i.e. $\theta_{dc} = 0°$. At an elevated temperature of $T = 3.6\,\mathrm{K}$, a spin lifetime of $T_1 = 4(1)\,\mathrm{ms}$ is measured.

Since no increase in fluorescence is observed during spin driving, we conclude that, at the operating temperature of $T = 50\,\mathrm{mK}$, the spin lifetime remains sufficiently long compared to the relevant experimental timescales. This indicates the absence of significant microwave-induced heating, since heating would lead to a visible increase in fluorescence.

A.4. Additional experimental setup details

The optical setup is the same as described in detail by Ioannis Karapatzakis in his thesis [72]. We therefore do not reproduce the full description here, but instead refer the reader to his work. A detailed overview of the optical setup is shown in Fig. A.3, which was taken from his thesis. For completeness, the setup is summarized in Sec. 2.3.2.

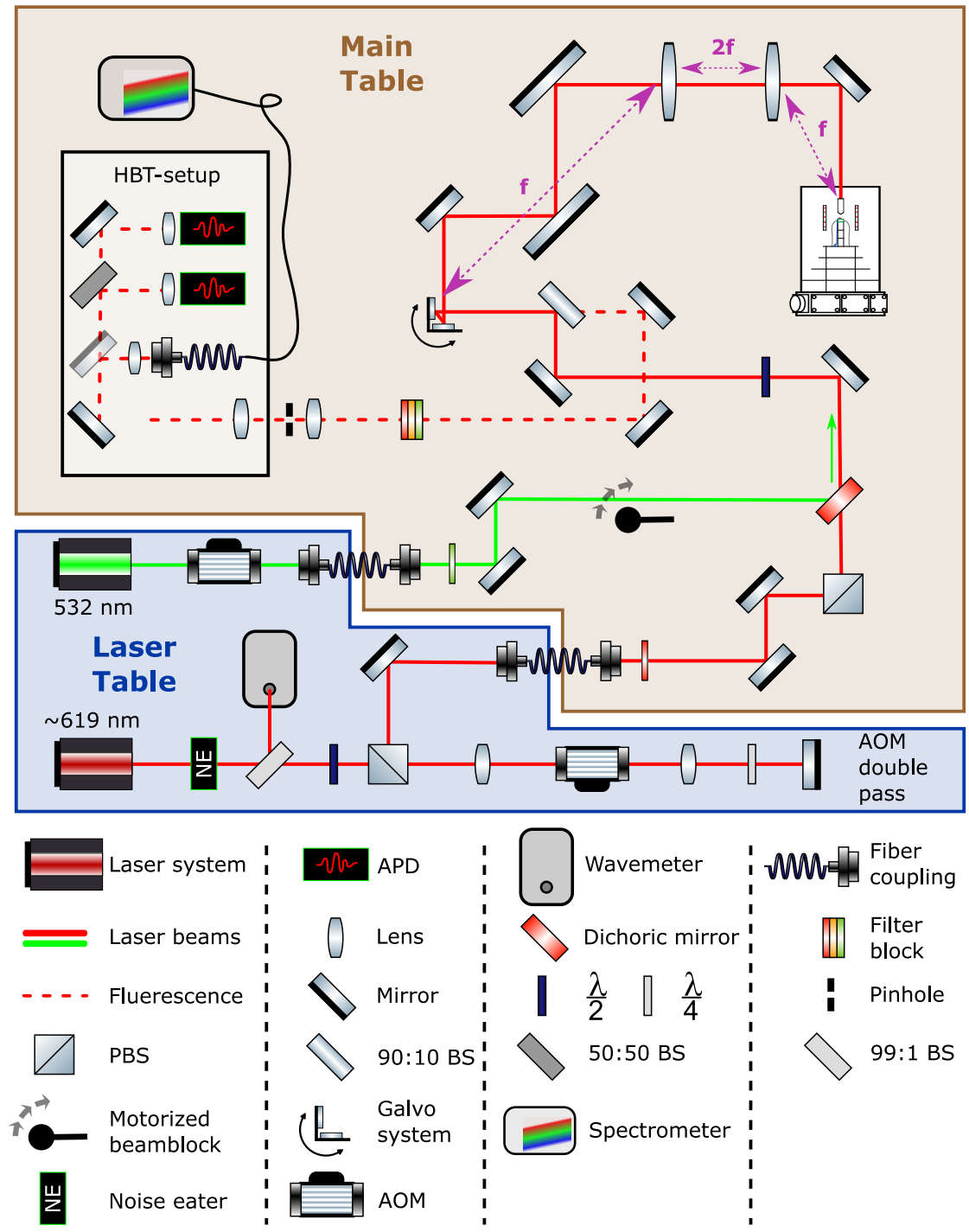

Figure A.3.: Optical setup of the experiment. The setup is distributed across two optical tables in the same laboratory: one dedicated to laser pulse generation (blue border) and one hosting the table-top cryostat and the detection components (brown border). Some of the components depicted in this image are from the ComponentLibrary by Alexander Franzen [93]. This figure was taken with permission from the thesis of Ioannis Karapatzakis [72].

A.5. List of abbreviations

Color centers

SnV	Tin-Vacancy
SiV	Silicon-Vacancy
GeV	Germanium-Vacancy
PbV	Lead-Vacancy
NV	Nitrogen-Vacancy

Theory

DJT	Dynamical Jahn-Teller (effect)
SALC	Symmetry-Adapted Linear Combinations
DFT	Density Functional Theory
SO	Spin-Orbit (coupling)
TLS	Two-level system
OU	Ornstein-Uhlenbeck (noise model)

Measurement techniques

ac	Alternating Current
dc	Direct Current
PLE	Photoluminescence Excitation
FWHM	Full Width at Half Maximum
PSB	Phonon Sideband
lab frame	Laboratory Coordinate System
EPR	Electron Paramagnetic Resonance
ODMR	Optically Detected Magnetic Resonance
NMR	Nuclear Magnetic Resonance
ODNR	Optically Detected Nuclear Resonance
ENDOR	Electron Nuclear Double Resonance
CPMG	Carr-Purcell-Meiboom-Gill (sequence)
RMBM	Randomized Benchmarking

Hyperfine Interactions

HF	Hyperfine (interaction)
NZ	Nuclear Zeeman (interaction)
NQ	Nuclear Quadrupole (interaction)
NN	Nuclear-Nuclear (interaction)
FC	Fermi Contact (interaction)
DD	Dipole-Dipole (interaction)

Hardware

AWG	Arbitrary Waveform Generator
MW (mw)	Microwave
RF (rf)	Radio frequency
mK	Millikelvin
TTL	Transistor-Transistor-Logic
AOM	Acousto Optical Modulator

List of Figures

List of Tables

Bibliography

[1] H. J. Kimble. "The quantum internet". In: *Nature* 453.7198 (2008), pp. 1023–1030. DOI: 10.1038/nature07127.

[2] C. H. Bennett, G. Brassard, and A. K. Ekert. "Quantum Cryptography". In: *Scientific American* 267.4 (1992), pp. 50–57.

[3] J. I. Cirac, P. Zoller, H. J. Kimble, et al. "Quantum State Transfer and Entanglement Distribution among Distant Nodes in a Quantum Network". In: *Physical Review Letters* 78.16 (1997), pp. 3221–3224. DOI: 10.1103/PhysRevLett.78.3221.

[4] S. Barz, E. Kashefi, A. Broadbent, et al. "Demonstration of Blind Quantum Computing". In: *Science* 335.6066 (2012), pp. 303–308. DOI: 10.1126/science.1214707.

[5] E. Knill, R. Laflamme, and W. H. Zurek. "Resilient Quantum Computation". In: *Science* 279.5349 (1998), pp. 342–345.

[6] V. Giovannetti, S. Lloyd, and L. Maccone. "Quantum-Enhanced Measurements: Beating the Standard Quantum Limit". In: *Science* 306.5700 (2004), pp. 1330–1336. DOI: 10.1126/science.1104149.

[7] H.-J. Briegel, W. Dür, J. I. Cirac, et al. "Quantum Repeaters: The Role of Imperfect Local Operations in Quantum Communication". In: *Physical Review Letters* 81.26 (1998), pp. 5932–5935. DOI: 10.1103/PhysRevLett.81.5932.

[8] L.-M. Duan, M. D. Lukin, J. I. Cirac, et al. "Long-distance quantum communication with atomic ensembles and linear optics". In: *Nature* 414.6862 (2001), pp. 413–418. DOI: 10.1038/35106500.

[9] A. Reiserer and G. Rempe. "Cavity-based quantum networks with single atoms and optical photons". In: *Reviews of Modern Physics* 87.4 (2015), pp. 1379–1418. DOI: 10.1103/RevModPhys.87.1379.

[10] W. K. Wootters and W. H. Zurek. "A single quantum cannot be cloned". In: *Nature* 299.5886 (1982), pp. 802–803. DOI: 10.1038/299802a0.

[11] L.-M. Duan and C. Monroe. "*Colloquium* : Quantum networks with trapped ions". In: *Reviews of Modern Physics* 82.2 (2010), pp. 1209–1224. DOI: 10.1103/RevModPhys.82.1209.

[12] V. Krutyanskiy, M. Canteri, M. Meraner, et al. "Telecom-Wavelength Quantum Repeater Node Based on a Trapped-Ion Processor". In: *Physical Review Letters* 130.21 (2023), p. 213601. DOI: 10.1103/PhysRevLett.130.213601.

[13] M. Żukowski, A. Zeilinger, M. A. Horne, et al. ""Event-ready-detectors" Bell experiment via entanglement swapping". In: *Phys. Rev. Lett.* 71 (26 1993), pp. 4287–4290. DOI: 10.1103/PhysRevLett.71.4287.

[14] C. H. Bennett, G. Brassard, C. Crépeau, et al. "Teleporting an unknown quantum state via dual classical and Einstein-Podolsky-Rosen channels". In: *Physical Review Letters* 70.13 (1993), pp. 1895–1899. DOI: 10.1103/PhysRevLett.70.1895.

[15] S. L. N. Hermans, M. Pompili, H. K. C. Beukers, et al. "Qubit teleportation between non-neighbouring nodes in a quantum network". In: *Nature* 605.7911 (2022), pp. 663–668. DOI: 10.1038/s41586-022-04697-y.

[16] N. Sangouard, C. Simon, H. de Riedmatten, et al. "Quantum repeaters based on atomic ensembles and linear optics". In: *Reviews of Modern Physics* 83.1 (2011), pp. 33–80. DOI: 10.1103/RevModPhys.83.33.

[17] R. Stockill, M. J. Stanley, L. Huthmacher, et al. "Phase-Tuned Entangled State Generation between Distant Spin Qubits". In: *Physical Review Letters* 119.1 (2017), p. 010503. DOI: 10.1103/PhysRevLett.119.010503.

[18] A. Delteil, Z. Sun, W.-b. Gao, et al. "Generation of heralded entanglement between distant hole spins". In: *Nature Physics* 12.3 (2016), pp. 218–223. DOI: 10.1038/nphys3605.

[19] M. T. Uysal, Ł. Dusanowski, H. Xu, et al. "Spin-Photon Entanglement of a Single Er 3 + Ion in the Telecom Band". In: *Physical Review X* 15.1 (2025), p. 011071. DOI: 10.1103/PhysRevX.15.011071.

[20] M. Schäfer, B. Kambs, D. Herrmann, et al. "Two-Stage, Low Noise Quantum Frequency Conversion of Single Photons from Silicon-Vacancy Centers in Diamond to the Telecom C-Band". In: *Advanced Quantum Technologies* 8.2 (2025), p. 2300228. DOI: 10.1002/qute.202300228.

[21] J. M. Brevoord, J. F. Geus, T. Turan, et al. "Quantum frequency conversion of single photons from a tin-vacancy center in diamond". In: *Optica Quantum* 3.6 (2025), pp. 583–589. DOI: 10.1364/OPTICAQ.576448.

[22] T. van Leent, M. Bock, F. Fertig, et al. "Entangling single atoms over 33 km telecom fibre". In: *Nature* 607.7917 (2022), pp. 69–73. DOI: 10.1038/s41586-022-04764-4.

[23] E. Bersin, M. Sutula, Y. Q. Huan, et al. "Telecom Networking with a Diamond Quantum Memory". In: *PRX Quantum* 5.1 (2024), p. 010303. DOI: 10.1103/PRXQuantum.5.010303.

[24] A. Tchebotareva, S. L. N. Hermans, P. C. Humphreys, et al. "Entanglement between a Diamond Spin Qubit and a Photonic Time-Bin Qubit at Telecom Wavelength". In: *Physical Review Letters* 123.6 (2019), p. 063601. DOI: 10.1103/PhysRevLett.123.063601.

[25] T. Strobel, M. Vyvlecka, I. Neureuther, et al. "Telecom-wavelength quantum teleportation using frequency-converted photons from remote quantum dots". In: *Nature Communications* 16.1 (2025), p. 10027. DOI: 10.1038/s41467-025-65912-8.

[26] M. Ruf, N. H. Wan, H. Choi, et al. "Quantum networks based on color centers in diamond". In: *Journal of Applied Physics* 130.7 (2021), p. 070901. DOI: 10.1063/5.0056534.

[27] D. L. Moehring, P. Maunz, S. Olmschenk, et al. "Entanglement of single-atom quantum bits at a distance". In: *Nature* 449.7158 (2007), pp. 68–71. DOI: 10.1038/nature06118.

[28] S. Ritter, C. Nölleke, C. Hahn, et al. "An elementary quantum network of single atoms in optical cavities". In: *Nature* 484.7393 (2012), pp. 195–200. DOI: 10.1038/nature11023.

[29] H. Bernien, B. Hensen, W. Pfaff, et al. "Heralded entanglement between solid-state qubits separated by three metres". In: *Nature* 497.7447 (2013), pp. 86–90. DOI: 10.1038/nature12016.

[30] B. Hensen, H. Bernien, A. E. Dréau, et al. "Loophole-free Bell inequality violation using electron spins separated by 1.3 kilometres". In: *Nature* 526.7575 (2015), pp. 682–686. DOI: 10.1038/nature15759.

[31] C. M. Knaut, A. Suleymanzade, Y.-C. Wei, et al. "Entanglement of nanophotonic quantum memory nodes in a telecom network". In: *Nature* 629.8012 (2024), pp. 573–578. DOI: 10.1038/s41586-024-07252-z.

[32] G. Balasubramanian, P. Neumann, D. Twitchen, et al. "Ultralong spin coherence time in isotopically engineered diamond". In: *Nature Materials* 8.5 (2009), pp. 383–387. DOI: 10.1038/nmat2420.

[33] M. H. Abobeih, J. Cramer, M. A. Bakker, et al. "One-second coherence for a single electron spin coupled to a multi-qubit nuclear-spin environment". In: *Nature Communications* 9.1 (2018), p. 2552. DOI: 10.1038/s41467-018-04916-z.

[34] N. Bar-Gill, L. M. Pham, A. Jarmola, et al. "Solid-state electronic spin coherence time approaching one second". In: *Nature Communications* 4.1 (2013), p. 1743. DOI: 10.1038/ncomms2771.

[35] C. E. Bradley, J. Randall, M. H. Abobeih, et al. "A Ten-Qubit Solid-State Spin Register with Quantum Memory up to One Minute". In: *Physical Review X* 9.3 (2019), p. 031045. DOI: 10.1103/PhysRevX.9.031045.

[36] S. Yang, Y. Wang, D. D. B. Rao, et al. "High-fidelity transfer and storage of photon states in a single nuclear spin". In: *Nature Photonics* 10.8 (2016), pp. 507–511. DOI: 10.1038/nphoton.2016.103.

[37] M. Pompili, S. L. N. Hermans, S. Baier, et al. "Realization of a multinode quantum network of remote solid-state qubits". In: *Science* 372.6539 (2021), pp. 259–264. DOI: 10.1126/science.abg1919.

[38] T. Legero, T. Wilk, A. Kuhn, et al. "Time-resolved two-photon quantum interference". In: *Applied Physics B* 77.8 (2003), pp. 797–802. DOI: 10.1007/s00340-003-1337-x.

[39] M. Ruf, M. IJspeert, S. van Dam, et al. “Optically Coherent Nitrogen-Vacancy Centers in Micrometer-Thin Etched Diamond Membranes”. In: *Nano Letters* 19.6 (2019), pp. 3987–3992. DOI: 10.1021/acs.nanolett.9b01316.

[40] H. Kaupp, C. Deutsch, H.-C. Chang, et al. “Scaling laws of the cavity enhancement for nitrogen-vacancy centers in diamond”. In: *Physical Review A* 88.5 (2013), p. 053812. DOI: 10.1103/PhysRevA.88.053812.

[41] L. Robledo, L. Childress, H. Bernien, et al. “High-fidelity projective read-out of a solid-state spin quantum register”. In: *Nature* 477.7366 (2011), pp. 574–578. DOI: 10.1038/nature10401.

[42] K. Nemoto, M. Trupke, S. J. Devitt, et al. “Photonic Architecture for Scalable Quantum Information Processing in Diamond”. In: *Physical Review X* 4.3 (2014), p. 031022. DOI: 10.1103/PhysRevX.4.031022.

[43] M. W. Doherty, N. B. Manson, P. Delaney, et al. “The nitrogen-vacancy colour centre in diamond”. In: *Physics Reports*. The nitrogen-vacancy colour centre in diamond 528.1 (2013), pp. 1–45. DOI: 10.1016/j.physrep.2013.02.001.

[44] L. Orphal-Kobin, K. Unterguggenberger, T. Pregnolato, et al. “Optically Coherent Nitrogen-Vacancy Defect Centers in Diamond Nanostructures”. In: *Physical Review X* 13.1 (2023), p. 011042. DOI: 10.1103/PhysRevX.13.011042.

[45] H. Bernien, L. Childress, L. Robledo, et al. “Two-Photon Quantum Interference from Separate Nitrogen Vacancy Centers in Diamond”. In: *Physical Review Letters* 108.4 (2012), p. 043604. DOI: 10.1103/PhysRevLett.108.043604.

[46] D. Riedel, I. Söllner, B. J. Shields, et al. “Deterministic Enhancement of Coherent Photon Generation from a Nitrogen-Vacancy Center in Ultrapure Diamond”. In: *Physical Review X* 7.3 (2017), p. 031040. DOI: 10.1103/PhysRevX.7.031040.

[47] A. Faraon, C. Santori, Z. Huang, et al. “Coupling of Nitrogen-Vacancy Centers to Photonic Crystal Cavities in Monocrystalline Diamond”. In: *Physical Review Letters* 109.3 (2012), p. 033604. DOI: 10.1103/PhysRevLett.109.033604.

[48] S. L. Mouradian, T. Schröder, C. B. Poitras, et al. “Scalable Integration of Long-Lived Quantum Memories into a Photonic Circuit”. In: *Physical Review X* 5.3 (2015), p. 031009. DOI: 10.1103/PhysRevX.5.031009.

[49] J. Heupel, M. Pallmann, J. Körber, et al. “Fabrication of High-Quality Thin Single-Crystal Diamond Membranes with Low Surface Roughness”. In: *physica status solidi (a)* 220.4 (2023), p. 2200465. DOI: https://doi.org/10.1002/pssa.202200465.

[50] D. Hunger, T. Steinmetz, Y. Colombe, et al. “A fiber Fabry–Perot cavity with high finesse”. In: *New Journal of Physics* 12.6 (2010), p. 065038. DOI: 10.1088/1367-2630/12/6/065038.

[51] E. Janitz, M. Ruf, M. Dimock, et al. “Fabry-Perot microcavity for diamond-based photonics”. In: *Physical Review A* 92.4 (2015), p. 043844. DOI: 10.1103/PhysRevA.92.043844.

[52] S. B. van Dam, M. Ruf, and R. Hanson. "Optimal design of diamond-air microcavities for quantum networks using an analytical approach". In: *New Journal of Physics* 20.11 (2018), p. 115004. DOI: 10.1088/1367-2630/aaec29.

[53] J. Körber, M. Pallmann, J. Heupel, et al. "Scanning Cavity Microscopy of a Single-Crystal Diamond Membrane". In: *Physical Review Applied* 19.6 (2023), p. 064057. DOI: 10.1103/PhysRevApplied.19.064057.

[54] M. Pallmann, K. Köster, Y. Zhang, et al. "Cavity-Mediated Collective Emission from Few Emitters in a Diamond Membrane". In: *Physical Review X* 14.4 (2024), p. 041055. DOI: 10.1103/PhysRevX.14.041055.

[55] G. Thiering and A. Gali. "Ab Initio Magneto-Optical Spectrum of Group-IV Vacancy Color Centers in Diamond". In: *Physical Review X* 8.2 (2018), p. 021063. DOI: 10.1103/PhysRevX.8.021063.

[56] T. Schröder, M. E. Trusheim, M. Walsh, et al. "Scalable focused ion beam creation of nearly lifetime-limited single quantum emitters in diamond nanostructures". In: *Nature Communications* 8.1 (2017), p. 15376. DOI: 10.1038/ncomms15376.

[57] E. N. Knall, C. M. Knaut, R. Bekenstein, et al. "Efficient Source of Shaped Single Photons Based on an Integrated Diamond Nanophotonic System". In: *Physical Review Letters* 129.5 (2022), p. 053603. DOI: 10.1103/PhysRevLett.129.053603.

[58] K. D. Jahnke, A. Sipahigil, J. M. Binder, et al. "Electron–phonon processes of the silicon-vacancy centre in diamond". In: *New Journal of Physics* 17.4 (2015), p. 043011. DOI: 10.1088/1367-2630/17/4/043011.

[59] J. R. Maze, A. Gali, E. Togan, et al. "Properties of nitrogen-vacancy centers in diamond: the group theoretic approach". In: *New Journal of Physics* 13.2 (2011), p. 025025. DOI: 10.1088/1367-2630/13/2/025025.

[60] D. D. Sukachev, A. Sipahigil, C. T. Nguyen, et al. "Silicon-Vacancy Spin Qubit in Diamond: A Quantum Memory Exceeding 10 ms with Single-Shot State Readout". In: *Physical Review Letters* 119.22 (2017), p. 223602. DOI: 10.1103/PhysRevLett.119.223602.

[61] A. Sipahigil, R. E. Evans, D. D. Sukachev, et al. "An integrated diamond nanophotonics platform for quantum-optical networks". In: *Science* 354.6314 (2016), pp. 847–850. DOI: 10.1126/science.aah6875.

[62] C. T. Nguyen, D. D. Sukachev, M. K. Bhaskar, et al. "Quantum Network Nodes Based on Diamond Qubits with an Efficient Nanophotonic Interface". In: *Physical Review Letters* 123.18 (2019), p. 183602. DOI: 10.1103/PhysRevLett.123.183602.

[63] C. T. Nguyen, D. D. Sukachev, M. K. Bhaskar, et al. "An integrated nanophotonic quantum register based on silicon-vacancy spins in diamond". In: *Phys. Rev. B* 100.16 (2019), p. 165428. DOI: 10.1103/PhysRevB.100.165428.

[64] M. K. Bhaskar, R. Riedinger, B. Machielse, et al. "Experimental demonstration of memory-enhanced quantum communication". In: *Nature* 580.7801 (2020), pp. 60–64. DOI: 10.1038/s41586-020-2103-5.

[65] P.-J. Stas, Y. Q. Huan, B. Machielse, et al. “Robust multi-qubit quantum network node with integrated error detection”. In: *Science* 378.6619 (2022), pp. 557–560. DOI: 10.1126/science.add9771.

[66] H. K. C. Beukers, C. Waas, M. Pasini, et al. “Control of Solid-State Nuclear Spin Qubits Using an Electron Spin-1/2”. In: *Phys. Rev. X* 15.2 (2025), p. 021011. DOI: 10.1103/PhysRevX.15.021011.

[67] A. Reiserer, N. Kalb, M. S. Blok, et al. “Robust Quantum-Network Memory Using Decoherence-Protected Subspaces of Nuclear Spins”. In: *Physical Review X* 6.2 (2016), p. 021040. DOI: 10.1103/PhysRevX.6.021040.

[68] T. Iwasaki, Y. Miyamoto, T. Taniguchi, et al. “Tin-Vacancy Quantum Emitters in Diamond”. In: *Physical Review Letters* 119.25 (2017), p. 253601.

[69] S. Meesala, Y.-I. Sohn, B. Pingault, et al. “Strain engineering of the silicon-vacancy center in diamond”. In: *Physical Review B* 97.20 (2018). DOI: 10.1103/PhysRevB.97.205444.

[70] I. Karapatzakis, J. Resch, M. Schrodin, et al. “Microwave Control of the Tin-Vacancy Spin Qubit in Diamond with a Superconducting Waveguide”. In: *Phys. Rev. X* 14.3 (2024), p. 031036. DOI: 10.1103/PhysRevX.14.031036.

[71] J. Resch, I. Karapatzakis, M. Elshorbagy, et al. “High-Fidelity Control of a ^{13}C Nuclear Spin Coupled to a Tin-Vacancy Center in Diamond”. In: *Phys. Rev. X* 16 (1 2026), p. 011060. DOI: 10.1103/bmc6-qvwq.

[72] I. Karapatzakis. “Microwave Control of the Tin-Vacancy Spin Qubit in Diamond with a Superconducting Waveguide”. PhD thesis. 2025. DOI: 10.5445/IR/1000187678.

[73] C. Hepp. “Electronic structure of the silicon vacancy color center in diamond”. PhD thesis. 2014. DOI: 10.22028/D291-23020.

[74] C. Hepp, T. Müller, V. Waselowski, et al. “Electronic Structure of the Silicon Vacancy Color Center in Diamond”. In: *Physical Review Letters* 112.3 (2014), p. 036405. DOI: 10.1103/PhysRevLett.112.036405.

[75] A. Gali and J. R. Maze. “*Ab initio* study of the split silicon-vacancy defect in diamond: Electronic structure and related properties”. In: *Physical Review B* 88.23 (2013), p. 235205. DOI: 10.1103/PhysRevB.88.235205.

[76] J. Görlitz, D. Herrmann, P. Fuchs, et al. “Coherence of a charge stabilised tin-vacancy spin in diamond”. In: *npj Quantum Information* 8.1 (2022), pp. 1–9. DOI: 10.1038/s41534-022-00552-0.

[77] Y. Narita, P. Wang, K. Ikeda, et al. “Multiple Tin-Vacancy Centers in Diamond with Nearly Identical Photon Frequency and Linewidth”. In: *Phys. Rev. Appl.* 19.2 (2023), p. 024061. DOI: 10.1103/PhysRevApplied.19.024061.

[78] M. K. Bhaskar, D. D. Sukachev, A. Sipahigil, et al. “Quantum Nonlinear Optics with a Germanium-Vacancy Color Center in a Nanoscale Diamond Waveguide”. In: *Physical Review Letters* 118.22 (2017), p. 223603. DOI: 10.1103/PhysRevLett.118.223603.

[79] J. Görlitz, D. Herrmann, G. Thiering, et al. “Spectroscopic investigations of negatively charged tin-vacancy centres in diamond”. In: *New Journal of Physics* 22.1 (2020), p. 013048. DOI: 10.1088/1367-2630/ab6631.

[80] G. Pieplow, M. Belhassen, and T. Schröder. “Efficient microwave spin control of negatively charged group-IV color centers in diamond”. In: *Phys. Rev. B* 109 (11 2024), p. 115409. DOI: 10.1103/PhysRevB.109.115409.

[81] F. S. Ham. “Dynamical Jahn-Teller Effect in Paramagnetic Resonance Spectra: Orbital Reduction Factors and Partial Quenching of Spin-Orbit Interaction”. In: *Physical Review* 138.6A (1965), pp. 1727–1740. DOI: 10.1103/PhysRev.138.A1727.

[82] X. Guo, A. M. Stramma, Z. Li, et al. “Microwave-Based Quantum Control and Coherence Protection of Tin-Vacancy Spin Qubits in a Strain-Tuned Diamond-Membrane Heterostructure”. In: *Phys. Rev. X* 13.4 (2023), p. 041037. DOI: 10.1103/PhysRevX.13.041037.

[83] J. M. Brevoord, L. G. C. Wienhoven, N. Codreanu, et al. “Large-range tuning and stabilization of the optical transition of diamond tin-vacancy centers by in situ strain control”. In: *Applied Physics Letters* 126.17 (2025), p. 174001. DOI: 10.1063/5.0251211.

[84] E. I. Rosenthal, C. P. Anderson, H. C. Kleidermacher, et al. “Microwave Spin Control of a Tin-Vacancy Qubit in Diamond”. In: *Phys. Rev. X* 13.3 (2023), p. 031022. DOI: 10.1103/PhysRevX.13.031022.

[85] V. Paulisch, H. Rui, H. K. Ng, et al. “Beyond adiabatic elimination: A hierarchy of approximations for multi-photon processes”. In: *The European Physical Journal Plus* 129.1 (2014), p. 12. DOI: 10.1140/epjp/i2014-14012-8.

[86] A. Schweiger and G. Jeschke. *Principles of pulse electron paramagnetic resonance*. Oxford, 2005.

[87] J. H. N. Loubser and J. A. v. Wyk. “Electron spin resonance in the study of diamond”. In: *Reports on Progress in Physics* 41.8 (1978), p. 1201. DOI: 10.1088/0034-4885/41/8/002.

[88] C. J. Foot. *Atomic physics*. Vol. 7. Oxford Master Series in Physics. 2005.

[89] K. Senkalla. “Group IV color center in diamond as promising quantum network nodes : the potential of germanium-vacancy as quantum memory”. PhD thesis. Universität Ulm, 2025. DOI: 10.18725/OPARU-56855.

[90] A. M. Stramma. “The tin-vacancy centre in diamond: a coherent spin-photon interface for quantum network nodes”. PhD thesis. 2024. DOI: 10.17863/CAM.112161.

[91] J. Resch. “Spin manipulation of Nitrogen-Vacancy centers in diamond for cavity-enhanced spin-photon interfaces”. Master’s thesis. Karlsruhe, 2021.

[92] A. Zilz. “Investigation of the rarefied gas flow in the pumping tube of a 3he/4he dilution refrigerator”. Master’s thesis. Karlsruhe, 2022.

[93] A. Franzen. *ComponentLibrary - CC BY-NC 3.0*. 2023. DOI: https://www.gwoptics.org/ComponentLibrary/.

[94] A. Faraon, P. E. Barclay, C. Santori, et al. "Resonant enhancement of the zero-phonon emission from a colour centre in a diamond cavity". In: *Nature Photonics* 5.5 (2011), pp. 301–305. DOI: 10.1038/nphoton.2011.52.

[95] S. D. Tchernij, T. Herzig, J. Forneris, et al. "Single-Photon-Emitting Optical Centers in Diamond Fabricated upon Sn Implantation". In: *ACS Photonics* 4.10 (2017), pp. 2580–2586. DOI: 10.1021/acsphotonics.7b00904.

[96] A. J. Häußler, P. Heller, L. P. McGuinness, et al. "Optical depth localization of nitrogen-vacancy centers in diamond with nanometer accuracy". In: *Optics Express* 22.24 (2014), pp. 29986–29995. DOI: 10.1364/OE.22.029986.

[97] L. De Santis, M. E. Trusheim, K. C. Chen, et al. "Investigation of the Stark Effect on a Centrosymmetric Quantum Emitter in Diamond". In: *Physical Review Letters* 127.14 (2021), p. 147402. DOI: 10.1103/PhysRevLett.127.147402.

[98] S. Aghaeimeibodi, D. Riedel, A. E. Rugar, et al. "Electrical Tuning of Tin-Vacancy Centers in Diamond". In: *Physical Review Applied* 15.6 (2021), p. 064010. DOI: 10.1103/PhysRevApplied.15.064010.

[99] S. Chakravarthi, C. Pederson, Z. Kazi, et al. "Impact of surface and laser-induced noise on the spectral stability of implanted nitrogen-vacancy centers in diamond". In: *Physical Review B* 104.8 (2021), p. 085425. DOI: 10.1103/PhysRevB.104.085425.

[100] G. Pieplow, C. G. Torun, C. Gurr, et al. "Quantum electrometer for time-resolved material science at the atomic lattice scale". In: *Nature Communications* 16.1 (2025), p. 6435. DOI: 10.1038/s41467-025-61839-2.

[101] P. Tamarat, T. Gaebel, J. R. Rabeau, et al. "Stark Shift Control of Single Optical Centers in Diamond". In: *Physical Review Letters* 97.8 (2006), p. 083002. DOI: 10.1103/PhysRevLett.97.083002.

[102] P. Tamarat, N. B. Manson, J. P. Harrison, et al. "Spin-flip and spin-conserving optical transitions of the nitrogen-vacancy centre in diamond". In: *New Journal of Physics* 10.4 (2008), p. 045004. DOI: 10.1088/1367-2630/10/4/045004.

[103] E. I. Rosenthal, S. Biswas, G. Scuri, et al. "Single-Shot Readout and Weak Measurement of a Tin-Vacancy Qubit in Diamond". In: *Phys. Rev. X* 14.4 (2024), p. 041008. DOI: 10.1103/PhysRevX.14.041008.

[104] R. Debroux, C. P. Michaels, C. M. Purser, et al. "Quantum Control of the Tin-Vacancy Spin Qubit in Diamond". In: *Phys. Rev. X* 11.4 (2021), p. 041041. DOI: 10.1103/PhysRevX.11.041041.

[105] M. H. Appel, A. Tiranov, A. Javadi, et al. "Coherent Spin-Photon Interface with Waveguide Induced Cycling Transitions". In: *Phys. Rev. Lett.* 126.1 (2021), p. 013602. DOI: 10.1103/PhysRevLett.126.013602.

[106] P. Gundlapalli, P. J. Vetter, G. Genov, et al. *High-Fidelity Single-Shot Readout and Selective Nuclear Spin Control for a Spin-1/2 Quantum Register in Diamond*. 2025. DOI: 10.48550/arXiv.2510.09164.

[107] B. D'Anjou and W. A. Coish. "Optimal post-processing for a generic single-shot qubit readout". In: *Physical Review A* 89.1 (2014), p. 012313. DOI: 10.1103/PhysRevA.89.012313.

[108] Ł. Cywiński, R. M. Lutchyn, C. P. Nave, et al. "How to enhance dephasing time in superconducting qubits". In: *Phys. Rev. B* 77.17 (2008), p. 174509. DOI: 10.1103/PhysRevB.77.174509.

[109] A. E. Rugar, S. Aghaeimeibodi, D. Riedel, et al. "Quantum Photonic Interface for Tin-Vacancy Centers in Diamond". In: *Physical Review X* 11.3 (2021), p. 031021. DOI: 10.1103/PhysRevX.11.031021.

[110] H. Lee, H. C. Kleidermacher, A. J. Stein, et al. "Quantum nanophotonic interface for tin-vacancy centers in thin-film diamond". In: *Physical Review Applied* 25.4 (2026), p. 044074. DOI: 10.1103/vwt7-b64x.

[111] I. B. W. Harris and D. Englund. "Coherence of group-IV color centers". In: *Physical Review B* 109.8 (2024), p. 085414. DOI: 10.1103/PhysRevB.109.085414.

[112] C. G. Torun, J. H. D. Munns, F. M. Herrmann, et al. "Optical probing of phononic properties of a tin-vacancy color center in diamond". In: *Phys. Rev. Res.* (2026). DOI: 10.1103/swkr-r6mb.

[113] J. N. Becker, B. Pingault, D. Groß, et al. "All-Optical Control of the Silicon-Vacancy Spin in Diamond at Millikelvin Temperatures". In: *Physical Review Letters* 120.5 (2018), p. 053603. DOI: 10.1103/PhysRevLett.120.053603.

[114] D. P. DiVincenzo. "The Physical Implementation of Quantum Computation". In: *Fortschritte der Physik* 48.9-11 (2000), pp. 771–783. DOI: 10.1002/1521-3978(200009)48:9/11<771::AID-PROP771>3.0.CO;2-E.

[115] N. Bar-Gill, L. M. Pham, C. Belthangady, et al. "Suppression of spin-bath dynamics for improved coherence of multi-spin-qubit systems". In: *Nature Communications* 3.1 (2012), p. 858. DOI: 10.1038/ncomms1856.

[116] V. Somjit, G. Grant, S. Chattaraj, et al. "Optimizing spin qubit coherence through materials codesign". In: *MRS Bulletin* (2026). DOI: 10.1557/s43577-026-01069-z.

[117] H.-P. Breuer and F. Petruccione. *The theory of open quantum systems*. Oxford, 2010.

[118] A. J. Leggett, S. Chakravarty, A. T. Dorsey, et al. "Dynamics of the dissipative two-state system". In: *Reviews of Modern Physics* 59.1 (1987), pp. 1–85. DOI: 10.1103/RevModPhys.59.1.

[119] Y. C. Cheng and R. J. Silbey. "Markovian Approximation in the Relaxation of Open Quantum Systems". In: *The Journal of Physical Chemistry B* 109.45 (2005), pp. 21399–21405. DOI: 10.1021/jp051303o.

[120] L. J. Rogers, K. D. Jahnke, M. H. Metsch, et al. "All-Optical Initialization, Readout, and Coherent Preparation of Single Silicon-Vacancy Spins in Diamond". In: *Physical Review Letters* 113.26 (2014), p. 263602. DOI: 10.1103/PhysRevLett.113.263602.

[121] A. Jarmola, V. M. Acosta, K. Jensen, et al. “Temperature- and Magnetic-Field-Dependent Longitudinal Spin Relaxation in Nitrogen-Vacancy Ensembles in Diamond”. In: *Physical Review Letters* 108.19 (2012), p. 197601. DOI: 10.1103/PhysRevLett.108.197601.

[122] J. Ahn, C. Wicker, N. Bitner, et al. “Extended spin relaxation times of optically addressed vanadium defects in silicon carbide at telecommunication frequencies”. In: *Physical Review Applied* 22.4 (2024), p. 044078. DOI: 10.1103/PhysRevApplied.22.044078.

[123] N. Lambert, E. Giguʿere, P. Menczel, et al. “QuTiP 5: The Quantum Toolbox in Python”. In: *Physics Reports* 1153 (2026), pp. 1–62. DOI: 10.1016/j.physrep.2025.10.001.

[124] M. F. Pascual-Winter, R.-C. Tongning, T. Chanelière, et al. “Spin coherence lifetime extension in Tm 3 + :YAG through dynamical decoupling”. In: *Physical Review B* 86.18 (2012), p. 184301. DOI: 10.1103/PhysRevB.86.184301.

[125] Z.-H. Wang, G. de Lange, D. Ristè, et al. “Comparison of dynamical decoupling protocols for a nitrogen-vacancy center in diamond”. In: *Phys. Rev. B* 85.15 (2012), p. 155204. DOI: 10.1103/PhysRevB.85.155204.

[126] G. de Lange, Z. H. Wang, D. Ristè, et al. “Universal Dynamical Decoupling of a Single Solid-State Spin from a Spin Bath”. In: *Science* 330.6000 (2010), pp. 60–63. DOI: 10.1126/science.1192739.

[127] J. R. Klauder and P. W. Anderson. “Spectral Diffusion Decay in Spin Resonance Experiments”. In: *Physical Review* 125.3 (1962), pp. 912–932. DOI: 10.1103/PhysRev.125.912.

[128] R. de Sousa. “Electron Spin as a Spectrometer of Nuclear-Spin Noise and Other Fluctuations”. In: *Electron Spin Resonance and Related Phenomena in Low-Dimensional Structures*. Ed. by M. Fanciulli. Berlin, Heidelberg, 2009, pp. 183–220. DOI: 10.1007/978-3-540-79365-6_10.

[129] L. Jiang, M. V. G. Dutt, E. Togan, et al. “Coherence of an Optically Illuminated Single Nuclear Spin Qubit”. In: *Physical Review Letters* 100.7 (2008), p. 073001. DOI: 10.1103/PhysRevLett.100.073001.

[130] K. Senkalla, G. Genov, M. H. Metsch, et al. “Germanium Vacancy in Diamond Quantum Memory Exceeding 20 ms”. In: *Phys. Rev. Lett.* 132.2 (2024), p. 026901. DOI: 10.1103/PhysRevLett.132.026901.

[131] M. Zahedian, V. Vorobyov, and J. Wrachtrup. “Blueprint for efficient nuclear spin characterization with color centers”. In: *Physical Review B* 109.21 (2024), p. 214111. DOI: 10.1103/PhysRevB.109.214111.

[132] B. A. Myers, A. Ariyaratne, and A. C. B. Jayich. “Double-Quantum Spin-Relaxation Limits to Coherence of Near-Surface Nitrogen-Vacancy Centers”. In: *Physical Review Letters* 118.19 (2017), p. 197201. DOI: 10.1103/PhysRevLett.118.197201.

[133] J. Medford, Ł. Cywiński, C. Barthel, et al. "Scaling of Dynamical Decoupling for Spin Qubits". In: *Phys. Rev. Lett.* 108.8 (2012), p. 086802. DOI: 10.1103/PhysRevLett.108.086802.

[134] J. H. Bodey, R. Stockill, E. V. Denning, et al. "Optical spin locking of a solid-state qubit". In: *npj Quantum Information* 5.1 (2019), p. 95. DOI: 10.1038/s41534-019-0206-3.

[135] M. H. Metsch, K. Senkalla, B. Tratzmiller, et al. "Initialization and Readout of Nuclear Spins via a Negatively Charged Silicon-Vacancy Center in Diamond". In: *Physical Review Letters* 122.19 (2019), p. 190503. DOI: 10.1103/PhysRevLett.122.190503.

[136] E. Knill, D. Leibfried, R. Reichle, et al. "Randomized benchmarking of quantum gates". In: *Physical Review A* 77.1 (2008), p. 012307. DOI: 10.1103/PhysRevA.77.012307.

[137] E. Magesan, J. M. Gambetta, and J. Emerson. "Scalable and Robust Randomized Benchmarking of Quantum Processes". In: *Physical Review Letters* 106.18 (2011), p. 180504. DOI: 10.1103/PhysRevLett.106.180504.

[138] T. Koch, C. Godfrin, V. Adam, et al. "Industrial 300 mm wafer processed spin qubits in natural silicon/silicon-germanium". In: *npj Quantum Information* 11.1 (2025), p. 59. DOI: 10.1038/s41534-025-01016-x.

[139] E. Magesan, J. M. Gambetta, and J. Emerson. "Characterizing quantum gates via randomized benchmarking". In: *Phys. Rev. A* 85.4 (2012), p. 042311. DOI: 10.1103/PhysRevA.85.042311.

[140] J. M. Epstein, A. W. Cross, E. Magesan, et al. "Investigating the limits of randomized benchmarking protocols". In: *Physical Review A* 89.6 (2014), p. 062321. DOI: 10.1103/PhysRevA.89.062321.

[141] C. G. Torun, M. Gökçe, T. K. Bracht, et al. "SUPER and femtosecond spin-conserving coherent excitation of a tin-vacancy color center in diamond". In: *Nature Communications* 17.1 (2026), p. 2154. DOI: 10.1038/s41467-026-69911-1.

[142] S. A. Wolf, J. J. Kennedy, and M. Nisenoff. "Properties of superconducting rf sputtered ultrathin films of Nb". In: *Journal of Vacuum Science and Technology* 13.1 (1976), pp. 145–147. DOI: 10.1116/1.568809.

[143] M. E. Trusheim, B. Pingault, N. H. Wan, et al. "Transform-Limited Photons From a Coherent Tin-Vacancy Spin in Diamond". In: *Physical review letters* 124.2 (2020), p. 023602. DOI: 10.1103/PhysRevLett.124.023602.

[144] N. Grimm, K. Senkalla, P. J. Vetter, et al. "Coherent Control of a Long-Lived Nuclear Memory Spin in a Germanium-Vacancy Multi-Qubit Node". In: *Phys. Rev. Lett.* 134.4 (2025), p. 043603. DOI: 10.1103/PhysRevLett.134.043603.

[145] T. H. Taminiau, J. J. T. Wagenaar, T. Van Der Sar, et al. "Detection and Control of Individual Nuclear Spins Using a Weakly Coupled Electron Spin". In: *Physical Review Letters* 109.13 (2012), p. 137602. DOI: 10.1103/PhysRevLett.109.137602.

[146] L. Childress, M. V. G. Dutt, J. M. Taylor, et al. "Coherent Dynamics of Coupled Electron and Nuclear Spin Qubits in Diamond". In: *Science* 314.5797 (2006), pp. 281–285. DOI: 10.1126/science.1131871.

[147] L. T. Hall, C. D. Hill, J. H. Cole, et al. "Ultrasensitive diamond magnetometry using optimal dynamic decoupling". In: *Physical Review B* 82.4 (2010), p. 045208. DOI: 10.1103/PhysRevB.82.045208.

[148] N. V. Prokof'ev and P. C. E. Stamp. "Theory of the spin bath". In: *Reports on Progress in Physics* 63.4 (2000), p. 669. DOI: 10.1088/0034-4885/63/4/204.

[149] T. Gaebel, M. Domhan, I. Popa, et al. "Room-temperature coherent coupling of single spins in diamond". In: *Nature Physics* 2.6 (2006), pp. 408–413. DOI: 10.1038/nphys318.

[150] G. R. Khutsishvili. "Spin diffusion". In: *Physics-Uspekhi* 8.5 (1966), pp. 743–769.

[151] S. Chandrasekhar. "Stochastic Problems in Physics and Astronomy". In: *Reviews of Modern Physics* 15.1 (1943), pp. 1–89. DOI: 10.1103/RevModPhys.15.1.

[152] J. R. Maze, J. M. Taylor, and M. D. Lukin. "Electron spin decoherence of single nitrogen-vacancy defects in diamond". In: *Physical Review B* 78.9 (2008), p. 094303. DOI: 10.1103/PhysRevB.78.094303.

[153] N. Mizuochi, P. Neumann, F. Rempp, et al. "Coherence of single spins coupled to a nuclear spin bath of varying density". In: *Physical Review B* 80.4 (2009), p. 041201. DOI: 10.1103/PhysRevB.80.041201.

[154] B. A. Myers, A. Das, M. C. Dartiailh, et al. "Probing Surface Noise with Depth-Calibrated Spins in Diamond". In: *Phys. Rev. Lett.* 113.2 (2014), p. 027602. DOI: 10.1103/PhysRevLett.113.027602.

[155] G. Wolfowicz, F. J. Heremans, C. P. Anderson, et al. *Qubit guidelines for solid-state spin defects*. 2020. DOI: 10.48550/arXiv.2010.16395.

[156] I. B. Harris, C. P. Michaels, K. C. Chen, et al. "Hyperfine Spectroscopy of Isotopically Engineered Group-IV Color Centers in Diamond". In: *PRX Quantum* 4 (4 2023), p. 040301. DOI: 10.1103/PRXQuantum.4.040301.

[157] M. Mohseni, L. Razinkovas, V. Žalandauskas, et al. "Magneto-optical properties of group-IV vacancy centers in diamond upon hydrostatic pressure". In: *Physical Review B* 112.15 (2025), p. 155201. DOI: 10.1103/fq19-lfmv.

[158] N. Kalb, P. C. Humphreys, J. J. Slim, et al. "Dephasing mechanisms of diamond-based nuclear-spin memories for quantum networks". In: *Physical Review A* 97.6 (2018), p. 062330. DOI: 10.1103/PhysRevA.97.062330.

[159] A. Gali, M. Fyta, and E. Kaxiras. "*Ab initio* supercell calculations on nitrogen-vacancy center in diamond: Electronic structure and hyperfine tensors". In: *Physical Review B* 77.15 (2008), p. 155206. DOI: 10.1103/PhysRevB.77.155206.

[160] R. Kuate Defo, E. Kaxiras, and S. L. Richardson. "Calculating the hyperfine tensors for group-IV impurity-vacancy centers in diamond using hybrid density functional theory". In: *Physical Review B* 104.7 (2021), p. 075158. DOI: 10.1103/PhysRevB.104.075158.

[161] M. Mohseni, G. Thiering, and A. Gali. *Magneto-optical properties of the neutral silicon-vacancy center in diamond under extreme isotropic strain fields*. 2026. DOI: 10.48550/arXiv.2602.10690.

[162] A. M. Edmonds, M. E. Newton, P. M. Martineau, et al. "Electron paramagnetic resonance studies of silicon-related defects in diamond". In: *Physical Review B* 77.24 (2008), p. 245205. DOI: 10.1103/PhysRevB.77.245205.

[163] K. Yang, W. Paul, S.-H. Phark, et al. "Coherent spin manipulation of individual atoms on a surface". In: *Science* 366.6464 (2019), pp. 509–512. DOI: 10.1126/science.aay6779.

[164] K. R. K. Rao and D. Suter. "Characterization of hyperfine interaction between an NV electron spin and a first-shell ^{13}C nuclear spin in diamond". In: *Physical Review B* 94.6 (2016), p. 060101. DOI: 10.1103/PhysRevB.94.060101.

[165] P. Neumann, N. Mizuochi, F. Rempp, et al. "Multipartite Entanglement Among Single Spins in Diamond". In: *Science* 320.5881 (2008), pp. 1326–1329. DOI: 10.1126/science.1157233.

[166] S. Felton, A. M. Edmonds, M. E. Newton, et al. "Hyperfine interaction in the ground state of the negatively charged nitrogen vacancy center in diamond". In: *Physical Review B* 79.7 (2009), p. 075203. DOI: 10.1103/PhysRevB.79.075203.

[167] F. Jelezko, T. Gaebel, I. Popa, et al. "Observation of Coherent Oscillation of a Single Nuclear Spin and Realization of a Two-Qubit Conditional Quantum Gate". In: *Physical Review Letters* 93.13 (2004), p. 130501. DOI: 10.1103/PhysRevLett.93.130501.

[168] X.-F. He, N. B. Manson, and P. T. H. Fisk. "Paramagnetic resonance of photoexcited N- V defects in diamond. II. Hyperfine interaction with the N 14 nucleus". In: *Physical Review B* 47.14 (1993), pp. 8816–8822. DOI: 10.1103/PhysRevB.47.8816.

[169] E. Vasilenko, V. Unni Chorakkunnath, J. Resch, et al. "Optically detected nuclear magnetic resonance of coherent spins in a molecular complex". In: *Nature Materials* (2026), pp. 1–6. DOI: 10.1038/s41563-026-02539-0.

[170] A. Ulanowski, J. Früh, F. Salamon, et al. *Cavity-enhanced optical readout and control of nuclear spin qubits*. 2026. DOI: 10.48550/arXiv.2603.01987.

[171] L. Jiang, J. S. Hodges, J. R. Maze, et al. "Repetitive Readout of a Single Electronic Spin via Quantum Logic with Nuclear Spin Ancillae". In: *Science* 326.5950 (2009), pp. 267–272. DOI: 10.1126/science.1176496.

[172] L. A. O'Neill, B. Joecker, A. D. Baczewski, et al. "Engineering local strain for single-atom nuclear acoustic resonance in silicon". In: *Applied Physics Letters* 119.17 (2021), p. 174001. DOI: 10.1063/5.0069305.

[173] R. de Sousa. "Dangling-bond spin relaxation and magnetic $1/f$ noise from the amorphous-semiconductor/oxide interface: Theory". In: *Physical Review B* 76.24 (2007), p. 245306. DOI: 10.1103/PhysRevB.76.245306.

[174] B. Smeltzer, J. McIntyre, and L. Childress. "Robust control of individual nuclear spins in diamond". In: *Phys. Rev. A* 80.5 (2009), p. 050302. DOI: 10.1103/PhysRevA.80.050302.

[175] M. V. G. Dutt, L. Childress, L. Jiang, et al. "Quantum Register Based on Individual Electronic and Nuclear Spin Qubits in Diamond". In: *Science* 316.5829 (2007), pp. 1312–1316. DOI: 10.1126/science.1139831.

[176] I. B. W. Harris, I. Christen, S. M. Patomäki, et al. *High-Fidelity Control of a Strongly Coupled Electro-Nuclear Spin-Photon Interface*. 2025. DOI: 10.48550/arXiv.2505.09267.

[177] N. Kalb, J. Cramer, D. J. Twitchen, et al. "Experimental creation of quantum Zeno subspaces by repeated multi-spin projections in diamond". In: *Nature Communications* 7.1 (2016), p. 13111. DOI: 10.1038/ncomms13111.

[178] N. Codreanu, T. Turan, D. B. Rodriguez, et al. *Above-Unity Coherent Cooperativity of Tin-Vacancy Centers in Diamond Photonic Crystal Cavities*. 2025. DOI: 10.48550/arXiv.2511.13375.

Erklärung zum Einsatz generativer KI

Der Einsatz generativer künstlicher Intelligenz (KI), insbesondere in Form großer Sprachmodelle, gewinnt in Forschung und wissenschaftlicher Praxis zunehmend an Bedeutung. Die vorliegende Dissertation wurde unter Beachtung der *Handreichung zur Nutzung von generativer künstlicher Intelligenz (KI) in studentischen Arbeiten im Studium, in Abschlussarbeiten und Promotionen an der Fakultät für Physik*[1] sowie der allgemeinen *Leitlinien zum Einsatz generativer KI am KIT*[2] erstellt. Darüber hinaus wurden die Grundsätze guter wissenschaftlicher Praxis berücksichtigt.

In dieser Arbeit wurde generative KI ausschließlich als unterstützendes Werkzeug für klar abgegrenzte Aufgaben eingesetzt. Dazu gehörten insbesondere die Strukturierung von Inhalten, etwa durch Vorschläge zur Gliederung von Abschnitten und zu Übergängen zwischen Textteilen, sowie die sprachliche Überarbeitung von Textpassagen, etwa hinsichtlich Grammatik, Stil, Verständlichkeit und Kohärenz einzelner Textabschnitte. Darüber hinaus wurde generative KI punktuell zur Unterstützung bei der technischen Umsetzung von Programmcode verwendet, etwa in Bezug auf Syntax, Visualisierung oder numerische Auswertung. Als verwendete Werkzeuge wurden insbesondere ChatGPT von OpenAI und Claude von Anthropic eingesetzt; die Nutzung beschränkte sich auf die oben genannten unterstützenden Tätigkeiten.

Nicht eingesetzt wurde generative KI zur Entwicklung wissenschaftlicher Fragestellungen, zur theoretischen Modellbildung, zur Generierung, Analyse oder Interpretation experimenteller oder numerischer Daten, zur Ableitung wissenschaftlicher Schlussfolgerungen oder zur Bewertung der wissenschaftlichen Qualität, Originalität oder Relevanz der in dieser Arbeit dargestellten Ergebnisse.

Die Verantwortung für sämtliche Inhalte dieser Dissertation liegt vollständig beim Autor. Alle durch generative KI unterstützten Inhalte wurden kritisch geprüft, eigenständig überarbeitet und inhaltlich verifiziert. Die Verwendung generativer KI erfolgte in dem Bewusstsein ihrer Grenzen, insbesondere hinsichtlich möglicher sachlicher Fehler, Verzerrungen und unvollständiger Quellenbezüge, sowie unter Wahrung der geltenden rechtlichen, ethischen und wissenschaftlichen Standards.

---

[1] Institut für Meteorologie und Klimaforschung, *Handreichung zur Nutzung von generativer künstlicher Intelligenz (KI) in studentischen Arbeiten im Studium, in Abschlussarbeiten und Promotionen an der Fakultät für Physik*, letzte Änderung: 03.06.2025, URL: `https://www.imktro.kit.edu/13269.php`, Zugriff am 18.05.2026.

[2] Karlsruher Institut für Technologie, *Leitlinien zum Einsatz generativer KI am KIT*, Stand: 30.06.2025, URL: `https://www.kit.edu/downloads/KI-Leitlinien-de.pdf`, Zugriff am 18.05.2026.

Danksagung

Nach über zehn Jahren am KIT geht meine Zeit in Karlsruhe zu Ende. Bei all den Menschen, die mich auf diesem Weg begleitet haben, möchte ich mich mit den folgenden Zeilen bedanken.

An erster Stelle möchte ich dir, David, danken für die Möglichkeit, meine Masterarbeit und anschließend meine Promotion bei dir machen zu dürfen. Deine Expertise und deine andauernde Motivation haben mich immer wieder aufs Neue begeistert. Schon als ich damals fürs Hauptseminar das erste Mal wieder aus deinem Büro kam, war ich überzeugt, daran hat sich seitdem nichts geändert. Deine entspannte Art, die Gruppe zu führen, deine Begeisterung für neue Ergebnisse und dein tiefes Verständnis der Materie haben diese Promotion möglich, spaßig und erfolgreich gemacht. Vielen vielen Dank!

Wolfgang, danke dir für die Übernahme der Zweitbetreuung. Deine offene und ehrliche Art hat dafür gesorgt, dass ich mich immer wohlgefühlt habe, auch wenn ich am Anfang ein bisschen Bammel hatte, zu dir in den Keller zu kommen und zu beichten, was wir mal wieder am Kryostaten getrieben hatten. Egal, ob am Wochenende, wenn der Kryostat Faxen gemacht hat, oder unter der Woche: Du warst da und hast geholfen und zugehört. Vielen Dank dir dafür!

Ganz besonders bedanken möchte ich mich bei dir, Ioannis. Ohne dich wäre das alles nicht möglich gewesen. Es war eine tolle Zeit, und ich hätte mir keinen besseren Laborpartner für die unzähligen Tage und Nächte im Labor und die hitzigen Diskussionen vorstellen können. Ich kenne ehrlich gesagt keinen Experimentalphysiker, der schneller denkt, aufbaut und misst als du. Ich bin wirklich froh, dass ich das alles mit dir machen durfte, und wenn irgendwer das SnV als Quantenknoten baut, dann du.

Evgenij, mit dir bin ich bei Trash-TV-Nächten, beim Neureuter Döner-Pizza-Mann, deinen legendären Grill-Abenden, bei Diät und Gym wirklich durch dick und dünn gegangen; durchaus wörtlich nehmen. Ich musste nie eine Sekunde überlegen, mit wem ich mir mein Zimmer auf den diversen Tagungen teilen sollte, und unseren China-Urlaub werde ich nie vergessen. Auch wenn es bei mir am Ende ein bisschen eingebrochen ist: Das bekommen wir wieder hin. Du bist einer meiner besten Freunde geworden, und mit dir hatte ich immer großartig viel Spaß und werde dich, egal in welches Neubaugebiet du ziehst, besuchen kommen. Das morgendliche Gossip-Gym wird mir definitiv fehlen.

Nola, wir haben uns erst spät in meiner Promotion und eher zufällig in der Weihnachtsfeier-Planung kennengelernt, und trotzdem ist daraus eine der schnellsten Freundschaften geworden, die ich je geschlossen habe. Von unseren Sonntags-Rentnerspaziergängen, der spooky Hütte im Schwarzwald zu den Heated-Rivalry-Abenden, ich bin wirklich froh, dass

du immer da warst und mir immer zugehört hast. Egal wo es uns am Ende hin verschlägt, es werden noch einige Pasta-Wein-Eis-Abende kommen.

Kerim, deine ruhige und entspannte Art tat mir und, ich denke, der ganzen Gruppe gut. Das gilt nicht nur für jeden Tag im Büro, die Croissant- und Cappuccino-Freitage, sondern auch besonders für unseren USA-Urlaub, in dem ich die Passenger Princess war. Vielen Dank, dass du immer da warst.

Luis, danke für die gute Laune und die schlechte Musik im Labor. Mit dir lässt sich auch nach der dritten Stunde, in der dein Piezo wieder mal hin und her fährt, noch hervorragend quatschen. Du bist ein absolut liebenswerter Mensch.

Der gesamten Hunger-Gruppe: Jonas, Vishnu, Monsieur Hessenauer, Andras, Svenja, Shalom, Max, Timon, Larissa, Nick und den Studis Matthias, Carlo, Julian, Michel, Tim und Mohamed, den Wernsdorfers, insbesondere Christoph, Dennis, Viktor, Thomas, Alex, Luca, Danilo und allen anderen, die ich eventuell vergessen habe, danke für den Zusammenhalt, die Hilfe, die Diskussionen, die Ausflüge und die vielen schönen Abende.

Genauso möchte ich allen anderen am PHI und in den Werkstätten, die im Hintergrund dafür sorgen, dass wir unsere Forschung überhaupt machen können, insbesondere Steffi und Claudia, danken; ohne euch läuft hier nichts.

Zum Schluss, aber am wichtigsten: Mama, Papa und Marie. Ihr habt mich immer unterstützt und mir gerade bei schwierigen Entscheidungen bestätigt, dass das, was sich gut anfühlt, auch das Richtige ist. Dass ich diesen Weg überhaupt gehen konnte, verdanke ich euch. Dafür bin ich euch unendlich dankbar.